A Class of origami-inspired lockable metamaterials

By

Amin Jamalimehr

Department of Mechanical Engineering

McGill university

Montreal, Quebec, Canada

August 2023

A Thesis submitted to McGill University in fulfillment of the requirements of the Degree of Doctor of Philosophy in Mechanical Engineering

Dedication

To

My loving wife, **Mahsa**,

My father, **Sattar**, *and my mother*, **Zahra**,

My adorable sister, **Sareh**.

And in the memory of

Victims of Iranian revolution of **Woman, Life, Freedom**.

Abstract

The resource dwindling of our planet calls for the development of environmentally-friendly materials that can preserve our environment. Paper is one of them and has long been used mainly for artwork, printing, and packaging. Only recently, the art of paper folding, i.e., Origami, has been leveraged to create structural materials that can spatially fold from a flat sheet into a structurally resistant material. This thesis proposes using folds and cuts in sheets of paper to generate a class of environmentally-friendly materials that attain both load-bearing and energy absorption capacity.

On the first front, chapter 2 introduces a strategy to impart multidirectional load-bearing capacity to a stacked structure of papers. Most origami concepts in the literature cannot provide load-bearing capacity, and those that can, do so in specific directions but collapse along the direction of deployment, limiting their use as structural materials. Here we introduce a rigidly foldable class of cellular metamaterials that can flat-fold and lock into several stiff states across multiple directions, including the deployment direction. Our metamaterials rigidly fold with one degree of freedom and can reconfigure into several flat-foldable and spatially-lockable folding paths due to face contact. Locking under compression yields topology and symmetry changes that impart multidirectional stiffness. Additionally, folding paths and mixed-mode configurations can be activated in situ to modulate their properties. Their load-bearing capacity, flat-foldability, and re-programmability can be harnessed for deployable structures, reconfigurable robots, and low-volume packaging.

A second trajectory explored in this thesis stems from relaxing the rigid foldability restriction of the origami panels to enable energy absorption and dissipation. Most of the existing multistable concepts used to absorb energy rely on inclined beams and shallow shells supported by heavy and bulky frames, which do not contribute to deformation and energy dissipation. In chapter 3, this thesis presents an origami-inspired multistable material with an extensive range of multistable reconfiguration that can substantially dissipate energy. The reconfiguration process consists of two phases. First, the panels rotate rigidly about their connection lines. Next, while a set of panels provide axial stiffness, the other set undergoes flexural deformation leading to snap-through instability. The axial stiffness offered by the first set of panels eliminates the need for stiff and bulky frames, culminating in a more efficient distribution of the base material. In addition, we propose a relatively simple yet effective method of manufacturing layered structures from paper

and polymeric sheets. The energy absorption capability and relatively easy manufacturing method make them a good candidate for the packaging industry.

Overall, this research contributes to the following fronts: (1) Developing a reconfigurable load-bearing paper-based material inspired by the art of paper folding; (2) Offering a strategy for designing paper-based energy absorbers; (3) Proposing a low-cost, lightweight, and sustainable material that is structural, flat-transportable and in situ deployable as well as safely disposable upon the end of its service life. The concept introduced here may find a wide range of applications, from aerospace, flexible electronics, and packaging to furniture.

Résumé

L'épuisement des ressources de notre planète appelle au développement de matériaux écologiques qui peuvent préserver notre environnement. Le papier est l'un d'entre eux et a longtemps été utilisé principalement pour les œuvres d'art, l'impression et l'emballage. Ce n'est que récemment que l'art du pliage du papier, c'est-à-dire l'Origami, a été mis à profit pour créer des matériaux structurels qui peuvent se plier dans l'espace à partir d'une feuille plate pour devenir un matériau structurellement résistant. Cette thèse propose d'utiliser les plis et les coupes dans les feuilles de papier pour générer une classe de matériaux écologiques qui atteignent à la fois une capacité de charge et d'absorption d'énergie.

Sur le premier point, le chapitre 2 présente une stratégie visant à conférer une capacité de charge multidirectionnelle à une structure empilée de papiers. La plupart des concepts d'origami de la littérature ne peuvent pas fournir de capacité de charge, et ceux qui le peuvent le font dans des directions spécifiques mais s'effondrent dans la direction du déploiement, ce qui limite leur utilisation comme matériaux structurels. Nous présentons ici une classe de métamatériaux cellulaires rigidement pliables qui peuvent se plier à plat et se verrouiller dans plusieurs états de rigidité dans plusieurs directions, y compris la direction de déploiement. Nos métamatériaux se plient de manière rigide avec un degré de liberté et peuvent se reconfigurer en plusieurs chemins de pliage à plat et verrouillables dans l'espace grâce au contact des faces. Le verrouillage sous compression entraîne des changements de topologie et de symétrie qui confèrent une rigidité multidirectionnelle. De plus, les chemins de pliage et les configurations en mode mixte peuvent être activés in situ pour moduler leurs propriétés. Leur capacité de charge, leur pliabilité à plat et leur reprogrammabilité peuvent être exploitées pour des structures déployables, des robots reconfigurables et des emballages à faible volume.

Une deuxième voie explorée dans cette thèse consiste à assouplir la restriction de pliabilité rigide des panneaux d'origami pour permettre l'absorption et la dissipation d'énergie. La plupart des concepts multi-stables existants utilisés pour absorber l'énergie reposent sur des poutres inclinées et des coquilles peu profondes soutenues par des cadres lourds et encombrants, qui ne contribuent pas à la déformation et à la dissipation de l'énergie. Dans le chapitre trois, cette thèse présente un matériau multi-stable inspiré de l'origami avec une gamme étendue de reconfiguration multi-stable qui peut dissiper une grande quantité d'énergie. Le processus de reconfiguration se compose de

deux phases. Tout d'abord, les panneaux tournent de manière rigide autour de leurs lignes de connexion. Ensuite, tandis qu'un ensemble de panneaux assure la rigidité axiale, l'autre ensemble subit une déformation en flexion, ce qui entraîne une instabilité de type "snap-through". La rigidité axiale offerte par le premier ensemble de panneaux élimine le besoin de cadres rigides et encombrants dans notre structure, ce qui se traduit par une distribution plus efficace du matériau de base. En outre, nous proposons une méthode relativement simple mais efficace de fabrication de structures en couches à partir de feuilles de papier ou de polymères. La capacité d'absorption d'énergie et la méthode de fabrication relativement facile en font un bon candidat pour l'industrie de l'emballage.

Dans l'ensemble, ces travaux de recherche contribuent aux objectifs suivants : (1) développer un matériau porteur reconfigurable à base de papier inspiré de l'art du pliage du papier ; (2) proposer une stratégie de conception d'absorbeurs d'énergie à base de papier ; (3) proposer un matériau peu coûteux, léger et durable qui soit structurel, transportable à plat et déployable in situ, et qui puisse être éliminé en toute sécurité à la fin de sa vie utile.

Acknowledgment

I am immensely thankful to my supervisor, Prof. Damiano Pasini, for his unwavering support and profound trust. His commitment to the personal and professional development of his students is truly commendable. Throughout my PhD journey, I have been enriched by his expert supervision, extensive technical acumen, and profound research expertise. As a supervisor, his diligence, dedication, and resourcefulness have consistently inspired me to strive for the utmost academic excellence. I would also like to express my appreciation to my co-supervisor, Prof. Abdolhamid Akbarzadeh, whose consistent support and technical expertise greatly facilitated my journey through my PhD studies.

I appreciate the nice friends from “The Pasini Group” whom I was pleased to meet and know. Particularly, I wish to thank my dear friend Ahmed Moussa who helped me so much in my first year, during my hardest moments. My other team members: Lu Liu, Meisam Asgari, Chuan Qiao, Amr Farag, Hang Xu, Ruizhe Ma, Shakurur Rahman, Asma El Elmi, Lei Wu, Wendy Li, and Abdulrahman Almessabi, Nicholas D’ambrosio, Arnob Islam and many others, thank you for the good times.

I would like to thank Prof. Jianyu Li, Prof. Yixiang Wang, Prof. Pascal Hubert, and Prof. Francois Barthelat who provide me with access to their tensile testers. A special thanks goes to Meisam Aghajani who provided technical assistance with manufacturing testing setups. I would like to thank members of “Lunch with Eshghi”, Hossein, Mohsen and Alireza, for memorable lunch hours and enjoyable *pointless* discussions. Many thanks to my dear friends Shahin Eskandari and Hossein Mofatteh for constructive scientific discussions which I believe culminated in mutual academic growth.

I want to extend my profound gratitude to my beloved wife, Mahsa. Your steadfast presence during the myriad challenges of my PhD studies has been an unwavering source of strength. Your encouragement and heartfelt support have transformed my academic pursuit into a voyage of joy and discovery. My appreciation for my loving parents and my dear sister knows no bounds; your sacrifices on my behalf evoke a deep sense of indebtedness and gratitude within me. Despite physical distance separating us, the mere sound of your comforting voices over the phone has consistently filled my heart with warmth, love, and unwavering support.

Claim of originality

The following list summarizes the main findings accomplished in this thesis.

- A class of rigidly-foldable origami-inspired mechanical metamaterial has been introduced to achieve multiple lockable and flat-foldable states. Lockable states are able to withstand large external loads in multiple directions.
- A method for manufacturing layered origami patterns has been proposed, which can be easily automated to increase the manufacturing rate.
- A series of innovative test setups has been developed that can be employed in research on origami-inspired structures.
- A class of multistable origami-based structures has been developed. It has been shown that these structures have an extensive range of multistable reconfigurations that can effectively dissipate energy.

Table of contents

List of figures

List of tables

Contribution of the author

This is a manuscript-based thesis consisting of two journal articles. The title of the articles, name of the authors, and their contributions are listed below:

1) Rigidly flat-foldable class of lockable origami-inspired metamaterials with topological stiff states

Amin Jamalimehr, Morad Mirzajanzadeh, Abdolhamid Akbarzadeh, and Damiano Pasini

Nature Communications 13, 1816 (2022). https://doi.org/10.1038/s41467-022-29484-1

Author Contributions:

A.J.: Conceptualization, Methodology, Software, Investigation, Validation, Writing – original draft, Writing - review & editing.

M.M.: Methodology, Investigation, Writing - original draft, Validation, Writing - review & editing.

H.A.: Supervision, Writing - review & editing, Project administration, Funding acquisition.

D.P.: Conceptualization, Methodology, Investigation, Supervision, Writing - original, Writing - review & editing, Project administration, Funding acquisition.

2) A multistable class of origami-inspired metamaterials for mechanical damping and vibration mitigation under oscillatory motion

Amin Jamalimehr, Abdolhamid Akbarzadeh, Damiano Pasini

To be submitted, 2023

Author Contributions:

A.J.: Conceptualization, Methodology, Software, Investigation, Validation, Writing – original draft, Writing - review & editing.

H.A.: Methodology, Investigation, Supervision, Writing - review & editing, Project administration, Funding acquisition.

D.P.: Conceptualization, Methodology, Investigation, Supervision, Writing - original, Writing - review & editing, Project administration, Funding acquisition

Chapter 1

Introduction and literature review

Chapter 1: Introduction and literature review

Materials contribute to chart human history. The significance of materials in human civilization is reflected in the system of names we currently use to denote three historic ages (e.g., Stone Age, Bronze Age and Iron Age). Materials have been the backbone of engineering development across sectors and disciplines. The rapid developments of the 20^{th} century, especially in the areas of manufacturing, have resulted in the emergence of new engineering materials with enhanced properties capable of attaining outstanding performance.

1.1 Metamaterials

Metamaterials are artificially engineered materials with exceptional thermal [1-3], photonic [4, 5], optical [6-8], electromagnetic [9], acoustic [10-13], or mechanical properties [14-19] that differ significantly from those of natural materials. Metamaterials are constructed by arranging small structures, known as unit cells, in a specific pattern, leading to unconventional behaviors. The unit cells can range from wires [20], beams [21], plates [22], shells [23], split-ring resonators [24], acoustic resonators [12, 13], gears [25, 26] and hinged links [27]. These materials can exhibit unprecedented properties, such as negative Poisson's ratio [15, 17, 28], negative [2, 3] and unlimited coefficient of thermal expansion [1], and negative refraction index [11]. Metamaterials are considered a novel field of study and hold great potential for a variety of technological applications, including super-resolution imaging [6-8], energy harvesting [29-32], electromagnetic shielding [33], noise reduction [34], impact mitigation [35-38], and vibration damping [39-42]. Figure 1-1 shows a series of applications of metamaterials from various fields of study.

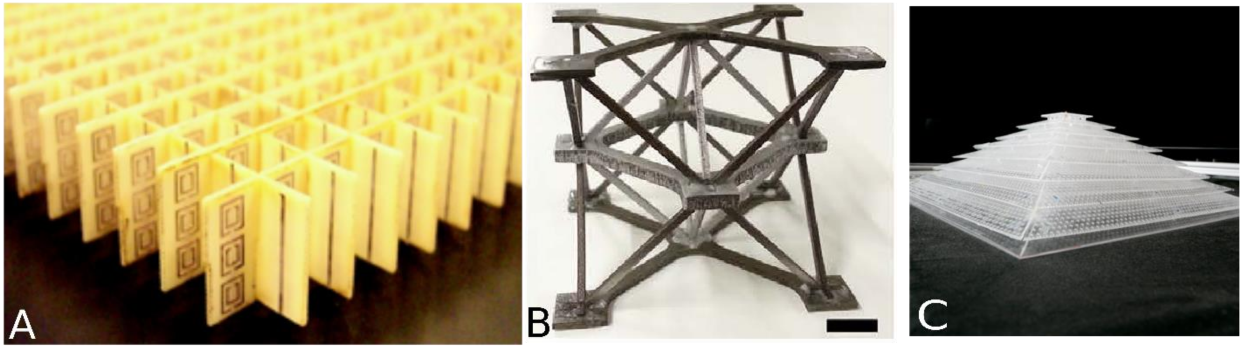

Figure 1-1 Examples of metamaterials; **A** Metamaterial lattice with negative refraction index. The array of square split-ring resonators gives the material a negative magnetic permeability, while the array of straight wires gives it a negative permittivity [43] **B** Architected material consisting of two constituents with tunable coefficient of thermal expansion [3]. **C** Metamaterial system proposed as a three-dimensional acoustic cloak, where acoustic waves cannot detect the object at the center of the pyramid [44]

1.2 Mechanical metamaterials

Mechanical metamaterials are a subset of metamaterials that exhibit unconventional mechanical properties, including negative stiffness [45, 46], negative Poisson's ratio [47-50], zero thermal expansion [1, 3], energy absorption [23, 42, 51, 52], energy dissipation [39, 42, 52], and energy entrapment [53]. The underlying structure of mechanical metamaterials often consists of periodically arranged building blocks [14]. With the emergence of novel manufacturing technologies, amorphous and non-periodic structures have also been introduced [14]. Figure 1-2 shows a collection of mechanical metamaterials.

Mechanical metamaterials can be loosely classified with respect to their characteristics [14], including the mechanical response of the base material, the underlying deformation mechanism in the base material and the topology of the deformable unit. The mechanical response of the base material can be of various types including linear elastic, hyperelastic, and viscoelastic. A deformable building block can be made of hinges, beams, and thin shells among other basic structural elements. The deformation can take place locally or throughout the structure of the material. A subclass of mechanical metamaterials with localized deformations is mechanism-based metamaterials [14].

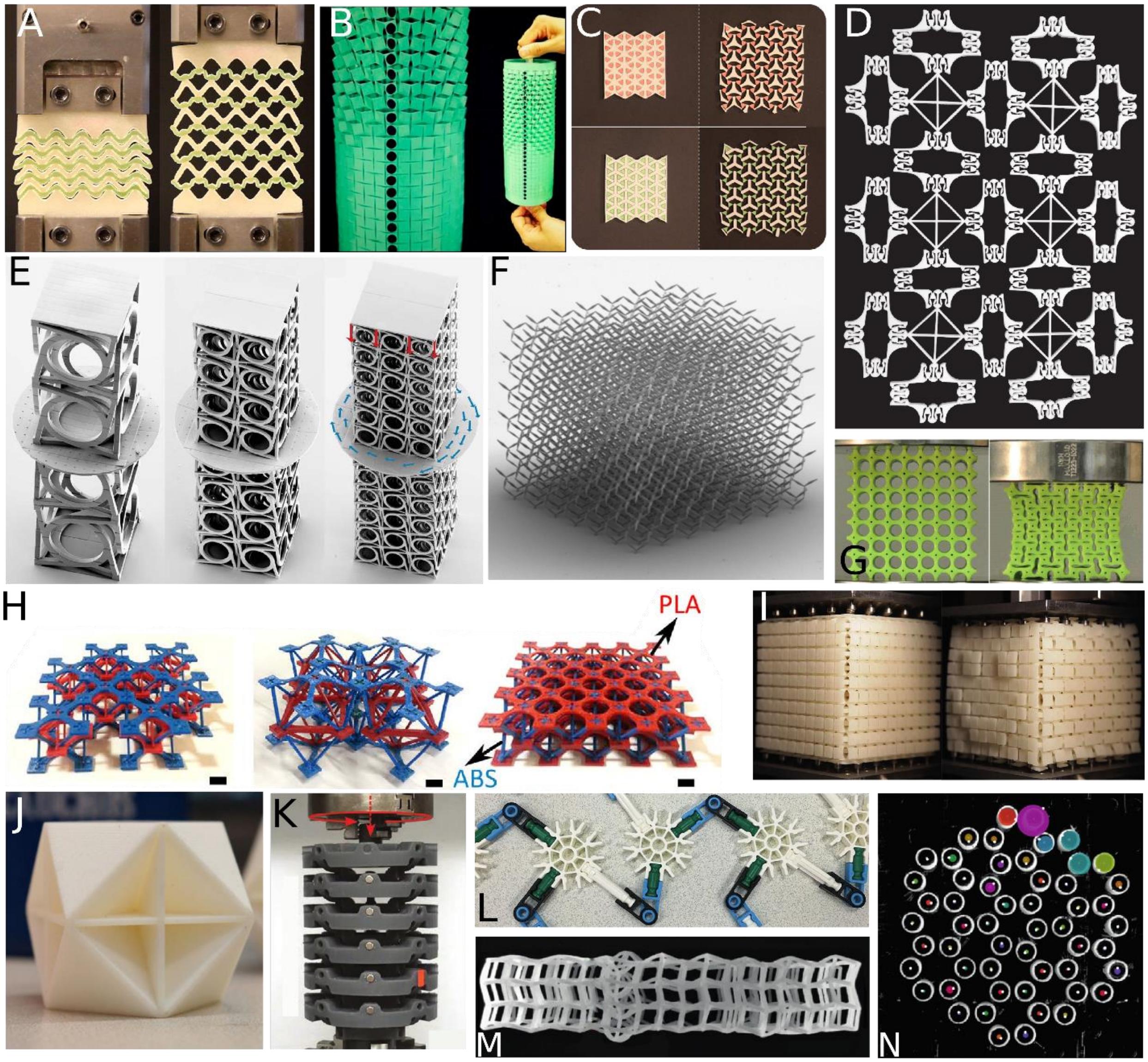

Figure 1-2 Examples of mechanical metamaterials; **A** Snapping metamaterial in tension [54], **B** Propagating instability along perforated shell [55], **C** Bistable auxetic metamaterials [49], **D** Two dimensional instability-based mechanical metamaterial [56], **E** Mechanical metamaterials with coupling of axial and rotational response [16], **F** Metamaterial with high bulk modulus to mass ratio, the shear modulus is approximately zero [57], **G** Instability induced negative Poisson's ratio [17], **H** Metamaterial with tunable coefficient of thermal expansion [3], **I** A combinatorial metacube consisting of 10 × 10 × 10 unit cells; under uniaxial compression distinct patterns can appear on the faces of the cube [58], **J** Unit cell of material with maximum stiffness to mass ratio (i.e. Hashin-Shtrikman bound) [22], **K** Magnetically assisted rotary damper [42], **L** A metamaterial with switchable topological polarization that alternate between deformable

and stiff states [25], **M** A metamaterial in which states of self-stress enable selective buckling [59], **N** Gyroscopic metamaterial preventing the scatter of sound waves from the boundaries to the bulk of the material [60]

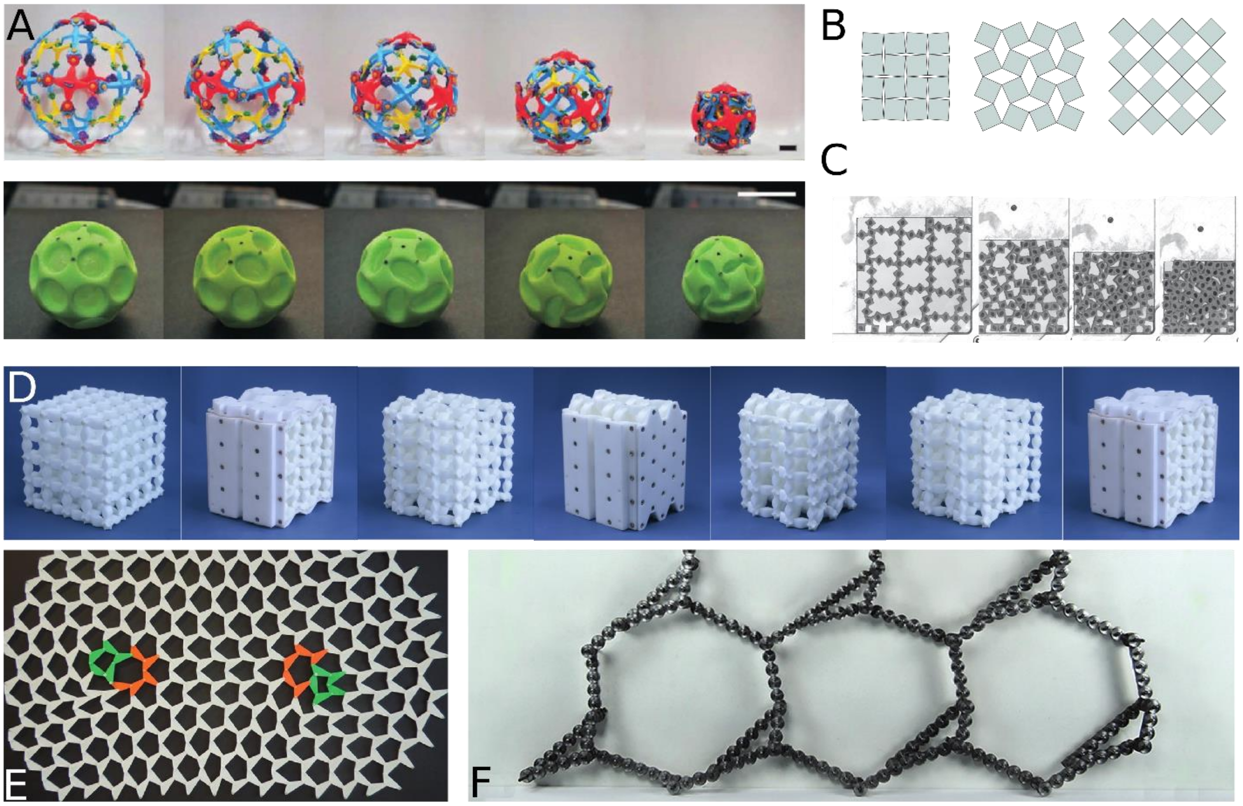

Figure 1-3 Examples of mechanism-based mechanical metamaterials: **A** Hoberman sphere, a popular toy and a pneumatically actuated mechanical metamaterial that has similar collapsible behavior to Hoberman sphere [61], **B** An auxetic material made of squares hinged at their vertices [62], **C** A shape changing metamaterial featuring multiple steps of deformation inspired by square based auxetic metamaterials in (B) [18], **D** A material with zero energy modes that can reconfigure to adopt its boundary to a variety of shapes [63], **E** Localization of zero mode (modes with zero elastic energy) around a dislocation in a topological metamaterial [27], and **F** Gears mounted on solid links, connected through joints and arranged into a lattice to form a geared topological metamaterial [26].

A widely studied class of mechanism-based materials stems from origami and kirigami principles. Origami and kirigami, the arts of paper folding and paper cutting, have recently received much attention in engineering and beyond.

1.3 Mechanism-based metamaterials

Mechanism-based metamaterials incorporate mechanical elements into their structure to allow some degree of motion [14]. The mechanical components, such as actuators, hinges, or beams, are designed to interact with each other and with external stimuli to produce specific mechanical responses [14]. This interaction allows the material to exhibit unique functionalities, such as changing its shape, acoustic properties, and thermomechanical behavior [14]. Slender elements, e.g., beams and shells, are the cornerstone of designing mechanical metamaterials since they allow for large reconfigurations. Large deformations lead to nonlinearities, including elastic, snap-through and snap-back instabilities. Nonlinearities and instabilities have been employed to incorporate advanced functionalities, such as multistability and programmability, into mechanical metamaterials. Figure 1-3 shows examples of mechanism-based metamaterials.

1.4 Origami

Origami is the traditional Japanese art of paper folding. The word "origami" comes from the Japanese words "ori" (to fold) and "kami" (paper). Origami has a long history in Japan, with the documented evidence of paper folding dating back to the 17th century [64]. Figure 1-4A shows the first documented origami principle. Today, origami is enjoyed by people of all ages and backgrounds, and it has also been used in various fields, such as mathematics [64, 65], science [66-69], engineering [70-88], and art design [89, 90]. The basic origami technique is to fold a flat sheet of paper into a desired shape. Three-dimensional shapes can be constructed from flat sheets by following a set of instructions collected in a folding diagram, which also contains the sequence of folding. Figure 1-4 shows the application of origami in several fields, from architecture and jewelry to fashion and art.

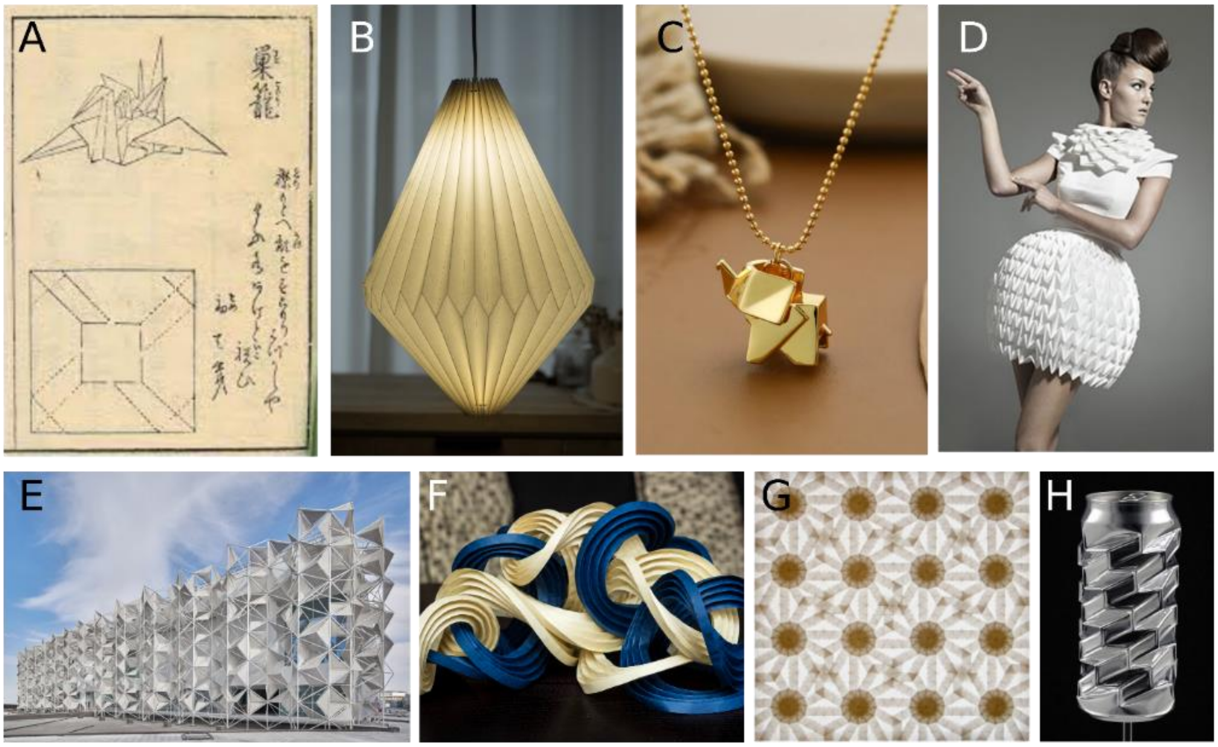

Figure 1-4 Application of origami patterns: **A** The first document on origami principles showing the fold lines and the final configuration, **B** Origami lamp shade, **C** Origami inspired jewelry, **D** Origami inspired dress, **E** Origami as façade of a building, **F** Decorative curved crease origami, **G** Twist tilling origami [65], and **H** Origami pattern as the texture of a beverage can.

1.5 Kirigami

Kirigami is a Japanese art that involves cutting and folding paper to create intricate designs and patterns. The word kirigami comes from the Japanese words “kiru” that means to cut, and “kami” that means paper. Unlike origami, the art of folding paper, kirigami allows cutting paper to create 3D models and designs. One advantage of kirigami over origami is that kirigami enables more complicated designs since cutting the base material provides more freedom than folding [91]. Kirigami is often used to create pop-up books, greeting cards, and other paper crafts. Figure 1-5 shows applications of kirigami in art and engineering.

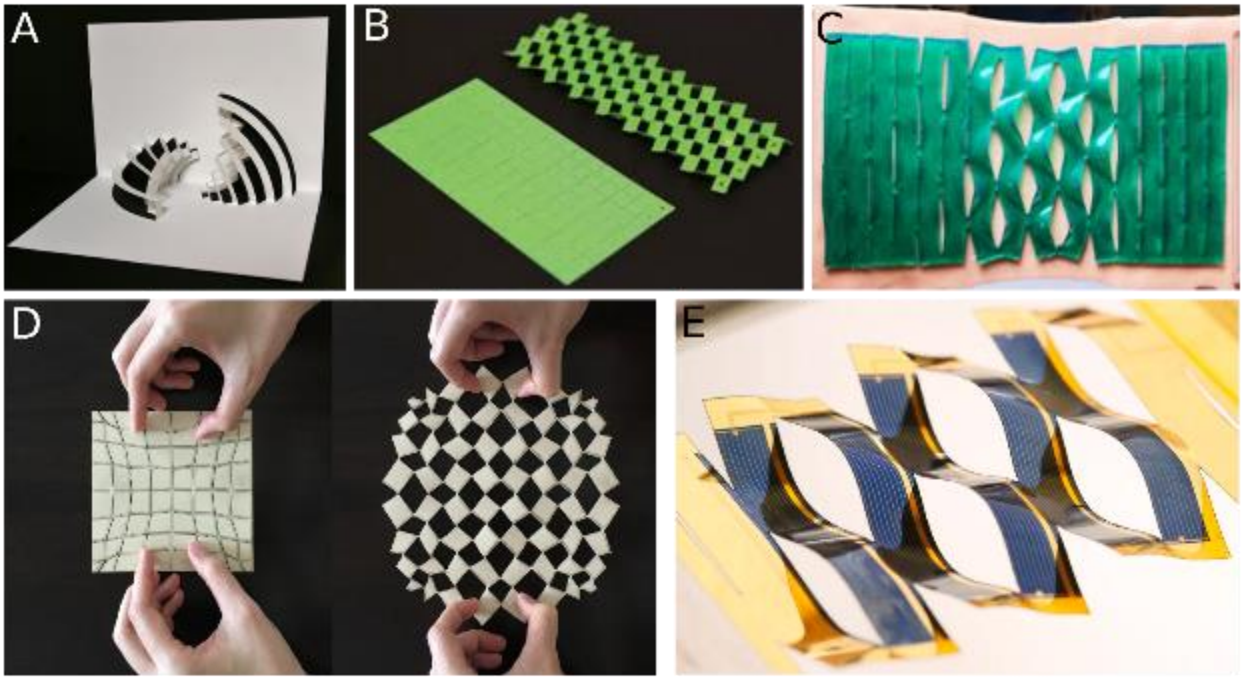

Figure 1-5 Kirigami-inspired structures and engineering applications of kirigami: **A** A classical pop-up kirigami, **B** An instability induced three-dimensional kirigami structure [92], **C** Stretchability of kirigami patterns inspired new bandages that better adhere to skin [93, 94], **D** Kirigami cuts as a means to program boundaries and surfaces [95], **E** Kirigami patterns as a means for tracking a solar path in flexible solar cells [96].

Kirigami is used in science [91, 97, 98] and engineering [99] to create structures that can fold and unfold, such as solar panels [96], medical devices, and robotic actuators [99]. Kirigami has also been used in designing facades of buildings and architectural structures, as it allows the creation of complex geometric shapes and patterns [100].

1.6 Mathematical tools

The study of origami/kirigami in mathematics focuses on the pattern geometry, topology, and mobility. The field encompasses various aspects of mathematics, including Euclidean and non-Euclidean geometry [64, 65], graph theory, knot theory, and algorithms [101]. Researchers in this field are interested in understanding the mathematical foundations of origami/kirigami, developing new methods for folding/cutting and deriving rules to assess and predict their reconfiguration. Mathematical tools are developed to gain deeper insights into the folding principles, which in turn are often applied in several engineering sectors, from aerospace, robotics [102], to materials science [67].

A nomenclature is required to understand origami from a mathematical point of view. Figure 1-6 shows the basic features and terminology commonly adopted in the origami field and throughout this thesis.

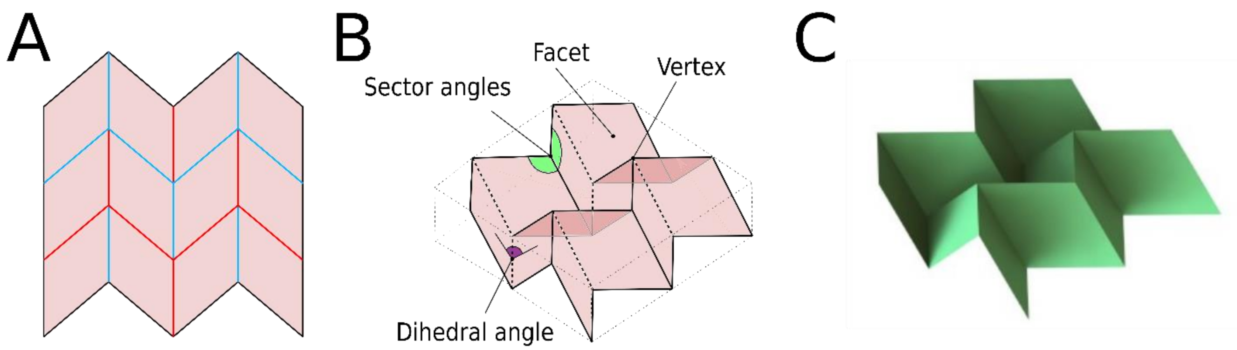

Figure 1-6 Nomenclature of origami: **A** Origami pattern in the fully developed (flat) configuration; red lines denote mountain folding while valley folds are indicated with blue lines. **B** A folded configuration **C** A render of a well-known origami pattern (Miura).

In general, origami can be considered as a series of flat panels (facets) connected at their edges. Figure 1-6A shows a fold pattern on which fold lines are assigned either a mountain or a valley folding. A fold line is called mountain (valley) folding, provided it leads to the convex (concave) dihedral angle between the connected faces (or facets) in the folded state, Figure 1-6B. The fold lines meet at a shared point of neighbor faces, namely a vertex. In the origami literature, a configuration is a state of folding that can be realized when the dihedral angles assume specific values, e.g., Figure 1-6C. Typically, in origami mathematics, the panels are assumed to be infinitely rigid. This assumption has formed the pure mathematical investigations and the study of origami systems as reconfigurable mechanisms.

The mathematical study of origami has culminated in several theorems that postulate the mechanism of shape formation by origami principles [65, 101]. These theorems help to classify origami systems which play a pivotal role in understanding the properties of origami patterns. Here we briefly discuss these classifications.

1.1.1 Developability and Flat-foldability

The first classification concerns only the origami's initial and final state. Developable origami patterns can be made by sequential folding of a flat sheet [64, 65], while non-developable origami patterns cannot be flattened into a monolithic sheet. Developable patterns are characterized by zero gaussian curvature in their initial and final pattern while non-developable patterns may acquire non-zero gaussian curvatures. Figure 1-7 shows examples of developable and non-developable origami patterns.

In the case of origami, *developability* refers to a property of the initial configuration of the pattern and describes its ability to unfold (flattened) without stretching or cuts. Another property known as *flat-foldability* refers to the final configuration and specifies the property of folding into a final flat surface. A flat-foldable origami can be folded into a two-dimensional shape [64, 65]. Flat-foldability is widely studied in mathematics of origami. Two types of flat-foldability have been classified in the literature, local and global. A locally flat-foldable pattern can be folded to a two-dimension configuration in the vicinity of a vertex. On the other hand, a globally flat-foldable pattern comprises several facets and vertices which can be folded as a whole into a two dimensional plane. Maekawa and Kawasaki theorems clearly stipulate the conditions for local flat-foldability [65]. However, global flat-foldability has been proved to be notoriously challenging and so far no decisive theorem has been derived to describe the global flat-foldability of a generic origami pattern [101]. Figure 1-8 shows examples of flat-foldable and non-flat foldable origami patterns. In summary, developability pertains to the initial configuration, while flat-foldability describes a property of the final configuration without considering the folding process.

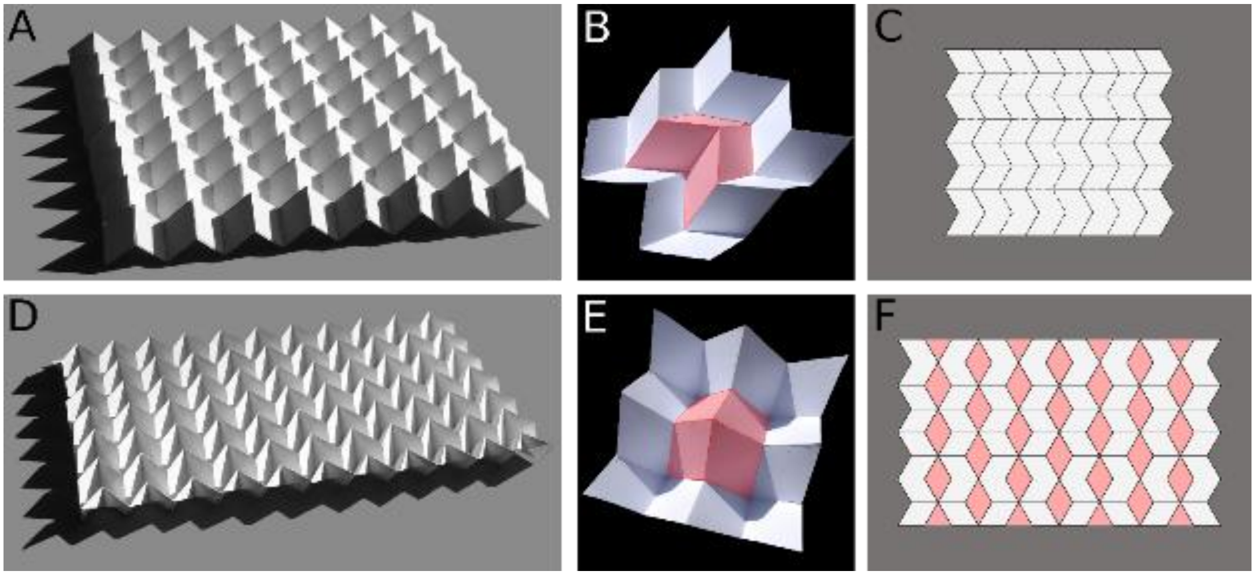

Figure 1-7 Developable and non-developable origami patterns [103]: **A** Miura origami pattern, a developable origami system, **B** The building block of the Miura pattern, **C** Fully developed configuration of Miura pattern; no cut is required to unfold the pattern, **D** Eggbox origami pattern, a non-developable origami system, **E** The building block of the eggbox pattern, **F** Fully developed configuration of eggbox pattern, where cuts (red regions) are required to unfold the pattern into a flat surface.

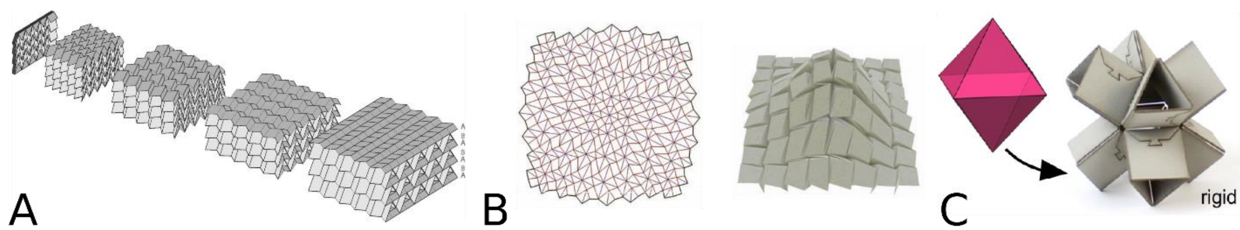

Figure 1-8 Flat foldable and non-flat foldable origami patterns; **A** A flat-foldable but non-developable origami pattern made of interleaved Miura pattern [104], **B** A modified square-based Ron Resch pattern, a developable but non-flat-foldable [105]; a non-flat-foldable but developable origami system, **C** Snapology, a non-flat-foldable and non-developable origami pattern [87].

1.1.2 Rigid-foldability

The next criterion for classifying origami systems examines the transition state from one shape to another. A rigid-foldable origami system can deploy with deformations exclusively concentrated only in the fold lines of the crease pattern [106]. Non-rigid-foldable origami systems require the deformation of panels during reconfiguration [71, 76, 77, 79]. Figure 1-9 shows examples of rigid-foldable and non-rigid foldable origami patterns.

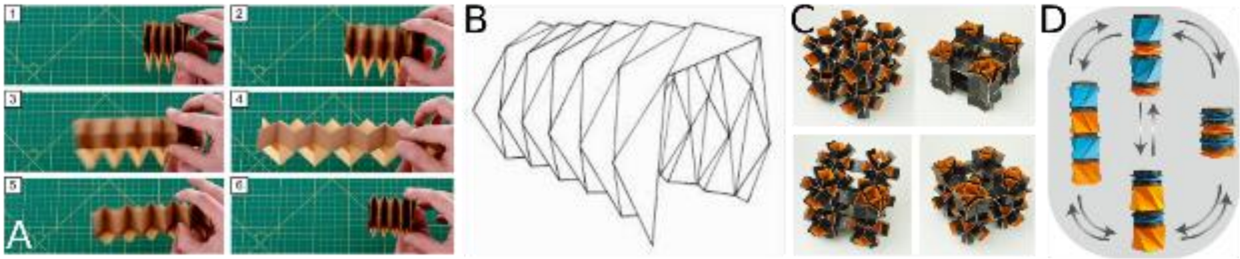

Figure 1-9 Rigid foldable versus non-rigid foldable origamis: **A** A zipper assembly of tubular origami, an example of a rigidly foldable pattern; the tubular system is made by assembling an eggbox pattern on a Miura system [107], **B** Yoshimura pattern, an example of a rigidly foldable pattern [108], **C** Snapology-inspired origami system, a non-rigid-foldable pattern [109], **D** Non-rigid-foldable Kresling pattern [81, 110]

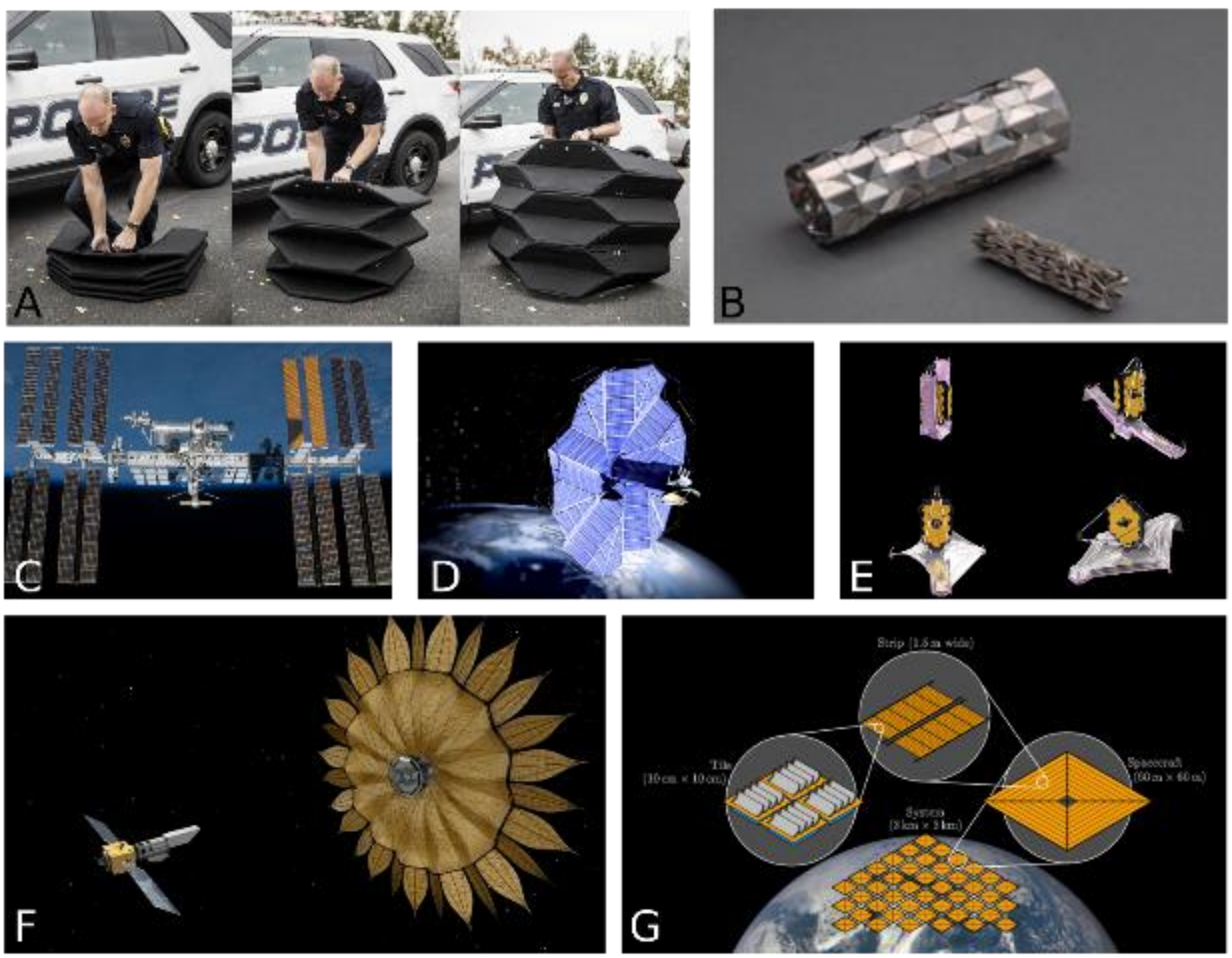

Figure 1-10 Application of origami in engineering; **A** Collapsable origami-inspired kevlar bullet-proof shield based on Yushimora origami system [111], **B** Origami-inspired artery stent [112], **C** Deployable solar panels of international space station [111], **D** An origami-inspired concept for deploying the solar panels of satellites [111], **E** Deployment of the solar shield of James Webb Space Telescope [113], **F** An origami-inspired solar shield [114], **G** A modular concept for deployment of solar panels in geostationary earth orbit; each module is made of deployable planar origami [115]

The theory of mechanisms [116, 117] can explain rigid foldability. In mechanism theory, a configuration is commonly described by the independent parameters that govern the mechanism motion, namely the degrees of freedom. In the framework of mechanism theory, origami can be modeled as a network of rigid bodies connected by hinge joints.

1.7 Choice of the base material

Origami relies on the selection of a suitable base material to facilitate their geometric folding and reconfiguration. The choice of the base material is highly dependent on the pattern and the manufacturing process; hence it is difficult to list general requirements. Nonetheless, we can highlight below key properties the base material of an origami could benefit from:

- Flexibility: The selected base material should exhibit adequate flexibility to enable precise folding around the creases without the risk of fracture and/or tear.
- Strength: The base material should possess the required degree of strength to maintain the integrity of the folded shapes. Brittle base materials may compromise their structural stability and durability.
- Size and Shape of the base material sheet: Origami are typically folded from a sheet of square or rectangular shape to generate a pattern that can transform into spatial reconfiguration. The selection of the size and shape of the base sheet to fold should thus account for these geometric considerations.
- Thickness: The thickness of the base material plays a pivotal role in the folding and contributes to the structural characteristics of the folded specimen. Thicker sheets are conducive to complex, three-dimensional origami patterns, while thinner substrates are preferred for traditional and delicate models.

- Memory: The base material is often chosen for its ability to retain the folded shape. Therefore, the base material is required to have limited spring back upon non-elastic folding. An elastoplastic material with resistance to cyclic folding can be considered as an adequate choice.
- Special properties imposed by a given manufacturing process: Advanced fabrication techniques for origami, such as wet-folding, may necessitate a base material with specific attributes. In such instances, the material is expected to retain its structural integrity when exposed to moisture, thereby accommodating the distinctive demands of wet-folding.

Besides the properties listed above, the functionality of the target origami also plays a role in the base-material selection. Advanced manufacturing strategies have also enabled the use of materials that are not traditionally used in the realm of origami [118].

1.8 Manufacturing technics

The type of origami manufacturing is highly dependent on the choice of the base material. Through the lens of folding, we can categorize the manufacturing methods into synchronous, gradual folding and pre-gathering processes. In synchronous processes, folding takes place along all fold lines simultaneously. On the other hand, gradual folding involves step-by-step transitions from a flat to the fully folded state. A pre-gathering technique introduces a feature in one direction followed by folding in other planar directions. The difference between gradual folding and pre-gathering technique is that in the former, the folding starts from a small area of the patten and then it is expanded to the whole pattern., whereas in the pre-gathering technique, all crease folding along a specific direction is introduced before switching to other directions. Figure 1-11 shows the conventional manufacturing technique of corrugated origami pattern.

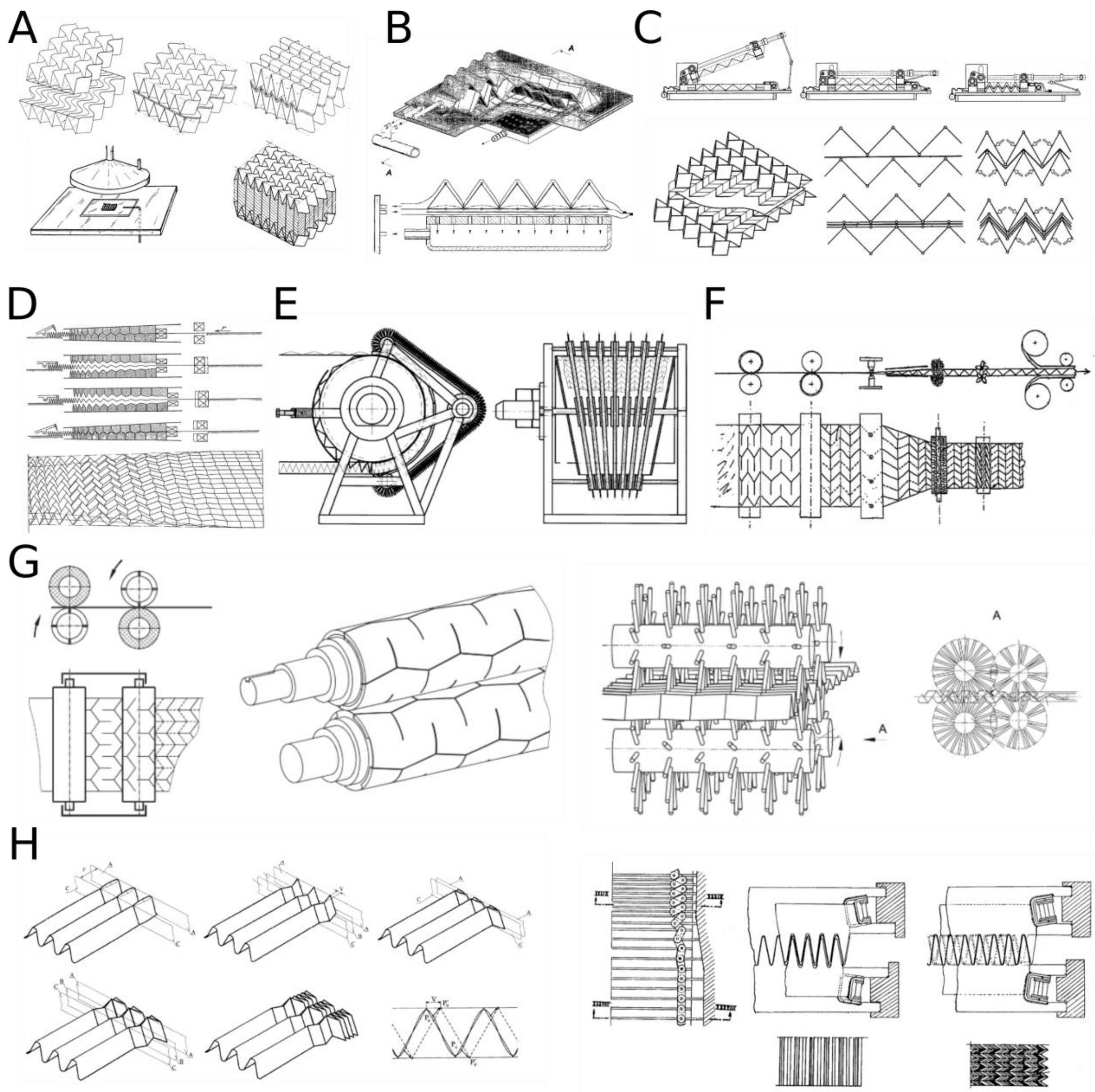

Figure 1-11 Conventional manufacturing techniques. **A-C** Synchronous manufacturing methods. **A** Combined molding and motive structure, joined at the mating fold lines. The base material here is sandwiched between the two structures, and then folded in vacuum [119]. **B** The blank is sucked onto the forming mandrel using an internal vacuum bag. Next, the folding process is done by vacuumization of the bag surrounding the auxiliary dies [120]. **C** A die designed to form corrugated sheet in a single step [121]. **D-G** Gradual manufacturing methods. **D** a folding method using a gradually deepening set of dies. In each stroke, the dies move apart, before adding a new row and deepening the existing folds [122]. **E** The base material is first pre-patterned, then a bristle belt presses the pre-folded sheet against a master sheet [123]. **F** One-step patterning and gathering method [124]. **G** In this technique, fold lines are embossed onto the base material using a series of rollers. Then bristles on the second pair of rollers fold the pattern [125]. **H** Pre-gathering manufacturing technique. For the transverse pattern orientation, the double corrugation is formed by cyclically clamping a pre-corrugated sheet using mating jaws, and inverting the longitudinal corrugations.

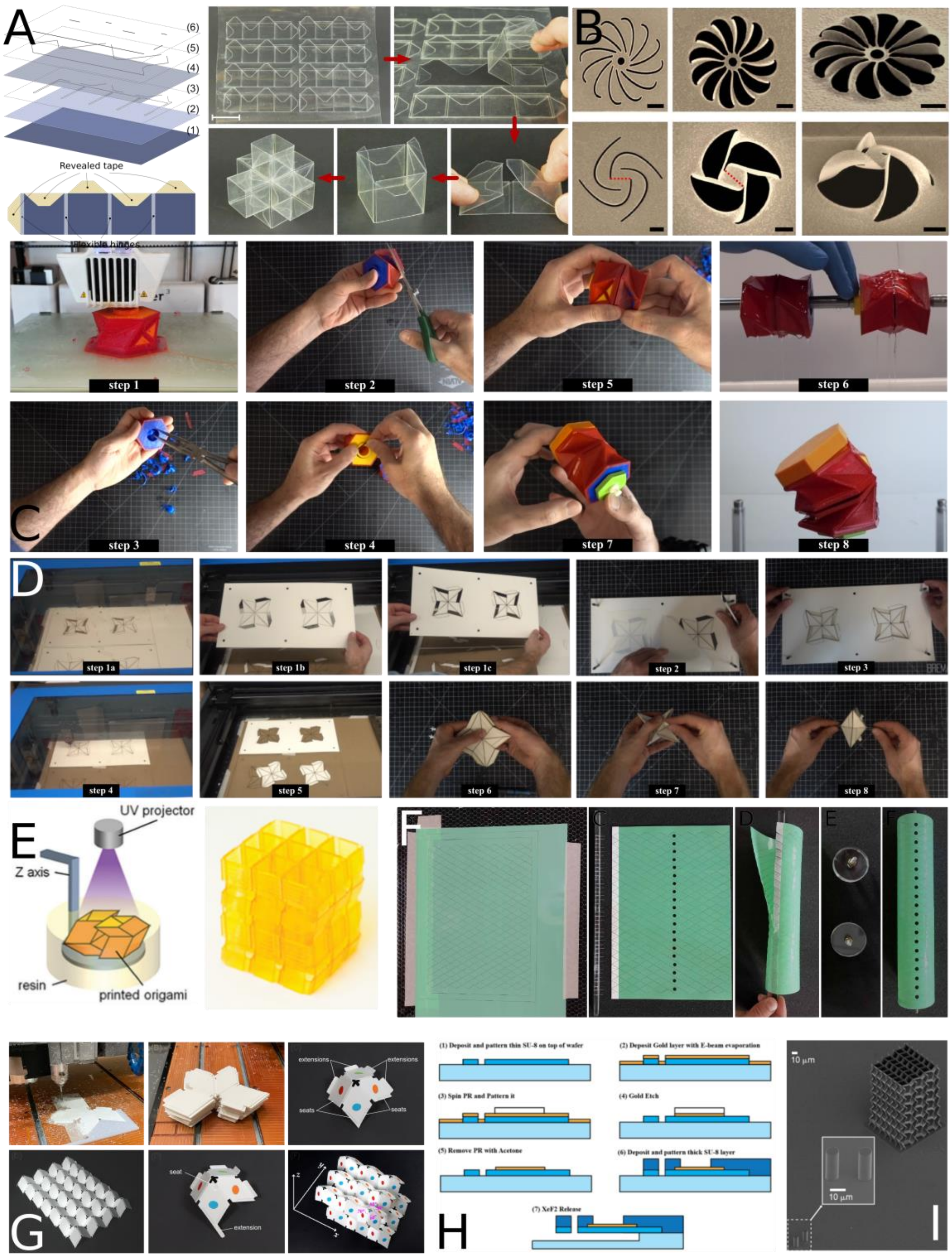

Figure 1-12 Recent developments in manufacturing of origami and kirigami. **A** A manufacturing method that involves stacking multiple layers of polymeric sheets and tapes. In each step, laser cutting is employed to remove parts of the stacked layers. The cover tape layers ultimately form the hinges of the specimen. The core polymeric sheet also adds stiffness to the panels [86]. **B** Laser cutting gold layers. Upon excitation by laser beam the patterns reconfigure permanently [118]. **C** Three-dimensional printing of inflatable origami sample [126]. **D** Layers of stiffening polymeric cores and tapes are cut by laser and assembled to

form an inflatable origami pattern [127]. **E** Digital light processing technique for printing complex origami patterns. A special mixture of curable resins ensures that the specimen remains flexible after exposure to ultraviolet light [128]. **F** Laser cutting of polymeric sheets and edge bonding to form a tubular kirigami pattern [129]. **G** A manufacturing technique that involves the machining of stiff panels and their connection utilizing flexible elastomeric hinges [78]. **H** A manufacturing technique inspired by nanofabrication. Different layers are chemically deposited and bond to form a flexible assembly of panels that can reconfigure upon applying electrical current through conductive layers [130]. **I** Two-photon beam printing is utilized to manufacture microscale origami patterns [131].

Recent advanced manufacturing such as three-dimensional printing has provided manufacturing alternatives for realizing origami/kirigami patterns. Figure 1-12 shows a series of origami-inspired materials manufactured by recently introduced strategies which in most cases involve several steps.

1.9 Applications of origami systems

Origami has long inspired the development of deployable structures in various fields, from aerospace engineering to medical devices. Perhaps aerospace applications have been the first engineering field benefiting from the reconfiguration property of origami systems. Origami structures have been used for solar panels [132-135], solar shields [136], and small deployable satellites [137]. However, recent advances in manufacturing technology have enabled their application in other fields, including biomedical applications, robotics, [134, 138]. Figure 1-10 shows applications of origami inspired structures.

The desired properties of origami that make it an ideal candidate for deployable structures include the following:

- Compactness: Origami-inspired folding techniques allow structures to be folded into a small, compact shape for transportation or storage and then readily and rapidly deployed into their final form when needed [139].

- Lightweightness: Made of thin layers, origami-inspired structures are lightweight, making them more accessible and cheaper for launch into space or transport into remote locations [127].
- Scalability: Origami structures can be designed to be easily scaled up or down in size, allowing for a wide range of applications from micro to meter scales [127].
- Cost-effectiveness: Integrating the cost associated with their manufacturing and assembling, origami-inspired structures are dramatically more affordable compared to traditional structures whose components are made independently and require a setup to assemble individual components.

Origami systems have shown potential for developing modular and repeated reconfigurable structures. Several origami patterns with one, two, and three-dimensional periodic patterns have been proposed recently [86, 87, 104]. The repeated arrays have enabled the incorporation of advanced functionalities into origami patterns including modulation of stiffness [86, 87], actuation [81, 86] and sensing [80].

1.10 Origami/Kirigami-inspired metamaterials

Origami and kirigami systems have recently contributed to the field of mechanical metamaterials thanks to a series of desirable properties. Firstly, origami and kirigami techniques can be used to create complex folding geometries that result in materials with unique mechanical [28, 69, 82, 86, 128, 139-146], optical [118], and thermal properties [147]. Secondly, the complex network of hinges/cuts and faces makes origami/kirigami ideal candidates for realizing complex configurations that are impossible to attain with linkage-based mechanisms [68, 79, 95, 148]. Lastly, origami and kirigami have unveiled the possibility of incorporating several functions into a single structure, such as load-bearing [73, 78, 86, 87, 107, 109, 144, 149, 150], sensing [47, 80, 81, 84, 151], actuation [81, 83, 84, 110, 129, 152, 153], energy harvesting [32, 154-158], programmability [78, 159-170], and multistability [79, 109, 126, 170-174]. Figure 1-13 shows applications of origami concepts capable of delivering more than one function in a single structure.

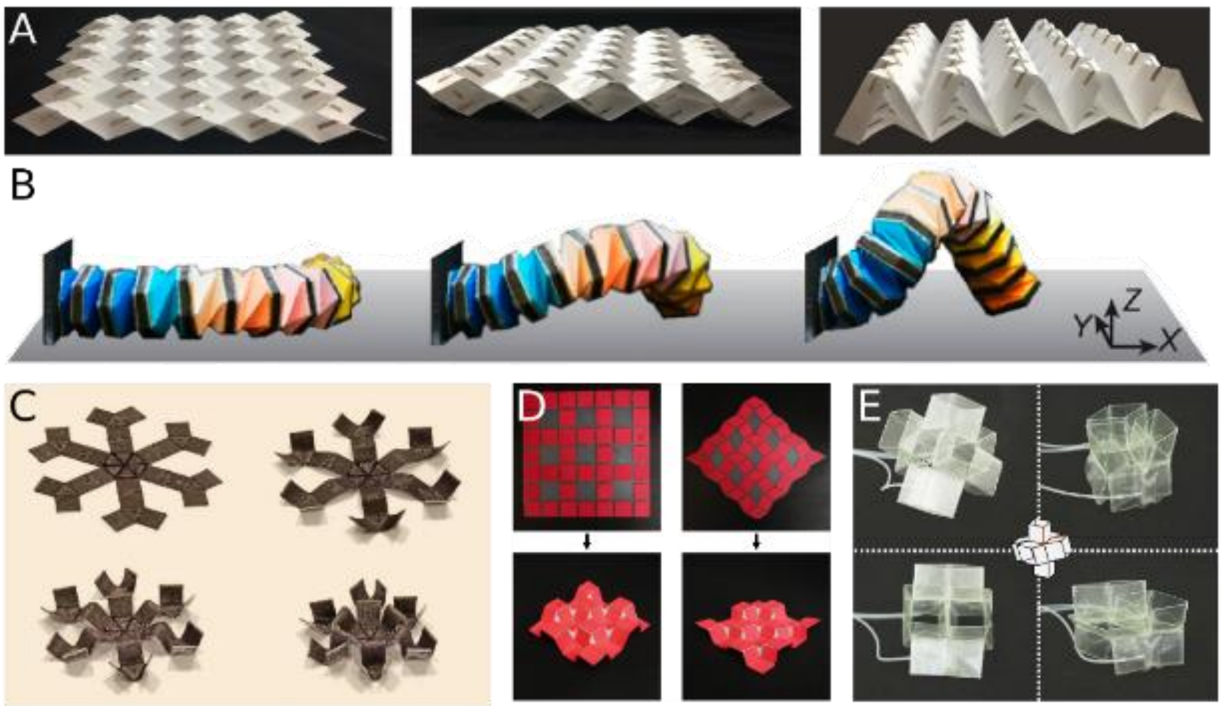

Figure 1-13 Application of origami concepts for multifunctionality; **A** A reconfigurable origami-inspired antenna [80], **B** Magnetically actuated origami-inspired robotic arm [83], **C** Magnetically actuated origami-inspired robot made by three-dimensional printing of magnetic ink [175], **D** Thermally actuated origami [176], and **E** Pneumatically actuated origami-inspired reconfigurable structure [86].

1.11 Load-bearing

Origami-based structures have been the source of inspiration for mechanical metamaterials with load-bearing capacity. Being load-bearing makes an origami system desirable for material systems that can switch from a floppy mode to a load-bearing (rigid) state. The mechanism of load-bearing capacity differs among the proposed designs. Yet, the main characteristics that explain the load-bearing capability in origami systems can be classified into the following eight groups: existence of an energy barrier [170, 173, 177], interlocking of the facets [144], external confinement [48], dead point of reconfiguration [86, 139], conflicting reconfiguration modes [149], internal locks

[178], curved creases [179], and intrinsic rigidity of the unit cell [87]. The examples of the aforementioned mechanisms are shown in Figure 1-14.

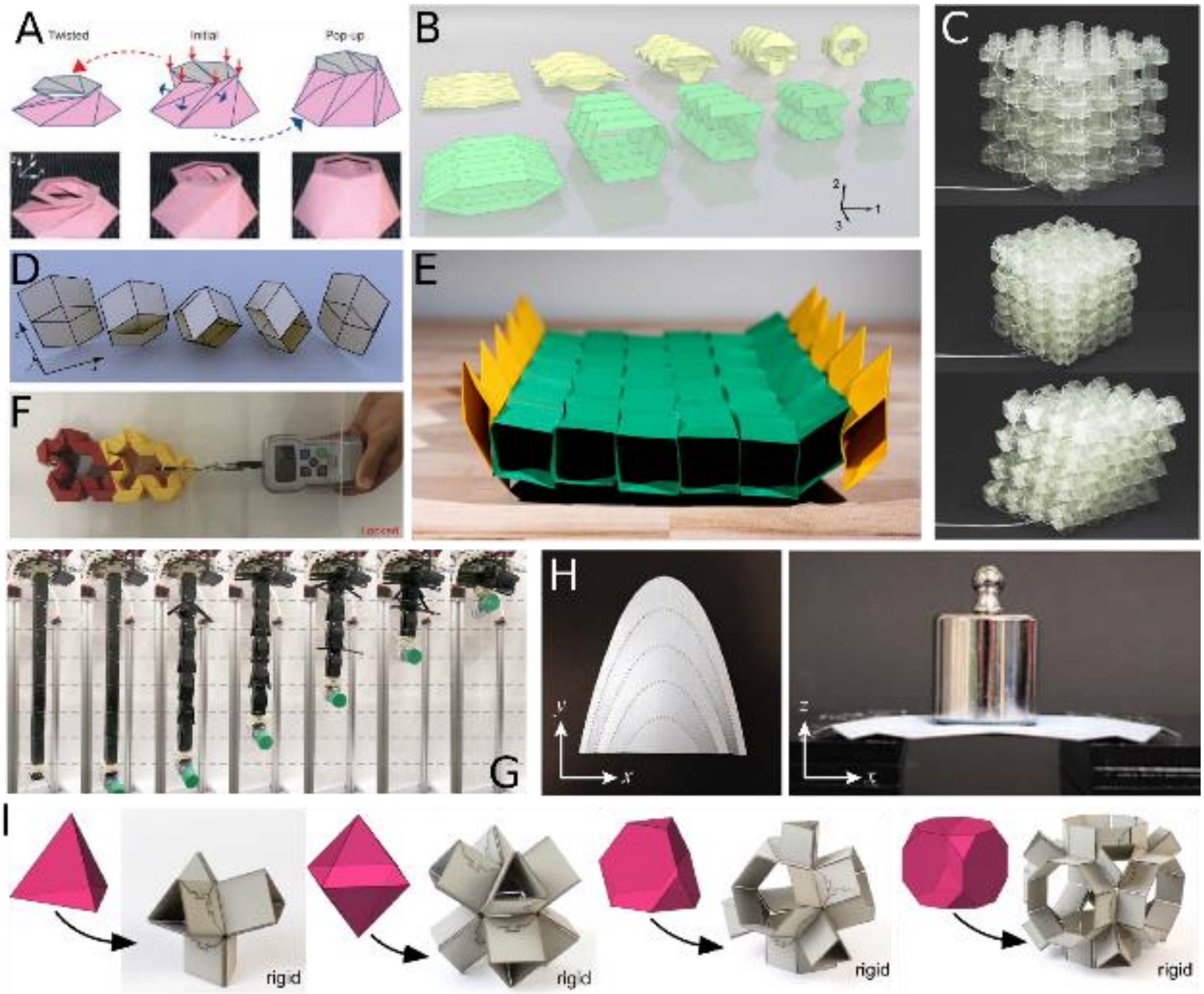

Figure 1-14 Examples of load-bearing mechanisms: **A** Load-bearing due to an energy barrier [142], **B** Contact induced load-bearing [144], **C** A load bearable structure at the deadpoint of the mechanism [86, 87], **D, E** Load bearing structures due to conflicting reconfiguration paths [107, 149], **F** Load bearing due to external confinement [48], **G** An internal locking mechanism makes the robotic arm load bearable in a specific configuration [178], **H** Curved crease imparts load bearing capability to a flat sheet, and **I** Load-bearing origami-inspired material with intrinsic rigidity [87].

Despite the ongoing research studies in deployable and load-bearing origami/kirigami-inspired materials, the stability of these materials against disturbance in the deployed direction have not received enough attention in the literature.

1.12 Reprogrammability

Some metamaterials offer the freedom to change their mechanical response after they have been fabricated. This property allowing *in-situ* changes of response and reconfiguration is often denoted as “reprogrammability”. The ability to reprogram the behavior of metamaterials post-fabrication enables a wide range of applications, including response tailoring [180-184], advanced sensing [51], imaging [8], locomotion [55], communication [80], and energy harvesting [31, 154, 156, 185]. In most cases, reprogrammability in metamaterials is achieved by incorporating a stimuli-responsive switching mechanism into the building block of the material. A change in the stimuli serves as a trigger and shifts the state of the switch leading to a change in the overall response of the metamaterial. Stimuli can be of various types, such as electrical, thermal [180], magnetic [9, 33, 175], and mechanical signals [23, 51, 182, 183].

A potential application of reprogrammable mechanical metamaterials is for deployable load-bearing structures. Origami and kirigami-inspired materials offer an enlarged reconfiguration space over other mechanical metamaterials [139, 144, 184]. Some origami patterns in literature provide a certain level of reprogrammability. Examples of reprogrammable origami/kirigami-inspired structures are shown in Figure 1-15. These concepts, however, fail to attain concurrently rigid-foldability, flat-foldability, and load-bearing capacity along the deployment direction. Non-flat-foldable concepts lack reconfigurability, making their size and volume large. Most existing concepts utilizing structural instability to achieve reconfigurability are non-rigid foldable. Instead, to fold, they must overcome a significant energy barrier that bends and stretches their panels, thus requiring a large input signal.

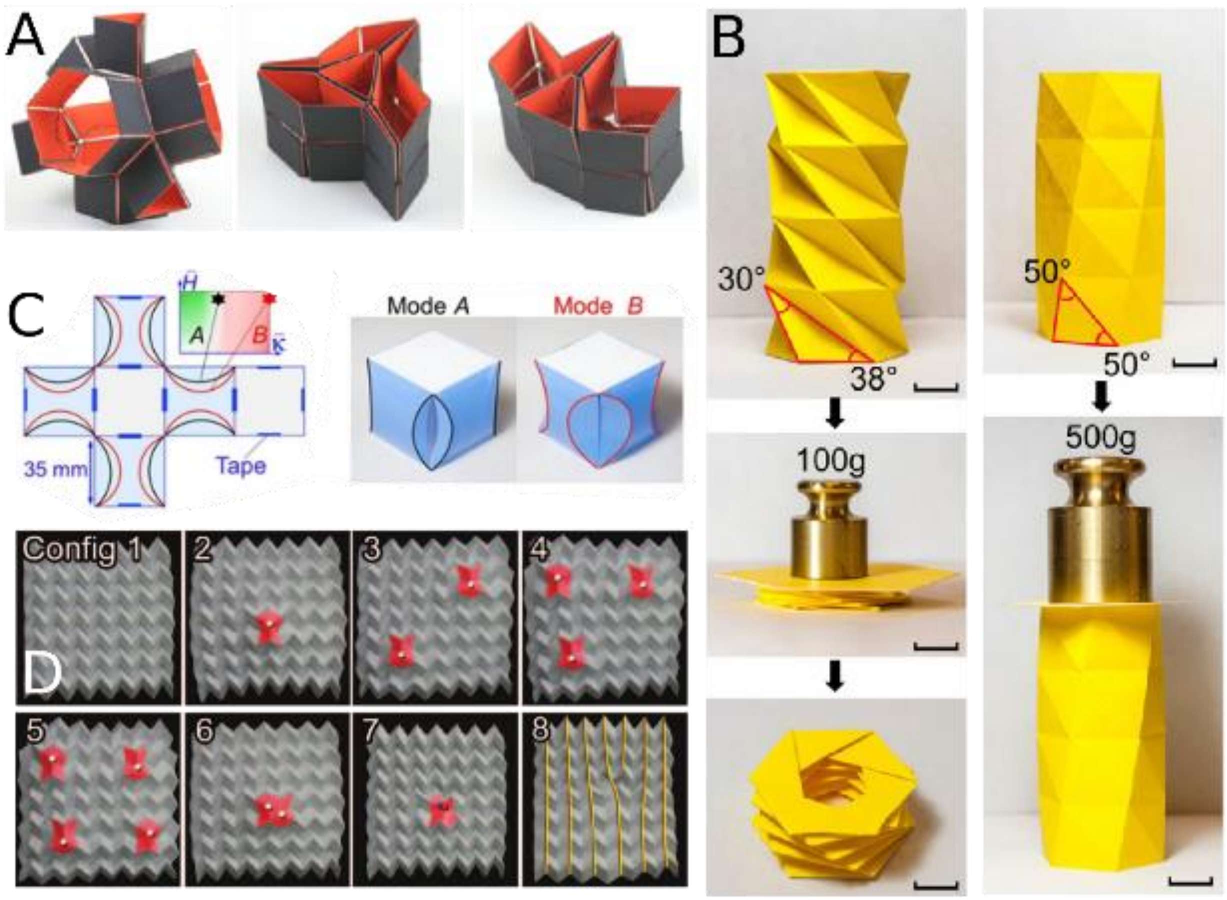

Figure 1-15 Examples of reprogrammable origami: **A** Energy barrier as a means for programming origami-inspired structure [109], **B** Different deployment and collapse routes leads to a switch from soft to rigid configurations [139], **C** Switchable curved creases are used to program the stiffness of the structure [184], and **D** Popping Miura cells in a tessellation affects the stiffness of the whole structure [166]

One of the challenges involving metamaterial reprogrammability is ensuring that the structure maintains its programmed configuration upon removal of the input (trigger) signal. To this end, several methods have been introduced, including the use of external confinement, exploiting the base material response transformation, using internal locking mechanisms, and incorporating energy barriers to separate the programmed configurations. The last method, multistability, has gained much attention in the arena of reprogrammable materials.

1.13 Multistability

Multistable mechanisms can exist in multiple distinct and stable states and can be switched between these states with the application of an external input. These mechanisms are widely used in various applications, including switches, locks, and grips. Multistable mechanisms typically consist of components that interact to produce several stable states. These components may include springs, levers, gears, or electronic components such as transistors. Thanks to their switching behavior, Multistable structures have recently gained much attention for the design of actuators, robots, microelectromechanical systems, energy harvesters, programmable devices, and metamaterials [14]. Multistable concepts have enabled the incorporation of advanced functionalities into mechanical metamaterials. Among these novel applications are energy trapping [42, 53], energy dissipation [42] and programmable behavior [23, 42, 51, 53, 56]. Examples of multistable mechanisms and materials are shown in Figure 1-16.

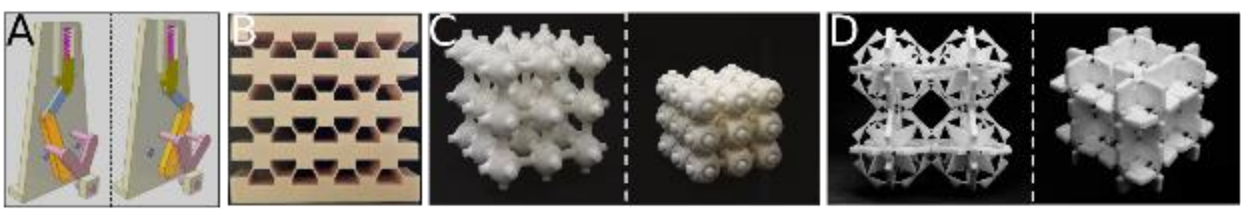

Figure 1-16 Examples of multistable mechainsms and materials; **A** A bistable mechanism, **B** A metamaterial made of inclined confined beams undergoing snap-through instability [53], **C** Perforated shellular structure showing multistability in different directions [23], **D** A metamaterial made of flexibly hinged links shows multistability in different directions [56].

There are numerous reports of multistability in non-rigid origami structures [66, 78, 79, 81, 109, 174, 186]. Multistability in non-rigid origami structures has been attributed to the interaction between the flexural deformation of the panels and the rotational stiffness of the hinges [66, 79, 110, 126, 141, 152, 173, 187, 188]. In a rigid-foldable origami, the interaction of the hinges can lead to a multistable response [78, 109, 170, 174, 189]. Examples of origami inspired multistable materials are shown in Figure 1-17.

The multistability behavior has been exploited to develop foldable tents [173], electrical switches [81], materials with tunable mechanical properties [109], shape-shifting structures [79], multi-response materials [109], and robotic arms [83, 84]. Figure 1-17 shows origami-inspired multistable structures/materials. Although various studies have demonstrated the emergence of Multistability in origami systems, applying these concepts to the design of cellular materials is limited [78, 109]. Complex shapes, complex reconfiguration space, and manufacturing challenges have limited the implementation of origami-based structures in developing multistable materials for real-world applications [78, 109]. Incorporating origami concepts in designing multistable systems is a relatively unexplored field of research.

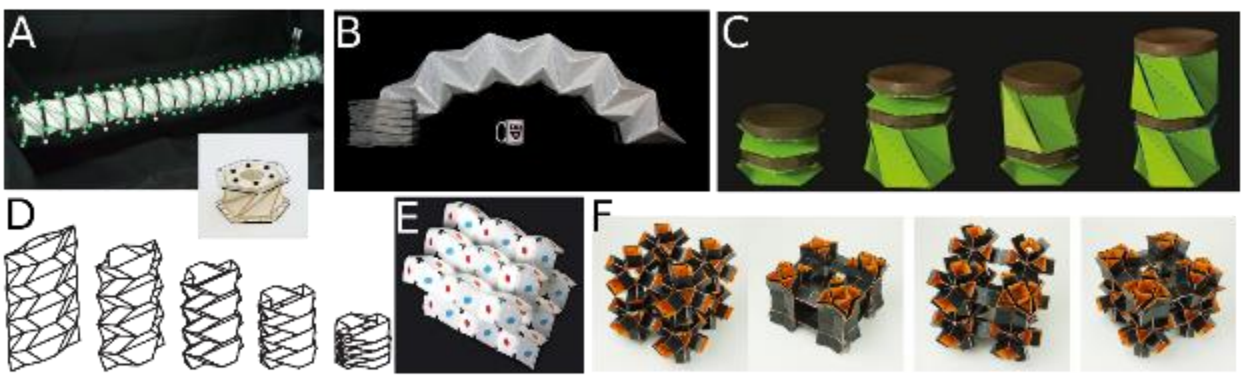

Figure 1-17 Exmaples of multistable origami systems; **A** A Origami-inspired impact mitigating system relying on rarefication solitary wave creation [145], **B** Inflatable deployable multistable origami-inspired structure [127], **C** Magnetically actuated multistable origami-inspired structure as a logic gate [81], **D** Re-entrant origami inspired tube with auxetic and multistable behavior [28], **E** A multistable rigidly-foldable origami inspired metamaterial [78], **F** Programmable metamaterial with multiple soft and rigid configurations [109]

1.14 The scope of the present work

The goal of this thesis is to develop an origami-inspired reconfigurable mechanical metamaterial that is both load-bearing and multistable. This goal is broken down into two complementary tasks. The first calls for the search of a class of origami-inspired metamaterials that are rigidly foldable and can withstand sizeable external loading. The second aims at leveraging the lessons learned from the first task to integrate multistability into the origami architecture and attain multifunctionality.

Specifically, the objectives of the former are to:

- Propose a framework for developing a class of origami-inspired metamaterials;
- Study the folding process through a systematic matrix-based mobility analysis;
- Systematically study the distinct reconfiguration kinematic paths and final configurations;
- Study their load-bearing capacity;
- Show their potential for in-situ programming of stiffness and strength;

For the latter, the specific objectives are to:

- Employ the insights of the first study to design a class of multistable mechanical metamaterials;
- Develop a simplified model that can predict the behavior of the hinges from experimentally obtained data;
- Propose a feasible manufacturing method that enables the attainment of large deformation in the panels;
- Investigate the role of geometric parameters and mechanical properties in the multistable behavior of the unit cell;
- Explain the behavior of interacting bistable units;
- Show their potential application for energy dissipation, energy absorption, and reprogrammability of stiffness and strength.

1.15 Structure of the thesis

This thesis is manuscript-based and consists of four chapters. Chapter 1 provides an introduction and literature review of origami-inspired metamaterials. In particular, the first part briefly introduces the background and is followed by a review of origami-inspired mechanical metamaterials. The second part surveys multistable materials, including their background, mechanism, and applications. The chapter concludes with the objectives and structure of the thesis.

Chapter 2 introduces a strategy to impart multidirectional load-bearing capacity to a stacked structure of papers. A rigidly foldable class of cellular metamaterials is introduced that can flat-fold and lock into several stiff states across multiple directions, including the deployment direction. These metamaterials rigidly fold with one degree of freedom and can reconfigure into several flat-foldable and spatially-lockable folding states. Locking under compression yields topology and symmetry changes that impart multidirectional stiffness. Additionally, folding paths and mixed-mode configurations can be activated in situ to modulate their properties. Their load-bearing capacity, flat-foldability, and programmability can be harnessed for deployable structures, reconfigurable robots, and low-volume packaging.

Chapter 3 explores the second trajectory that stems from relaxing the rigid foldability restriction of the origami panels to enable energy absorption and dissipation. This thesis presents an origami-inspired multistable material with an extensive range of multistable reconfigurations that can dissipate energy effectively. The reconfiguration process consists of two phases. First, the panels rotate rigidly about their connection lines. Next, while a set of panels provide axial stiffness, the other set undergoes flexural deformation leading to snap-through instability. The axial stiffness offered by the first set of panels eliminates the need for stiff and bulky frames in our structure, culminating in a more efficient distribution of the base material. In addition, a relatively simple yet effective method is proposed for manufacturing layered structures from paper or polymeric sheets. The energy absorption capability and relatively easy manufacturing method make the proposed structure a good candidate for the packaging industry.

Finally, Chapter 4 highlights the main results and contributions of this thesis and concludes with a brief description of possible paths for future work.

1.16 References

1. Xu, H., A. Farag, and D. Pasini, *Multilevel hierarchy in bi-material lattices with high specific stiffness and unbounded thermal expansion.* Acta Materialia, 2017. 134: p. 155-166.
2. Xu, H., A. Farag, and D. Pasini, *Routes to program thermal expansion in three-dimensional lattice metamaterials built from tetrahedral building blocks.* Journal of the Mechanics and Physics of Solids, 2018. 117: p. 54-87.
3. Xu, H. and D. Pasini, *Structurally efficient three-dimensional metamaterials with controllable thermal expansion.* Scientific Reports, 2016. 6(April).
4. Litchinitser, N.M. and V.M. Shalaev, *Photonic metamaterials.* Laser Physics Letters, 2008. 5(6): p. 411-411.
5. Soukoulis, C.M. and M. Wegener, *Past achievements and future challenges in the development of three-dimensional photonic metamaterials.* Nature photonics, 2011. 5(9): p. 523-530.
6. Lu, D. and Z. Liu, *Hyperlenses and metalenses for far-field super-resolution imaging.* Nature communications, 2012. 3(1): p. 1205.
7. Lee, Y.U., et al., *Metamaterial assisted illumination nanoscopy via random super-resolution speckles.* Nature communications, 2021. 12(1): p. 1559.
8. Ma, Q., et al., *Super-resolution imaging by metamaterial-based compressive spatial-to-spectral transformation.* Nanoscale, 2017. 9(46): p. 18268-18274.
9. Fan, K. and W.J. Padilla, *Dynamic electromagnetic metamaterials.* Materials Today, 2015. 18(1): p. 39-50.
10. Cummer, S.A., J. Christensen, and A. Alù, *Controlling sound with acoustic metamaterials.* Nature Reviews Materials, 2016. 1(3): p. 1-13.
11. Fok, L. and X. Zhang, *Negative acoustic index metamaterial.* Physical Review B, 2011. 83(21): p. 214304-214304.
12. Huang, G.L. and C.T. Sun, *Band gaps in a multiresonator acoustic metamaterial.* Journal of Vibration and Acoustics, 2010. 132(3).
13. Lee, S.H., et al., *Acoustic metamaterial with negative modulus.* Journal of Physics: Condensed Matter, 2009. 21(17): p. 175704-175704.
14. Bertoldi, K., et al., *Flexible mechanical metamaterials.* Nature Reviews Materials, 2017. 2(11): p. 17066-17066.

15. Wang, Y.C. and R.S. Lakes, *Composites with inclusions of negative bulk modulus: Extreme damping and negative poisson's ratio.* Journal of Composite Materials, 2005. 39(18): p. 1645-1657.
16. Frenzel, T., M. Kadic, and M. Wegener, *Three-dimensional mechanical metamaterials with a twist.* Science, 2017. 358(6366): p. 1072-1074.
17. Bertoldi, K., et al., *Negative Poisson's ratio behavior induced by an elastic instability.* Advanced materials, 2010. 22(3): p. 361-366.
18. Coulais, C., et al., *Multi-step self-guided pathways for shape-changing metamaterials.* Nature, 2018. 561(7724): p. 512-515.
19. Lubbers, L.A. and M. van Hecke, *Excess Floppy Modes and Multi-Branched Mechanisms in Metamaterials with Symmetries.* 2018. 1: p. 1-5.
20. Moestopo, W.P., et al., *Pushing and Pulling on Ropes: Hierarchical Woven Materials.* Advanced Science, 2020. 7(20): p. 1-8.
21. Meza, L.R., et al., *Resilient 3D hierarchical architected metamaterials.* Proceedings of the National Academy of Sciences of the United States of America, 2015. 112(37): p. 11502-11507.
22. Berger, J.B., H.N.G. Wadley, and R.M. McMeeking, *Mechanical metamaterials at the theoretical limit of isotropic elastic stiffness.* Nature, 2017. 543(7646): p. 533-537.
23. Shi, J., et al., *Programmable Multistable Perforated Shellular.* Advanced Materials, 2021. 33(42).
24. Smith, D.R., et al., *Calculation and measurement of bianisotropy in a split ring resonator metamaterial.* Journal of Applied Physics, 2006. 100(2): p. 24507-24507.
25. Rocklin, D.Z., et al., *Transformable topological mechanical metamaterials.* Nature Communications, 2017. 8: p. 1-9.
26. Meeussen, A.S., J. Paulose, and V. Vitelli, *Geared topological metamaterials with tunable mechanical stability.* Physical Review X, 2016. 6(4): p. 041029.
27. Paulose, J., B.G.-g. Chen, and V. Vitelli, *Topological modes bound to dislocations in mechanical metamaterials.* Nature Physics, 2015. 11(2): p. 153-156.
28. Yasuda, H. and J. Yang, *Reentrant origami-based metamaterials with negative Poisson's ratio and bistability.* Physical Review Letters, 2015. 114(18): p. 1-5.
29. Almoneef, T.S. and O.M. Ramahi, *Metamaterial electromagnetic energy harvester with near unity efficiency.* Applied Physics Letters, 2015. 106(15): p. 153902.
30. Chen, Z., et al., *Metamaterials-based enhanced energy harvesting: A review.* Physica B: Condensed Matter, 2014. 438: p. 1-8.
31. Emam, S.A. and D.J. Inman, *A Review on Bistable Composite Laminates for Morphing and Energy Harvesting.* Applied Mechanics Reviews, 2015. 67(6): p. 060803-060803.
32. Miranda, R., et al., *Mechanics of smart origami sunscreens with energy harvesting ability.* Mechanics Research Communications, 2020. 105: p. 103503.
33. Zhang, Y., et al., *High-performance broadband electromagnetic interference shielding optical window based on a metamaterial absorber.* Optics Express, 2020. 28(18): p. 26836-26849.
34. Aladwani, A., A. Almandeel, and M. Nouh, *Fluid-structural coupling in metamaterial plates for vibration and noise mitigation in acoustic cavities.* International Journal of Mechanical Sciences, 2019. 152: p. 151-166.
35. Barthelat, F., Z. Yin, and M.J. Buehler, *Structure and mechanics of interfaces in biological materials.* Nature Reviews Materials, 2016. 1(4): p. 1-16.

36. Mirkhalaf, M., T. Zhou, and F. Barthelat, *Simultaneous improvements of strength and toughness in topologically interlocked ceramics.* Proceedings of the National Academy of Sciences, 2018. 115(37): p. 201807272-201807272.
37. Yin, Z., A. Dastjerdi, and F. Barthelat, *Tough and deformable glasses with bioinspired cross-ply architectures.* Acta Biomaterialia, 2018. 75: p. 439-450.
38. Yin, Z., F. Hannard, and F. Barthelat, *Impact-resistant nacre-like transparent materials.* Science, 2019. 364(6447): p. 1260-1263.
39. Bacquet, C.L., et al., *Metadamping: dissipation emergence in elastic metamaterials.* Advances in applied mechanics, 2018. 51: p. 115-164.
40. Van Belle, L., et al., *The impact of damping on the sound transmission loss of locally resonant metamaterial plates.* Journal of Sound and Vibration, 2019. 461: p. 114909.
41. Hussein, M.I. and M.J. Frazier, *Metadamping: An emergent phenomenon in dissipative metamaterials.* Journal of Sound and Vibration, 2013. 332(20): p. 4767-4774.
42. Seyedkanani, A. and A. Akbarzadeh, *Magnetically Assisted Rotationally Multistable Metamaterials for Tunable Energy Trapping–Dissipation.* Advanced Functional Materials, 2022: p. 2207581.
43. Smith, D.R., et al., *Composite medium with simultaneously negative permeability and permittivity.* Physical review letters, 2000. 84(18): p. 4184.
44. Zigoneanu, L., B.-I. Popa, and S.A. Cummer, *Three-dimensional broadband omnidirectional acoustic ground cloak.* Nature materials, 2014. 13(4): p. 352-355.
45. Hewage, T.A.M., et al., *Double-Negative Mechanical Metamaterials Displaying Simultaneous Negative Stiffness and Negative Poisson's Ratio Properties.* Advanced Materials, 2016. 28(46): p. 10323-10332.
46. Lakes, R.S., *Extreme damping in compliant composites with a negative-stiffness phase.* Philosophical Magazine Letters, 2002. 81(2): p. 95-100.
47. Jiang, Y., et al., *Auxetic Mechanical Metamaterials to Enhance Sensitivity of Stretchable Strain Sensors.* Advanced Materials, 2018. 30(12): p. 1-8.
48. Kamrava, S., et al., *Origami-based cellular metamaterial with auxetic, bistable, and self-locking properties.* Scientific Reports, 2017. 7: p. 46046-46046.
49. Rafsanjani, A. and D. Pasini, *Bistable auxetic mechanical metamaterials inspired by ancient geometric motifs.* Extreme Mechanics Letters, 2016. 9: p. 291-291.
50. Shang, X., et al., *Durable bistable auxetics made of rigid solids.* Journal of Materials Research, 2018. 33(3): p. 300-300.
51. Mofatteh, H., et al., *Programming Multistable Metamaterials to Discover Latent Functionalities.* 2022. 2202883: p. 1-16.
52. Tan, X., et al., *Bioinspired flexible and programmable negative stiffness mechanical metamaterials.* Advanced Intelligent Systems, 2023: p. 2200400.
53. Shan, S., et al., *Multistable Architected Materials for Trapping Elastic Strain Energy.* Advanced Materials, 2015. 27(29): p. 4296-4301.
54. Rafsanjani, A., A. Akbarzadeh, and D. Pasini, *Snapping Mechanical Metamaterials under Tension.* Advanced Materials, 2015. 27(39): p. 5931-5935.
55. Rafsanjani, A., et al., *Propagation of pop ups in kirigami shells.* Proceedings of the National Academy of Sciences, 2019. 116(17): p. 8200-8205.
56. Haghpanah, B., et al., *Architected Materials: Multistable Shape-Reconfigurable Architected Materials (Adv. Mater. 36/2016).* Advanced Materials, 2016. 28(36): p. 8065-8065.

57. Bückmann, T., et al., *An elasto-mechanical unfeelability cloak made of pentamode metamaterials.* Nature communications, 2014. 5(1): p. 4130.
58. Coulais, C., et al., *Combinatorial design of textured mechanical metamaterials.* Nature, 2016. 535(7613): p. 529-532.
59. Paulose, J., A.S. Meeussen, and V. Vitelli, *Selective buckling via states of self-stress in topological metamaterials.* Proceedings of the National Academy of Sciences, 2015. 112(25): p. 7639-7644.
60. Nash, L.M., et al., *Topological mechanics of gyroscopic metamaterials.* Proceedings of the National Academy of Sciences, 2015. 112(47): p. 14495-14500.
61. Shim, J., et al., *Buckling-induced encapsulation of structured elastic shells under pressure.* Proceedings of the National Academy of Sciences, 2012. 109(16): p. 5978-5983.
62. Grima, J.N. and K.E. Evans, *Auxetic behavior from rotating squares.* Journal of materials science letters, 2000. 19: p. 1563-1565.
63. Hu, Z., et al., *Engineering zero modes in transformable mechanical metamaterials.* Nature Communications, 2023. 14(1): p. 1266.
64. Lang, R.J., *Origami design secrets: mathematical methods for an ancient art*. 2012: CRC Press.
65. Lang, R.J., *Twists, Tilings, and Tessellations: Mathematical Methods for Geometric Origami*. 2017: AK Peters/CRC Press.
66. Silverberg, J.L., et al., *Origami structures with a critical transition to bistability arising from hidden degrees of freedom.* Nature Materials, 2015. 14(4): p. 389-393.
67. Chen, S. and L. Mahadevan, *Rigidity percolation and geometric information in floppy origami.* Proceedings of the National Academy of Sciences of the United States of America, 2019. 116(17): p. 8119-8124.
68. Dudte, L.H., et al., *Programming curvature using origami tessellations.* Nature Materials, 2016. 15(5): p. 583-583.
69. Wei, Z.Y., et al., *Geometric mechanics of periodic pleated origami.* Physical review letters, 2013. 110(21): p. 215501-215501.
70. Eidini, M. and G.H. Paulino, *Unraveling metamaterial properties in zigzag-base folded sheets.* Science Advances, 2015. 1(8): p. 1-8.
71. Filipov, E.T., et al., *Bar and hinge models for scalable analysis of origami.* International Journal of Solids and Structures, 2017. 124: p. 26-26.
72. Filipov, E.T., G.H. Paulino, and T. Tachi, *Origami tubes with reconfigurable polygonal cross-sections.* Proceedings of the Royal Society A: Mathematical, Physical and Engineering Sciences, 2016. 472(2185).
73. Filipov, E.T., G.H. Paulino, and T. Tachi, *Deployable Sandwich Surfaces with High Out-of-Plane Stiffness.* Journal of Structural Engineering, 2018. 145(2): p. 04018244-04018244.
74. Filipov, E.T., T. Tachi, and G.H. Paulino, *Origami tubes assembled into stiff, yet recon[1] E. T. Filipov, T. Tachi, and G. H. Paulino, "Origami tubes assembled into stiff, yet reconfigurable structures and metamaterials," Proc. Natl. Acad. Sci., vol. 112, no. 40, p. 12321, 2015.figurable structur.* Proceedings of the National Academy of Sciences, 2015. 112(40): p. 12321-12321.
75. Lin, Z., et al., *Folding at the Microscale: Enabling Multifunctional 3D Origami-Architected Metamaterials.* Small, 2020. 16(35): p. 1-9.

76. Liu, K., et al., *Big influence of small random imperfections in origami-based metamaterials: Influence of Imperfections in Origami.* Proceedings of the Royal Society A: Mathematical, Physical and Engineering Sciences, 2020. 476(2241).
77. Liu, K. and G.H. Paulino, *Nonlinear mechanics of non-rigid origami: An efficient computational approach.* Proceedings of the Royal Society A: Mathematical, Physical and Engineering Sciences, 2017. 473(2206).
78. Liu, K., et al., *Triclinic Metamaterials by Tristable Origami with Reprogrammable Frustration.* Advanced Materials, 2022. 2107998: p. 1-11.
79. Liu, K., T. Tachi, and G.H. Paulino, *Invariant and smooth limit of discrete geometry folded from bistable origami leading to multistable metasurfaces.* Nature Communications, 2019. 10(1).
80. Nauroze, S.A., et al., *Continuous-range tunable multilayer frequency-selective surfaces using origami and inkjet printing.* Proceedings of the National Academy of Sciences of the United States of America, 2018: p. 201812486-201812486.
81. Novelino, L.S., et al., *Untethered control of functional origami microrobots with distributed actuation.* Proceedings of the National Academy of Sciences of the United States of America, 2020. 117(39): p. 24096-24101.
82. Pratapa, P.P., K. Liu, and G.H. Paulino, *Geometric Mechanics of Origami Patterns Exhibiting Poisson's Ratio Switch by Breaking Mountain and Valley Assignment.* Physical Review Letters, 2019. 122(15).
83. Wu, S., et al., *Stretchable origami robotic arm with omnidirectional bending and twisting.* Proceedings of the National Academy of Sciences of the United States of America, 2021. 118(36): p. 1-9.
84. Ze, Q., et al., *Soft robotic origami crawler.* Science Advances, 2022. 8(13): p. 1-10.
85. Zhao, Z., et al., *3D printing of complex origami assemblages for reconfigurable structures.* Soft Matter, 2018: p. 8051-8059.
86. Overvelde, J.T.B., et al., *A three-dimensional actuated origami-inspired transformable metamaterial with multiple degrees of freedom.* Nature Communications, 2016. 7: p. 1-8.
87. Overvelde, J.T.B., et al., *Rational design of reconfigurable prismatic architected materials.* Nature, 2017. 541(7637): p. 347-352.
88. Teoh, Z.E., et al., *Rotary-actuated folding polyhedrons for midwater investigation of delicate marine organisms.* Science Robotics, 2018. 3(20): p. 1-9.
89. Lefteri, C., *Making It Second Edition: Manufacturing Techniques for Product Design*. 2012: Laurence King Publishing.
90. Loper, B., *Mind-Blowing Modular Origami: The Art of Polyhedral Paper Folding: Use Origami Math to fold Complex, Innovative Geometric Origami Models*. 2016: Tuttle Publishing.
91. Castle, T., et al., *Additive lattice kirigami.* Science Advances, 2016. 2(9): p. e1601258-e1601258.
92. Rafsanjani, A. and K. Bertoldi, *Buckling-Induced Kirigami.* Physical Review Letters, 2017. 118(8): p. 1-5.
93. Zhao, R., et al., *Kirigami enhances film adhesion.* Soft Matter, 2018. 14(13): p. 2515-2525.
94. Hwang, D.-G., K. Trent, and M.D. Bartlett, *Kirigami-inspired structures for smart adhesion.* ACS applied materials & interfaces, 2018. 10(7): p. 6747-6754.
95. Choi, G.P.T., L.H. Dudte, and L. Mahadevan, *Programming shape using kirigami tessellations.* Nature Materials, 2019. 18(9): p. 999-1004.

96. Lamoureux, A., et al., *Dynamic kirigami structures for integrated solar tracking.* Nature Communications, 2015. 6: p. 8092-8092.
97. Castle, T., et al., *Making the cut: Lattice kirigami rules.* Physical Review Letters, 2014. 113(24): p. 1-5.
98. Sussman, D.M., et al., *Algorithmic Lattice Kirigami: A Route to Pluripotent Materials.* 2015.
99. Hong, Y., et al., *Boundary curvature guided programmable shape-morphing kirigami sheets.* Nature Communications, 2022. 13(1): p. 530.
100. Li, Y., et al., *Shape-morphing materials and structures for energy-efficient building envelopes.* Materials Today Energy, 2021. 22: p. 100874.
101. Demaine, E.D. and J. O'Rourke, *Geometric folding algorithms: linkages, origami, polyhedra*. 2008: Cambridge university press.
102. Felton, S., et al., *A method for building self-folding machines.* Science, 2014. 345(6197): p. 644-646.
103. Schenk, M., *Folded Shell Structures.* 2011(August): p. 149-149.
104. Schenk, M. and S.D. Guest, *Geometry of Miura-folded metamaterials.* Proceedings of the National Academy of Sciences, 2013. 110(9): p. 3276-3281.
105. Tachi, T., *Designing freeform origami tessellations by generalizing Resch's patterns.* Journal of mechanical design, 2013. 135(11): p. 111006.
106. Demaine, E.D. and J. O'Rourke, *Geometric folding algorithms: linkages, origami, polyhedra*. 2007: Cambridge university press.
107. Filipov, E.T., T. Tachi, and G.H. Paulino, *Origami tubes assembled into stiff, yet reconfigurable structures and metamaterials.* Proceedings of the National Academy of Sciences, 2015. 112(40): p. 12321-12326.
108. Eidini-Nezhad, M., *Origami-inspired structures and materials: analysis and metamaterial properties and Seismic design of hybrid masonry structural systems*. 2015.
109. Iniguez-Rabago, A., Y. Li, and J.T.B. Overvelde, *Exploring multistability in prismatic metamaterials through local actuation.* Nature Communications, 2019. 10(1): p. 1-10.
110. Nayakanti, N., S.H. Tawfick, and A.J. Hart, *Twist-coupled Kirigami cells and mechanisms.* Extreme Mechanics Letters, 2018. 21: p. 17-17.
111. Howell, L.L. [cited 2023 March 26th]; Available from: https://www.me.byu.edu/faculty/larryhowell.
112. Rodrigues, G.V., et al., *Nonlinear dynamics of an adaptive origami-stent system.* International Journal of Mechanical Sciences, 2017. 133(April): p. 303-318.
113. Laboratory, J.P. [cited 2023 March 26th]; Available from: https://www.jpl.nasa.gov/.
114. Arya, M. [cited 2023 March 26th]; Available from: https://morphingspace.stanford.edu/.
115. Pellegrino, S. [cited 2023 March 26th]; Available from: https://www.pellegrino.caltech.edu/.
116. Calladine, C.R. and S. Pellegrino, *First-order infinitesimal mechanisms.* International Journal of Solids and Structures, 1991. 27(4): p. 505-515.
117. Pellegrino, S. and C.R. Calladine, *Matrix analysis of statically and kinematically indeterminate frameworks.* International Journal of Solids and Structures, 1986. 22(4): p. 409-409.
118. Liu, Z., et al., *Nano-kirigami with giant optical chirality.* Science Advances, 2018. 4(7): p. 1-9.

119. Victor, G.L., *Process and devices for chevroning pliable sheet material*. 1968, Google Patents.
120. Akishev, N.I., I.M. Zakirov, and A.V. Nikitin, *Device for sheet material corrugation*. 2009, Google Patents.
121. Khaliulin, V., I. Dvoeglazov, and V. Inkin, *Isometric forming of relief plates using vacuum energy.* Kuznechno-Shtampovochnoe Proizvodstvo(Obrabotka Metallov Davleniem)(Russia), 2002. 1: p. 17-24.
122. Victor, G.L., *Arrangement for the mechanical and continuous production of developable herring-bone structures*. 1960, Google Patents.
123. Zakirov, I.d.M., *Device for continuous corrugating of rolled material*. 2009: Russia.
124. Kehrle, R., *Method and apparatus for producing a composite structural panel with a folded material core*. 2005, Google Patents.
125. Zakirov, I.d.M., *Method for production of chevron filler and device for its realisation*. 2006: Russia.
126. Melancon, D., et al., *Inflatable Origami: Multimodal Deformation via Multistability.* Advanced Functional Materials, 2022. 32(35).
127. Melancon, D., et al., *Multistable inflatable origami structures at the metre scale.* Nature, 2021. 592(7855): p. 545-550.
128. Zhao, Z., et al., *3D Printing of Complex Origami Assemblages for Reconfigurable Structures.* 2018.
129. Rafsanjani, A., et al., *Propagation of Pop-ups in Kirigami Shells.* Bulletin of the American Physical Society, 2019.
130. Zhu, Y., et al., *Elastically and plastically foldable electrothermal micro-origami for controllable and rapid shape morphing.* Advanced Functional Materials, 2020. 30(40): p. 2003741.
131. Lin, Z., et al., *Folding at the microscale: Enabling multifunctional 3D origami-architected metamaterials.* Small, 2020. 16(35): p. 2002229.
132. Jasim, B. and P. Taheri. *An origami-based portable solar panel system*. in *2018 IEEE 9th Annual Information Technology, Electronics and Mobile Communication Conference (IEMCON)*. 2018. IEEE.
133. Chen, T., et al., *Autonomous deployment of a solar panel using elastic origami and distributed shape-memory-polymer actuators.* Physical Review Applied, 2019. 11(6): p. 064069.
134. Debnath, S. and L. Fei, *Origami theory and its applications: a literature review.* World Academy of Science, Engineering and Technology, 2013: p. 1131-1135.
135. Miura, K., *Map fold a la Miura style, its physical characteristics and application to the space science.* Research of Pattern Formation, 1994: p. 77-90.
136. Bowen, L., et al. *Dynamic modeling and analysis of an origami-inspired optical shield for the starshade spacecraft*. in *Smart Materials, Adaptive Structures and Intelligent Systems*. 2016. American Society of Mechanical Engineers.
137. Rubio, A.J., et al., *A foldable reflectarray on a hexagonal twist origami structure.* IEEE Open Journal of Antennas and Propagation, 2021. 2: p. 1108-1119.
138. Zhao, W., et al., *Origami derived self-assembly stents fabricated via 4D printing.* Composite Structures, 2022. 293: p. 115669.

139. Zhai, Z., Y. Wang, and H. Jiang, *Origami-inspired, on-demand deployable and collapsible mechanical metamaterials with tunable stiffness.* Proceedings of the National Academy of Sciences, 2018. 0: p. 201720171-201720171.
140. Shen, Y., et al., *Origami-inspired metamaterial absorbers for improving the larger-incident angle absorption.* Journal of Physics D: Applied Physics, 2015. 48(44): p. 445008-445008.
141. Tachi, T. and G.H. Paulino, *Invariant and smooth limit of discrete geometry folded from bistable origami leading to multistable metasurfaces.* (2019): p. 1-10.
142. Wo, Z. and E.T. Filipov, *Stiffening multi-stable origami tubes by outward popping of creases.* Extreme Mechanics Letters, 2023. 58: p. 101941.
143. Yao, M., et al., *A reconfiguration strategy for modular robots using origami folding.* International Journal of Robotics Research, 2019. 38(1): p. 73-89.
144. Yasuda, H., et al., *Origami-Based Cellular Structures with In Situ Transition between Collapsible and Load-Bearing Configurations.* Advanced Engineering Materials, 2019. 21(12): p. 1-8.
145. Yasuda, H., et al., *Origami-based impact mitigation via rarefaction solitary wave creation.* Science Advances, 2019. 5(5): p. 1-9.
146. Yasuda, H., et al., *Origami-based tunable truss structures for non-volatile mechanical memory operation.* Nature Communications, 2017. 8(1).
147. Boatti, E., N. Vasios, and K. Bertoldi, *Origami metamaterials for tunable thermal expansion.* Advanced Materials, 2017. 29(26): p. 1700360-1700360.
148. Arya, M., et al., *Large aperture deployable reflectarray antenna*. 2021, Google Patents.
149. Cheung, K.C., et al., *Origami interleaved tube cellular materials.* Smart Materials and Structures, 2014. 23(9).
150. Suto, K., et al., *An Edge-Extrusion Approach to Generate Extruded Miura-Ori and Its Double Tiling Origami Patterns.*
151. Sun, R., et al., *Kirigami stretchable strain sensors with enhanced piezoelectricity induced by topological electrodes.* Applied Physics Letters, 2018. 112(25): p. 251904-251904.
152. Pagano, A., et al., *A crawling robot driven by multi-stable origami.* Smart Materials and Structures, 2017. 26(9).
153. Rafsanjani, A., et al., *Kirigami skins make a simple soft actuator crawl.* Science Robotics, 2018. 3(15): p. eaar7555-eaar7555.
154. Tao, K., et al., *Origami-inspired electret-based triboelectric generator for biomechanical and ocean wave energy harvesting.* Nano Energy, 2020. 67: p. 104197.
155. Zhang, H., et al., *Origami-tessellation-based triboelectric nanogenerator for energy harvesting with application in road pavement.* Nano Energy, 2020. 78: p. 105177.
156. Wang, Y., et al., *Origami triboelectric nanogenerator with double-helical structure for environmental energy harvesting.* Energy, 2020. 212: p. 118462.
157. Rösch, A.G., et al., *Fully printed origami thermoelectric generators for energy-harvesting.* npj Flexible Electronics, 2021. 5(1): p. 1.
158. Hu, G., et al., *Triboelectric energy harvesting using an origami-inspired structure.* Applied Energy, 2022. 306: p. 118037.
159. Fang, H., et al., *Programmable Self-Locking Origami Mechanical Metamaterials.* Advanced Materials, 2018. 30(15): p. 1-9.
160. Kamrava, S., *Origami-based structures with programmable properties.* 2017(August).

161. Kamrava, S., et al., *Programmable Origami Strings.* Advanced Materials Technologies, 2018. 3(3): p. 1-8.
162. Li, S., H. Fang, and K.W. Wang, *Recoverable and Programmable Collapse from Folding Pressurized Origami Cellular Solids.* Physical Review Letters, 2016. 117(11): p. 1-5.
163. Liu, K., et al., *Programmable Deployment of Tensegrity Structures by Stimulus-Responsive Polymers.* Scientific Reports, 2017. 7(1): p. 1-8.
164. Liu, W., H. Jiang, and Y. Chen, *3D Programmable Metamaterials Based on Reconfigurable Mechanism Modules.* Advanced Functional Materials, 2022. 32(9).
165. Martinez, R.V., et al., *Elastomeric origami: Programmable paper-elastomer composites as pneumatic actuators.* Advanced Functional Materials, 2012. 22(7): p. 1376-1384.
166. Silverberg, J.L., et al., *Using origami design principles to fold reprogrammable mechanical metamaterials.* Science, 2014. 345(6197): p. 647-650.
167. Tang, Y., et al., *Programmable active kirigami metasheets with more freedom of actuation.* Proceedings of the National Academy of Sciences of the United States of America, 2019. 116(52): p. 26407-26413.
168. Tang, Y., et al., *Programmable Kiri-Kirigami Metamaterials.* Advanced Materials, 2017. 29(10): p. 1604262-1604262.
169. Wang, F., et al., *Patterning Curved Three-Dimensional Structures With Programmable Kirigami Designs.* Journal of Applied Mechanics, 2017. 84(6): p. 061007-061007.
170. Zhang, X., et al., *Kirigami-based metastructures with programmable multistability.* Proceedings of the National Academy of Sciences, 2022. 119(11): p. e2117649119.
171. Bhovad, P. and S. Li, *Using Multi-Stable Origami Mechanism for Peristaltic Gait Generation: A Case Study.* 2018: p. V05BT07A061-V05BT07A061.
172. Li, Y. and S. Pellegrino, *A Theory for the Design of Multi-Stable Morphing Structures.* Journal of the Mechanics and Physics of Solids, 2020. 136: p. 103772-103772.
173. Melancon, D., et al., *Multistable inflatable origami structures at the meter-scale.* Nature, 2021. (accepted)(August 2020).
174. Waitukaitis, S., et al., *Origami multistability: From single vertices to metasheets.* Physical review letters, 2015. 114(5): p. 55503-55503.
175. Kim, Y., et al., *Printing ferromagnetic domains for untethered fast-transforming soft materials.* Nature, 2018. 558(7709): p. 274-279.
176. Cui, J., F.R. Poblete, and Y. Zhu, *Origami/Kirigami-Guided Morphing of Composite Sheets.* Advanced Functional Materials, 2018. 28(44): p. 1-7.
177. Wo, Z. and E.T. Filipov, *Stiffening multi-stable origami tubes by outward popping of creases.* Extreme Mechanics Letters, 2023. 58: p. 101941-101941.
178. Kim, S.-J., et al., *An origami-inspired, self-locking robotic arm that can be folded flat.* Science Robotics, 2018. 3(16): p. eaar2915-eaar2915.
179. Woodruff, S.R. and E.T. Filipov, *Curved creases redistribute global bending stiffness in corrugations: theory and experimentation.* Meccanica, 2021. 56(6): p. 1613-1634.
180. Ma, R., L. Wu, and D. Pasini, *Contact-Driven Snapping in Thermally Actuated Metamaterials for Fully Reversible Functionality.* Advanced Functional Materials, 2023. 33(16): p. 2213371.
181. Wu, L. and D. Pasini, *In situ switchable local resonance in elastic metamaterials through bistable topological transformation.* Applied Physics Letters, 2023. 122(22).

182. Wu, L. and D. Pasini, *In-situ Activation of Snap-through Instability in Multi-response Metamaterials through Multistable Topological Transformation.* Advanced Materials, 2023: p. 2301109.
183. Wu, L. and D. Pasini, *Topological Transformation with Emerging Zero Modes in Multistable Metamaterials for Reprogrammable Flexural Stiffness.* Physical Review Applied, 2023. 19(6): p. L061001.
184. Zhai, Z., et al., *In situ stiffness manipulation using elegant curved origami.* Science Advances, 2020. 6(47): p. 1-10.
185. Qi, S., et al., *Acoustic energy harvesting based on a planar acoustic metamaterial.* Applied Physics Letters, 2016. 108(26): p. 263501.
186. Filipov, E.T. and M. Redoutey, *Mechanical characteristics of the bistable origami hypar.* Extreme Mechanics Letters, 2018. 25: p. 16-26.
187. Kim, W., et al., *Bioinspired dual-morphing stretchable origami.* Science Robotics, 2019. 4(36).
188. Mintchev, S., J. Shintake, and D. Floreano, *Bioinspired dual-stiffness origami.* 2018. 0275(July): p. 1-8.
189. Faber, J.A., A.F. Arrieta, and A.R. Studart, *Bioinspired spring origami.* Science, 2018. 359(6382): p. 1386-1391.

Chapter 2

Rigidly flat-foldable class of lockable origami-inspired metamaterials with topological stiff states

Chapter 2: Rigidly flat-foldable class of lockable origami-inspired metamaterials with topological stiff states

Amin Jamalimehr[1†], Morad Mirzajanzadeh[1†], Abdolhamid Akbarzadeh[2], and Damiano Pasini[1*]

[1]Department of Mechanical Engineering, McGill University, Montreal, QC, Canada

[2] Department of Bioresource Engineering, McGill University, Montreal, QC, Canada

[†]Authors contributed equally.

[*]Corresponding author. E-mail: damiano.pasini@mcgill.ca

Nature Communications, 13, 1816 (2022)

2.1 Abstract

Origami crease patterns have inspired the design of reconfigurable materials that can transform their shape and properties through folding. Unfortunately, most designs cannot provide load-bearing capacity, and those that can, do so in certain directions but collapse along the direction of deployment, limiting their use as structural materials. Here, we merge notions of kirigami and origami to introduce a rigidly foldable class of cellular metamaterials that can flat-fold and lock into several states that are stiff across multiple directions, including the deployment direction. Our metamaterials rigidly fold with one degree of freedom and can reconfigure into several flat-foldable and spatially-lockable folding paths due to face contact. Locking under compression yields topology and symmetry changes that impart multidirectional stiffness. Additionally, folding paths and mixed-mode configurations can be activated in situ to modulate their properties. Their load-bearing capacity, flat-foldability, and reprogrammability can be harnessed for deployable structures, reconfigurable robots, and low-volume packaging.

2.2 Introduction

Origami and kirigami, the arts of folding and cutting paper, have inspired the development of a plethora of scale-invariant reconfigurable materials and structures that can deploy either spatially or in-plane [127, 190]. These concepts have been implemented across disciplines, from mechanical memories [146], robotic actuators [55, 81, 83, 152, 153], thermally tunable structures [147, 191], multistable devices [28, 50, 79, 109, 192], complex 3D geometries [91, 95], and programmable surfaces [68, 82, 98, 193] to flexible electronics [80, 96]. Origami crease and kirigami cut patterns also proffer mechanical metamaterial designs with distinct geometric and mechanical properties, such as reconfigurability [86, 87], flat-foldability [70, 86, 104, 107, 149, 194], and bistable auxeticity [49, 50] among others.

Of recent interest are *in situ* reprogrammable folding metamaterials [139, 144, 159, 166, 167, 184, 195] which harness an inherent coupling between the folding pattern and the geometry of motion. Here, rigid-foldability, flat-foldability, and load-bearing are distinct characteristics that can describe the modality of folding and the realization of certain functional performances. Rigid-foldability indicates that folding is solely controlled by the crease lines acting as rotational hinges, and not the deformation of the rigid panels [196]. Alternatively, in non-rigid-foldable patterns, both panel compliance and crease lines govern folding. Flat-foldability is a property that imparts a high level of reconfigurability by allowing spatial transformations leading into one or more flat states. Load-bearing in a foldable metamaterial simply denotes the capacity to offer structural resistance to a load applied in any given configuration across multiple directions.

Existing origami-inspired metamaterials offer a certain level of programmability, yet they are unable to attain concurrently rigid-foldability, flat-foldability, and load-bearing capacity along the deployment direction. One reason stems from the kinematics of their unit cell, which controls the way the crease pattern folds. Foldable metamaterials using the Miura-ori [70, 104], interleaved [149], and tubular [28, 72, 107] patterns as well as cylindrical structures based on waterbomb patterns [195], and other unit cells, utilize crease geometry that exhibits some but not all of the properties defined above. For example, rigid-foldable material systems with multiple degrees of freedom (DoFs) [86, 87], are either floppy or require precise control of the folding sequence, a characteristic that severely limits their capacity to withstand multidirectional loads. Alternatively, non-flat-foldable concepts [159, 195] have limited reconfigurability, making their size and volume large, and most existing concepts utilizing structural instability [81, 109, 127, 166, 195] or the Kresling pattern [110, 139] to achieve reconfigurability are non-rigid-foldable. To fold, they must overcome a large energy barrier that bends and stretches their panels, thus sacrificing load-bearing capacity. On the other hand, foldable patterns that offer some load resistance can do so in certain directions only and mainly loses stiffness in the deployment direction [28, 48, 72, 86, 87, 107, 144]. This aspect can be problematic in applications where during service the load direction is uncertain, hence potentially reverting a stiff into a floppy configuration.

From the current state of the art, an interesting question arises: Can a crease pattern be conceived to reconcile the conflicting nature of rigid-foldability, flat-foldability, and load-bearing capacity in multiple directions, including that of deployment? This paper presents a framework for designing a topological class of rigidly flat-foldable metamaterials that are reprogrammable in situ to reconfigure along multiple directions, some flat-foldable and others lockable, where the latter is multi-directionally stiff even along the deployment direction. Our basis combines origami and kirigami concepts to introduce a crease pattern that is built cellular in its flat configuration, and subsequently stacked with the minimum number of layers to steer folding along one trajectory. To imbue reconfigurability, excisions are introduced in a crease pattern so as to relax the deformation constraints enacted by the rigidity of the faces of the parent origami, and to enable face contact within their intracellular spaces. Besides load-bearing capacity, our concept offers additional hallmarks including topology and symmetry switching that altogether enlarge the degree of in situ programmability. Finally, a simple yet effective fabrication process that can be easily automated is presented to impart three-dimensionality in the flat configuration.

2.3 Results

2.3.1 Geometry of reconfigurable unit chain

To generate a rigidly-foldable unit that is flat-foldable and can lock into a stiff state upon panel self-contact, we start from a primitive network of bars connected in a planar loop. The network is a planar *N*-bar linkage that forms a regular *N* even-sided polygon. Figure 2-1A shows the generative process is exemplified with a network of four bars, each of length a and enclosing a square void. Extruding each bar outward to the length b (red arrow) in the *x*-*y* plane and at a given angle $\phi \in \left[\frac{\pi}{N}, \pi - \frac{\pi}{N}\right]$ yields four parallelograms, which we connect using isosceles triangles with a vertex angle of $\lambda = 2\pi/N$. By prescribing the folding profiles (dash lines) at each boundary between interfacing panels, we obtain a planar assembly of rigid surfaces that altogether can spatially fold along their connecting valley (V) and mountain (M) folding lines. The conceptual process can be thought as complementary to the fabrication steps, where the unit void is first excised from a planar sheet of paper (kirigami cuts), and then folded along prescribed dashed lines (origami folds), thereby generating a hybrid architecture.

The fold lines of both V and M panels enable the system to act as a kinematic chain. Here we define its configurational changes (Figure 2-1A) using m independent dihedral angles θ_1, θ_2, …, θ_m. Each dihedral angle specifies the angle between the triangular panel and its adjacent quad panel as shown in Figure 2-1A, and m denotes the mobility or nontrivial degrees of freedom (DoF) of the kinematic chain that exclude rigid-body motions. Since two dihedral angles, one concave and the other convex, can always be identified between connected panels, we here consider a dihedral angle as convex. In addition, we assume the mountain and valley fold lines are constrained to remain on two parallel planes during folding. This strategy, as explained later, is enforced by using unit chain stacking, and it enables the unit to engage motion along a single DoF. In this case, the out-of-plane rise h can be expressed as a function of three geometric parameters by

$$h = a \sin\phi \sin\theta_1 \tag{3-1}$$

During folding, a process that decreases θ_1, the "unit kinematic chain", in short "unit chain", can reach a lock state, denoted with the superscript "L", where self-contact between panels forbids any further motion (right sketch in Figure 2-1A). In a lock state, the acute dihedral angles are given by

$$\theta^L = \cos^{-1}\left(\cot\phi \tan\frac{\lambda}{2}\right) \tag{3-2}$$

The generative process illustrated in Figure 2-1A for a unit chain with square primitive can now be abstracted to other primitives, i.e., regular N even-sided polygons, by merely varying N. The outcome is a class of planar unit chains that spatially reconfigure within the voids and lock upon self-contact of their panels, thus behaving stiff under compression. Figure 2-1B illustrates five of them, each for a given N. The first three rows show their initial fully developed state, the partially folded states, and one among the lock configurations they can attain. The last two rows depict their most compact in-plane tessellation and their out-of-plane stacking in paperboard specimens, where each layer is flipped with respect to the *x-y* plane and bonded at the triangular panels of the adjacent layers (above and below).

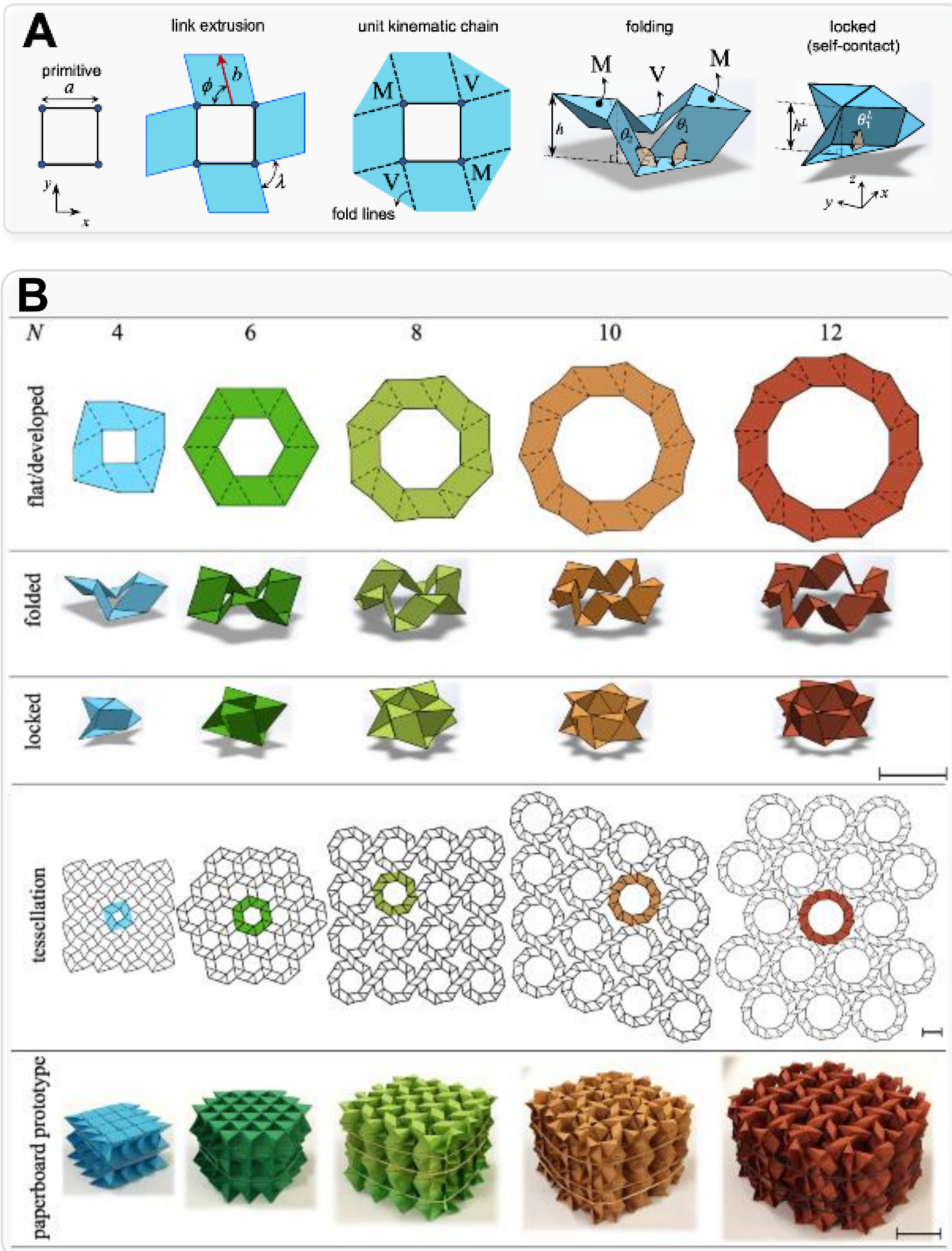

Figure 2-1 Origami inspired metametrial **A** The building block of our reconfigurable class of rigidly flat-foldable materials. Primitive regular polygon describing a four-bar linkage, followed by in-plane angled

(ϕ) extrusion (red arrow of length b) of constitutive links; connection of extruded panels with isosceles triangular panels; addition of fold lines and assignment of a mountain (M) and valley (V). Upon folding, the unit chain reconfigures to reach its lock state (specified with "L") where contact is established between panels. **B** Concept abstraction to generate unit chains with an *N* even-sided regular polygon for representative N, i.e., 4, 6, 8, 10, and 12. The first three rows show respectively the developed, partially folded, and one of the (multiple) lock states. The last two rows show the in-plane tessellation and their paperboard proof-of-concepts. The latter are multilayered spatial realizations obtained with the minimum number of layers, i.e., an even number of layers preserving their symmetry with respect to *x-y* plane, that provides one degree of freedom. Rubber bands are here used to hold the unloaded configuration of the prototypes in their lock state, as the transition to the lock state requires the application of compressive forces in the *x-y* plane, as explained later in the manuscript. Scale bars = 30 mm.

2.3.2 Kinematic model

Upon folding, the panels of the unit chain (Figure 2-1A) are in relative motion before coming into contact. To study kinematics, we make a set of assumptions. First, we assume the panels as infinitely rigid and the fold lines as pure rotational hinges. Second, to ease the formulation of the kinematic constraints, we replace the unit chain with a triangulated network of inextensible elements connected through pin joints (see Section 2.6.1 for details). Third, the edges of the triangular panels are modelled as bars, whereas we replace quad panels with two triangles satisfying the planarity condition of their interplanar angles over the entire folding process (see Section 2.6.1 for details). With the assumptions above, we now examine a generic pin-jointed network of inextensible bars and determine the number of mechanisms i.e., *DoFs*, and types of motion, i.e., *kinematic paths*, our unit chain can attain in space.

2.3.3 Number of Degrees of Freedom

To determine the mobility of our unit chain, we formulate the rigidity matrix R pertinent to its structural assembly. In general, the number of degrees of freedom, m, for a pin-jointed triangulated network is given by $m = 3j - n_K - r$, where j is the total number of joints, n_K the number of external kinematic constraints, and r the rank of R (see Section 2.6.1 for details). For our unit chain, m also represents the number of independent dihedral angles. For the unit chain $\widehat{\mathrm{N}}_4$ in Figure

2-1A, $m = 5$ represents the number of mechanisms it can attain, i.e., its DoFs. m can be reduced to 1 if the mountain and valley fold lines are constrained to remain on two parallel planes during the folding process. The specific values and the relationships these dihedral angles assume define distinct types of motion, as described below.

2.3.4 Kinematic paths

There are specific trajectories our unit chain can follow during motion. Each of them can be uniquely defined by a relation between the independent parameters, in our case the dihedral angles. For example, the equality of dihedral angles, i.e., $\theta_1 = \theta_2$, represents one type of motion, whereas $\theta_1 = \pi - \theta_2$ describes another type of motion. Each relationship between angles defines a given trajectory, namely a *kinematic path*. For example, the kinematic path shown in Figure 2-1A can be defined by the relation of equality between its dihedral angles.

2.3.5 Unit stacking as a pathway to reduce mobility.

If the triangular panels shown in Figure 2-1A do not remain parallel during folding, our unit chain is endowed with manifold DoFs, which for $\widehat{\mathrm{N}}_4$ are five. Having too many DoFs, m, can be problematic, as the unit chain acts as a multi-degree-of-freedom mechanism; in this case, the unit tends to be floppy, and folding cannot be unequivocally and easily controlled for use as a reconfigurable load-bearing material. One way to prune m is to act along the third direction (z), and stack layers of unit chains one on the top of the other. Figure 2-2A shows this strategy applied to $\widehat{\mathrm{N}}_6$. Here, the mountain facets of the triangular panels of the top unit are bonded to the valley facets of the adjacent unit (below). By stacking and bonding three unit chains, the mountain and valley triangular panels are set to lie in parallel planes. If made out of a real material with sufficiently high elastic modulus, the non-negligible thickness of the triangular panels has the effect of restricting the relative rotation range of two connected quad panels, allowing only equal and opposite rotation to satisfy kinematic compatibility and to avoid encountering the energy barrier caused by the bending or stretching panels during deformation (see Section 2.6.2 and Figure 2-8).

The strategy above is simple yet effective. It not only turns off DoFs, but also provides the potency for a robust reconfiguration along a single route. Having now layers of unit chains, we can denote a generic multilayered *N* even-sided unit chain with *n* stacking layers by $\mathrm{N}_N\mathrm{n}_n$. Through a rigidity analysis of $\mathrm{N}_N\mathrm{n}_n$, we can assess the role of layer stacking, n, on the DoFs (Section 2.6.1). The outcome of this investigation is shown in Figure 2-2B, where $\theta_i \neq \pi/2$ is assumed, and $\theta_i = \pi/2$ refers to the kinematic bifurcation. From the plot, we gather that the DoFs of the single layer unit chains increases linearly with N through the relation $m = 2N - 3$ which can be reduced to 1 if multiple layers are stacked upon them. Stacking layers can thus enact reconfigurability along one single path. The minimum number of layers, $\bar{n}$, necessary to trim m to 1 is not unique, rather it depends on the unit chain primitive. Figure 2-2B shows that for unit chains N_4 and N_6, $\bar{n}$ = 3, whereas for $\mathrm{N}_{N>6}$, $\bar{n}$ = 5. We now focus on multilayered units with a single DoF prior to bifurcation, denoted by $\mathrm{N}_N\mathrm{n}_{\bar{n}}$, and investigate their behaviour at the instant of kinematic bifurcation and post-bifurcation.

2.3.6 Kinematic bifurcation: emergence of lock and flat-fold modes

In the early stage of folding, our $\mathrm{N}_N\mathrm{n}_{\bar{n}}$ chain can travel along one route governed by $\bar{n}$. However, as soon as it reaches a configuration where all its dihedral angles are $\pi/2$, i.e., *kinematic bifurcation*, the DoFs instantaneously grow, and multiple kinematic paths become active (Figure 2-2A and Figure 2-2C). We classify the post-bifurcation modes into either two-dimensional (2D) *flat-foldable*, or three-dimensional (3D) *lockable* (Figure 2-2C). Flat-foldable modes are fully flat patterns that are distinct from the initial state. Lockable modes describe 3D states with contact between adjacent panels that impart compressive stiffness.

We can show (Section 2.5.1) that our single-DoF multilayered unit chains possess only two types of dihedral angle pairs (Figure 2-2A and Figure 2-2D), acute $\mathcal{A}$ and obtuse $\mathcal{O}$, obeying the relation $\mathcal{A} + \mathcal{O} = \pi$ during the entire range of motion. A given sequence with angle pairs, e.g., two $\mathcal{A}$s and one $\mathcal{O}$ depicted in Figure 2-2D, can be simply denoted by the series of angle pairs, e.g., $\mathcal{A}\mathcal{A}\mathcal{O}$, and in compact form with the power indicating the repeated pairs, e.g., $\mathcal{A}^2\mathcal{O}$. This notation allows discriminating between kinematic modes that emerge at bifurcation. Given the modes defined by a repeating sequence of $\mathcal{A}\mathcal{O}$, such as $\mathcal{A}\mathcal{O}\mathcal{A}\mathcal{O}\mathcal{A}\mathcal{O}$ ... (or simply $\overline{\mathcal{A}\mathcal{O}}$), cannot be tessellated in-plane, we denote them as irregular modes as opposed to the regular ones which are tileable in-plane (Section 2.6.4).

With the above, we systematically characterize the regular modes of a generic $\mathrm{N}_N\mathrm{n}_{\bar{n}}$ and determine the total number of possible reconfiguration modes. We use the Pólya enumeration theorem of combinatorics (Section 2.6.3) to (i) count the regular modes and then (ii) define their kind. The problem of finding all independent regular modes of a generic $\mathrm{N}_N\mathrm{n}_{\bar{n}}$ unit can be treated as the classical necklace problem. The goal is to reconstruct the colored pattern of a necklace of several beads, each colored either in white or black ($\mathcal{A}$ or $\mathcal{O}$), from the knowledge of a limited set of information (Section 2.5.1). By using a predictor-corrector type incremental method (Section 2.6.1), we can now visualize the post-bifurcation kinematic paths of $\widehat{\mathrm{N}}_4\mathrm{n}_4$, $\widehat{\mathrm{N}}_6\mathrm{n}_4$, $\widehat{\mathrm{N}}_8\mathrm{n}_5$, $\widehat{\mathrm{N}}_{10}\mathrm{n}_5$.

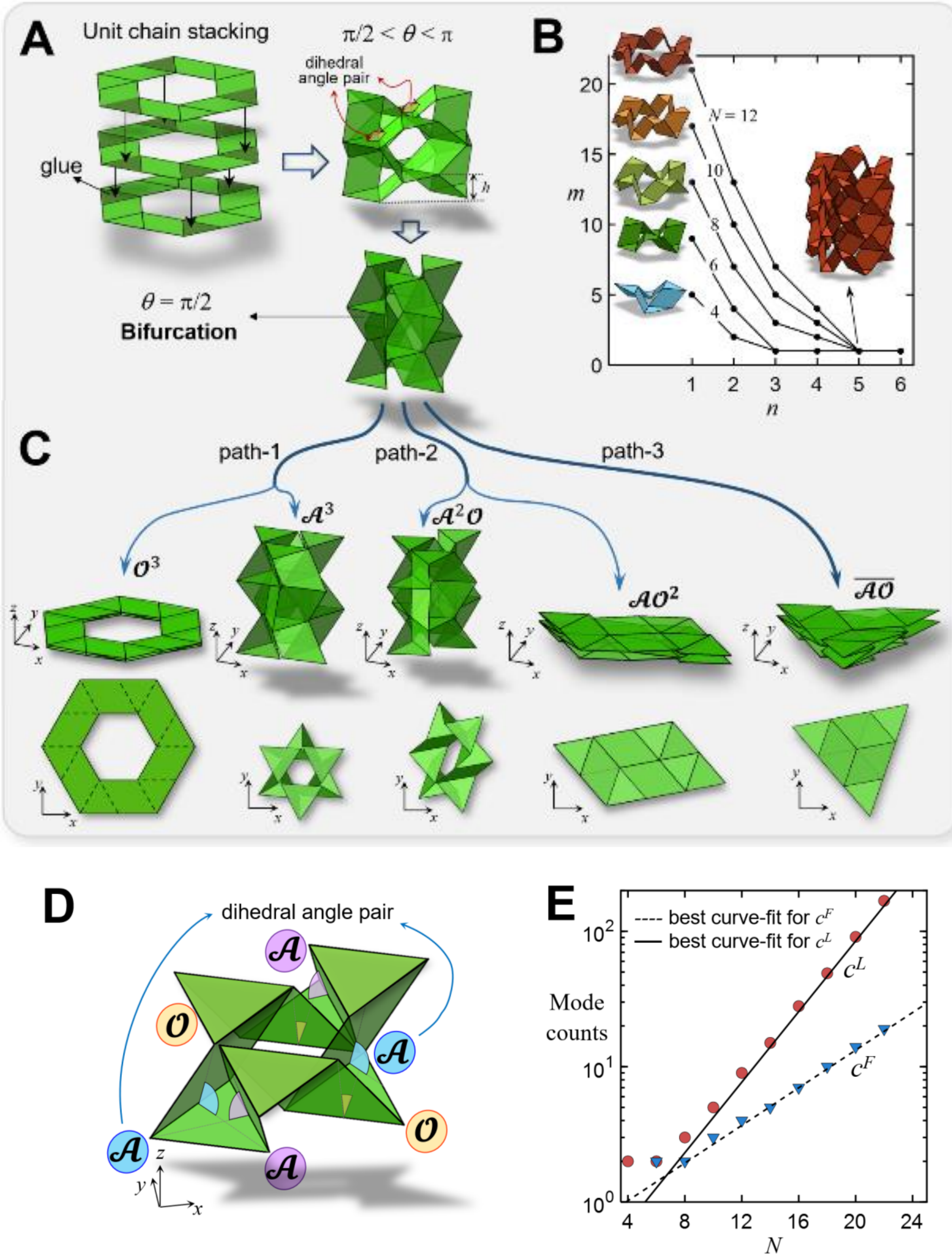

Figure 2-2 Stacking layers as a means for reducing degrees of freedom. **A** Unit chain stacking for a three-layered unit $\widehat{\mathrm{N}}_6\mathrm{n}_3$. On its right, a representative pre-bifurcation reconfiguration with $\theta < \pi$ (above) and

the bifurcation state with $\theta = \pi/2$ (below). **B** Pre-bifurcation DoFs, m, plotted as a function of the number of stacked layers, n, for given N even-sided primitives ($N = 4, 6, 8, 10, 12$). **C** Isometric and top views of five post-bifurcation modes belonging to three kinematic paths: four regular modes, of which two are locked ($\mathcal{A}^3$ and $\mathcal{A}^2\mathcal{O}$) and two flat-folded ($\mathcal{O}^3$ and $\mathcal{A}\mathcal{O}^2$), and one irregular mode ($\overline{\mathcal{A}\mathcal{O}}$). **D** Zoom on the top layer of $\widehat{\mathrm{N}}_6\mathrm{n}_3$ in lock mode $\mathcal{A}^2\mathcal{O}$ showing the arrangement of pairs of valley dihedral angles (in color). E Mode counts calculated from discrete data points for $N > 4$ along with the best curve fits characterizing the number of flat-foldable c^F and lockable c^L modes vs. N for a generic multilayered unit $\mathrm{N}_N\mathrm{n}_{\bar{n}}$ (semi-log plot).

To understand the relation between the total number of post-bifurcation modes and the sides of the unit chain primitive N, Figure 2-2E plots the total number of lockable modes c^L and flat-foldable modes c^F versus N. The best curve fits are included to provide phenomenological closed-form relations that characterize folding paths and differentiate lockable modes ($c^L = 0.21\exp(0.3N)$) from flat-foldable modes ($c^F = 0.54\exp(0.16N)$) as a function of N for a generic $\mathrm{N}_N\mathrm{n}_{\bar{n}}$. The results show that the number of regular modes grows exponentially, hence providing a rich platform to program lockable paths (Table 2-1).

2.3.7 Symmetry and topology

From a single multilayered unit chain, we now turn to its periodic and multilayered tessellation forming a material system. Multilayered unit chains are connected to follow a tessellation pattern (see Section 2.6.4) that replicates a crystallographic arrangement of atoms. Figure 2-3 shows the top view of representative patterns for N = 4, 6, 8, and 10. While several others exist, here we focus on tessellations with the most compact pattern. The goal is to show that upon folding along a given path our material systems undergo switches in symmetry and apparent topology, both hallmarks of in situ programmability.

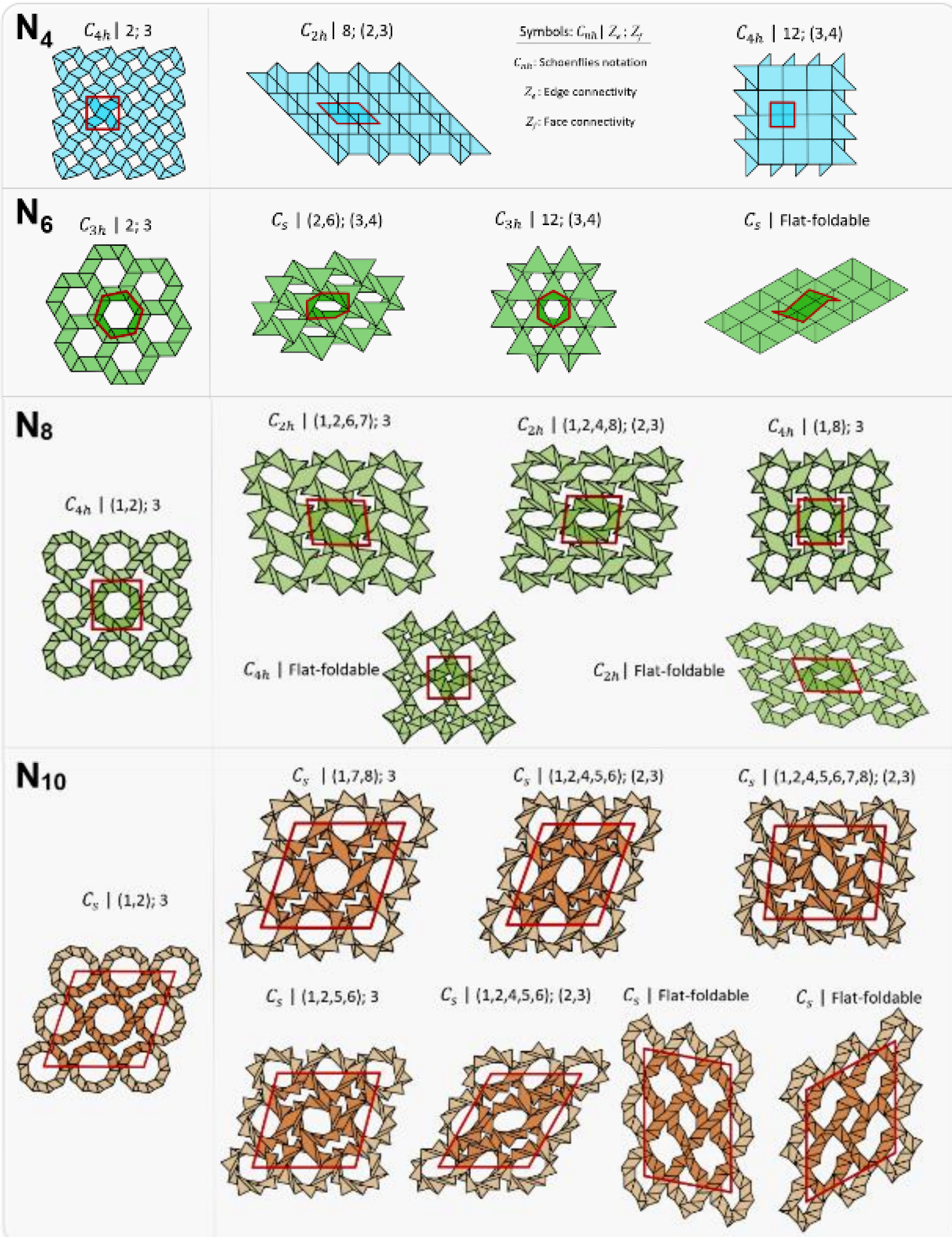

N4
C_{4h} | 2; 3
C_{2h} | 8; (2,3)
Symbols: C_{nh} | Z_e ; Z_f
C_{nh}: Schoenflies notation
Z_e: Edge connectivity
Z_f: Face connectivity
C_{4h} | 12; (3,4)
N6
C_{3h} | 2; 3
C_s | (2,6); (3,4)
C_{3h} | 12; (3,4)
C_s | Flat-foldable
N8
C_{2h} | (1,2,6,7); 3
C_{2h} | (1,2,4,8); (2,3)
C_{4h} | (1,8); 3
C_{4h} | (1,2); 3
C_{4h} | Flat-foldable
C_{2h} | Flat-foldable
N10
C_s | (1,7,8); 3
C_s | (1,2,4,5,6); (2,3)
C_s | (1,2,4,5,6,7,8); (2,3)
C_s | (1,2); 3
C_s | (1,2,5,6); 3
C_s | (1,2,4,5,6); (2,3)
C_s | Flat-foldable
C_s | Flat-foldable

Figure 2-3 Various reconfiguration modes of origami-inspired metamaterial from the top view. Flat-foldable and lockable modes of in-plane tessellated systems made of multilayered unit chains $\widehat{\mathrm{N}}_4\mathrm{n}_{\bar{n}}$, $\widehat{\mathrm{N}}_6\mathrm{n}_{\bar{n}}$, $\widehat{\mathrm{N}}_8\mathrm{n}_{\bar{n}}$, and $\widehat{\mathrm{N}}_{10}\mathrm{n}_{\bar{n}}$ (qualitative sketches out-of-scale). Group points using Schoenflies notation are shown for all modes. C_n refers to an n-fold rotation axis, C_{nh} refers to C_n with the addition of a mirror plane perpendicular to the axis of rotation, and C_s denotes a group with only a mirror plane (C_{1h}). Edge and face connectivity are only shown for lockable modes. Z_e is the number of edges that meet at a point (joint). Z_f represents the number of faces that meet at an edge. The values of Z_e and Z_f for each configuration are shown after a vertical line separating them from their Schoenflies notation; parentheses are used whenever more than one connectivity value exists. For each configuration, multiple values of Z_e and Z_f may exist for a given joint and edge within the lattice. In these cases, all the values are reported in parentheses.

Notions of crystallography become handy to study changes in symmetry. Each pattern is formed by tessellating in-plane a representative unit (red boundaries in Figure 2-3) defined by the periodic vectors. Upon reconfiguration, the material system at bifurcation can access a new kinematic path that causes the smooth transition of certain dihedral angle pairs from $\mathcal{A}$ to $\mathcal{O}$; the result is a break in symmetry. This phenomenon is visualized by the patterns that followed those in the first column of Figure 2-3, each denoted by their crystallographic point group and Schoenflies symbol. A variation in the lattice point groups translates into a change of the elastic constants defining the elastic tensor; the symmetry shift endows the material system with another set of elastic properties. For example, the lattice made of $\widehat{\mathrm{N}}_4\mathrm{n}_{\bar{n}}$ (first row of Figure 2-3) is shown in one of its lock modes, $\mathcal{AO}$, in the second column. In this mode, $\mathcal{AO}$ has C_{2h} symmetry, i.e., a twofold rotational symmetry, and its elastic compliance matrix contains 13 elastic constants defining a monoclinic behavior. Upon switching to lock mode $\mathcal{A}^2$ (third column), its symmetry changes to C_{4h}, a fourfold rotational symmetry, resulting in an elastic compliance matrix with seven independent constants.

Besides symmetry, another aspect enabling in situ programmability is the apparent change of topology undergone after bifurcation. Here topology is defined by connectivity through Z_f, the number of faces that meet at an edge, which is equivalent to a fold-line as opposed to a cut-edge, and Z_e, the number of edges meeting at a vertex. The values of Z_e and Z_f are calculated for the corresponding spatial lattice upon the assumption that in the lock state coincident edges and vertices form a single edge and a single vertex (values on top of each configuration in Figure 2-3). A change in Z_e and Z_f denotes topology differentiation in the physical space, whereas topology is invariant to other geometric parameters, such as the length of the primitive void. Results show an increase in connectivity values from the partially folded state to the lock state (see also Section 2.6.7). A break in topology impacts the deformation mode of the panels, which transition from bending to stretching [197], as shown later. The versatility to impart topological changes by traveling across a kinematic bifurcation can be used not only to tune the mechanical and physical properties in situ (see also Sections 2.6.11, 2.6.12, and 2.6.13), but also to switch the mechanism of deformation.

2.3.8 Energy landscape

Prior to bifurcation, our multilayered system $\mathrm{N}_N\mathrm{n}_{\bar{n}}$ folds with one DoF through the application of in-plane forces. At the point of kinematic bifurcation, however, multiple kinematic paths become accessible. The entry into a specific path depends on the interplay between the components of the compressive forces, applied in its plane at the bifurcation instant. To study their role, we examine a generic $\mathrm{N}_N\mathrm{n}_n$ (with $n \geq \bar{n}$) bi-axially and uniformly compressed and investigate the energy landscape of each kinematic path. The goal is to find the path and pertinent mode with the lowest energy level.

To formulate the total energy of $\mathrm{N}_N\mathrm{n}_n$ we assume infinitely rigid panels and frictionless rotational springs (hinges) of uniform stiffness per unit length, k. We consider our unloaded system in mode $O^{N/2}$, with all dihedral angle pairs being obtuse; this is the zero-energy state of the system denoted by θ^0 specifying a configuration that is either flat or partially folded due to the presence of residual stresses induced by manufacturing. θ^L, on the other hand, is the acute dihedral angle of the lock unit. We assume $\theta^0 > \pi/2$, a condition implying that upon the application of an out-of-plane load (z direction in Figure 2-1A), our system can only fold from its zero-energy state to its fully developed configuration.

2.3.9 Mode-phase diagram: the role of in-plane confinement

We consider a pair of compressive in-plane forces, f_x and f_y, applied uniformly, quasi-statically, and oriented along the principal directions x and y (Figure 2-1A). We define the biaxiality ratio $r_B = f_y/f_x$ with $f_y \in [0,\infty)$, $f_x \in (0,\infty)$ and $r_B \in [0,1]$ to discriminate between the relative magnitude of the applied forces, and derive an expression of the total energy as a function of the applied forces and the dihedral angle, i.e., $\Pi = \Pi(\theta, f_x, f_y)$ or $\Pi = \Pi(\theta, f_x, r_B)$ (Section 2.6.13).

Two representative systems $\widehat{\mathrm{N}}_4\mathrm{n}_n$ and $\widehat{\mathrm{N}}_6\mathrm{n}_n$ (with $n \geq \bar{\mathrm{n}}$ and geometric parameter $\bar{b} = b/a = 1$) are examined. Their energy landscapes can be mapped into mode-phase diagrams (see Section 2.5.2) and their application showcased in demonstrative scenarios defined by families of applied in-plane forces. Each family is specified by (f_x,r_B) where r_B is maintained constant over the entire loading history. We consider two load families. The first is (f_x,$r_B = 1/3$), where f_x and f_y can be proportionally scaled to respect the one third ratio; the (dimensionless) total energy landscape of one specific case ($f_x = 1$, $r_B = 1/3$) of that family is shown in Figure 2-4A by the blue curve for a system with $n = 3$ and $\theta^0 = \pi$. In Figure 2-4B, (f_x,$r_B = 1/3$) is shown by the blue load-path ABCD crossing three domains. In the light-yellow region, an increase of the force magnitudes from A to B is not sufficient to reconfigure our system, which remains flat ($\theta = \pi$) in its fully developed state. Once the load magnitude reaches the first domain boundary (black dash line), point B, the system starts to fold along the only kinematic path (yellow region) up to bifurcation (black solid line), point C. Immediately after bifurcation, the system can in principle access two modes ($\mathcal{AO}$ and $\mathcal{A}^2$ branches in Figure 2-4A), yet it enters $\mathcal{AO}$ due to the lower energy it requires for activation. After entering in mode $\mathcal{AO}$, the system momentarily continues to reconfigure until it locks at point D (Figure 2-4A, B). At this stage regardless of the magnitude of f_x and f_y satisfying $r_B = 1/3$, no further folding is possible as the panels have come into contact, thus imparting stiffness.

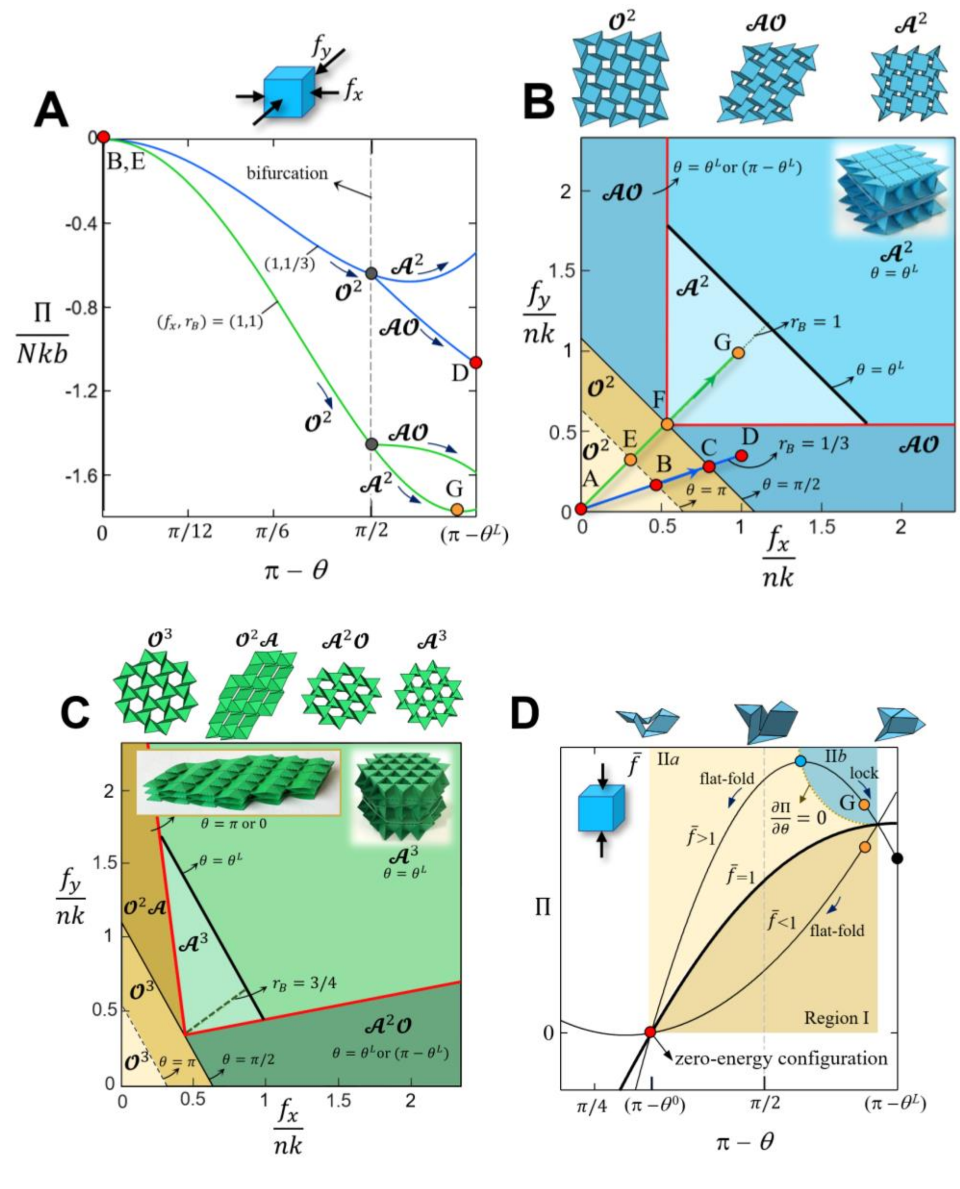

Figure 2-4 Energy analysis of the origami-inspired metamaterial. **A** Dimensionless total energy landscape of $\widehat{\mathrm{N}}_4\mathrm{n}_{\bar{n}}$ unit subjected to two representative in-plane biaxial forces: $(f_x, r_B = f_y/f_x) = (1,1/3)$, shown in blue, and $(1,1)$ shown in green. **B** Mode-phase diagram of $\widehat{\mathrm{N}}_4\mathrm{n}_n$ unit subjected to dimensionless forces

describing in-plane biaxial confinement $f_x/(nk)$ and $f_y/(nk)$, where k is the rotational stiffness of the hinges per unit length: Family-load paths ABCD and AEFG describing uniform scaling of the applied forces. **C** Mode-phase diagram of $\widehat{\mathrm{N}}_6\mathrm{n}_n$ unit under in-plane biaxial loads. Complementary information to plots B and C about the orientation of the lattice relative to the load direction is given in Figure 2-12 and Figure 2-13. **D** Schematic total energy landscape of $\widehat{\mathrm{N}}_4\mathrm{n}_{\bar{n}}$ subjected to representative uniformly applied out-of-plane loads: $\bar{f} < 1$, $\bar{f} = 1$, $\bar{f} > 1$, where $\bar{f} = f_o/f^L$. Three regions emerge for mode $\mathcal{A}^2$: Region I (light brown) shows the configuration space in which the unit under compressive load $\bar{f} < 1$ folds in mode $\mathcal{O}^2$ towards a state in proximity to its zero-energy configuration; Region iIa (light yellow) shows the configuration space where the unit despite being subject to $\bar{f} > 1$ still fold in mode $\mathcal{O}^2$ towards a state in proximity to its fully developed state; Region iIb (blue) illustrates the lockable domain, describing folding states where the unit has been brought by in-plane forces to a dihedral angle above the threshold of maximum energy (dot boundary); from this state the sole application of $\bar{f} > 1$ makes the unit spontaneously folds in mode $\mathcal{A}^2$ until its panels contact.

The second family of in-plane forces is $(f_x, r_B = 1)$, shown in Figure 2-4B by the green load-path AEFG. The total energy landscape of one specific load case $(f_x = 1, r_B = 1)$ for that family is illustrated in Figure 2-4A (green). Similar to ABCD, the system remains in its flat configuration for a load increase from A to E. A further increase of the in-plane confinement makes the system exit the initial region (black dash line) and gradually deform up to the bifurcation point F (second boundary threshold). Thereafter, it enters the lowest energy branch ($\mathcal{A}^2$ in Figure 2-4A and light blue region in Figure 2-4B) with an energetically stable state that occurs slightly prior to its lock state, point G. An additional load increase makes the system fold until it reaches its lock state (dark blue region in Figure 2-4B).

The map in Figure 2-4B shows that the only way for $\widehat{\mathrm{N}}_4\mathrm{n}_n$ to access mode $\mathcal{A}^2$ is with $r_B = 1$; in contrast, any other values of r_B would bring the system to lock in mode $\mathcal{AO}$. This is an outcome that is distinctive to $\widehat{\mathrm{N}}_4\mathrm{n}_n$, and does not necessarily translate to other systems. For instance, for $\widehat{\mathrm{N}}_6\mathrm{n}_n$, more kinematic paths are available, i.e., multiple ranges of r_B exist to switch between modes. Figure 2-4C shows the mode-phase diagram of $\widehat{\mathrm{N}}_6\mathrm{n}_n$. Here, $r_B = 0.74$ (diagonal in the light green region) defines a condition for which the system, initially in $\mathcal{O}^3$ mode, enters $\mathcal{A}^3$ mode immediately after bifurcation. For $r_B > 0.74$, the unit enters its lockable mode $\mathcal{A}^2\mathcal{O}$ (dark green), whereas for $r_B < 0.74$, it accesses its flat-foldable mode $\mathcal{O}^2\mathcal{A}$ (brown region). Once entered in the post-bifurcation mode with minimum energy, the system remains in that region until it locks. At this stage, the system is rigid under compression and can no longer reconfigure; no other regions beyond the red boundaries (Figure 2-4B, C) are accessible. The mode-phase diagrams depend on the geometric parameters $\bar{b}$ and ϕ only, the former being a nonlinear scale factor, and the latter governing the slope of the lines separating mode-regions and the loading path (biaxiality ratio r_B) of a given mode (see also Section 2.6.13). They enable the choice of in-plane confining forces to attain desired post-bifurcation modes. The role of out-of-plane confinement is examined in the following.

2.3.10 Lock state domains governed by out-of-plane force

Our goal is to determine the magnitude of an out-of-plane (*z* axis in Figure 2-1A) compressive force f_o necessary to bring and keep the system in its lock state without the need of in-plane confining forces.

For the demonstrative purpose, we examine $\widehat{\mathrm{N}}_4\mathrm{n}_n$ folding in mode $\mathcal{A}^2$. Figure 2-4D schematically shows its energy curves (see Section 2.5.3) for three representing values of the out-of-plane load normalized by the lock load, i.e., $\bar{f} = f_o/f^L$ where the lock load f^L is the minimum out-of-plane force at the lock state (see Section 2.5.2). The interplay between f_o and f^L gives rise to three domains:

Region I (light brown): $\bar{f} < 1$. Since $f_o < f^L$, the system cannot access the lock state from a given configuration.

Region iIa (yellow): $\bar{f} > 1, \frac{\partial \Pi}{\partial \theta} < 0$ and $\frac{\partial^2 \Pi}{\partial \theta^2} < 0$ – recall Π is expressed as a function of $(\pi - \theta)$. Partially folded at a given dihedral angle, the system is prone to fold back to its fully developed (flat) state.

Region iIb (blue): $\bar{f} > 1, \frac{\partial \Pi}{\partial \theta} > 0$, and $\frac{\partial^2 \Pi}{\partial \theta^2} < 0$. This is the lockable domain (see Section 2.5.2).

If in-plane forces lead the system to reach one unstable dihedral angle (blue point in Figure 2-4B), a small perturbation prompts the system to naturally abandon it. Once the in-plane forces succeed in generating dihedral angles smaller than those described by Eq. (2-5) in Section 2.5.2, our system can access the descending path in the lockable domain. Here spontaneous folding towards the lock state occurs, and in-plane forces are no longer needed. The magnitude of the out-of-plane action ($f_o > f^L$) enables lifting the in-plane confinement. Once in the lockable domain, e.g., orange point, the system is drawn to fold towards a stable configuration of equilibrium until it arrests due to panel contact (black point).

The analysis above has revealed the interplay between in-plane and out-of-plane confinement. The former can be imparted through the biaxiality ratio to program and steer the reconfiguration mode (either lockable or flat-foldable) during the folding process. The latter, in particular its magnitude ($f_o > f^L$) and the threshold value of the dihedral angle, i.e., the lockable domain boundary, set the conditions for spontaneous folding into the lock state without the need for in-plane compression. Once contact is attained, our system becomes a stiff structure (see Sections 2.5.4 and 2.6.7), and it is ready to sustain compressive loads exerted in all three directions, as described below.

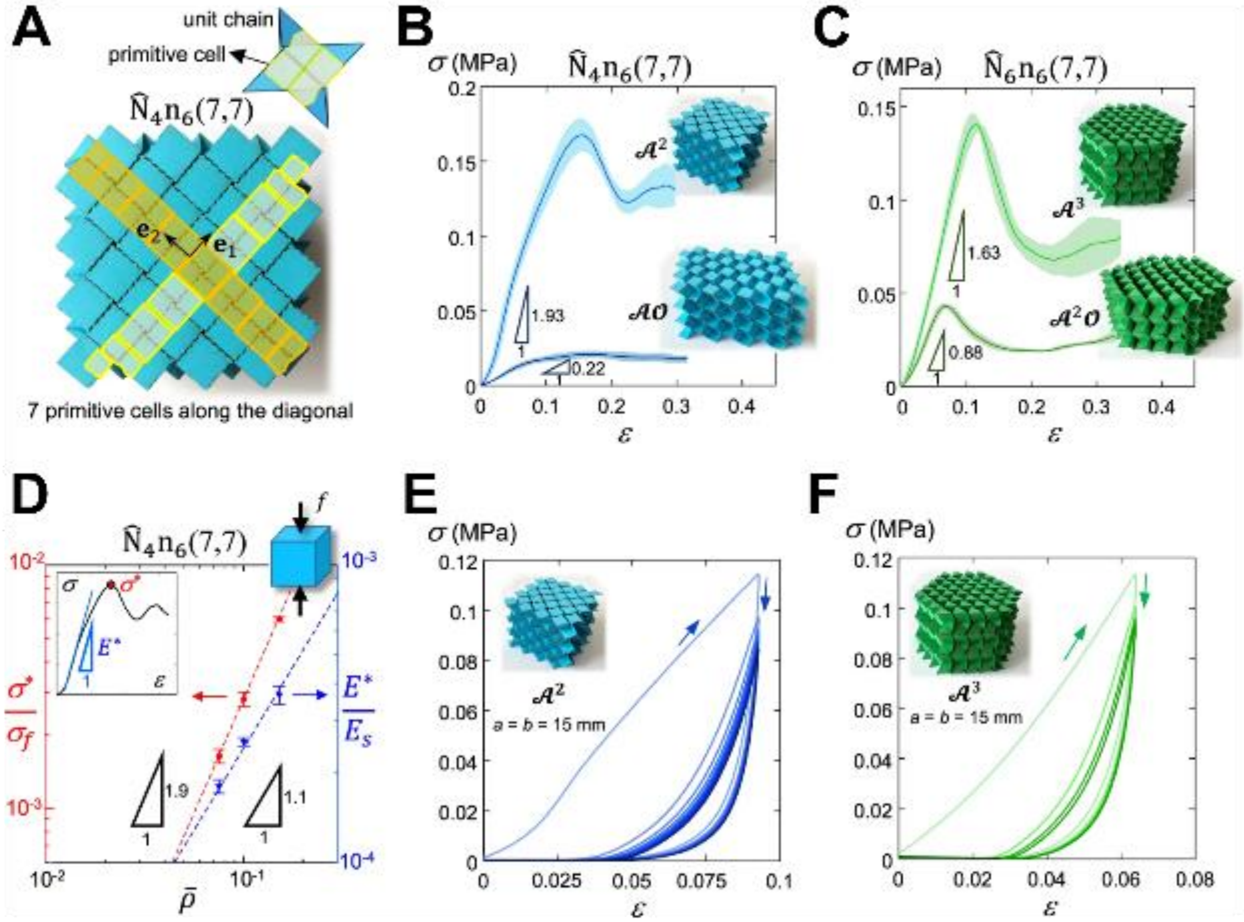

Figure 2-5 Out-of-plane loading of the origami-inspired metamaterial. Fabricated samples and measured properties of $\widehat{\mathrm{N}}_4\mathrm{n}_6(7,7)$ and $\widehat{\mathrm{N}}_6\mathrm{n}_6(7,7)$ unit in dissimilar lock modes; **A** Top view illustration of $\widehat{\mathrm{N}}_4\mathrm{n}_6(7,7)$ sample showing its primitive unit cell, and tessellation base vectors and tessellation levels. Engineering stress-strain curves measured for **B** $\widehat{\mathrm{N}}_4\mathrm{n}_6(7,7)$ in two lock configurations $\mathcal{A}^2$ and $\mathcal{AO}$, and for **C** $\widehat{\mathrm{N}}_6\mathrm{n}_6(7,7)$ in two lock configurations $\mathcal{A}^3$ and $\mathcal{A}^2\mathcal{O}$. In **B** and **C** the shaded domain describes the dispersion of the results obtained from testing three samples. **D** Normalized compressive Young's modulus (triangle symbols) and normalized yield strength (circle symbols) of $\widehat{\mathrm{N}}_4\mathrm{n}_6(7,7)$ vs. relative density. Error bars represent the standard deviation of our measurements. The subset in **D** schematically illustrates how the compressive Young's modulus E^* and yield strength σ^* were measured. Cyclic (compressive loading-unloading) response of **E** $\widehat{\mathrm{N}}_4\mathrm{n}_6(7,7)$ (after ten cycles) and **F** $\widehat{\mathrm{N}}_6\mathrm{n}_6(7,7)$ (after four cycles) in their most compact lock modes $\mathcal{A}^2$ and $\mathcal{A}^3$, respectively, showing the cyclic response stabilizes nearly after four cycles. In these experiments, the unloading is performed at 75% of the compressive strength of the initial cycle of each sample.

2.3.11 Mechanical performance and programmability

We examine a set of representative proof-of-concept specimens made of cellulose paperboard in their lock states under compression. The purpose is to demonstrate their capacity to achieve in situ distinct mechanical properties by uniform and nonuniform application of confining forces. Experimentally investigated are the Young's modulus E^* (the tangent of the compressive stress-strain curve in the first loading cycle assessing panel engagement as opposed to initial slippage) and the yield strength σ^* (the first peak stress before densification); relative density and Poisson's ratio are given in the closed form in Sections 2.6.11 and 2.6.12. We avoid finite-size effects by tessellating in-plane $l_{\mathrm{e}_1} = l_{\mathrm{e}_2} = 7$ unit-cells along the base vectors $\{\mathrm{e}_1, \mathrm{e}_2\}$ and stacking $n = 6$ layers (see Figure 2-5A and Section 2.5.5). A generic tessellated system is thus denoted by $\widehat{\mathrm{N}}_N \mathrm{n}_n(l_{\mathrm{e}_1}, l_{\mathrm{e}_2})$, and below two representative systems, $\widehat{\mathrm{N}}_4\mathrm{n}_6(7{,}7)$ and $\widehat{\mathrm{N}}_6\mathrm{n}_6(7{,}7)$, are examined.

2.3.12 Load-bearing capacity

Figure 2-5A shows the top view of $\widehat{\mathrm{N}}_4\mathrm{n}_6(7{,}7)$ along with an inset of a representative primitive unit cell (yellow) in the lock mode $\mathcal{A}^2$. Figure 2-5B reports its engineering stress-strain curves obtained in two lock configurations $\mathcal{A}^2$ and $\mathcal{AO}$, and Figure 2-5C the corresponding response of $\widehat{\mathrm{N}}_6\mathrm{n}_6(7{,}7)$ in its two lock configurations $\mathcal{A}^3$ and $\mathcal{A}^2\mathcal{O}$. The shaded domain describes the dispersion of the results obtained from testing three samples for each material system in a given mode. Three regions emerge: (i) An initial nonlinear regime, describing panels not yet engaged under compression, hence unable to establish a proper contact. (ii) A linear material response for both locked states of each system. (iii) The stress-peak and the following regime, both indicative of progressive panel buckling and creasing. For $\widehat{\mathrm{N}}_4\mathrm{n}_6(7{,}7)$ switching from $\mathcal{A}^2$ to $\mathcal{AO}$, the Young's modulus and yield strength reduce approximately by an order of magnitude. For $\widehat{\mathrm{N}}_6\mathrm{n}_6(7{,}7)$ switching from $\mathcal{A}^3$ to $\mathcal{A}^2\mathcal{O}$, the corresponding reductions are approximately three and two times. Minor deviations emerge in regions (i) and (ii), as opposed to large values attained in region (iii) far from the peak. Our measurements are comparable with values reported for kirigami-based concepts made of similar material [198].

2.3.13 Scaling laws

Figure 2-5D shows the normalized Young's modulus, $\frac{E^*}{E_s}$, and normalized yield strength, $\frac{\sigma^*}{\sigma_f}$, (where E_s and σ_f are the Young's modulus and failure stress of the base material in the machine direction, MD) for $\widehat{\mathrm{N}}_4\mathrm{n}_6(7{,}7)$ measured at three values of relative density. The results are obtained for samples with geometric parameters $a = b = 10$ mm, 15 mm, and 20 mm; for each of them, five identical samples were fabricated and tested. The normalized Young's modulus scales almost linearly with the relative density ($\frac{E^*}{E_s} \propto \bar{\rho}^{1.1}$), where $\bar{\rho} \propto (t/a)$ (see Section 2.6.11), hence obeying the classical scaling law of stretching dominated structures. The normalized yield strength, on the other hand, scales almost quadratically with relative density ($\frac{\sigma^*}{\sigma_f} \propto \bar{\rho}^{1.9}$), a scaling law deviating from the buckling or yield failure predictions of stretching dominated 3D plate-lattices. This can be attributed to the presence of additional failure mechanisms, which are governed by hinge stiffness, panel contact and the presence of geometrical imperfections, a topic of ongoing research.

2.3.14 Cyclic response

Figure 2-5E and F show the cyclic loading-unloading curves of $\widehat{\mathrm{N}}_4\mathrm{n}_6(7{,}7)$ and $\widehat{\mathrm{N}}_6\mathrm{n}_6(7{,}7)$ under compression. Given their similarity, only the response of $\widehat{\mathrm{N}}_4\mathrm{n}_6(7{,}7)$ is examined. The hysteretic behavior might be attributed to the friction of faces and edges coming to contact, the viscoelastic-viscoplastic nature of the base material (cellulose paperboard) as well as the local accumulation of plastic damage, which is also responsible for progressive softening. This is caused by the repeated strain of the weak crease ligaments which amplify their detrimental effect at each cycle until the response stabilizes. This occurs after approximately four cycles. Thereafter, no appreciable softening can be observed at higher strains nor significant variations of the modulus. At the end of the test, a strain of 0.04 is registered, indicating a permanent set not fully recovered even after several hours from the test end. These characteristics are qualitatively comparable with those observed in soft polymeric lattices exhibiting viscoelasticity and localized plasticity under cyclic loading [199]. Further work is required to quantitatively assess the response we observed and the role of the governing factors.

2.3.15 Multidirectional stiffness

$\widehat{\mathrm{N}}_4\mathrm{n}_6(7,7)$ in the lock configuration $\mathcal{A}^2$ is tested under in-plane and out-of-plane compression (Figure 2-6A) along two in-plane directions (A and B) at 45° and 90° with respect to the *x* axis, and along the *z*-direction. Representative curves of their engineering stress-strain responses in Figure 2-6B attest a comparable yet distinct elastic response and load-bearing capacity. The largest strength (A) and stiffness (B) observed during in-plane testing are attributed to the presence of double-layered panels, i.e., quad panels bonded to stack layers, an aspect that confers additional anisotropy and larger strength to bear the compressive load beyond the elastic regime. The difference between the initial in-plane responses (more compliant for the unit loaded at 45°) is due to the occurrence of a shear deformation that is dominant at the start of the compression test. Overall, our paperboard $\widehat{\mathrm{N}}_4\mathrm{n}_6(7,7)$ specimens with $a = b = 15$ mm and locked in mode $\mathcal{A}^2$ weighs ~ 40 g, and can withstand up to 850 N under compression along the z-direction, while up to 1450 N when compressed in the in-plane directions. In the lock mode $\mathcal{A}^3$, $\widehat{\mathrm{N}}_6\mathrm{n}_6(7,7)$ with identical geometric parameters and weight can resist 1000 N under out-of-plane compression.

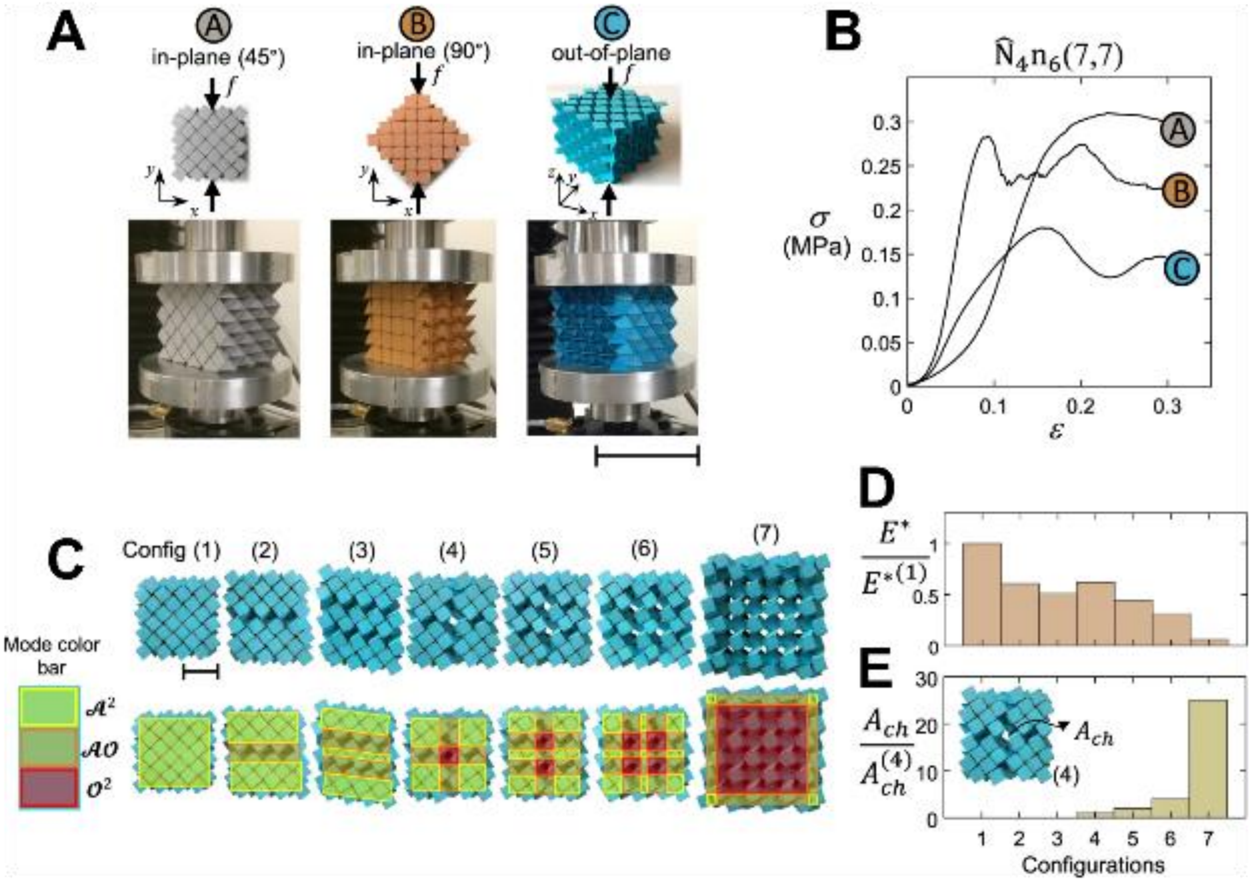

Figure 2-6 Multidirectional and Multimodal load-bearing capability of the origami-inspired metamaterial. **A** Directions (two in-plane and one out-of-plane) of the applied compressive loads relative to the orientation of the $\widehat{N}_4 n_6(7,7)$ specimen, and **B** their corresponding representative engineering stress-strain responses: Scale bar in $\boldsymbol{a} = 100$ mm. **C** Top view of seven mixed-mode configurations of $\widehat{N}_4 n_6(7,7)$ with $a = b = 10$ mm: Scale bar in $c = 30$ mm. Regions of a given mixed-mode highlighted in semitransparent color for $\mathcal{A}^2$, $\mathcal{O}^2$ and $\mathcal{AO}$. Out-of-plane normalized compressive Young's modulus **D** and normalized open-channel (void) area in the out-of-plane direction E for the seven configurations shown in **C**.

2.3.16 Mixed-mode configurations

Uniformly applied forces at the instant of kinematic bifurcation cause the material system to fold into one of its lock modes, each with its own set of properties (e.g., Figure 2-5B and C). Here we examine the outcome of a nonuniform set of forces locally applied in given zones, hence bringing the system into a mixed-mode configuration, i.e., a state that is partially folded and encompasses a combination of lockable and flat-foldable modes. Figure 2-6C depicts seven mixed-mode configurations among several others for our $\widehat{N}_4 n_6(7,7)$ specimen with square primitive side $a =$

$b = 10$ mm. The top row shows the emergence of voids from configurations 4 to 7. In the second row, the distribution of the attainable modes, i.e., $\mathcal{A}^2$, $\mathcal{O}^2$ and $\mathcal{AO}$, which can concurrently form in a given mixed-mode, is highlighted with a given color. Figure 2-6D reports Young's modulus normalized with respect to that of the configuration (1), i.e., $E^{*(1)}$, measured in each mixed-mode configuration. Measurements of Young's modulus E^* for $\widehat{\mathrm{N}}_4\mathrm{n}_6(7,7)$ shows only a 1.2-fold decrease when the tessellation level (3,3) increases to (7,7) (see Figure 2-20B). The difference is small compared to the decrease observed for a switch from mode $\mathcal{A}^2$ to $\mathcal{AO}$ (Figure 2-5B) or $\mathcal{O}^2$ (Figure 2-6D). This result suggests that the stiffness values of mixed-mode configurations are relatively insensitive to finite-size effects. In general, the addition of mode-regions $\mathcal{O}^2$ and $\mathcal{AO}$ reduces stiffness, e.g., a drop to half is observed when configuration (1) switches to (3). Configuration (4) including all three mode-regions shows slightly higher stiffness than configuration (2), a counterintuitive result that might be attributed to the distribution of mode-regions with a twofold symmetry, as opposed to configurations (2) and (3), which exhibits reflection symmetry only. In this mode, only a single channel (an out-of-plane void) is formed as opposed to configurations (1), (2), and (3), which have no open channels or voids. Figure 2-6E shows the normalized open-channel area $\frac{A_{ch}}{A_{ch}^{(4)}}$ changes upon reconfiguration, where A_{ch} is the open-channels area in the out-of-plane direction and $A_{ch}^{(4)}$ that of configuration (4) with a single channel. The change in the open-channel area can be considered as a descriptor of the system permeability, which scales linearly with the conduit area as in a porous medium. The trends show that the compressive Young's modulus and permeability are antagonists. While not quantified here, this qualitative result attests the versatility of our systems to tune on-the-fly flow permeability. Further work is required to quantify this aspect in detail.

2.4 Discussion

This work has introduced a class of reprogrammable rigidly flat-foldable metamaterials that are topological and load-bearing in multiple directions including the deployment direction. By merging notions of origami-folding with kirigami-cuts, we have created foldable patterns made of chains that are shaped with an N even-sided regular polygonal primitives defining the inner void. Cellular excisions relax certain deformation constraints imposed by panel planarity and connectivity of the parent origami. The strategy enables folding within the embedded voids with multiple DoFs, which can be reduced upon stacking. This trait simplifies the fabrication process and eases its automation (see Section 2.6.16). At the bifurcation instant, however, the DoFs grow, and multiple kinematic paths become temporarily accessible. Some lead to 3D stiff (locked) configurations, and others to 2D flat-folded states; this hallmark extends the level of programmability offered by existing origami concepts. When tessellated, our metamaterials undergo symmetry and topology transformations that are amenable to in situ modulation in uniform and mixed-mode configurations, each with its own set of properties.

Our foldable metamaterials offer functionalities that can be used as lightweight deployable and self-locking materials, low-volume transportable packaging, actuators, and lockable robotic systems that tune stiffness upon actuation. Their rigid-foldability also enables the adoption of stiff materials other than paper [196]. In addition, the load-bearing capacity in their densest lock configuration is not limited to any specific directions, rather it is offered along their three main directions, paving the way to their use as omnidirectionally structural, yet rigidly flat-foldable mechanical metamaterials. This aspect is distinct from current origami metamaterials featuring a trade-off between reconfigurability and load-bearing capacity, the latter being limited to certain directions [28, 48, 70, 72, 86, 87, 104, 107, 144, 149, 159, 166, 194]. These concepts, when used to withstand volumetric pressure in their deployed state or another set of multidirectional forces, would collapse as they remain floppy at least in one direction. Volumetric pressure can be either externally or internally applied. Examples of the former include remotely operated vehicles, such as shape-changing vessels and submarines, made of structural components that need to deploy underwater and provide multidirectional stiffness and strength to resist water pressure during operation. Examples of the latter include inflatable systems, such as air tents, inflatable shelters, and buildings, saving boats and vests, which can not only be packed into a flat or other compact flat-folded configurations but also safely maintain their deployed state if punctured. Our metamaterials can thus work as the skeleton of puncture-resistant inflatable systems that lock in place after deployment, without collapse or losing their functionality due to unforeseen deflation. Furthermore, the capacity to switch permeability while remaining stiff can find application in the design of adaptive porous media and breathable walls for civil engineering, or as smart-valves for medical implants where fluid flow could be modulated in situ by structure rather than by external occlusions.

2.5 Methods

2.5.1 Identification of lockable and flat-foldable modes

We systematically study the relations that define the post-bifurcation modes belonging to a given kinematic path for a single-DoF stacked unit chain $\mathrm{N}_N\mathrm{n}_{\bar{n}}$. As illustrated in Figure 2-2A, in the pre- and post-bifurcation stages, the triangular panels (six in dark green in the middle layer) in each set of mountains and valleys remain parallel as $\bar{n} = 3$. Three of them are mountain panels that lay in a mountain plane, and the others rest in a valley plane. The distance between them is h (Figure 2-2A) which can be calculated through relation (2-1). In a given plane, there are six fold lines (two per triangle) which form a total of six dihedral angles. The fold lines that are parallel form a pair of dihedral angles (Figure 2-2A). This pair can contain either equal or supplementary angles, a condition that defines the type of post-bifurcation mode. Equality of dihedral angles in each pair defines regular modes, which in Figure 2-2C belong to paths 1 and 2; this implies that the reconfiguration of the unit chain leads to a folded pattern that is compatible with its original tessellation. In contrast, supplementarity of dihedral angles in all pairs, i.e., the dihedral angles sum up to $180°$ in each pair, gives rises to irregular modes, and path 3 in Figure 2-2C shows an example. Irregular modes can be attained only in a single unit chain but not in a tessellated pattern, as they forego folding congruence between the initial and the final pattern, revealing that the flat-foldable tessellation cannot be unpacked to its initial pattern. Only one irregular mode exists for $\mathrm{N}_N\mathrm{n}_{\bar{n}}$ with $N > 4$ and $N/2$ equal to an odd number, e.g., modes of $\widehat{\mathrm{N}}_6\mathrm{n}_3$ shown in Figure 2-2B.

Given the folding incompatibility of irregular modes, we now focus on the regular counterparts and study the conditions that can be used for a given kinematic path to count the number of existing modes and define the characteristics of each of them. Our goal is to demonstrate the existence of relations between distinct pairs of dihedral angles, which in turn govern the kinematic paths $\mathrm{N}_N\mathrm{n}_{\bar{n}}$ can access post-bifurcation. We first introduce some basic notions for our analysis. In the denomination of dihedral angles, we specify acute angles with $\mathcal{A}$ and obtuse angles with $\mathcal{O}$. The geometry of the units enforces the condition $\mathcal{A} + \mathcal{O} = \pi$ during their entire range of motion. As an example, three pairs of valley dihedral angles are illustrated in Figure 2-2D, two $\mathcal{A}$s (violet and blue) and one $\mathcal{O}$ (yellow) for a total of six valley dihedral angles. Since in $\mathrm{N}_N\mathrm{n}_{\bar{n}}$, which has 1 DoF, each pair contains equal angles, all $\mathcal{A}$s are equal as are all $\mathcal{O}$s. A given sequence with angle pairs, e.g., two $\mathcal{A}$s and one $\mathcal{O}$ depicted in Figure 2-2D, can be simply denoted by the series of angle pairs, e.g., $\mathcal{A}\mathcal{A}\mathcal{O}$, and in compact form with the power indicating the repeated pairs, e.g., $\mathcal{A}^2\mathcal{O}$. This notation allows discriminating between kinematic modes that emerge at bifurcation. For example,

$\widehat{\mathrm{N}}_6\mathrm{n}_3$ (Figure 2-2C) can travel along four regular modes: $\mathcal{O}^3$ (three obtuse angles are engaged only), $\mathcal{A}^3$ (three acute angles are engaged only), $\mathcal{A}^2\mathcal{O}$ (two acute angles and one obtuse angle), $\mathcal{A}\mathcal{O}^2$ (one acute and two obtuse), and one irregular, shown with $\overline{\mathcal{A}\mathcal{O}}$. Modes containing identical pairs of dihedral angles belong to the same kinematic path, and we designate them by swapping $\mathcal{A}$s and $\mathcal{O}$s, i.e., $\mathcal{A}^2\mathcal{O}$ and $\mathcal{A}\mathcal{O}^2$ belong to path 2, and $\mathcal{A}^3$ and $\mathcal{O}^3$ to path 1.

With the notions above, we can now systematically characterize the regular modes of a generic $\mathrm{N}_N\mathrm{n}_{\bar{n}}$ and determine the total number of possible reconfiguration modes. The problem of finding all independent regular modes of a generic $\mathrm{N}_N\mathrm{n}_{\bar{n}}$ unit can now be treated as the classical necklace problem. In our case, the equivalent necklace is our unit chain $\mathrm{N}_N\mathrm{n}_{\bar{n}}$ with $N/2$ colored beads (Figure 2-2D), and each color represents a type of dihedral angles, either $\mathcal{A}$ or $\mathcal{O}$. By applying the Pólya enumeration theory, we determine all reconfiguration modes our $\mathrm{N}_N\mathrm{n}_{\bar{n}}$ chain can attain from knowledge of $N/2$ numbers of $\mathcal{A}$ and $\mathcal{O}$. We also assume that the beads can be rotated around the necklace and that the necklace can be flipped over. By applying this theory to $\widehat{\mathrm{N}}_6\mathrm{n}_3$, for instance, all the possible modes can be collected in a generating function of the form $\mathcal{A}^3 + \mathcal{A}^2\mathcal{O} + \mathcal{A}\mathcal{O}^2 + \mathcal{O}^3$, which describes the four regular modes illustrated in Figure 2-2, and where the sum of the powers of $\mathcal{A}$ and $\mathcal{O}$ in each mode is $N/2$. Similar results can be obtained for other unit chains, $\mathrm{N}_N\mathrm{n}_{\bar{n}}$ (see Sections 2.6.3 and Figure 2-9 for more details).

2.5.2 Energy of the in-plane confinement and mode-phase diagram

We start with $\widehat{\mathrm{N}}_4\mathrm{n}_n$ described by the representative set of parameters: $k = 1/3\,\mathrm{N}$, $n = 3$, $\theta^0 = \pi$ and $a = b = 15\,\mathrm{mm}$. Figure 2-4A illustrates two typical curves of the dimensionless total energy, each for a given value of (f_x, r_B). Upon bifurcation, when $\theta = \pi/2$, the total energy curve splits into two branches, each representing a reconfiguration mode $\mathcal{A}\mathcal{O}$ and $\mathcal{A}^2$. Between these two, the system chooses the mode which has the lowest energy level. This outcome can be determined by examining (i) the magnitude of the energy of all branches immediately before and after the bifurcation, and (ii) the gradient of the energy of all branches at bifurcation, for example, $\frac{\partial \Pi_{\mathcal{A}^2}}{\partial \theta}|_{\theta=\pi/2}$ and $\frac{\partial \Pi_{\mathcal{AO}}}{\partial \theta}|_{\theta=\pi/2}$ (see Section 2.6.13 for more details). The magnitude and the ratio of the in-plane biaxial loads, i.e., (f_x,r_B), govern the relative energy level of each energy branch, dictating the configuration mode our system would travel after bifurcation. For example, Figure 2-4A shows the role of r_B in entering a given post-bifurcation mode. For a load case (f_x,r_B)=(1,1/3), the system at bifurcation chooses the $\mathcal{AO}$ energy branch until reaching the lock state in this mode; in contrast once subjected to (f_x,r_B)=(1,1), the system follows the $\mathcal{A}^2$ energy branch to reach the lock state.

The example above suggests the prospect to generate a mode-phase diagram that maps the activation of a given mode with respect to the relative magnitude of the in-plane confinement forces f_x and f_y. Figure 2-4B visualizes such a map for $\widehat{\mathrm{N}}_4\mathrm{n}_n$ with $a = b = 15$ mm and $\theta^0 = \pi$. Each color is assigned to a region that describes a given configuration mode. The boundaries separating modes $\mathcal{AO}$ and $\mathcal{A}^2$ are obtained by equating the gradient of the total energy of each branch at bifurcation, $\left(\frac{\partial \Pi_{\mathcal{A}^2}}{\partial \theta}|_{\theta=\frac{\pi}{2}} = \frac{\partial \Pi_{\mathcal{AO}}}{\partial \theta}|_{\theta=\frac{\pi}{2}}\right)_{\theta=\frac{\pi}{2}}$.

2.5.3 Formulation of the energy of the out-of-plane confinement

We start by expressing the potential energy of the hinges as $V = V(\theta) = 2nNkb(\theta - \theta^0)^2$ and the work of a uniformly applied external force fo as $W_o = nf_o a \sin\phi\,(\sin\theta^0 - \sin\theta)$ where we recall n is the number of stacked layers and the other parameters are defined in Figure 2-1A. The potential energy due to gravity is neglected since the panels of our system are made of cellulose paperboard, lightweight material with the gravitational potential energy of few orders of magnitude lower than that of the hinges and the work of the external forces. If we introduce $V' = V(\pi - \theta)$, and denote a generic mode with $\mathcal{A}^{\xi}\mathcal{O}^{\xi'}$, where ξ is the total number of valley pairs for the acute dihedral angles ($\mathcal{A}$) and ξ' counts the total number of valley pairs for the obtuse dihedral angles ($\mathcal{O}$) with $\xi + \xi' = N/2$, we can express the total energy $\Pi = \Pi(\theta, f_o)$ of the $A^{\xi}O^{\xi'}$mode as

$$\begin{cases} \Pi = \dfrac{2\xi}{N}(V - V') + V' - W_o & \forall \xi < 2 \qquad \pi/2 \leq \theta \leq \pi \\ \Pi = \dfrac{2\xi'}{N}(V' - V) + V - W_o & \forall \xi \geq 2 \qquad \theta^L \leq \theta \leq \pi \end{cases} \tag{2-3}$$

The first expression in Eq. (2-3) describes the total energy of the system in mode $\mathcal{A}^{\xi}\mathcal{O}^{\xi'}$ prior to bifurcation, while the second gives the total energy after bifurcation.

Under an out-of-plane force, a generic system $\mathrm{N}_N\mathrm{n}_n$ is in equilibrium at the lock state when the total energy has a stationary value. Given $\mathrm{N}_N\mathrm{n}_n$ has one DoF, and the total energy and its derivative are continuous functions, we can determine the minimum out-of-plane force f^L at the lock state by solving $\frac{\partial \Pi(\theta, f_o)}{\partial \theta}|_{\theta=\theta L} = 0$ for $\xi \geq 2$, which yields:

$$f^L = -4kb\frac{2\xi(\pi - 2\theta^0) - N(\pi - \theta^L - \theta^0)}{a \sin\phi \cos\theta^L} \tag{2-4}$$

Equations (2-3) and (2-4) can be used to map the total energy landscape of a system under a uniform out-of-plane compression as a function of the supplementary of the dihedral angle θ, i.e., $\pi - \theta$ (Figure 2-1A). For demonstrative purpose, we examine $\widehat{\mathrm{N}}_4\mathrm{n}_n$ folding in mode $\mathcal{A}^2$ with $\theta^0 = 2\pi/3$. Figure 2-4D shows its energy curves (Eq. (2-3)) for three representing values of the out-of-plane load normalized by the lock load, i.e., $f = f_o/f^L$. Setting $\bar{f} = 1$ yields the boundary (thick curve) between two energy domains, one (below) satisfying $\bar{f} < 1$ and the other (above) $\bar{f} > 1$. The red point, which all curves (three shown) pass through, represents the zero-energy state, described above as the state of the system immediately after manufacturing, either flat (ideal case) or marginally folded due to residual stress from fabrication.

Subject to uniform out-of-plane compression, our material system can fold into its lock state under two conditions. First, the magnitude of the uniformly applied force f_o should be above the minimum out-of-plane force, f^L, required to lock up the unit. Second, the dihedral angle of our unit should be larger than a threshold value defined by the maximum energy barrier of the system. The interplay between f_o and f^L described by these conditions gives rise to three domains:

Region I (light brown): $\bar{f} < 1$. Here fall configurations are defined by supplementary angles for which our system can reach an equilibrium that is either stable if $\frac{\partial^2 \Pi}{\partial \theta^2} > 0$, or unstable if $\frac{\partial^2 \Pi}{\partial \theta^2} < 0$. Since $f_o < f^L$, the system cannot access the lock state from a given configuration, e.g., lower orange point, and it tends to fold back to its equilibrium point along the "flat-fold" direction towards the zero-energy point (red).

Region II: $\bar{f} > 1$. In this domain, our system can potentially reach the lock state, but a difference in the outcome exists as determined by the stability of equilibrium. Region II splits into two subdomains (iIa and iIb), each defined by the slope of the energy curve, i.e., the sign of $\frac{\partial \Pi}{\partial \theta}$, where-we recall-$\Pi$ is expressed as a function of $(\pi - \theta)$.

Region iIa (yellow): $\frac{\partial \Pi}{\partial \theta} < 0$ and $\frac{\partial^2 \Pi}{\partial \theta^2} < 0$. The condition of equilibrium here is unstable despite the out-of-plane force being larger than the minimum locking force. In this region, a system partially folded at a given dihedral angle by the applied in-plane forces is prone to fold back to its fully developed (flat) state.

Region iIb (blue): $\frac{\partial \Pi}{\partial \theta} > 0$ and $\frac{\partial^2 \Pi}{\partial \theta^2} < 0$. This is the lockable domain, bounded by the locus of points (dot line), which satisfies the condition $\frac{\partial \Pi}{\partial \theta} = 0$ for all $\bar{f} > 1$. Upon imposing the condition $\frac{\partial \Pi(\theta, f_o)}{\partial \theta} = 0$ in Eq. (2-3), we can express the dihedral angle θ as a function of the load fo when the energy is maximum, $\frac{\partial \Pi}{\partial \theta} = 0$, from which we obtain

$$f_o(\theta) = -16kb \frac{(\theta - \theta^0)}{a \sin \phi \cos \theta} \tag{2-5}$$

Substituting Eq. (2-5) into Eq. (2-3) yields the lockable domain boundary of maximum energy (dot bound in Figure 2-4D) given as a function of the dihedral angle ($\theta^L \leq \theta \leq \frac{\pi}{2}$ and $\xi = 2$):

$$\Pi = V(\theta) + 16nkb \frac{(\theta - \theta^0)}{\cos \theta} (\sin \theta^0 - \sin \theta) \tag{2-6}$$

Equation (2-6) traces points of the dot boundary that are unstable configurations of equilibrium, where the total energy attains maximum values, one of which is shown by the blue point of the representative energy curve $\bar{f} > 1$.

2.5.4 Rigidity under compression

Once folded into the lock state, our multilayered unit chain $\mathrm{N}_N\mathrm{n}_{\bar{n}}$ inherits compressive load-bearing capacity as panels reach contact and prevent further motion. We study the load-bearing capacity of our class of foldable material systems in relation to their layer stacking. The condition that guarantees their structural rigidity in one of their lock states can be determined by studying their pin-jointed counterpart made of a triangulated network (Figure 2-1C). We can formulate the general problem that predicts the rigidity of a structure by theoretical analysis (see Sections 2.6.1 and 2.6.7). While the units are subjected to compressive loads, we assume coincident bars as a single bar and multiple coincident joints as a single joint. The results can be expressed for a single unit chain as a function of the number of bars and joints at its lock and partially folded configurations along with the conditions of rigidity (see Section 2.6.7).

Carried out for the general lock state $\mathcal{A}^{N/2}$, where all dihedral angles are acute, our rigidity analysis reveals that N_4 becomes rigid with a single layer, whereas at least two layers must be stacked for N_6 and three layers for $\mathrm{N}_N > 6$. Knowing the minimum number of stacked layers provides an essential guideline to make our unit chain stiff in a lock state under compression.

2.5.5 Experimental methods

Test samples were built out of cellulose paperboard material (200 g m−2 Fabriano Craft paper) with a dry thickness $t = 0.21$ mm. Each flat sheet was perforated via laser cutting (CM1290 laser cutter, SignCut Inc.) along prescribed patterns, followed by manual-folding and layer bonding (using a commercial Polyvinyl acetate, commonly known as white glue). Fold lines were obtained with cuts of 2 mm length spaced uniformly at 1.4 mm intervals. Experiments were performed with a BOSE ElectroForce-3510 tester (Bose Corporation, Framingham, Massachusetts) and a BOSE load-cell with a load capacity of 12.5 kN. Displacement-control was used with a quasi-static ramp loading and strain rate of $10^{-3}\ \mathrm{s}^{-1}$. Manufacturing and testing were performed at room temperature (22 °C) with a relative humidity of about 30%. To measure the properties, e.g., Young's modulus, we used both the displacement data obtained from the crosshead displacement readings as well as Digital Image Correlation (CCD camera—PointGrey) for comparative purposes. The largest difference in measurements provided by the two techniques was below 3%. Young's modulus and yield strength were measured as the initial (linear region) slope (maximum strain at 0.05) and the first peak in the stress-strain curve, respectively, for the first loading cycle (see subset in Figure 2-5D). Cyclic loading-unloading experiments were carried out using a displacement-control module at the same strain rate. The direction of the load was reversed when the load reached ~75% of the first cycle peak load.

All samples were realized with the following geometric parameters $a = b = 15$ mm and $\phi = 60°$ and loaded in the out-of-plane in compression unless stated otherwise. The relative density is defined by $\bar{\rho} = \frac{\rho^*}{\rho_s}$ (density of our reconfigurable cellular material, ρ^*, divided by the density of the solid material, ρs). To vary relative density, three values were used $a = b = 10$, 15, and 20 mm. Specimens were compressed between two smooth flat platens of Aluminum. Initially, samples were brought to their lock position manually and kept in this configuration by wrapping them up with a rubber band. To assess the role of the rubber band during the experiments, we repeated a few compression tests without a rubber band. In these instances, we started the experiment while the sample was wrapped with a rubber band, and then cut it after applying 2% of the peak load, i.e., ~28 N for $\widehat{\mathrm{N}}_4\mathrm{n}_6(7,7)$. The results attest that the stress-strain curves were almost identical to those obtained on samples confined with a rubber band for the entire duration of the tests. See also Sections 2.6.14 and 2.6.15 for further details about the properties of the paperboard.

2.6 Appendix

2.6.1 Kinematic Analysis

To study the mobility of our unit kinematic chain (Figure 2-7A), we use a surrogate bar network where the planar faces are replaced with pin-jointed bars (Figure 2-7B and C). This assembly consists of n_b inextensible bars, n_j pin joints and rigid triangular panels; quad panels are replaced by a set of two connected rigid triangles, thus eliminating in-plane shear deformation. The rigidity of each quad or triangular panel is ensured by imposing two constraints: (i) bar inextensibility and (ii) panel coplanarity for the triangular faces making up a quad panel (Figure 2-7C and D).

To determine the first set of constraints for panel rigidity, we first denote the position of joint i by vector x_i^1 and joint j by vector x_j; the bar connecting joint i to joint j is given by the vector $\mathrm{r}_{ij} = \pm(\mathrm{x}_i - \mathrm{x}_j)$ with length $l_{ij} = \|\mathrm{r}_{ij}\|$ where $\| \quad \|$ represents the vector norm. With this notation, the first-order inextensibility condition for bar r_{ij} can be written by equating the first derivative of the bar length l_{ij} to zero, $dl_{ij} = 0$, as

$$\mathrm{r}_{ij}.\left(d\mathrm{x}_i - d\mathrm{x}_j\right) = 0 \tag{2-7}$$

where $d\mathrm{x}_i$ and $d\mathrm{x}_j$ are the infinitesimal displacements of the joints i and j, respectively. The second set of constraints imposes panel planarity for the quad faces, to impede the rotation of triangular faces that make the quad panel. It is formulated as follows. Assume a quad panel connecting joints i, j, k and l and comprising two triangular panels p (connecting joints i, j and k) and q (connecting joints i, j and l) with the normal vectors $\mathrm{n}_p = \mathrm{r}_{ij} \times \mathrm{r}_{ik}$ and $\mathrm{n}_q = \mathrm{r}_{ij} \times \mathrm{r}_{il}$ (Figure 2-7D). The angle between two adjacent panels p and q can be expressed as $d\omega = \cos^{-1} \frac{\mathrm{n}_p \cdot \mathrm{n}_q}{\|\mathrm{n}_p\|\|\mathrm{n}_q\|}$. Equating the first differential of the angle ω to zero, $d\omega = 0$, gives the coplanarity condition for the quad panel as

$$\frac{\partial\omega}{\partial\mathrm{x}_i} d\mathrm{x}_i + \frac{\partial\omega}{\partial\mathrm{x}_j} d\mathrm{x}_j + \frac{\partial\omega}{\partial\mathrm{x}_k} d\mathrm{x}_k + \frac{\partial\omega}{\partial\mathrm{x}_l} d\mathrm{x}_l = 0 \tag{2-8}$$

The rigidity constraints, Eqs. (2-7) and (2-8), can be expressed in matrix form for all panels as

$$\mathrm{R}.\,d\mathrm{x} = \begin{bmatrix}\mathrm{B}\\ \mathrm{P}\end{bmatrix}.\,d\mathrm{x} = 0 \tag{2-9}$$

where R is the rigidity matrix consisting of the inextensibility constraints (compatibility) matrix B and the planarity constraints matrix P, and $d\mathrm{x}$ is the infinitesimal displacement vector of the joints.

The relations above can now be used to determine the number of degrees of freedom m, of the pin-jointed triangulated network as [200]

$$m = dn_j - n_K - r \tag{2-10}$$

where n_K is the number of external kinematic constraints, such as those confining the rigid motions, and r is the rank of the rigidity matrix R in Eq. (2-9). In Eq. (2-10), d represents the dimensions of the problem; for spatial mechanisms d is 3. For an infinitesimally rigid structure m is zero, while for infinitesimal mechanisms $m > 0$.

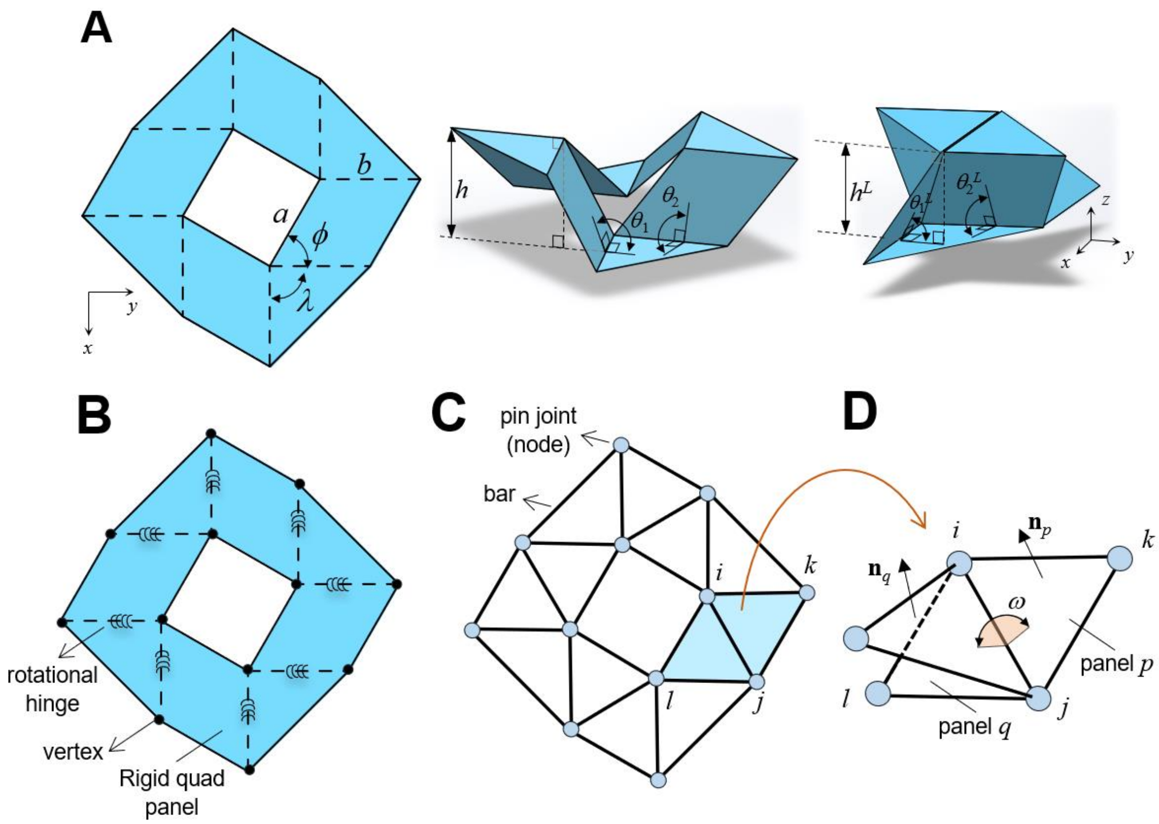

Figure 2-7 Reconfiguration parameters and constraints of a kinematic unit chain. **A** Geometric parameters describing our reconfigurable unit with $N = 4$. Superscript L assigned to a given variable in the first locked configuration mode of the unit chain, when all dihedral angels θ_i are equal. **B** Equivalent network of rigid panels connected through flexible hinges replaced by a bar and pin-joint mechanism in **C** described by parameters used to impose planarity condition, **D**.

With the rigidity matrix, we can now use the singular value decomposition (SVD) to determine the kinematic paths that our unit can travel upon bifurcation and track its configuration using a predictor-corrector type incremental method [201].

The SVD of the rigidity matrix $\mathrm{R} = \mathrm{W}\mathrm{V}^T\mathrm{U}^T$ is composed of a set of left singular values matrices $\mathrm{U} = [\mathrm{U}_r \vdots \mathrm{U}_m]$ and right singular values matrices $\mathrm{W} = [\mathrm{W}_r \vdots \mathrm{W}_s]$,[1] and a set of non-zero singular values matrix

$$\mathrm{V} = \begin{bmatrix} \mathrm{diag}(v_1, \dots, v_r) & 0 \\ 0 & 0 \end{bmatrix} \tag{2-11}$$

U is a block matrix comprising the extensional deformation submatrix $\mathrm{U}_r = [\bar{\mathrm{u}}_1, \dots, \bar{\mathrm{u}}_r]$ and the orthogonal sets of m inextensional deformation (mechanism) vectors $\mathrm{U}_m = [\mathrm{u}_1, \dots, \mathrm{u}_m]$. W comprises a kinematically compatible extension matrix $\mathrm{W}_r = [\bar{\mathrm{w}}_1, \dots, \bar{\mathrm{w}}_r]$ and the orthogonal sets of s kinematically incompatible extension (states of self-stress) vectors $\mathrm{W}_s = [\mathrm{w}_1, \dots, \mathrm{w}_s]$, [201].

Prior to bifurcation, our unit stands in a configuration defined by the vector C^i and can move along one path defined by the dihedral angle relation $\theta_1 = \theta_2 = \dots = \theta_m$. Post bifurcation can follow multiple paths, each specified by its own configuration $\mathrm{C}^{i'}$. To find $\mathrm{C}^{i'}$, we introduce a displacement amplitude parameter δ, and impose a small displacement to C^i by adding a finite amplitude of its inextensional deformation u_j^i, previously obtained from the first-order SVD. This leads to a new set of configurations

$$\mathrm{C}^{i'} = \mathrm{C}^i + \delta \mathrm{u}_j^i . \mathrm{sign}(\mathrm{u}_j^{i-1} . \mathrm{u}_j^i) \tag{2-12}$$

[1] s denotes the number of states of self-stress (redundant constraints present in the structure) and can be calculated using $s = n_b + n_P - r$, in which n_P is the number of planarity constraints.

where $\mathrm{sign}(\mathrm{u}_j^{i-1}.\mathrm{u}_j^i)$ ensures that the sign of δ controls the reconfiguration direction, as SVD does not guarantee the direction of the inextensional deformation u_j^i, [202].

When we use the linear perturbation equation, Eq. (2-7), to obtain the updated configuration, the length of the inextensible bars does not remain constant. To eliminate the excess elongation e of the bars imposed by Eq. (2-7), we iteratively find the nearest strain-free configuration by adding a correcting nodal displacement vector (d), [202]

$$\mathrm{d} = -\sum_{j=1}^{r} \frac{\bar{\mathrm{w}}_j^T \mathrm{e}}{v_j} \bar{\mathrm{u}}_j \tag{2-13}$$

to the predicted configuration $\mathrm{C}^{i'}$ as

$$\mathrm{C}^{i+1} = \mathrm{C}^{i'} + \mathrm{d} \tag{2-14}$$

When a new path has been found, we must control the independency of the kinematic paths. We do so by comparing the newly found path with other paths. This strategy is necessary since using the predictor-corrector algorithm with the first-order analysis does not guarantee that the obtained path converges to a distinct finite mechanism. The predictor-corrector algorithm is implemented in MATLAB and all the simulations are based on an in-house developed code.

While the aforementioned algorithm can be used to execute large displacement simulations with any desired level of accuracy, it is not sufficient to find all the possible post-bifurcation kinematic paths. To this end, we resort to principles of *Pólya Enumeration Theory,* which enables to find all independent post-bifurcation kinematic paths, as explained in Section 2.6.3.

2.6.2 Additional constraints imposed by unit chain stacking

A single unit kinematic chain has multiple degrees of freedom that lead to certain configurations, and the fully developed (flat) one is one among others. To reduce its degrees of freedom, we resort to layers stacking, which leads our unit to share certain panels with those of the units placed above and below. Figure 2-8A shows a physical prototype where only the triangular panels are shared between two units, whereas the others are not shared. Here the non-zero thickness of adjacent hinged panels causes an offset between the hinges. Figure 2-8B shows the only possible rigid-body motion the planes can undergo. The quad planes cannot rotate in the same direction, such as that shown in Figure 2-8C. This is due to the actions exerted by planes and hinges. The outcome is that both plane interference and hinge offset come to play and geometrically constraint the unit to respect the rigid body motion. For example, the motion in Figure 2-8C would be possible only if the quad planes can undergo flexural deformation (Figure 2-8D), which violates our rigid motion assumption.

2.6.3 Pólya Enumeration Theorem

The post-bifurcation kinematic analysis given in the previous section cannot guarantee that all post-bifurcation paths are found [202]. We now use principles of *Pólya Enumeration Theory* [203] to identify (and count) all independent post-bifurcation kinematic paths and available modes. The Pólya Enumeration Theorem is instrumental to search the reconfiguration modes of our unit kinematic chain.

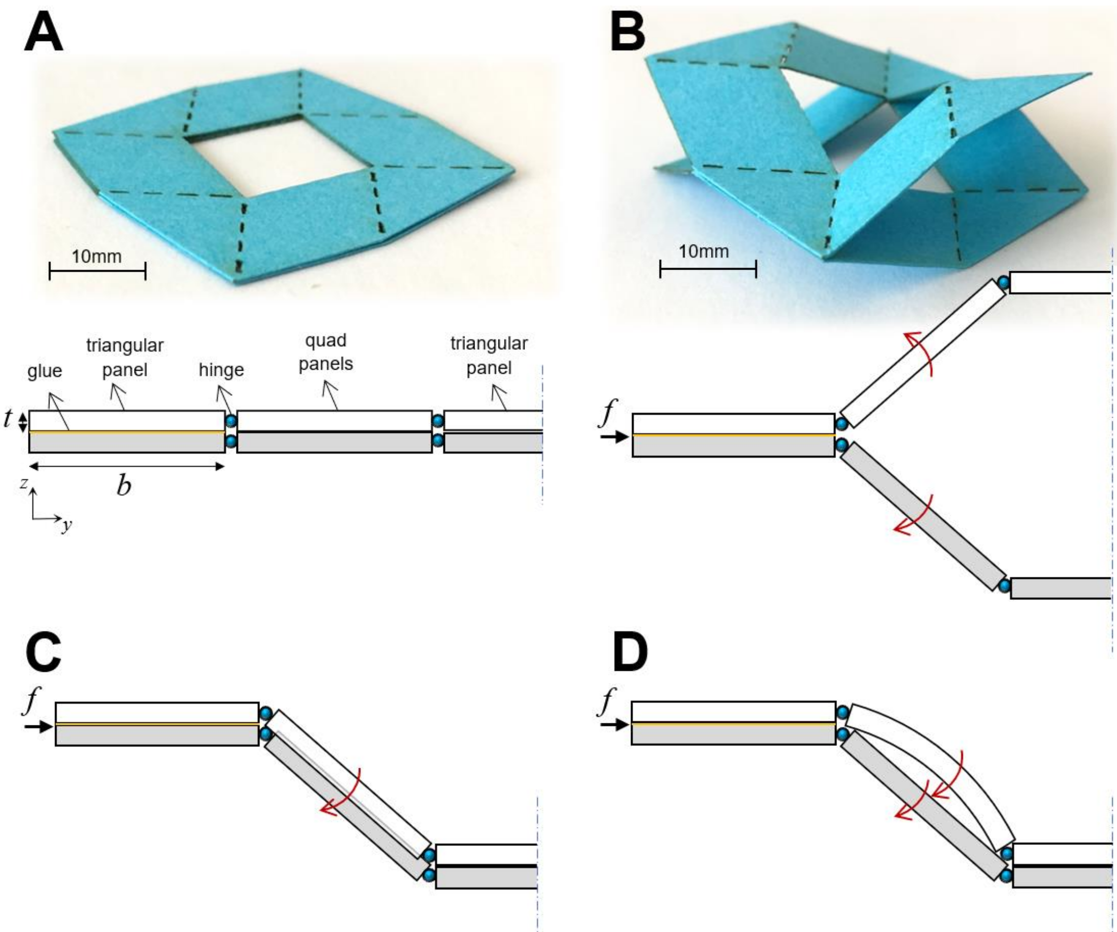

Figure 2-8 Admissible reconfigurations. **A** Flat configuration for a two-layered unit kinematic chain $\widehat{\mathrm{N}}_4\mathrm{n}_2$ made of non-negligible thickness panels. **B** A kinematic path of the multilayered units, where two adjacent quad panels rotate in opposite directions under in-plane load *f*. **C** Example of inadmissible kinematic path for two quad panels rotating in identical direction under in-plane load *f*; this kinematic path violates the rigidity assumption of the panels and is feasible only if the neighboring panels can deform, **D**.

As stated in the manuscript, the problem of finding all independent *regular* modes of $\mathrm{N}_N\mathrm{n}_n$ is equivalent to the classical necklace problem in combinatorics. There, the goal is to find the number of necklace arrangements we can construct from knowledge of $N/2$ numbers of colored beads, each painted in two distinct colors, e.g., white or black. In our case, the dihedral angle $\mathcal{A}$ of our unit chain represents one color, e.g., white, and $\mathcal{O}$ the other, e.g., black. Due to the mountain and valley assignment, the transformations are defined on hypothetical $N/2$ sided polygons since congruent triangular faces are located on every other corner of the original chain. Thus, the necklace problem of an N even-sided polygonal unit chain, N_N, with constraints of mountains and valleys degenerates to an $N/2$ sided necklace.

We start by stretching the necklace with $N/2$ beads into the shape of a uniform $N/2$-sided regular polygon with one bead at each corner. Let define the set of the vertices of this polygon by $S = \{\chi_1, \chi_2, \dots, \chi_{N/2}\}$ and the set of binary colors by $R = \{\mathcal{A}, \mathcal{O}\}$ and introduce set X = {all possible coloring arrangement of S by $R\}$. Next, we define rigid body transformations on the necklace. We assume that the beads can rotate around the necklace, and the necklace can be flipped over. The operations of beads rotation around the necklace and flip over are considered as *rigid motions* applied to the necklace.

Figure 2-9 depicts the set of all rigid body motions each N_N unit chain with N = 4, 6, 8 and 10 can undergo. We denote them with the set $G = \{\pi_1, \pi_2, \dots, \pi_N\}$ where π_j $(j = 1, \dots, N)$ are the members of the Dihedral symmetry group $D_{N/2}$ for a uniform $N/2$-sided regular polygon, which acts on the set X of the necklace problem. The members of G are defined as

$$\begin{aligned} &\pi_i \in G|\; i \leq \frac{N}{2}:\; \pi_i = \mathrm{Rot}_z\left((i-1)\frac{4\pi}{N}\right) \\ &\pi_i \in G|\; i > \frac{N}{2}:\; \pi_i = \mathrm{Ref}_{a_i} \end{aligned} \tag{2-15}$$

where $\mathrm{Rot}_z(\alpha)$ is the rotation operator about the z axis through the angle α and Ref_{a_i} is a reflection operator about the axis a_i whose angles with the x axis can be obtained from

$$\begin{aligned} &\text{If } \tfrac{N}{2} \in \mathbb{E} : \beta_i = (i-1)\tfrac{2\pi}{N} \qquad \text{for} \quad i \leq N \text{ , and} \\ &\text{If } \tfrac{N}{2} \in \mathbb{O} : \beta_i = (i-1)\tfrac{4\pi}{N} \qquad \text{for} \quad i \leq \tfrac{N}{2}. \end{aligned} \tag{2-16}$$

As each rigid motion permutes the elements in X and S, we can represent these rigid motions by their permutations on S or X. For each N, there are exactly N rigid body transformations, $N/2$

rotation operations and $N/2$ reflection operations (Figure 2-9). We note that for N_4 two rigid body motions are equivalent.

Figure 2-9 shows both the original unit kinematic chain and its necklace counterpart at the top of each table for a given *N*. In each case, the dark and light shadings of the kinematic unit chain (left) denote the mountain- and valley-faces, respectively. In the necklace representation (right), each number specifies a corresponding pair of valley dihedral angles. For example, N_4 has two pairs of valley-dihedral angle and thus its equivalent necklace has 2 beads, shown as ① and ②. Below the first row of each kinematic chain, the possible rigid motion operations (rotation and reflection) are shown. In particular, the successive application of rigid-body motions makes the vertices alternate and form a periodic loop, namely a cycle. A cycle is described by a number, or a series of numbers placed in one bracket underneath each kinematic unit chain. The length of a cycle is the number of elements in each bracket. A string of cycles, i.e. a sequence of brackets, describes a rigid-motion.

To illustrate the above, we consider N_6 as an example for the case of 0° rotation. We note the vertex assignment is identical to the initial assignment. The transformation corresponding to its rigid motion is the identity operation which maps every vertex to itself regardless of the number of times the transformation is applied. Its vertex counterpart can be written as (1)(2)(3). By using the *Pólya's enumeration theorem,* this rigid motion is made of three cycles, each of length one. On the other hand, a 120° rotation applied to N_6 is described by (132), which consists of 1 cycle of length three.

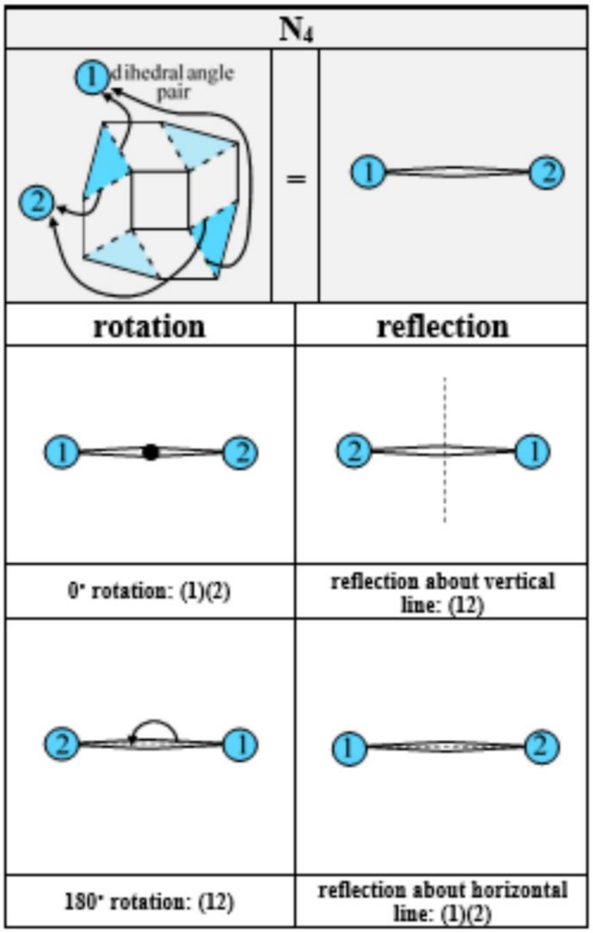
N4
dihedral angle pair
=
rotation
reflection
0° rotation: (1)(2)
reflection about vertical line: (12)
180° rotation: (12)
reflection about horizontal line: (1)(2)

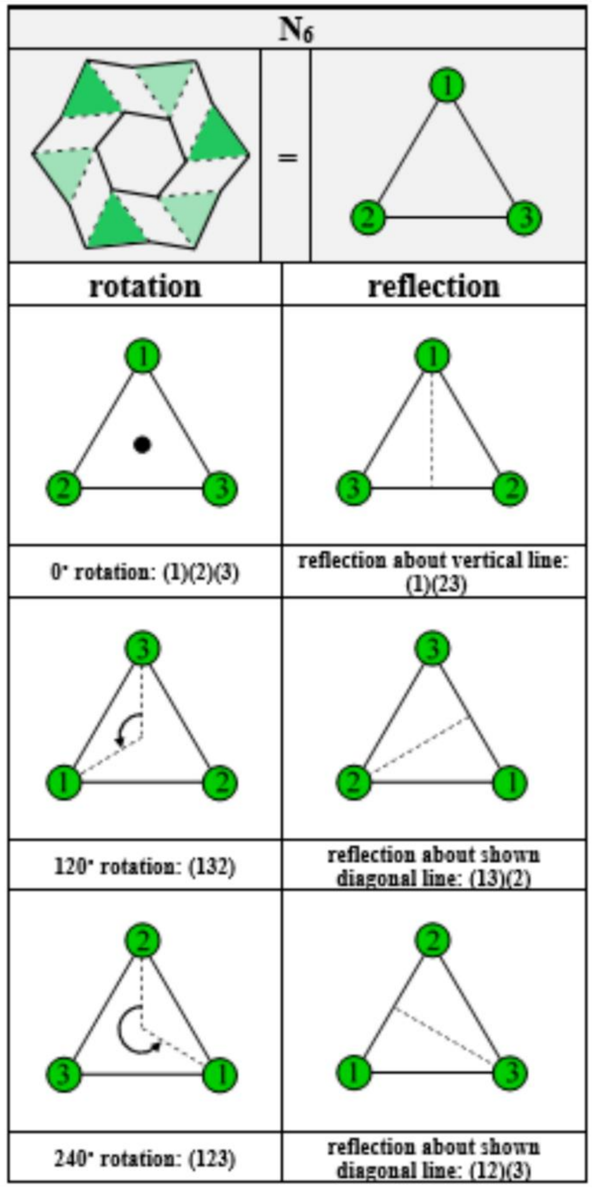
N6
=
rotation
reflection
0° rotation: (1)(2)(3)
reflection about vertical line: (1)(23)
120° rotation: (132)
reflection about shown diagonal line: (13)(2)
240° rotation: (123)
reflection about shown diagonal line: (12)(3)

N_8

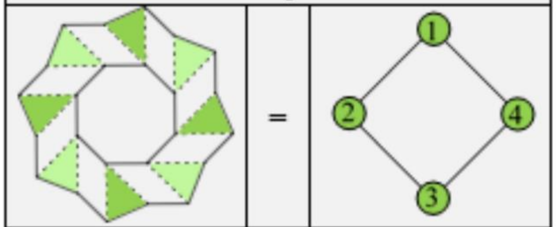

rotation	reflection
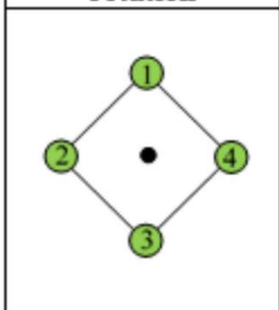	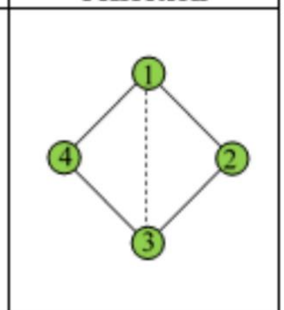
0° rotation: (1)(2)(3)(4)	reflection about 1-3 line: (1)(24)(3)
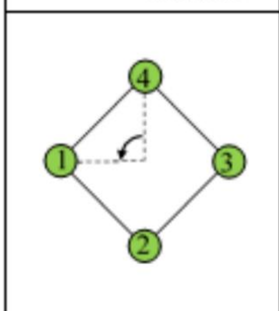	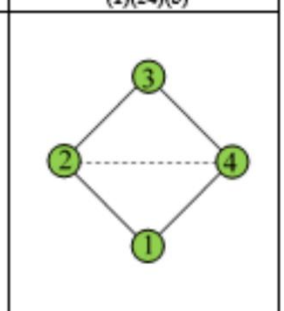
90° rotation: (1234)	reflection about 2-4 line: (13)(2)(4)
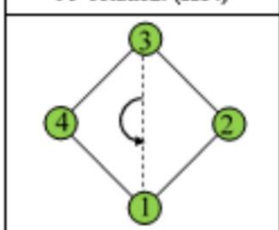	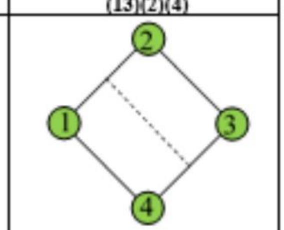
180° rotation: (13)(24)	reflection about shown diagonal line: (12)(34)
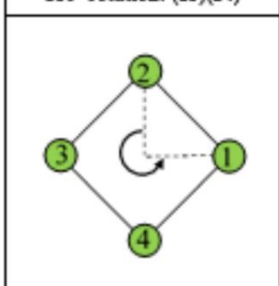	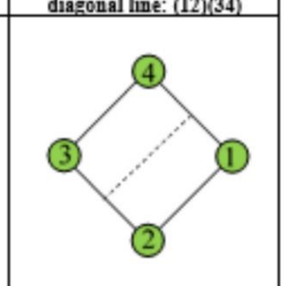
270° rotation: (1432)	reflection about shown diagonal line: (14)(23)

N_{10}

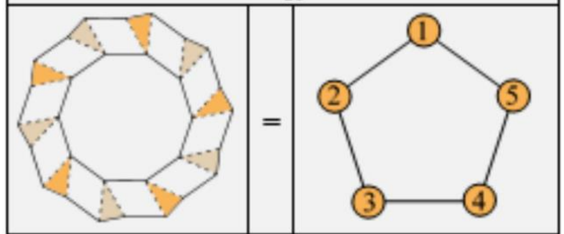

rotation	reflection
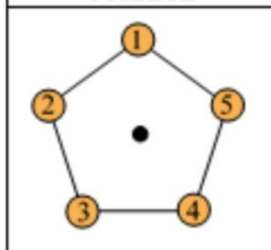	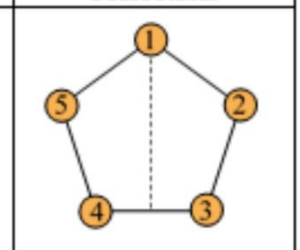
0° rotation: (1)(2)(3)(4)(5)	reflection about vertical line: (1)(25)(34)
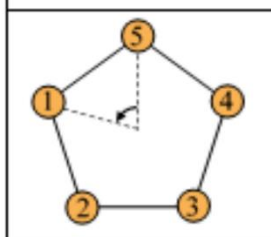	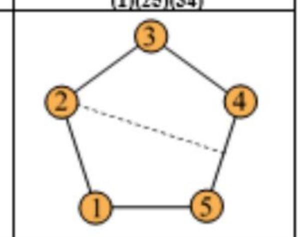
72° rotation: (15432)	reflection about shown diagonal line: (13)(2)(45)
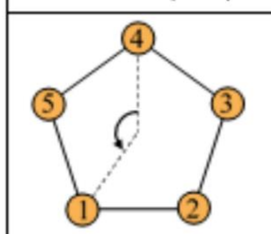	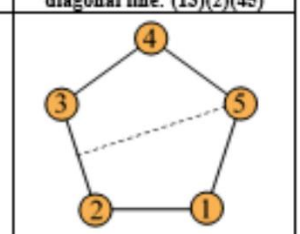
144° rotation: (14253)	reflection about shown diagonal line: (14)(23)(5)
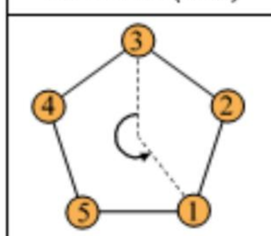	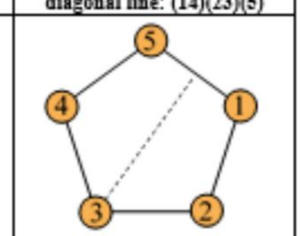
216° rotation: (13524)	reflection about shown diagonal line: (15)(24)(3)
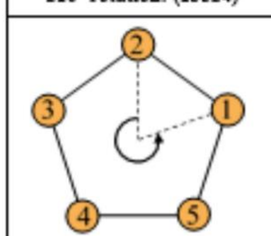	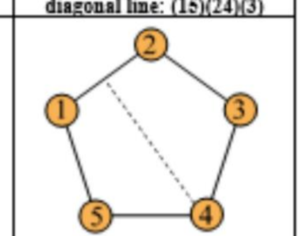
288° rotation: (12345)	reflection about shown diagonal line: (12)(35)(4)

Figure 2-9 Group operations on kinematic unit chains. Schematic representation of unit kinematic chain with $N = 4$, 6, 8 and 10 (left) and its equivalent necklace (right). Two valley "dihedral angle pairs" are shown as an example for N_4 only.

Below the first row are the possible rigid body motions of each unit chain can undergo. The alternating light and dark colors on the triangular faces of the kinematic chain refer to mountain and valley assignments respectively. The equivalent necklace has numbered vertices and is used to describe a given rigid motion. Below each given motion is a sequence of parentheses describing the rigid body motion expressed in cycle notation. A black dot represents zero-degree rotation. A combination of dashed lines and circular arcs represent the rotation operations. A dashed line is used for reflection operations and indicates the mirror line.

Assume $\pi_j \in G$ is a rigid motion operation that can be described by a combination of its cycles. Now we can assign a monomial to every π_j. The monomial is the product of $\chi_{i_1}, \chi_{i_2}, \ldots, \chi_{i_\tau}$ where $i_1, i_2, \ldots i_\tau$ represent the lengths of the cycles in the rigid operation π_j. The monomial can be written as $f_{\pi_j} = \chi_{i_1}\chi_{i_2} \cdots \chi_{i_\tau}$, and the cycle index $f(\chi_1, \chi_2, \ldots, \chi_w)$ of G acting on S can be written as the sum of the monomials

$$f(\chi_1, \chi_2, \ldots, \chi_w) = \frac{1}{|G|} \sum_{\pi_j \in G} f_{\pi_j} \tag{2-17}$$

where w is the length of the longest cycle in the vertex representation of each of $\pi_j \in G$ in Figure 2-9. The number of distinct patterns in X under the corresponding action of G on X is $f(\varrho, \varrho, \ldots, \varrho)$, where ϱ is the length of the set R, $\varrho = |R|$; in our case $\varrho = 2$.

If we denote the general set of color arrangements by $R = \{\mathcal{C}_1, \mathcal{C}_2, \ldots, \mathcal{C}_\tau\}$, the pattern inventory of X can be defined as $f\left(\mathcal{C}_1 + \mathcal{C}_2 + \cdots + \mathcal{C}_\tau, {\mathcal{C}_1}^2 + {\mathcal{C}_2}^2 + \cdots + {\mathcal{C}_\tau}^2, \ldots, {\mathcal{C}_1}^w + {\mathcal{C}_2}^w + \cdots + {\mathcal{C}_\tau}^w\right)$. The Pólya Enumeration Theorem states that if $\kappa \mathcal{C}_1^{i_1} \mathcal{C}_2^{i_2} \ldots \mathcal{C}_\tau^{i_\tau}$ appears in the pattern inventory of X, then there are κ patterns in X where $\mathcal{C}_1$ appears i_1 times, $\mathcal{C}_2$ appears i_2 times, …, and $\mathcal{C}_\tau$ appears

i_τ times. The summation of the coefficients κ of the pattern inventory gives the number of necklace arrangements. For example, the $\mathrm{N}_8\mathrm{n}_n$ unit is analogous to a necklace with four beads where $R = \{\mathcal{A}, \mathcal{O}\}$ and its pattern inventory becomes $f(\mathcal{A}+\mathcal{O}, \mathcal{A}^2+\mathcal{O}^2, \mathcal{A}^3+\mathcal{O}^3, \mathcal{A}^4+\mathcal{O}^4) = \mathcal{A}^4 + \mathcal{A}^3\mathcal{O} + 2\mathcal{A}^2\mathcal{O}^2 + \mathcal{A}\mathcal{O}^3 + \mathcal{O}^4$. The mode is lockable when at least two successive acute dihedral angles $\mathcal{A}$ exist in the pattern sequence. For example, in the case of $\mathrm{N}_8\mathrm{n}_n$, the lockable mechanisms are $\mathcal{A}^2\mathcal{O}^2$ (i.e., the one with the sequence of $\mathcal{A}\mathcal{A}\mathcal{O}\mathcal{O}$), $\mathcal{A}^3\mathcal{O}$ and $\mathcal{A}^4$.

2.6.4 Tessellations: from individual stacks of unit cells to a periodic cellular material

Each unit chain can aggregate with others to form a periodic material system that can reconfigure along either lockable or flat-foldable modes. To examine their in-plane tessellation patterns (see Figure 2-1B), we refer to the most compact periodic array our $\mathrm{N}_N\mathrm{n}_n$ forms in 2 dimensions, with centroids falling onto a simple Bravais lattice of the *base-centered orthorhombic* family (Figure 2-10A).

Here, we study ways our multilayered unit chains can be connected to tile the *x-y* plane while preserving its characteristic kinematics. Two classes of tessellation containing similar unit chains can be realized[1]:

i) Most packed tessellation patterns. This class describes the densest lattices that can be made out of our primitive units,

ii) Less packed tessellation patterns. This class includes realizations of other possible low-density lattices; it is analyzed through the notion of macro-chains.

[1] Note that we do not examine here connections of dissimilar unit chains.

Table 2-1 Final configurations of different kinematic unit chains. Top view of the nearly developed, locked and flat-folded states of $\mathrm{N}_N\mathrm{n}_n$ unit kinematic chains for $N = 4$, 6, 8 and 10. Light orange shading indicates flat-foldability and light blue refers to lockability. The number of modes per given N is reported in the last row.

N	4	6	8	10
Developed (initial) state	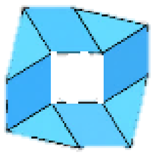	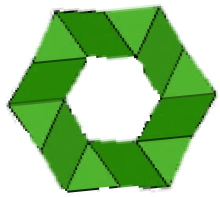	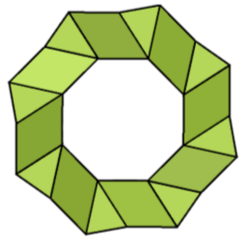	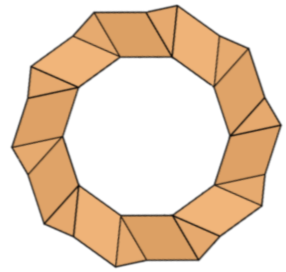
Locked state		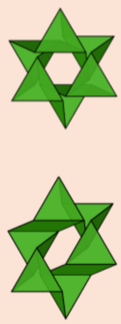		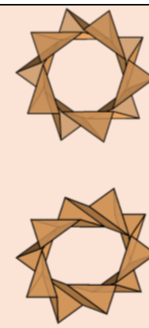
Flat-folded state		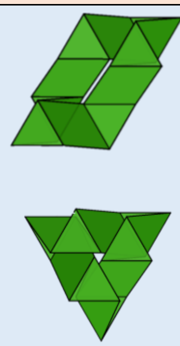		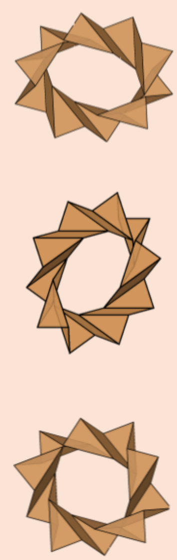

			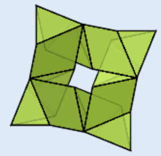	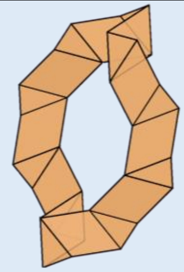 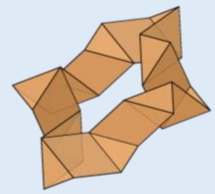 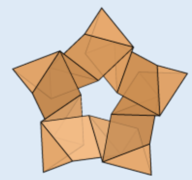
# of modes (N-2)	2	4	6	8

2.6.5 Most packed tessellation patterns:

The most compact form of tessellation can be described by a periodic array of $\mathrm{N}_N\mathrm{n}_n$ multilayered unit chains in two dimensions, whose centroids (centers of mass) fall onto a simple Bravais lattice of the *base-centered orthorhombic* family with basis vectors $\{\mathrm{e}_1, \mathrm{e}_2\}$.

Let us consider a rhombus constructed from vertices that are the centroids of the four adjacent unit chains in a tessellated pattern (Figure 2-10A). The geometric constraints imply that its vertex angle $\gamma \equiv \cos^{-1}(\mathrm{e}_1 \cdot \mathrm{e}_2) \geq \frac{\pi}{3}$ impedes the overlap of unit chains along the short diagonal of the rhombus (Figure 2-10A). Additionally, the vertex angle γ must be made of ζ segments of λ (where $\lambda = \frac{2\pi}{N}$), i.e., $\gamma = \zeta\lambda = \zeta\frac{2\pi}{N}$, and its supplementary angle γ' must be made of ζ' segments of λ, i.e., $\gamma' = \zeta'\lambda$. All admissible angles γ can be obtained by solving the linear Diophantine equation [204]

$$\zeta + \zeta' = N/2 \tag{2-18}$$

which is written assuming the condition $\gamma + \gamma' = \pi$ (see Figure 2-10A).

Table 2-2 shows all possible solutions $(\zeta\ ,\zeta')$ of Eq (2-18) for a given *N* (representing the unit kinematic chain $\mathrm{N}_N\mathrm{n}_n$), with the resulting vertex angle γ $(= \zeta\frac{2\pi}{N})$. The choice of the smallest ζ among both solutions (if two solutions exist) gives the most packed pattern. For example, for *N* =16 we have two possible solutions of Eq. (2-18): $(\zeta\ ,\zeta')$ = (3,5) and (4,4), from which we calculate the resultant vertex angle γ as 67.50˚ and 90˚. The former gives the most packed tessellation pattern. On the other hand, if $\gamma = \frac{\pi}{3}$, the tessellation belongs to the *hexagonal* family, while $\gamma = \frac{\pi}{2}$ results in a tessellation of the *tetragonal* family.

Table 2-2 All possible solutions of Eq. (2-18). i.e., $(\zeta\ ,\zeta')$, and resultant acute rhombus angles γ for the most compact tessellation patterns of $\mathrm{N}_N\mathrm{n}_n$ for N = 4 to 22.

N	Number of solutions of Eq. (2-18)	Possible solutions of $(\zeta\ ,\zeta')$	Angle of rhombus $\gamma = \zeta\lambda$
4	1	(1,1)	90˚
6	1	(1,2)	60˚
8	1	(2,2)	90˚
10	1	(2,3)	72˚
12	2	(3,3), (2,4)	90˚, 60˚
14	1	(3,4)	77.14˚
16	2	(3,5), (4,4)	67.50˚, 90˚
18	2	(3,6), (4,5)	60˚, 100˚
20	2	(5,5), (4,6)	90˚, 72˚
22	2	(4,7), (5,6)	65.45˚, 81.82˚

Unit kinematic chains can connect along the periodic base vectors, e_1 and e_2, through the base of the isosceles triangulated panels (Figure 2-10). In certain cases, e.g., *hexagonal* family $(\gamma = \frac{\pi}{3})$ with an odd ζ (see for example, the case $N = 18$ in Table 2-3), the base of the isosceles triangulated panels coincide, and an extra bond (connection) along the short diagonal of the rhombus can be considered. The bonds in the most packed tessellation patterns of $\mathrm{N}_4\mathrm{n}_n$ and $\mathrm{N}_6\mathrm{n}_n$ are a shared parallelogram panel intersecting the basis vectors $\vec{\mathrm{e}}_1$ and $\vec{\mathrm{e}}_2$.

2.6.6 Less-packed tessellation patterns using macro chains

An alternative way to tessellate our pattern is to start from a macro-chain containing primitive units. A macro-chain is constructed by the in-plane connection of a certain number of similar $\mathrm{N}_N\mathrm{n}_n$ unit chains, i.e., units with prescribed N, to form a regular polygon; this is done by replacing each edge with one primitive unit, e.g., Figure 2-10C-D.

The shape of macro-chains is governed by the geometry of their constituents. Their existence can be formulated as follows. Let denote the i^{th} positive factor of N with $\mathcal{M}_i$. For any given $\mathcal{M}_i > 4$ one $\mathcal{M}_i$-sided regular polygonal macro-chain ($\mathrm{N}_N^{\mathcal{M}_i}\mathrm{n}_{\bar{n}}$) exists provided either of $\mathcal{M}_i$ or $\frac{N}{2\mathcal{M}_i}(\mathcal{M}_i - 2)$ becomes an even number. $\mathrm{N}_N^{\mathcal{M}_i}\mathrm{n}_{\bar{n}}$ is a macro-chain connecting the centroids of the unit chains $\mathrm{N}_N\mathrm{n}_{\bar{n}}$.

In-plane tessellations of macro-chains can be formulated using the method described above if they fall into one of the Bravais lattice families[1]. Figure 2-10B illustrates the smallest macro-chain, i.e., $\mathrm{N}_{16}^{4}\mathrm{n}_{\bar{n}}$, and its tessellation that can be built using the unit kinematic chain $\mathrm{N}_{16}\mathrm{n}_{\bar{n}}$. Figure 2-10C, D and E shows examples of possible tessellations one can imagine using the macro-chain of $\mathrm{N}_{16}^{8}\mathrm{n}_{\bar{n}}$; several more exist that are beyond the scope of this work. In the figures, orange lines indicate the connectivity between units in a macro-chain, and red lines describe the connectivity of macro-chains in the tessellation.

[1] $\mathcal{M}_i = 4$ results in the Bravais lattice of the tetragonal family and $\mathcal{M}_i = 3$ results in the Bravais lattice of the hexagonal family.

In the tessellations of $\mathrm{N}_N^{\mathcal{M}_i}\mathrm{n}_{\bar{n}}$ macro-chains, the connection of the macro-chains may be much more complex than that of the single unit chains, as inter-chain connections can also be established, e.g., red dash-lines in Figure 2-10C. Here, the main bonds between macro-chains occur either through the bases of the isosceles triangulated panels that intersect the direction vectors $\vec{\mathrm{e}}_1$ and $\vec{\mathrm{e}}_2$ (see Figure 2-10C and D) or through the overlapped unit-chains $\mathrm{N}_N\mathrm{n}_{\bar{n}}$ as shown in Figure 2-10E.

The results of the analysis above exemplify the breadth of the design space one can attain through the selection of alternative tessellation patterns. The design space is rich and diverse. Each tessellation pattern is characterized by its own set of rigid foldability attributes, physical properties, and load-bearing capacity.

2.6.7 Rigidity

As explained in the main text, to study the mobility of our unit, we replace the actual panels with their bar and hinge counterparts. Upon *locking*, certain bars and hinges coincide (Figure 2-11). This holds if at the lock state we assume there is full contact between edges and faces, and thus relevant bars and hinges condense into a single bar and a single hinge. Such an assumption underpins our rigidity analysis and is considered valid as long as the direction of the force is unchanged [197].

To analyze the rigidity of our unit chains, one panel is constrained to eliminate rigid body motions. Table 2-3 shows the number of bars and hinges in the fully developed and $\mathcal{A}^{\frac{N}{2}}$ locked states for a single layer of a given unit. For example, for $N = 4$, the number of bars upon locking is reduced from 36 to 30, while the joints of four pairs coincide. The reduction in the number of joints and bars bring about an increase in connectivity which in turn can lead to rigidity. For certain patterns, a certain number of layers (last row) are required to achieve rigidity. The analysis indicates that other locked configurations presented in Table 2-1 can also satisfy the rigidity condition (i.e., $m = 0$ in Eq. (2-10)).

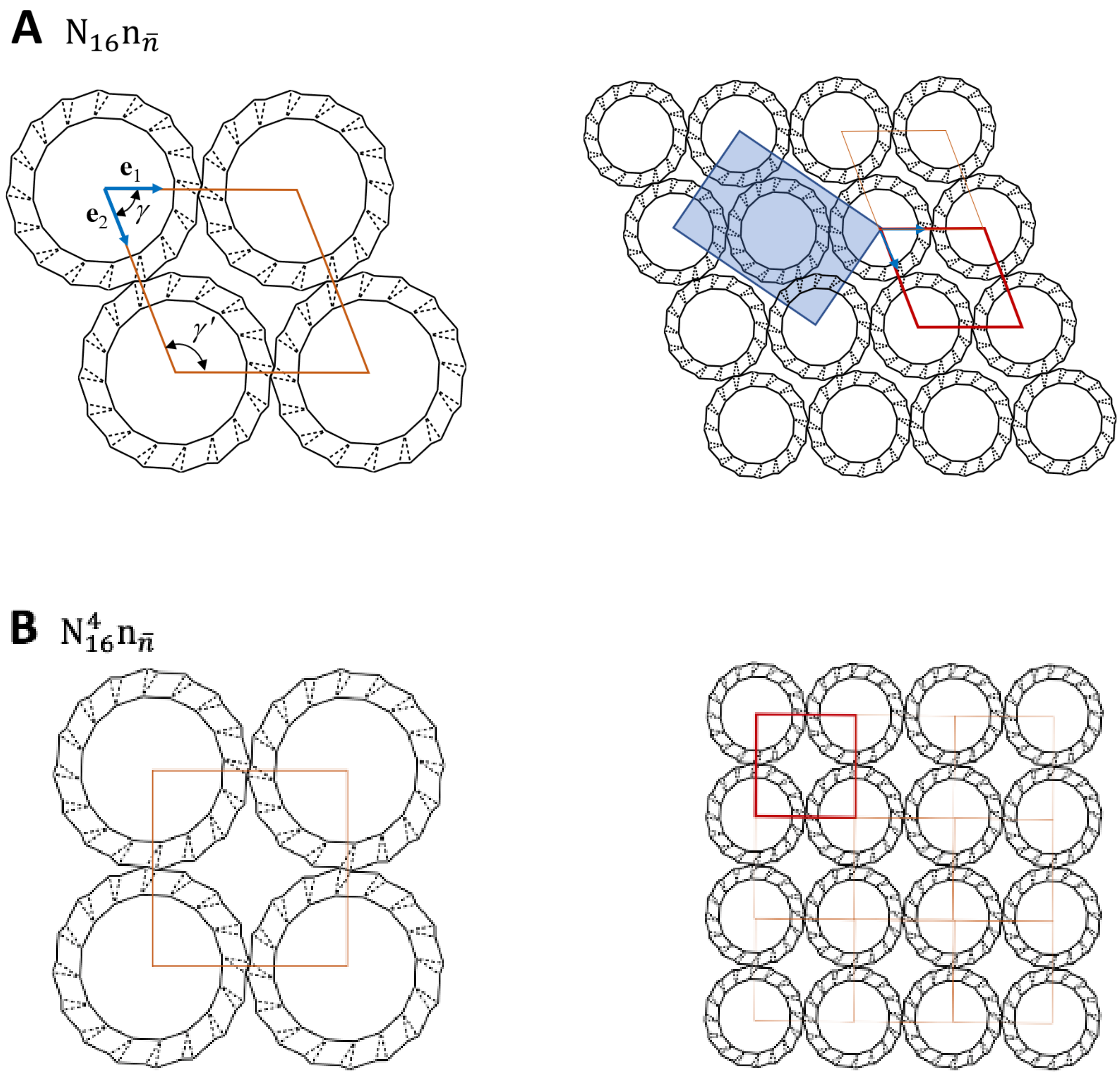

C $N^8_{16}n_{\bar{n}}$

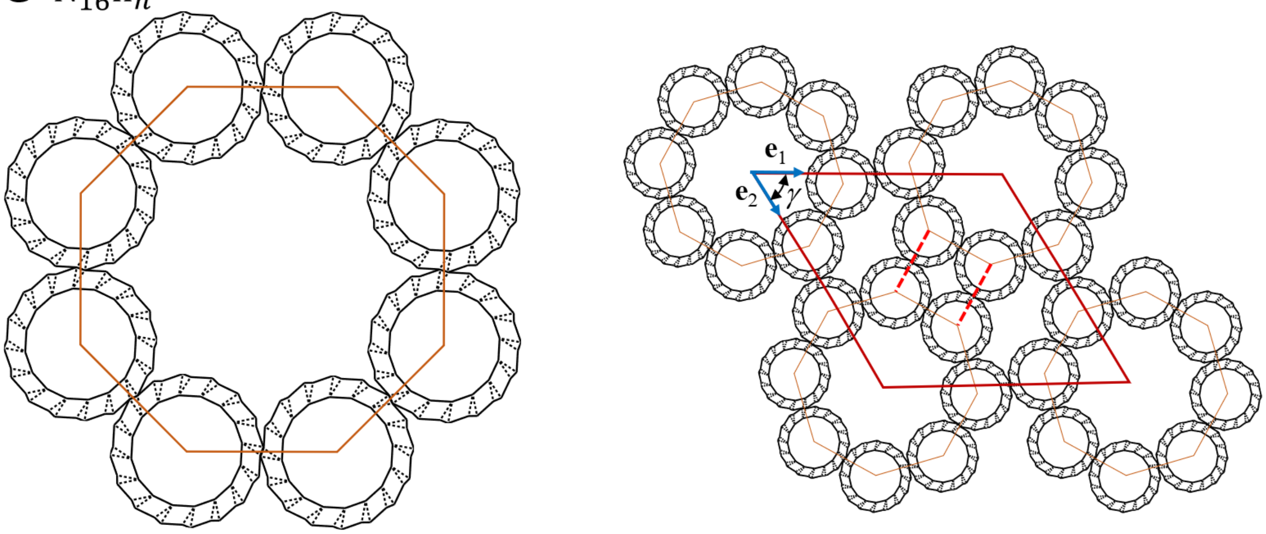

D $N^8_{16}n_{\bar{n}}$

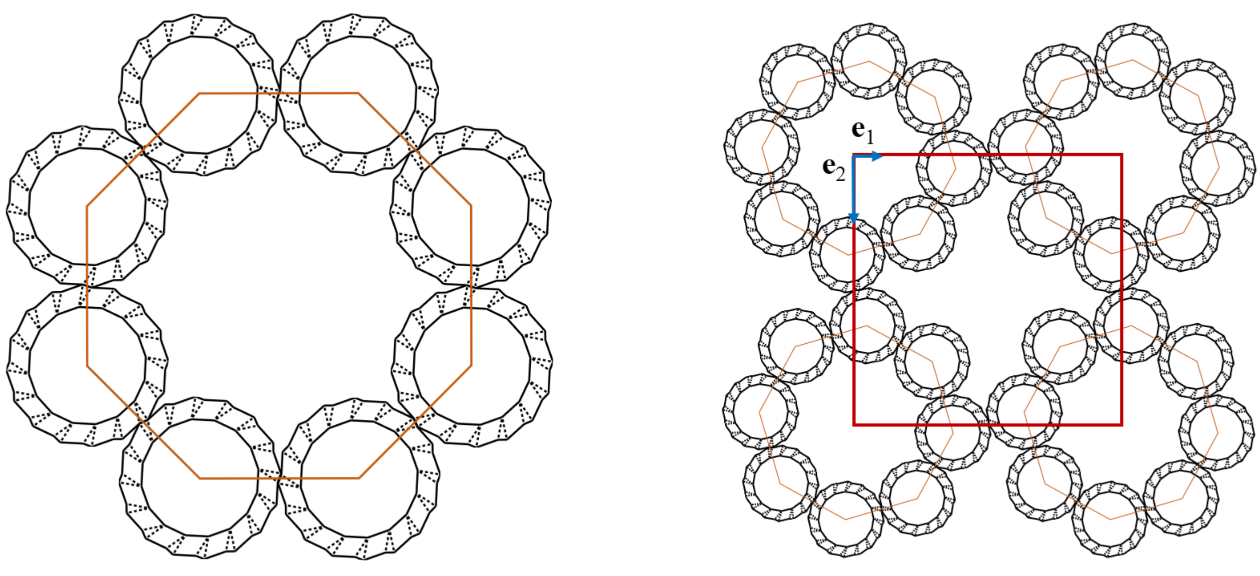

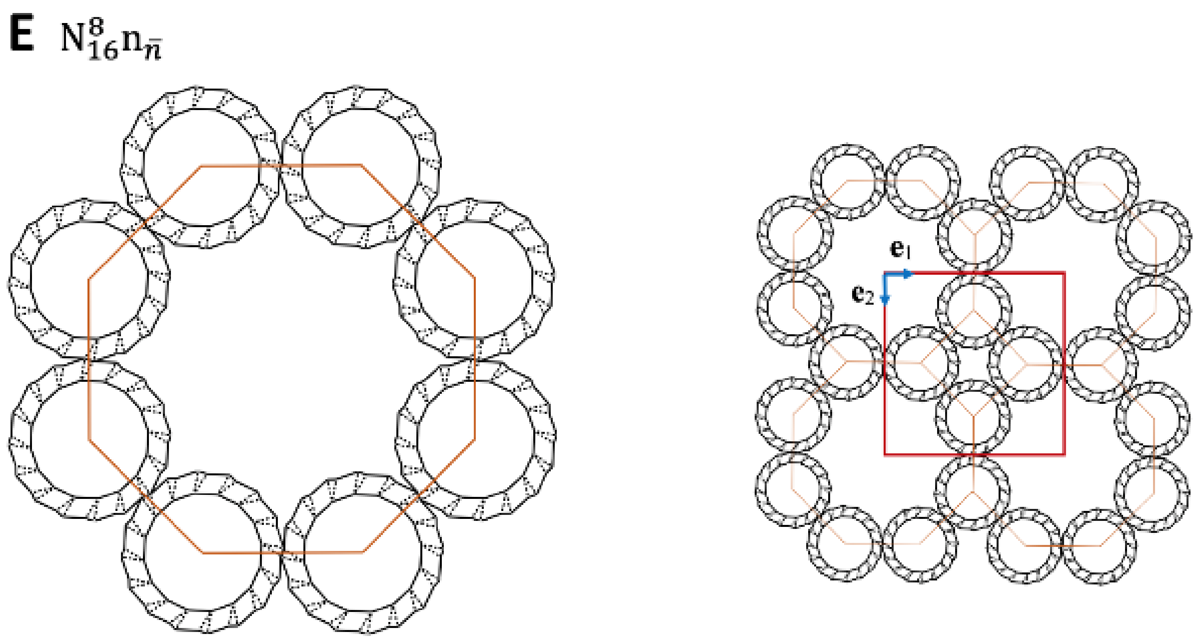

Figure 2-10 Compact and Non-compact tessellations. **A** In-plane view of most compact tessellations for $N_{16}n_{\bar{n}}$ along with other possible less-packed tessellations for $N^8_{16}n_{\bar{n}}$ shown in **B-E**.

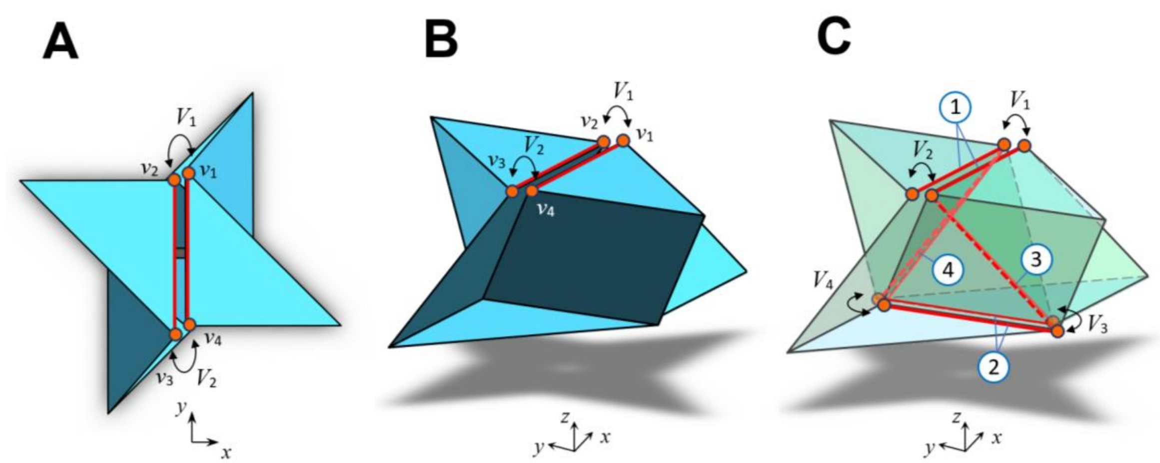

Figure 2-11 Coinciding joints and bars. Schematic of N_4n_1 unit kinematic chain showing alignment of joints and bars upon locking. **A** Top view and **B** isometric view immediately prior to locking, in **A** and **B** the coinciding points are (v_1, v_2) and (v_3, v_4), concisely shown by the pairs V_1 and V_2 respectively. **C** Isometric view showing all bars and hinges before reaching full contact, thus condensing into one element. Vertex pairs are shown by V_i; numbers in circles denote coinciding lines/edges.

2.6.8 Geometric mechanics of representative unit cell (RUC)

During reconfiguration, our units pass a kinematic bifurcation instant which provides access to dissimilar kinematic paths, each having modes that can be either flat-foldable and lockable. Each path has its own physical characteristics, e.g., geometry, relative density and Poisson's ratio. In this section, we first derive the closed-form expressions that describe changes in properties upon folding for $\mathrm{N}_4\mathrm{n}_n$ and $\mathrm{N}_6\mathrm{n}_n$ units. Next, we derive the representative energy landscape relations for given lockable and flat-foldable modes and generate energy-phase diagram that can explain the underlying physics of activation through in-plane confinement.

Table 2-3 Rigidity of different kinematic unit chains. Bar and joint counts of $\mathrm{N}_N\mathrm{n}_n$ unit kinematic chains (top row) for $N = 4$, 6, 8, 10 and 12 during folding (light pink) and at the locked state (light blue), along with the number of layers to attain rigidity (dark blue). Red solid and shaded red circles represent vertices laying respectively on mountain and valley planes.

Pattern	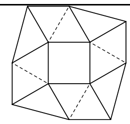	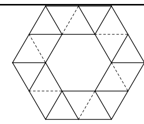	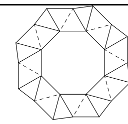	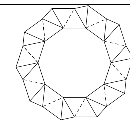	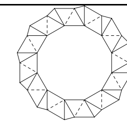
Joints (during folding)	12	18	24	30	36
Bars (during folding)	24	36	48	60	72
Joints (locked state)	8	12	16	20	24
Bars (locked state)	18	30	40	50	60
Top view	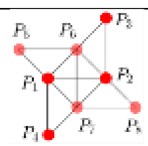	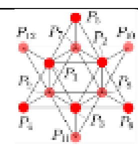	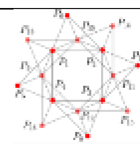	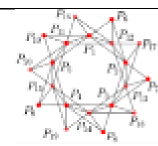	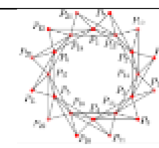
Riquired layers for rigidity	1	2	3	3	3

2.6.9 RUC model with boundary and loading conditions for $\mathrm{N}_4\boldsymbol{n}_n$ unit

We examine a representative unit cell for $\mathrm{N}_4\mathrm{n}_n$ that can describe the behavior of its entire periodic tessellation. Figure 2-12 shows the RUC with its own geometric parameters and loading conditions in a Cartesian coordinate system.

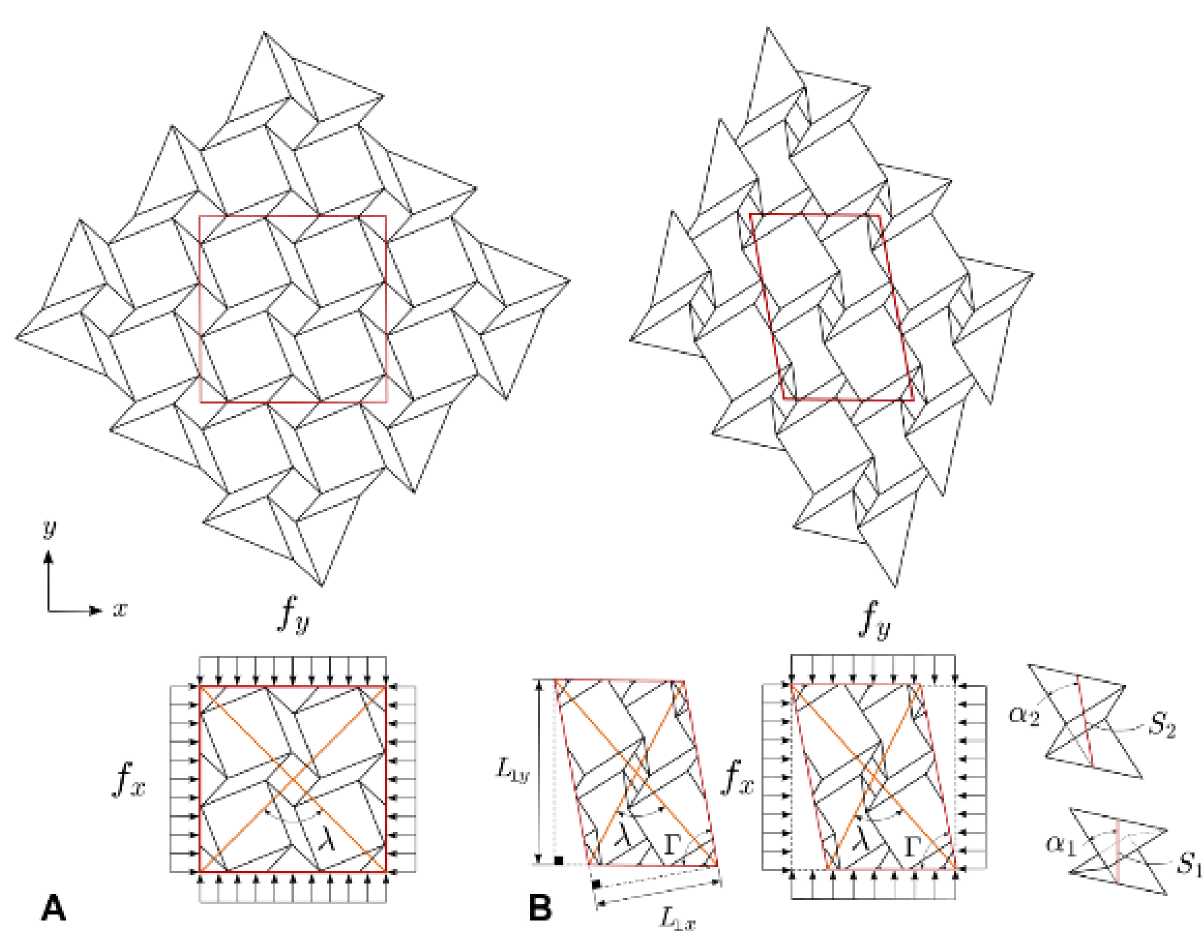

Figure 2-12 Biaxial reconfiguration of square based pattern. Top view of the most compact tessellations of $\mathbf{N_4 n_n}$ under two locking modes **A** $\mathcal{A}^2$ (or $\mathcal{O}^2$), **B** $\mathcal{A}\mathcal{O}$ and geometric parameters used in the calculation of the total energy. RUC shown in red squares for each mode.

In modes $\mathcal{O}^2$ and $\mathcal{A}^2$, the RUC is a square (red) with side $L_1 = 2S_1$, in which S_1 is the length of the line connecting the mid-points of the bases of two adjacent triangles separated by a parallelogram (right of Figure 2-12B) and can be calculated as

$$S_1^2 = (a\cos\phi)^2 + (b - a\sin\phi\cos\theta)^2. \tag{2-19}$$

Upon kinematic bifurcation, the square shape of the RUC switches to a parallelogram. One of its sides can be computed from Eq. (2-19), while the other side $L_2 = 2S_2$ can be calculated by replacing $\pi - \theta$ in Eq. (2-19) as

$$S_2^2 = (a\cos\phi)^2 + (b + a\sin\phi\cos\theta)^2. \tag{2-20}$$

To obtain the skewness angle of the parallelogram angle Γ in Figure 2-12B, we first calculate the angles α_1 and α_2 from

$$\begin{aligned} \alpha_1 &= \tan^{-1}\left(\frac{a\cos\phi}{b - a\sin\phi\cos\theta}\right) \\ \alpha_2 &= \tan^{-1}\left(\frac{a\cos\phi}{b + a\sin\phi\cos\theta}\right) \end{aligned} \tag{2-21}$$

and then, replace them in the relation

$$\Gamma = 90^\circ - \alpha_1 + \alpha_2. \tag{2-22}$$

Then, the cross-section area of the RUC in the *x*-*y* plane can be obtained from

$$A_{RUC} = L_1 L_2 \sin\Gamma \tag{2-23}$$

2.6.10 RUC model with boundary and loading conditions for $\mathrm{N}_6\boldsymbol{n}_n$ unit

We now examine $\mathrm{N}_6\mathrm{n}_n$ unit and derive geometric relations that describe the deformations of its kinematic paths. In this case, the smallest unit with parallel edges is a rectangle. The length of the line connecting the midpoints of the two adjacent triangles are

$$S_1^2 = (a\cos\phi)^2 + \left(\frac{2h}{3} - a\sin\phi\cos\theta\right)^2 \tag{2-24}$$

In $\mathcal{O}^3$ and $\mathcal{A}^3$ modes, the sides of the RUC shown in Figure 2-13 are given by

$$\begin{aligned} L_x &= 3S_1 \\ L_y &= \sqrt{3}S_1 \end{aligned} \tag{2-25}$$

A kinematic bifurcation can bring the unit into $\mathcal{A}^2\mathcal{O}$ or $\mathcal{O}^2\mathcal{A}$ modes. The new length of the line connecting the midpoints of the two adjacent triangles, S_2, can be obtained by replacing $\pi - \theta$ in Eq. (2-18) as

$$S_2^2 = (a\cos\phi)^2 + \left(\frac{2h}{3} + a\sin\phi\cos\theta\right)^2. \tag{2-26}$$

The angles α_1 and α_2 representing the inclination of the S_1 and S_2 lines with respect to the vertical axis can be obtained as

$$\alpha_1 = \tan^{-1}\left(\frac{a\cos\phi}{\frac{2h}{3} - a\sin\phi\cos\theta}\right) \text{ and } \alpha_2 = \tan^{-1}\left(\frac{a\cos\phi}{\frac{2h}{3} + a\sin\phi\cos\theta}\right). \tag{2-27}$$

After bifurcation, the hexagons that are defined by the centroids of the triangular faces are distorted. The internal angles ψ_i can be determined as a function of the inclination angles α_1 and α_2 as

$$\begin{aligned} \psi_1 &= 120^\circ + \alpha_1 - \alpha_2, \\ \psi_2 &= 240^\circ - \psi_1, \\ \psi_3 &= 120^\circ. \end{aligned} \tag{2-28}$$

If we connect the centroids of every other triangle around a unit chain, we obtain a triangle. The sides of this triangle relates to S_1 and S_2, and ψ_is through

$$\begin{aligned} L_1^2 &= S_1^2 + S_2^2 - 2S_1S_2\cos\psi_1, \\ L_2^2 &= S_1^2 + S_2^2 - 2S_1S_2\cos\psi_2, \\ L_3 &= S_1\sqrt{3}\,. \end{aligned} \tag{2-29}$$

The parallelogram of the RUC is defined by two triangles. One of the sides of the parallelogram is L_1 while the other side is given by

$$L_1'^{\,2} = 2L_1^2 + 2L_3^2 - L_2^2. \tag{2-30}$$

Now, using the cosine rule, we obtain

$$\lambda_2 = \cos^{-1}\left(\frac{L_1^2 + L_3^2 - L_2^2}{2L_1L_3}\right). \tag{2-31}$$

The angle of the parallelogram can be obtained from

$$\Gamma = \lambda_2 + \lambda_2' \tag{2-32}$$

where λ_2' can be calculated using the sine rule as

$$\frac{L_1'}{\sin\lambda_1} = \frac{L_1}{\sin\lambda_2'}\,. \tag{2-33}$$

Then, the cross-section area of the RUC in the *x-y* plane can be obtained from

$$A_{RUC} = L_1 L_1' \sin\Gamma. \tag{2-34}$$

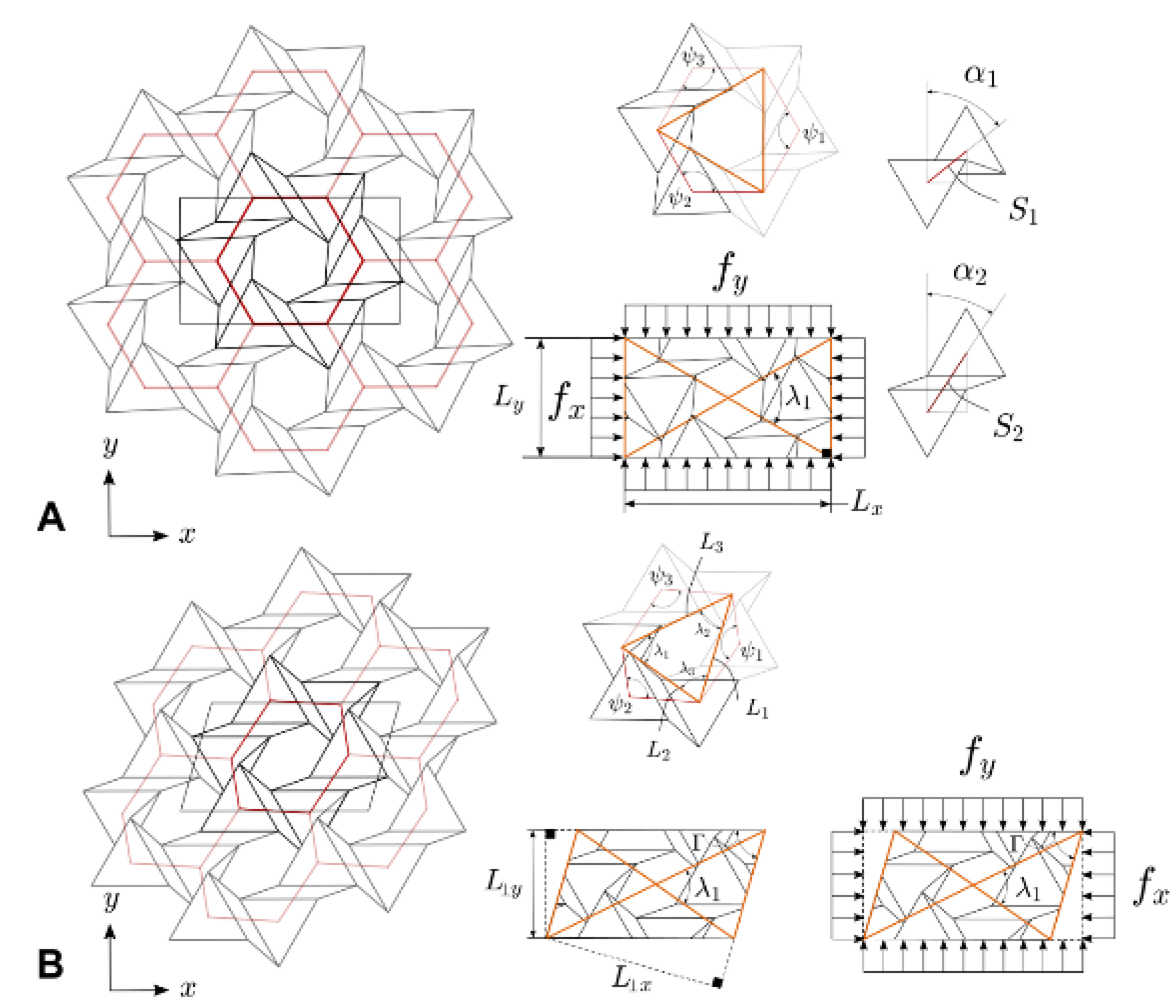

Figure 2-13 Biaxial reconfiguration of trinagle based pattern. Top view of the most compact tessellations of the $N_6 n_n$ under two locking modes **A** $\mathcal{A}^3$ and **B** $\mathcal{A}^2\mathcal{O}$ along with their geometrical parameters used in the calculation of the energy of the hinges (Section 2.6.13). RUC shown in black squares for each mode.

2.6.11 Relative Density

The relative density of our multimodal rigid-foldable materials upon reconfiguration (and transition between modes) can be expressed as a function of the dihedral angle θ and other geometric parameters of the unit chain for a given tessellation type. In addition, upon kinematic bifurcation, multiple paths emerge, and a distinct relative density can be associated to each given kinematic path. Figure 2-14 shows the relevant geometric parameters for $\mathrm{N}_{10}\mathrm{n}_n$, here taken as example for the analysis.

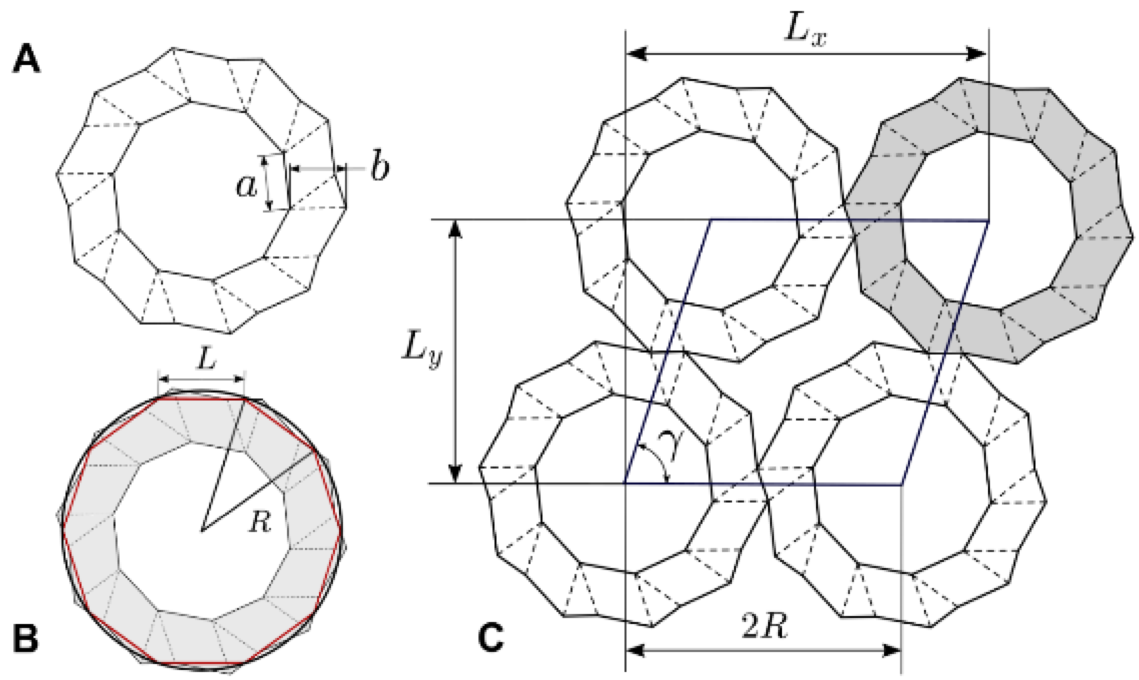

Figure 2-14 Unit cell of tessellation of kinematic unit chain. **A** Geometric parameters of a unit kinematic chain; **B** Connecting the mid-point of the bases of the triangles yields an N-sided polygon, shown in red; **C** Geometric parameters of the Bravais lattice tessellation. Regardless of *N*, four units can always be combined to form a rhombus defined by the angle γ, which is obtained from Eq. (2-18).

Figure 2-14B shows that by connecting the mid-points of the bases of the triangles, we obtain a regular polygon (red decagon here). R is the radius of the circumscribing circle of the polygon. The side of the polygon, L, is given by

$$L = \sqrt{(a\cos\phi)^2 + (b\sin\lambda - a\sin\phi\cos\phi)^2}, \tag{2-35}$$

which relates to R through

$$L = 2R \sin\frac{\lambda}{2}. \tag{2-36}$$

The volume of the rhombus shown in Figure 2-14 with height h (recall that it is a 3D structure) for modes $\mathcal{O}^{N/2}$ and $\mathcal{A}^{N/2}$ can be related to R using

$$V_f = 4aR^2 \sin\theta \sin\phi \sin\gamma. \tag{2-37}$$

The volume of the solid material inside the rhombus is

$$V_s = Nt\left(\frac{1}{2}b^2 \sin\lambda + ab\sin\phi\right). \tag{2-38}$$

Therefore, the relative density can be expressed as

$$\bar{\rho} = \frac{V_s}{V_f} = \frac{Nt\left(\frac{1}{2}b^2 \sin\lambda + ab\sin\phi\right)}{4aR^2 \sin\theta \sin\phi \sin\gamma}. \tag{2-39}$$

Figure 2-15 shows the relative density calculated for the $\widehat{\mathrm{N}}_4\mathrm{n}_n$ and $\widehat{\mathrm{N}}_6\mathrm{n}_n$ lattices when they reconfigure through their two kinematic paths. While Eq. (2-39) can be used to obtain the relative density of $\widehat{\mathrm{N}}_N\mathrm{n}_{\bar{n}}$ units in their uniform reconfiguration (for modes $\mathcal{O}^{N/2}$ and $\mathcal{A}^{N/2}$), we resort to Figure 2-12 and Figure 2-13 for the parameters defining the RUC to calculate the relative density of other kinematic paths. The volume of the solid material within the RUC can still be obtained from Eq. (2-37). The volume of the RUC can be obtained by multiplying the height by the area of the cross-section of the RUC in the *x-y* plane. We observe the relative density of flat-foldable modes approaches infinity as the lattice approaches its flat-foldable configuration. Also, each deformation mode attains a certain minimum relative density during the reconfiguration process. As we expect, lock mode $\mathcal{A}^{N/2}$ has the highest density of all locked configurations, while $\mathcal{O}^{N/2}$ is the least dense flat-foldable mode.

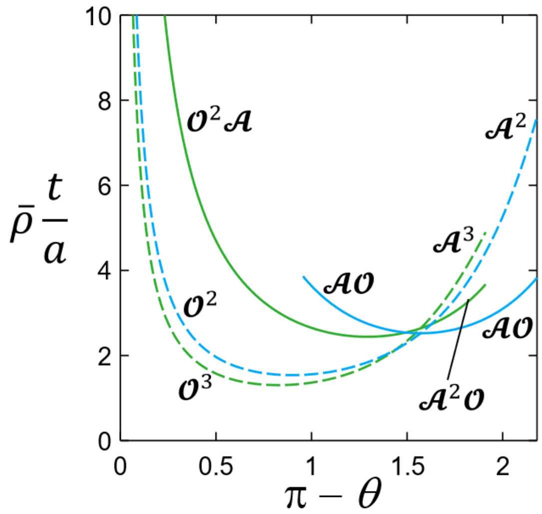

Figure 2-15 Relative densitiy vs. dihedral angle for square and triangle based patterns along different kinematic paths. Relative density computed for $\widehat{\mathrm{N}}_4\mathrm{n}_n$ and $\widehat{\mathrm{N}}_6\mathrm{n}_n$ lattices during reconfiguration along their two kinematic paths; *t* is the panel thickness, and *a* is the length of the sides of the primitive regular polygon.

2.6.12 Poisson's Ratio

During folding our metamaterials exhibit auxetic in-plane behavior. The following derives expressions of the Poisson's ratio that emerge at given modes.

2.6.12.1 Poisson's ratio of $\mathcal{A}^{N/2}$ and $\mathcal{O}^{N/2}$ modes

To obtain the expressions of the Poisson's ratio for $\widehat{\mathrm{N}}_n\mathrm{n}_n$, we begin by tessellating the rhombus of Figure 2-14. By doing so, we can express the increments of the strains, i.e., $d\varepsilon_x$, $d\varepsilon_y$ and $d\varepsilon_z$, in terms of the derivatives of the parameters $\mathcal{L}_x$, $\mathcal{L}_y$ and the height of the $\widehat{\mathrm{N}}_n\mathrm{n}_n$ unit. We first express $\mathcal{L}_x$, $\mathcal{L}_y$ as a function of the radius of the circumscribing circle, *R* and the skewness angle γ.

$$\begin{aligned} \mathcal{L}_x &= 2R(1+\cos\gamma) \\ \mathcal{L}_y &= 2R\sin\gamma \end{aligned} \tag{2-40}$$

ν_{xy}, the Poisson's ratio in *x*-*y* plane, can be written as the ratio of the increments of the in-plane strains

$$\nu_{xy} = -\frac{d\varepsilon_y}{d\varepsilon_x} = -\frac{d\mathcal{L}_x/\mathcal{L}_x}{d\mathcal{L}_y/\mathcal{L}_y} = -1. \tag{2-41}$$

This value remains constant during the folding process. ν_{xz} and ν_{yz}, the out-of-plane Poisson's ratios, can be obtained from

$$\nu_{xz} = \nu_{yz} = -R\cot\theta\frac{d\theta}{dR} \tag{2-42}$$

Taking the derivative of Eqs. (S34) and substituting the derivatives of R and θ from Eqs. (S29) and (S30) into Eq. (S36), we obtain

$$\nu_{xz} = \nu_{yz} = \frac{((a\cos\phi)^2 + (b\sin\lambda - a\sin\phi\cos\theta)^2)\cos\theta}{a(b\sin\lambda - a\sin\lambda\cos\theta)\sin\phi\sin^2\theta} \tag{2-43}$$

Interestingly, we observe a change in the sign of the out of plane Poisson's ratios. This entails that passing the kinematic bifurcation, our folding metamaterials in $\mathcal{A}^{N/2}$ mode have omnidirectional auxetic behavior.

2.6.12.2 Poisson's Ratio of Other Modes

The Poisson's ratio in other modes depends on the lattice (i.e., *N*) and the kinematic path. We examine here $\widehat{\mathrm{N}}_4\mathrm{n}_n$ and $\widehat{\mathrm{N}}_6\mathrm{n}_n$ and present the results of the Poisson's ratio for other mode shapes.

To simplify the calculation, we refer to the RUC in Figure 2-12 and Figure 2-13. In this case, the in-plane Poisson's ratio expression can be written as

$$\nu_{xy} = -\frac{d\varepsilon_y}{d\varepsilon_x} = -\frac{d\mathcal{L}_y/\mathcal{L}_y}{d\mathcal{L}_x/\mathcal{L}_x} = -\frac{dL_\perp/L_\perp}{dL_1/L_1} = -\frac{d(L_2\sin\Gamma)/L_2\sin\Gamma}{dL_1/L_1} \tag{2-44}$$

where the parameters L_1, L_2 and Γ are presented in Eq. (2-19), Eq. (2-20) and Eq. (2-22) for N_4 pattern. The expression for the Poisson's ratio of N_6 pattern can be written as

$$\nu_{xy} = -\frac{d\varepsilon_y}{d\varepsilon_x} = -\frac{d\mathcal{L}_y/\mathcal{L}_y}{d\mathcal{L}_x/\mathcal{L}_x} = -\frac{dL_\perp/L_\perp}{dL_1'/L_1'} = -\frac{d(L_2\sin\Gamma)/L_2\sin\Gamma}{dL_1'/L_1'} \tag{2-45}$$

The parameter L_2, L_1' and Γ can be obtained from Eqs. (2-29), (2-30) and (2-32). Figure 2-16 shows the in-plane Poisson's ratio calculated for $\widehat{\mathrm{N}}_4\mathrm{n}_n$ and $\widehat{\mathrm{N}}_6\mathrm{n}_n$ evolving along their kinematic paths. We observe that the in-plane Poisson's ratio of each lattice highly depends on the tessellation and kinematic path as opposed to that of the modes $\mathcal{A}^{N/2}$and $\mathcal{O}^{N/2}$.

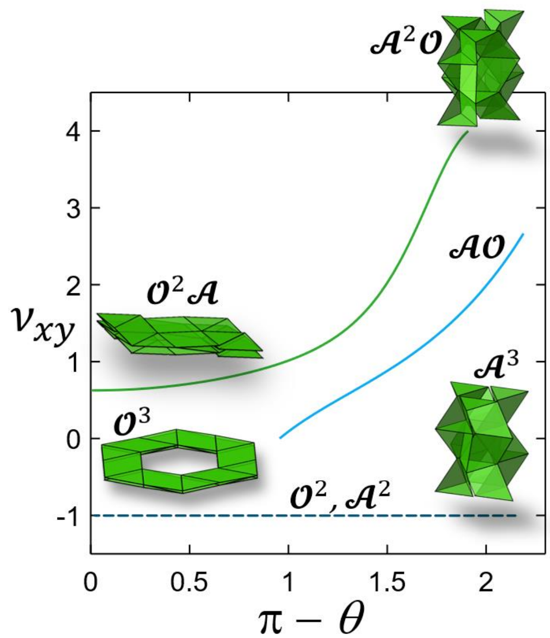

Figure 2-16 Poisson's ratio vs. dihedral angle for square and triangle-based patterns along different kinematic paths. Poisson's ratio calculated for the $\widehat{\mathrm{N}}_4\mathrm{n}_n$ and $\widehat{\mathrm{N}}_6\mathrm{n}_n$ lattices along their kinematic paths.

2.6.13 Energy Analysis

Here we derive the energy expressions for $\mathrm{N}_4\mathrm{n}_n$ and $\mathrm{N}_6\mathrm{n}_n$ as a function of their geometric parameters. Our analysis assumes the rigid panels are hinged with linear rotational springs, which represent the compliance of finite-thickness ligaments connecting panels. We also assume that our hinges maintain a linear behavior for most of the folding process.

2.6.13.1 Energy expression of $\mathrm{N}_N\mathrm{n}_n$ under in-plane biaxial loading

In this section we discuss the energy expressions for in-plane loading of $\mathrm{N}_N\mathrm{n}_n$. The expressions are derived with reference to Figure 2-12 and Figure 2-13. The total potential energy of RUC can be written as

$$\Pi = \sum_{i=1}^{\xi} nkb(\theta - \theta^0)^2 + \sum_{i=1}^{\xi'} nkb(\pi - \theta - \theta^0)^2 - \int_{L_{\perp x0}}^{L_{\perp x}} f_x d\ell - \int_{L_{\perp y0}}^{L_{\perp y}} f_y d\ell \tag{2-46}$$

where ξ is the total number of pairs for the acute dihedral angles ($\mathcal{A}$) and ξ' counts the total number of pairs for the obtuse dihedral angle ($\mathcal{O}$) with $\xi + \xi' = \frac{N}{2}$. n is the number of stacked layers, k the stiffness per unit length of the hinge, b the extrusion length, θ and θ^0 are the current and initial (zero-energy configuration) dihedral angles respectively, i indicates the pair of parallelograms with identical dihedral angle, f_x and f_y are the in-plane forces. $L_{\perp_x}$ and $L_{\perp_y}$ are the distances of the boundaries of RUC where f_x and f_y are applied (Figure 2-12), and can be defined as

$$\begin{aligned} L_{\perp_x} &= L_x \sin\Gamma \\ L_{\perp_y} &= L_y \sin\Gamma \end{aligned} \tag{2-47}$$

Moreover, the initial distances of the RUC boundaries are $L_{\perp_{x0}}$ and $L_{\perp_{y0}}$. Eq. (2-46) is valid for all in-plane loading conditions of $\mathrm{N}_N\mathrm{n}_n$.

2.6.13.2 Energy analysis of $\mathrm{N}_4\mathrm{n}_n$ under in-plane biaxial loading

Starting from a flat configuration (i.e., $\xi = 0$, $\theta^0 = 0$), and applying biaxial loads, we can find a closed form expression of the critical bucking load that is necessary to move from a flat configuration to $\mathcal{O}^2$ mode. By taking the first variation of the energy expression with $\xi' = 0$ in the first mode and setting $\theta = 180°$, we obtain the critical load as

$$f_x + f_y = \frac{nNkb}{2a\sin\phi}\frac{\sqrt{(b + a\sin\phi)^2 + (a\cos\phi)^2}}{(b + a\sin\phi)}. \tag{2-48}$$

This boundary is shown by line I in Figure 2-17. Passing the bifurcation, $\mathrm{N}_4\mathrm{n}_n$ buckles into its first mode. A load increase makes the metamaterial to continue its deformation in the $\mathcal{O}^2$ mode until $f_x + f_y$ reaches the following limit corresponding to the kinematic bifurcation at $\theta = 90°$ (line II in Figure 2-17),

$$f_x + f_y = \frac{nNk\pi}{4a\sin\phi}\sqrt{(a\cos\phi)^2 + b^2}. \tag{2-49}$$

To determine the post bifurcation behavior, we compare the slope of the energy for different modes at $\theta = 90°$. The path taken by our metamaterial is the one with the lowest gradient.

To obtain the boundaries of $\mathcal{AO}$ and $\mathcal{A}^2$ modes, i.e., lines III and IV in Figure 2-17, we note that the $\mathcal{AO}$ mode is activated when the slope of the energy at $\theta = 90°$ is below the slope of the energy in $\mathcal{A}^2$ mode. This condition can be written as

$$(\delta\Pi_{\mathcal{AO}} < \delta\Pi_{\mathcal{A}^2})|_{\theta=\frac{\pi}{2}} \rightarrow \left(\frac{\partial\Pi_{\mathcal{AO}}}{\partial\theta} < \frac{\partial\Pi_{\mathcal{A}^2}}{\partial\theta}\right)\Big|_{\theta=\frac{\pi}{2}} \rightarrow \left(\frac{\partial\Pi}{\partial\theta}\Big|_{\xi'=1} < \frac{\partial\Pi}{\partial\theta}\Big|_{\xi'=0}\right)\Big|_{\theta=\frac{\pi}{2}}. \tag{2-50}$$

Upon substituting the derivative of Eq. (2-46) into Eq. (2-50), and rearranging we obtain

$$f_x \text{ or } f_y \leq nNk\pi\frac{\sqrt{b^2+a^2\cos^2\phi}}{8a\sin\phi}. \tag{2-51}$$

The equality signs in Eq. (2-51) defines the boundary of $\mathcal{AO}$ ($\mathcal{OA}$) with $\mathcal{A}^2$, (lines III and IV in Figure 2-17). If the compressive forces are equal while passing the bifurcation (line V in Figure 2-17), the metamaterial shifts to mode $\mathcal{A}^2$. The reconfiguration in mode $\mathcal{A}^2$ continues until the loads reach a limit defined by the lock angle. This limit is obtained by taking the variation of Eq. (2-46) and solving for $\theta = \theta^L$ as

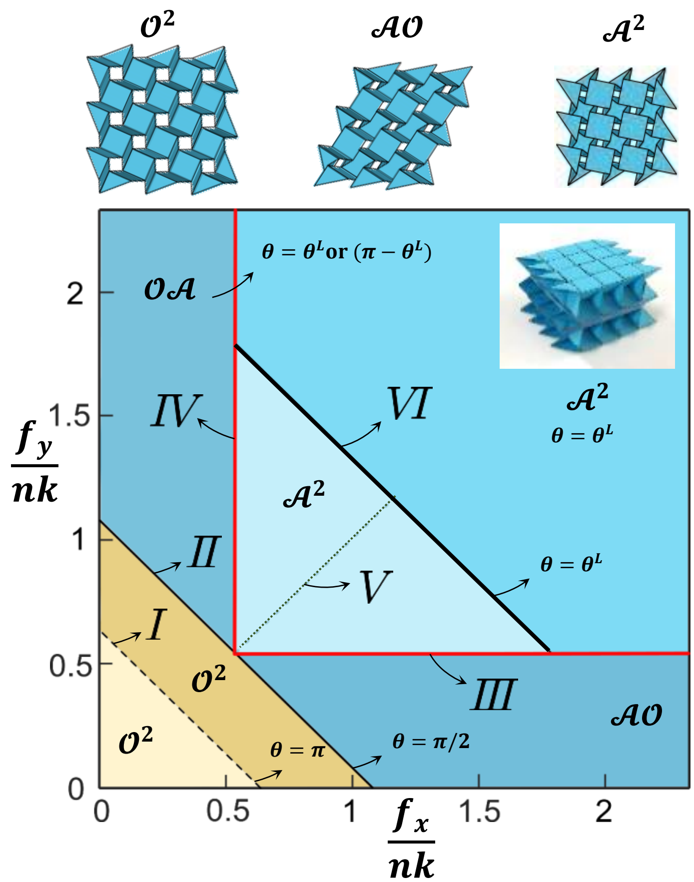

Figure 2-17 Kinematic phase diagram of square based pattern.

$$f_x + f_y = \frac{kb(\pi - \theta^L)}{2a\sin\phi\sin\theta^L}\frac{\sqrt{(a\cos\phi)^2 + (b + a\sin\phi\cos\theta^L)^2}}{b + a\sin\phi\cos\theta^L}. \tag{2-52}$$

This limit is shown by line VI in Figure 2-17.

2.6.13.3 Energy analysis of $\mathrm{N}_6\boldsymbol{n}_n$ under in-plane biaxial loading

To obtain the reconfiguration behavior of $\mathrm{N}_6\mathrm{n}_n$ we use Eq. (2-46). The length of the sides of RUC in Figure 2-18 can be obtained by using

$$\begin{aligned} L_{\perp_x} &= L_1\sin\Gamma, \\ L_{\perp_y} &= L_1'\sin\Gamma. \end{aligned} \tag{2-53}$$

The parameters L_1, L_1' and Γ are calculated from Eqs. (2-29), (2-30) and (2-32), respectively. In the case of N_6, ξ is equal to 3 for mode $\mathcal{A}^3$ while for mode $\mathcal{A}^2\mathcal{O}$, ξ is 2.

Figure 2-18 shows the phase diagram of N_6. Initially, the metamaterial is assumed to be flat. By compressing it, a certain limit is reached and the metamaterial buckles to $\mathcal{O}^3$ (line I in Figure 2-18). This deformation mode is maintained until the metamaterial reaches $\theta = 90°$ (line II in Figure 2-18). This also applies to the case of N_4; at the bifurcation point, the ratio of the forces plays a major role in governing the deformation path that follows. The boundaries of $\mathcal{A}^2\mathcal{O}$, $\mathcal{O}^2\mathcal{A}$ and $\mathcal{A}^3$ modes can be obtained by comparing the slope of the corresponding energy expressions. The smallest slope defines the deformation after the kinematic bifurcation. Therefore, we can write

$$(\delta\Pi_{\mathcal{A}^2\mathcal{O}} \leq \delta\Pi_{\mathcal{A}^3})|_{\theta=\frac{\pi}{2}} \rightarrow \left(\frac{\partial\Pi_{\mathcal{A}^2\mathcal{O}}}{\partial\theta} \leq \frac{\partial\Pi_{\mathcal{A}^3}}{\partial\theta}\right)\Big|_{\theta=\frac{\pi}{2}} \rightarrow \left(\frac{\partial\Pi}{\partial\theta}\Big|_{\xi'=2} < \frac{\partial\Pi}{\partial\theta}\Big|_{\xi'=3}\right)\Big|_{\theta=\frac{\pi}{2}}, \tag{2-54}$$

which can be simplified as

$$f_x\left(\frac{2}{3} - \sqrt{3}\frac{a}{h}\cos\phi\right) + f_y\left(\frac{2}{\sqrt{3}} + \frac{a}{h}\cos\phi\right) \leq 2K\pi\frac{\sqrt{\left(\frac{2h}{3}\right)^2 + (a\cos\phi)^2}}{ah\sin\phi}. \tag{2-55}$$

Note that the equality sign represents line III in Figure 2-18. The boundary of $\mathcal{O}^2\mathcal{A}$ and $\mathcal{A}^3$ can be obtained from

$$(-\delta\Pi_{\mathcal{A}^3} \leq \delta\Pi_{\mathcal{O}^2\mathcal{A}})|_{\theta=\frac{\pi}{2}} \rightarrow \left(-\frac{\partial\Pi_{\mathcal{A}^3}}{\partial\theta} \leq \frac{\partial\Pi_{\mathcal{O}^2\mathcal{A}}}{\partial\theta}\right)\Big|_{\theta=\frac{\pi}{2}} \rightarrow \left(\frac{\partial\Pi}{\partial\theta}\Big|_{\xi'=3} < \frac{\partial\Pi}{\partial\theta}\Big|_{\xi'=1}\right)\Big|_{\theta=\frac{\pi}{2}}, \tag{2-56}$$

which can be simplified to

$$f_x\left(\frac{10}{3} + \sqrt{3}\frac{a}{h}\cos\phi\right) + f_y\left(\frac{2}{\sqrt{3}} - \frac{a}{h}\cos\phi\right) \leq 10kb\pi\frac{\sqrt{\left(\frac{2h}{3}\right)^2 + (a\cos\phi)^2}}{ah\sin\phi}. \tag{2-57}$$

Here, the equality sign represents line IV in Figure 2-18. There is a certain ratio that induces metamaterial to deform into its $\mathcal{A}^3$ mode (line V in Figure 2-18A). The boundaries defined by Eq. (2-55) and (2-57) intersect the boundary of the kinematic bifurcation at a point with the load ratio given by

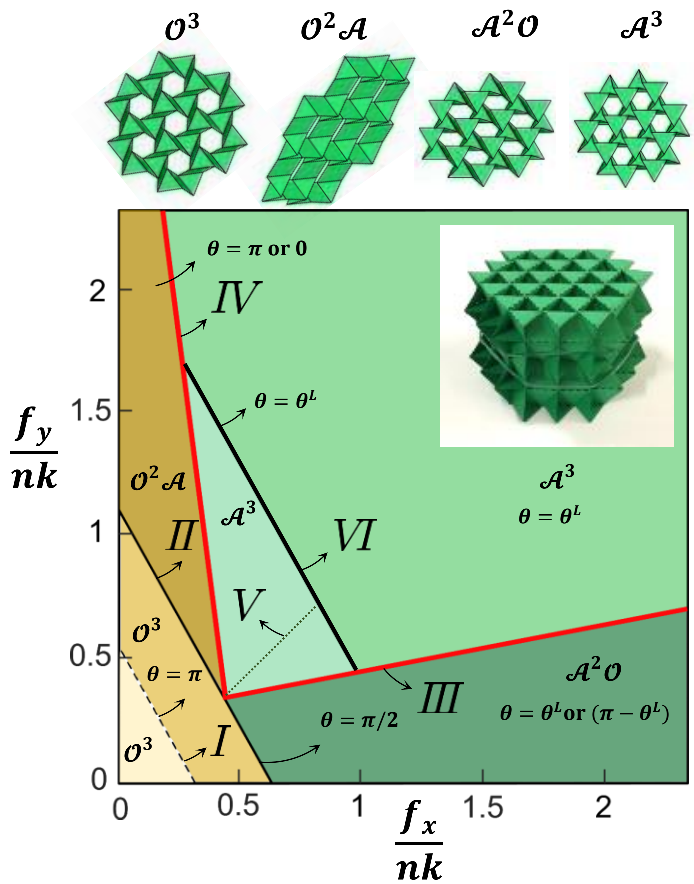

Figure 2-18 Kinematic phase diagram of triangle based pattern.

$$\frac{f_x}{f_y} = \frac{\begin{vmatrix} 2R & \frac{2}{\sqrt{3}}+\frac{a}{h}\cos\phi \\ 10R & \frac{2}{\sqrt{3}}-\frac{a}{h}\cos\phi \end{vmatrix}}{\begin{vmatrix} \frac{2}{3}-\sqrt{3}\frac{a}{h}\cos\phi & 2R \\ \frac{10}{3}+\sqrt{3}\frac{a}{h}\cos\phi & 10R \end{vmatrix}},\ R = kb\pi\frac{\sqrt{\left(\frac{2h}{3}\right)^2+(a\cos\phi)^2}}{ah\sin\phi}, \tag{2-58}$$

where $|\ \ |$ denotes the determinant. As per the case of N_4, the metamaterial locks into its $\mathcal{A}^3$ mode provided that the load ratio of Eq. (2-58) is maintained during the reconfiguration.

2.6.14 Base material characterization

To characterize the Young's modulus of the base paperboard material we realized rectangular samples of dimensions 240 mm × 5 mm (30 mm on each side for the grip) as suggested in literature [205] for a better outcome than that provided by standardized methods, i.e., ISO 1924–2 (see the left of Figure 2-19). The stress-strain response of the base paperboard material of our proof-of-concept prototype has been characterized using in-plane uniaxial tensile tests conducted on rectangular samples. Tests were carried out under in-plane uniaxial tension along two main directions, i.e., machine direction (MD) and cross direction (CD) (Figure 2-19). The results show that the tensile Young's modulus and strength of our paperboard sheets in the MD direction is about 7.9 gPa and 57 mPa, respectively, roughly two times higher than the values obtained in the CD direction. The difference we observe can be attributed to the pulp and paper process which tends to align the network of cellulose fibers in the MD direction.

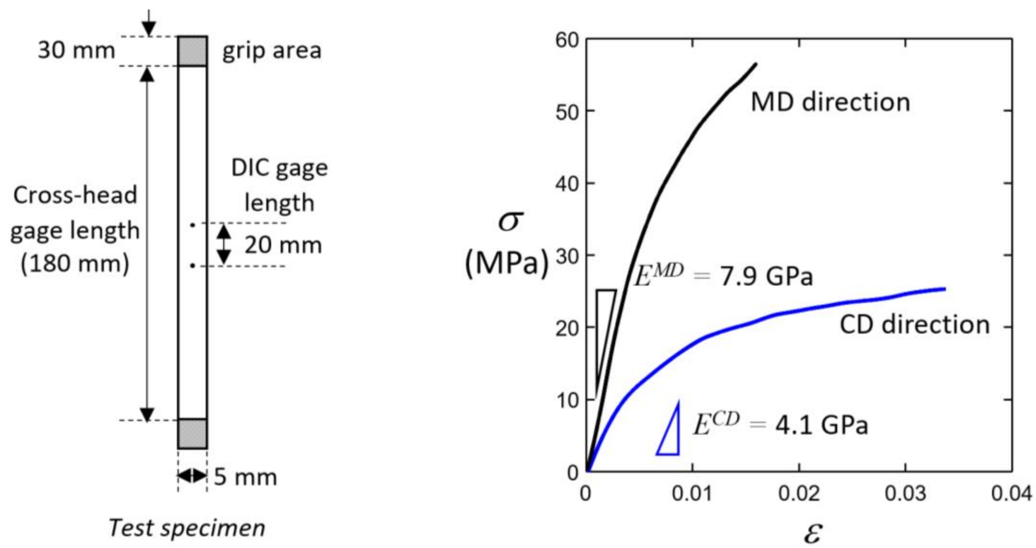

Figure 2-19 Tensile sample and testing results. Specimen geometry of base paperboard material along with their uniaxial stress-strain responses in the machine direction (MD) and cross (CD) direction.

2.6.15 Response of periodic cellular material

Prior to carrying a series of experiments on our material system, we studied the properties of finite size specimens to ensure they are representative of those of their periodic counterparts. We study the role of in-plane and out-of-plane tessellation of our material building block with the goal of determining the smallest material system (minimum number of unit-cells in all three directions) that represents the response of an unbounded periodic material.

To perform our convergence analysis of tessellation level, we examine two representative units, $\widehat{\mathrm{N}}_4\mathrm{n}_n$ and $\widehat{\mathrm{N}}_6\mathrm{n}_n$, and adopt the notation $(l_{\mathrm{e}_1}, l_{\mathrm{e}_2})$ to refer to an in-plane level of tessellation where the primitive unit is tessellated l_{e_1} times in the in-plane direction e_1 and l_{e_2} times in e_2. Given the role of tessellation along the three directions, we denote our material system as $\widehat{\mathrm{N}}_N\mathrm{n}_n(l_{\mathrm{e}_1}, l_{\mathrm{e}_2})$, and study two representative systems, $\widehat{\mathrm{N}}_4\mathrm{n}_6(7{,}7)$ and $\widehat{\mathrm{N}}_6\mathrm{n}_6(7{,}7)$. The out-ot-plane tessellation is assessed by the number of layers n stacked in the third direction. Our experiments investigate:

(A) In-plane tessellation. For a single layer sample $\widehat{\mathrm{N}}_4\mathrm{n}_1$, determine the minimum number of in-plane unit cells that is representative of the unbounded in-plane tessellation.

(B) Out-of-plane tessellation. For a multilayer specimen $\widehat{\mathrm{N}}_4\mathrm{n}_n$ with minimum number of in-plane unit cells, assess the minimum number of stacking layers, n, that can parallel the response of the unbounded periodic domain.

(C) Comparison between of $\widehat{\mathrm{N}}_4\mathrm{n}_1$ and $\widehat{\mathrm{N}}_6\mathrm{n}_1$ at given levels of tessellation.

(A) Mechanical response of single-layer specimen. Figure 2-20A shows the primitive unit-cell of the locked unit $\widehat{\mathrm{N}}_4\mathrm{n}_1$ along with the effective area of four tessellation levels (1,1), (2,2), (3,3) and (4,4), each shown by a color ranging from brown to yellow. In Figure 2-20B, C, the statistical values of Young's moduli and yield strength (as measured in the subset of Figure 2-20B) of a single layer sample show that by increasing the number of unit-cells, the convergence for both parameters occur at the tessellation level of (7,7). Beyond this level, negligible changes in properties can be observed. (7,7) can thus be considered as the minimum level of tessellation representing the periodic unbounded response.

(B) Mechanical response of multilayered specimens. The role of layer stacking (*z*-direction) was assessed for a specimen with (7,7) tessellation level (Figure 2-20D). The results in Figure 2-20E, F show that adding n layers results in a convergence of the Young's modulus and strength at $n = 6$. Beyond this value, only marginal changes can be observed, indicating that the periodic response of $\widehat{\mathrm{N}}_4\mathrm{n}_6$ with tessellation level $(7,7)$ is attained with a minimum of 6 layers stacked in the *z*-direction.

(C) Comparison of the mechanical response of $\widehat{\mathrm{N}}_4\mathrm{n}_1$ and $\widehat{\mathrm{N}}_6\mathrm{n}_1$ at given levels of tessellation. Figure 2-20G shows the primitive unit cell of the locked unit kinematic chain $\widehat{\mathrm{N}}_6\mathrm{n}_1$ along with the manufactured paper sample with a tessellation level $(7,7)$. Figure 2-20H and I show respectively the Young's modulus and the yield strength of the single layer $\widehat{\mathrm{N}}_6\mathrm{n}_1$ and compare them with those of $\widehat{\mathrm{N}}_4\mathrm{n}_1$ at given levels of tessellation. The results show that a single unit chain, i.e., tessellation level $(1,1)$, has the highest stiffness, but the lowest strength. Upon increasing the tessellation level up to $(7,7)$, the stiffness decreases for both units; on the other hand, for $\widehat{\mathrm{N}}_4\mathrm{n}_1$ the strength monotonically increases, while for $\widehat{\mathrm{N}}_6\mathrm{n}_1$we observe first an increase and then a decrease. Beyond the tessellation level (7,7) the mechanical properties tested in our experiment do not show noticeable changes (Figure 2-20H and I). Hence $(7,7)$ is the minimum level of tessellation that we identify as representative of the unbounded periodic response.

2.6.16 Manufacturability

Most of the current concepts in the literature require a laborious process of fabrication, which often adds a further layer of sophistication. In several cases, the fabrication of a single three-dimensional unit cell requires several steps (cutting, folding, and gluing) [86, 87]. The spatial assembly of multiple unit cells is another elaborate undertaking, as each cell needs to be attached one by one in space to its neighbor via edge-to-edge bonding [86, 87, 104]. Alternatively, 3D printing has been effectively used to fabricate origami-based materials [75, 107, 128, 149]. The high stiffness of the 3D printed hinges, however, has been shown to sacrifice foldability [107, 128, 149]. In addition, 3D printing has been used mainly with soft materials [75, 128], thereby bringing to realization prototypes with limited load-bearing capacity.

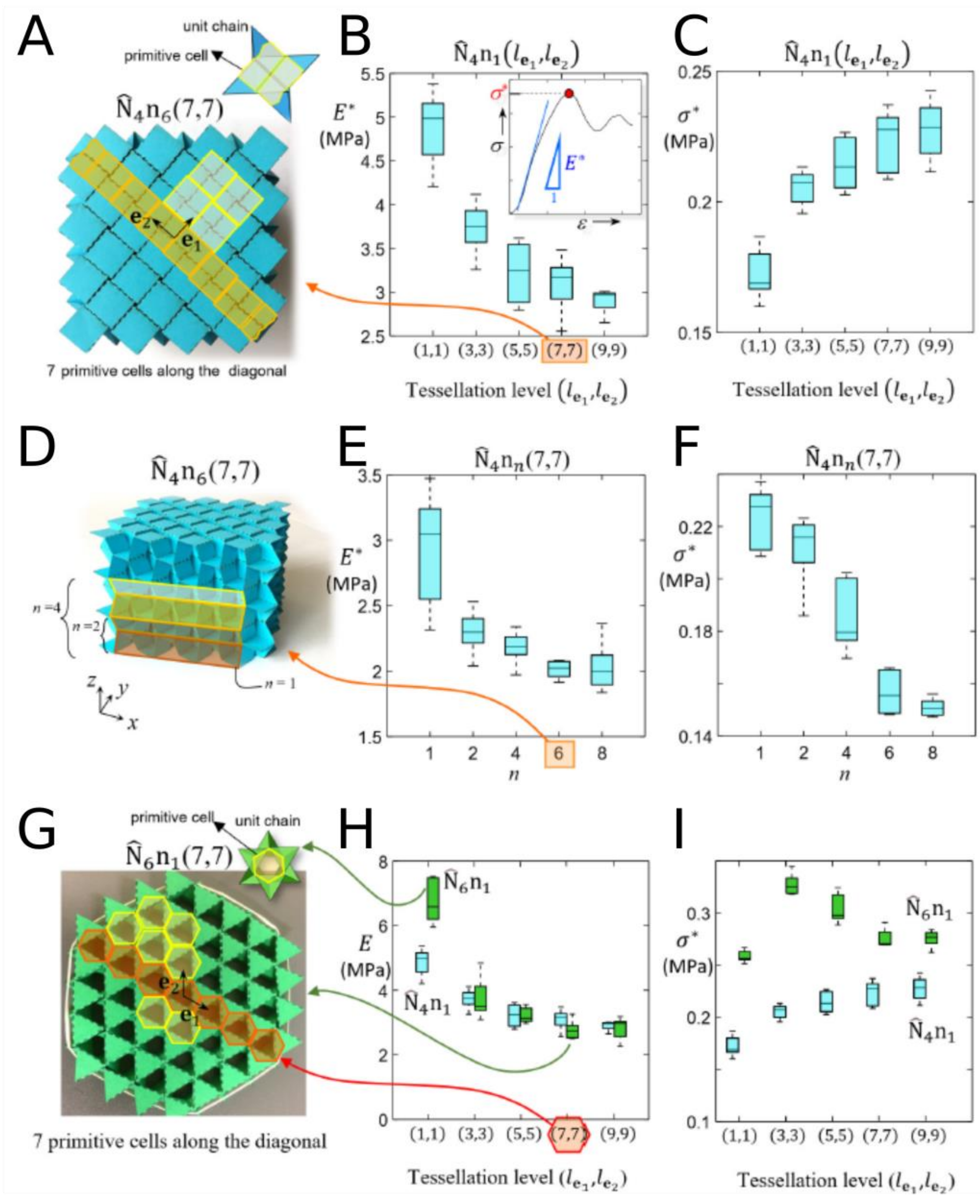

Figure 2-20 Convergence study of square and triangle-based patterns. Fabricated samples and measured properties of $\hat{N}_4n_n$ unit locked in mode $\mathcal{A}^2$; statistical data for each given geometry are test results of five

samples. **A** Top view illustration of manufactured unit chain showing its unit chain and tessellation levels. Compressive Young's modulus **B** and yield strength **C** for a sample with one layer only and given planar tessellation levels. The subset in **B** schematically illustrates how the compressive Young's modulus E^* and yield strength $\boldsymbol{\sigma}^*$ were measured. **D** Material system $\widehat{\mathrm{N}}_6\mathrm{n}_4$ with representative number, n, of stacked layers. Measured compressive Young's modulus E^* **E** and yield strength σ^* **F** for given numbers of stacking layers n. **G** Top view of representative fabricated $\widehat{\mathrm{N}}_6\mathrm{n}_1$ sample with unit chain area in locked mode $\mathcal{A}^3$ and tessellation level (7,7). Yellow hexagons represent the top area of our primitive unit cells used for the calculation of the stress values. Compressive Young's modulus **H** and yield strength **I** of $\widehat{\mathrm{N}}_6\mathrm{n}_1$ and $\widehat{\mathrm{N}}_4\mathrm{n}_1$ at given tessellation levels. For each tessellation level, five tests were conducted.

In our work, we use a relatively straightforward process with two fabrication steps that can be easily automated. From a single layer of the base material, we introduce in one step the tessellation of shaped voids and folding lines through laser cutting. After partially folding one kirigami layer along the origami crease pattern, we stack identical layers and bond (here, using glue) their triangular faces. This process does not require the assembly of 3D unit cells in space, rather three-dimensionality is imparted in the flat configuration where the constituent layers are stacked and bonded together. As a result, the flat multilayered crease pattern can be easily folded in space since each layer is geometrically constrained to lay between parallel planes. Such characteristics enable to bypass the more laborious procedures currently pursued in the literature.

2.7 References

1. Melancon, D., et al., *Multistable inflatable origami structures at the metre scale.* Nature, 2021. 592(7855): p. 545-550.
2. Zhang, Y., et al., *A mechanically driven form of Kirigami as a route to 3D mesostructures in micro/nanomembranes.* Proceedings of the National Academy of Sciences, 2015. 112(38): p. 11757-11764.
3. Yasuda, H., et al., *Origami-based tunable truss structures for non-volatile mechanical memory operation.* Nature Communications, 2017. 8(1).
4. Pagano, A., et al., *A crawling robot driven by multi-stable origami.* Smart Materials and Structures, 2017. 26(9).
5. Rafsanjani, A., et al., *Kirigami skins make a simple soft actuator crawl.* Science Robotics, 2018. 3(15): p. eaar7555-eaar7555.
6. Novelino, L.S., et al., *Untethered control of functional origami microrobots with distributed actuation.* Proceedings of the National Academy of Sciences of the United States of America, 2020. 117(39): p. 24096-24101.
7. Rafsanjani, A., et al., *Propagation of pop ups in kirigami shells.* Proceedings of the National Academy of Sciences, 2019. 116(17): p. 8200-8205.

8. Wu, S., et al., *Stretchable origami robotic arm with omnidirectional bending and twisting.* Proceedings of the National Academy of Sciences of the United States of America, 2021. 118(36): p. 1-9.
9. Boatti, E., N. Vasios, and K. Bertoldi, *Origami metamaterials for tunable thermal expansion.* Advanced Materials, 2017. 29(26): p. 1700360-1700360.
10. Liu, L., et al., *Encoding kirigami bi-materials to morph on target in response to temperature.* Scientific reports, 2019. 9(1): p. 19499.
11. Iniguez-Rabago, A., Y. Li, and J.T.B. Overvelde, *Exploring multistability in prismatic metamaterials through local actuation.* Nature Communications, 2019. 10(1): p. 1-10.
12. Hull, T.C., et al., *Origami structures with a critical transition to bistability arising from hidden degrees of freedom.* Nature Materials, 2015. 14(4): p. 389-393.
13. Yasuda, H. and J. Yang, *Reentrant origami-based metamaterials with negative Poisson's ratio and bistability.* Physical Review Letters, 2015. 114(18): p. 1-5.
14. Liu, K., T. Tachi, and G.H. Paulino, *Invariant and smooth limit of discrete geometry folded from bistable origami leading to multistable metasurfaces.* Nature Communications, 2019. 10(1).
15. Shang, X., et al., *Durable bistable auxetics made of rigid solids.* Journal of Materials Research, 2018. 33(3): p. 300-300.
16. Castle, T., et al., *Additive lattice kirigami.* Science Advances, 2016. 2(9): p. e1601258-e1601258.
17. Choi, G.P.T., L.H. Dudte, and L. Mahadevan, *Programming shape using kirigami tessellations.* Nature Materials, 2019. 18(9): p. 999-1004.
18. Dudte, L.H., et al., *Programming curvature using origami tessellations.* Nature Materials, 2016. 15(5): p. 583-583.
19. Pratapa, P.P., K. Liu, and G.H. Paulino, *Geometric Mechanics of Origami Patterns Exhibiting Poisson's Ratio Switch by Breaking Mountain and Valley Assignment.* Physical Review Letters, 2019. 122(15).
20. An, N., et al., *Programmable Hierarchical Kirigami.* Advanced Functional Materials, 2020. 30(6): p. 1906711.
21. Sussman, D.M., et al., *Algorithmic Lattice Kirigami: A Route to Pluripotent Materials.* 2015.
22. Lamoureux, A., et al., *Dynamic kirigami structures for integrated solar tracking.* Nature Communications, 2015. 6: p. 8092-8092.
23. Nauroze, S.A., et al., *Continuous-range tunable multilayer frequency-selective surfaces using origami and inkjet printing.* Proceedings of the National Academy of Sciences of the United States of America, 2018: p. 201812486-201812486.
24. Overvelde, J.T.B., et al., *Rational design of reconfigurable prismatic architected materials.* Nature, 2017. 541(7637): p. 347-352.
25. Overvelde, J.T.B., et al., *A three-dimensional actuated origami-inspired transformable metamaterial with multiple degrees of freedom.* Nature Communications, 2016. 7: p. 1-8.
26. Filipov, E.T., T. Tachi, and G.H. Paulino, *Origami tubes assembled into stiff, yet reconfigurable structures and metamaterials.* Proceedings of the National Academy of Sciences, 2015. 112(40): p. 12321-12326.
27. Schenk, M. and S.D. Guest, *Geometry of Miura-folded metamaterials.* Proceedings of the National Academy of Sciences, 2013. 110(9): p. 3276-3281.

28. Eidini, M. and G.H. Paulino, *Unraveling metamaterial properties in zigzag-base folded sheets.* Science Advances, 2015. 1(8): p. 1-8.
29. Lv, C., et al., *Origami based mechanical metamaterials.* Scientific Reports, 2014. 4.
30. Cheung, K.C., et al., *Origami interleaved tube cellular materials.* Smart Materials and Structures, 2014. 23(9).
31. Rafsanjani, A. and D. Pasini, *Bistable auxetic mechanical metamaterials inspired by ancient geometric motifs.* Extreme Mechanics Letters, 2016. 9: p. 291-291.
32. Fang, H., et al., *Programmable Self-Locking Origami Mechanical Metamaterials.* Advanced Materials, 2018. 30(15): p. 1-9.
33. Zhai, Z., Y. Wang, and H. Jiang, *Origami-inspired, on-demand deployable and collapsible mechanical metamaterials with tunable stiffness.* Proceedings of the National Academy of Sciences, 2018. 0: p. 201720171-201720171.
34. Silverberg, J.L., et al., *Using origami design principles to fold reprogrammable mechanical metamaterials.* science, 2014. 345(6197): p. 647-650.
35. Mukhopadhyay, T., et al., *Programmable stiffness and shape modulation in origami materials: Emergence of a distant actuation feature.* Applied Materials Today, 2020. 19: p. 100537.
36. Tang, Y., et al., *Programmable active kirigami metasheets with more freedom of actuation.* Proceedings of the National Academy of Sciences of the United States of America, 2019. 116(52): p. 26407-26413.
37. Zhai, Z., et al., *In situ stiffness manipulation using elegant curved origami.* Science Advances, 2020. 6(47): p. 1-10.
38. Yasuda, H., et al., *Origami-Based Cellular Structures with In Situ Transition between Collapsible and Load-Bearing Configurations.* Advanced Engineering Materials, 2019. 21(12): p. 1-8.
39. Evans, T.A., et al., *Rigidly foldable origami gadgets and tessellations.* Royal Society Open Science, 2015.
40. Filipov, E.T., G.H. Paulino, and T. Tachi, *Origami tubes with reconfigurable polygonal cross-sections.* Proceedings of the Royal Society A: Mathematical, Physical and Engineering Sciences, 2016. 472(2185).
41. Nayakanti, N., S.H. Tawfick, and A.J. Hart, *Twist-coupled Kirigami cells and mechanisms.* Extreme Mechanics Letters, 2018. 21: p. 17-17.
42. Kamrava, S., et al., *Origami-based cellular metamaterial with auxetic, bistable, and self-locking properties.* Scientific Reports, 2017. 7: p. 46046-46046.
43. Wagner, M.A., et al., *Programmable, active lattice structures: Unifying stretch-dominated and bending-dominated topologies.* Extreme Mechanics Letters, 2019. 29: p. 100461.
44. Wang, X., S.D. Guest, and R.D. Kamien, *Keeping It Together: Interleaved Kirigami Extension Assembly.* Physical Review X, 2020. 10(1): p. 11013-11013.
45. Gavazzoni, M., S. Foletti, and D. Pasini, *Cyclic response of 3D printed metamaterials with soft cellular architecture: The interplay between as-built defects, material and geometric non-linearity.* Journal of the Mechanics and Physics of Solids, 2022. 158: p. 104688.
46. Pellegrino, S. and C.R. Calladine, *Matrix analysis of statically and kinematically indeterminate frameworks.* International Journal of Solids and Structures, 1986. 22(4): p. 409-428.

47. Pellegrino, S., *Structural computations with the singular value decomposition of the equilibrium matrix.* International Journal of Solids and Structures, 1993. 30(21): p. 3025-3035.
48. Kumar, P. and S. Pellegrino, *Computation of kinematic paths and bifurcation points.* International Journal of Solids and Structures, 2000. 37(46): p. 7003-7027.
49. Klima, R., N. Sigmon, and E. Stitzinger, *Applied Abstract Algebra with MapleTM and MATLAB®: A Maple and MATLAB Approach*. Vol. 34. 2015: CRC Press.
50. Mordell, L.J., *Diophantine equations*. 1969: Academic Press.
51. Yoshihara, H. and M. Yoshinobu, *In-plane shear strength of paper measured by asymmetric four-point bending test.* Holzforschung, 2015. 69(1): p. 41-46.
52. Zhao, Z., et al., *3D Printing of Complex Origami Assemblages for Reconfigurable Structures*. 2018.
53. Lin, Z., et al., *Folding at the Microscale: Enabling Multifunctional 3D Origami-Architected Metamaterials.* Small, 2020. 16(35): p. 1-9.

The link between Chapter 2 and Chapter 3

Chapter 2 has introduced a class of reprogrammable origami-inspired metamaterials with rigid flat-foldability inspired by the principles of origami. This class of origami materials is load-bearing in multiple directions, including the deployment direction. By integrating origami-folding and kirigami-cutting principles, we have developed foldable patterns consisting of chains that take the form of N even-sided regular polygons, thereby establishing an internal void. The excisions allow for the relaxation of constraints on the deformation imposed by the planarity of the panels and the connectivity of the parent origami structure. This approach facilitates folding within the enclosed voids, offering multiple degrees of freedom that can be reduced through stacking. The kinematic analysis of the unit chain has shown the existence of a kinematic bifurcation point along their kinematic path. Post-bifurcation, multiple paths become available and can be harnessed to modulate their structural behavior in flat-foldable or locked configurations. A discussion on the energy landscape has led to the development of energy phase diagrams that explain energetically favorable rigid foldable reconfigurations.

Among the insights gained from chapter 2, several have stood out for generalizing the geometry of the kinematic chains. In particular, the geometric constraints can be relaxed to enable exploring the role of other so far unexplored geometric parameters governing folding. In addition, chapter 2 has confined the investigation to rigidly foldable deformation modes only, hence neglecting the possibility for the panels to deform and eventually snap in a given direction. This response cannot be explained under the rigid-foldability assumption and thus becomes the motivation of the next chapter, where panel deformation is admitted and leveraged to induce a multistable response upon folding.

Chapter 3

A multistable class of origami-inspired metamaterials for mechanical damping and vibration mitigation under oscillatory motion

Chapter 3: A multistable class of origami-inspired metamaterials for mechanical damping and vibration mitigation under oscillatory motion

Amin Jamalimehr[1†], Abdolhamid Akbarzadeh[2], and Damiano Pasini[1*]

[1]Department of Mechanical Engineering, McGill University, Montreal, QC, Canada

[2] Department of Bioresource Engineering, McGill University, Montreal, QC, Canada

[*] Corresponding author.

To be submitted

3.1 Introduction

Origami and kirigami, the ancient arts of folding and cutting paper, have recently spearheaded the design of a plethora of scale-invariant reconfigurable structures [1, 2] and materials [3, 4]. Their application ranges from robotic actuators [5-12], flexible electronics [13-15], thermally tunable structures [16], impact mitigation devices [17, 18], programmable surfaces [19-21], and deployable structures [22]. Origami and kirigami patterns have also been leveraged to develop mechanical metamaterials with unconventional properties, including reconfigurability [3, 22-24], flat-foldability [3, 22, 23], multistability [25-27], re-programmable materials [22, 28-33], and load-bearing capability [22, 34-37] among others.

Of emerging interest in origami-inspired metamaterials is the promise they offer for re-programming their response *in-situ*, i.e., post-fabrication [22, 28-32]. Both rigidly [3, 22, 23, 37-39] and non-rigidly foldable [25, 40-42] origami systems have been investigated to attain on the fly reprogrammable folding and response tuning. During folding, the former group reconfigures via hinge rotation of non-deformable panels only, whereas the latter group also through the flexure of their constituent faces. Folding and properties reprogrammability in metamaterials typically requires the application of an external stimulus, such as air pressure [43], thermal variation [44], light [45], magnetic field [9, 10, 12], or mechanical load [3, 22, 23, 25, 37-42], which allow reconfiguration changes and switch in distinct states, each with its own set of properties.

Of special interest to this work are strategies capable of preserving a given configuration upon removal of the external stimuli without permanent damage. Multistability is one - among others - effective strategy widely employed in origami metamaterials [25]. It is often leveraged to switch between at least two stable folding states that are separated by a significant energy barrier [25, 30]. Previous studies in origami metamaterials have successfully resorted to multistability to generate novel functionalities including locomotion [8, 9], deployability [1, 25, 46], shape shifting capability [42], response tunability of embedded in electronic devices [32, 47] and cushioning [48]. Yet not much has been so far accomplished in origami metamaterials to leverage the notion of multistable snapping for energy dissipation and vibration mitigation. Generating multistability-induced damping in metamaterials has important implications as it can offer sizeable advantages over conventional damping mechanisms, such as material viscoelasticity. The large displacement range a multistable metamaterial can attain provides freedom to reprogram on demand the damping response at values dictated by a given application and potentially beyond those offered by other conventional means of damping.

In this study, we build upon our previous work on rigidly foldable origami to present a generalized class of foldable metamaterials with void excisions that tap into cyclic multistable snapping to deliver mechanical damping and reprogram their energy dissipation performance. To this end, we relax the geometric restrictions of rigid body reconfigurability enforced on the primitive building blocks to enable compliant folding where the constitutive panels undergo monostable and multistable snapping to access a wide range of reconfigurations from flat-foldable to spatially locked. At the core of our multistable class of origami-inspired metamaterials stands the potential to switch from rigid-body to deformable-panel folding via snap-through instability, an outcome that broadens their geometric and reconfiguration space. This enrichment enables to tune *in-situ* a range of mechanical responses including the snapping-induced damping as well as the final configuration, which can be either flat-foldable for flat-packed storage and transportation with minimum space or spatially lockable for load-bearing applications.

3.2 Geometry of reconfigurable unit chain

To develop a reconfigurable kinematic unit, we present a generative process that starts from a primitive linkage made of a two-dimensional assembly of bars that can form any *N* even-sided convex parallelogon, beyond the regular polygon we previously investigated [22]. Figure 3-1A shows the process applied to a representative linkage of four bars (*N*=4) with sides a_1 and a_2 and interspacing angle α. From the central polygon, the edges in the *x*-*y* plane are extruded outward to preserve the lengths b_i and the angles of extrusion ϕ_i of opposite bars. The outcome is a set of four parallelograms connected at the vertices of the original quadrilateral. The gaps between parallelograms form triangular faces with interspacing angles defined by λ $(= \pi - \phi_1 + \phi_2)$ and $\lambda'(= \pi - \lambda)$.

The process above enables to generate a reconfigurable kinematic chain of panels that can rigidly fold along the edges of its mountain (M) and valley (V) triangles. To describe its geometry, we introduce three dimensionless independent parameters $\bar{a} = a_2/a_1$, $\bar{b}_1 = b_1/a_1$ and $\bar{b}_2 = b_2/a_1$, which we use along with other three independent parameters to denote the unit cell as $\mathrm{N}_4(\bar{a}, \alpha, \bar{b}_1, \bar{b}_2, \phi_1, \phi_2)$, where N_4 refers to the class of unit cells defined by a parallelogram void (Figure 3-1A and B), a generalization of our previous work. Complementary to the concept generation is the fabrication process which requires the excision of voids from a paperboard, the partial perforation of fold lines, and the face folding along crease lines yielding a three-dimensional reconfiguration.

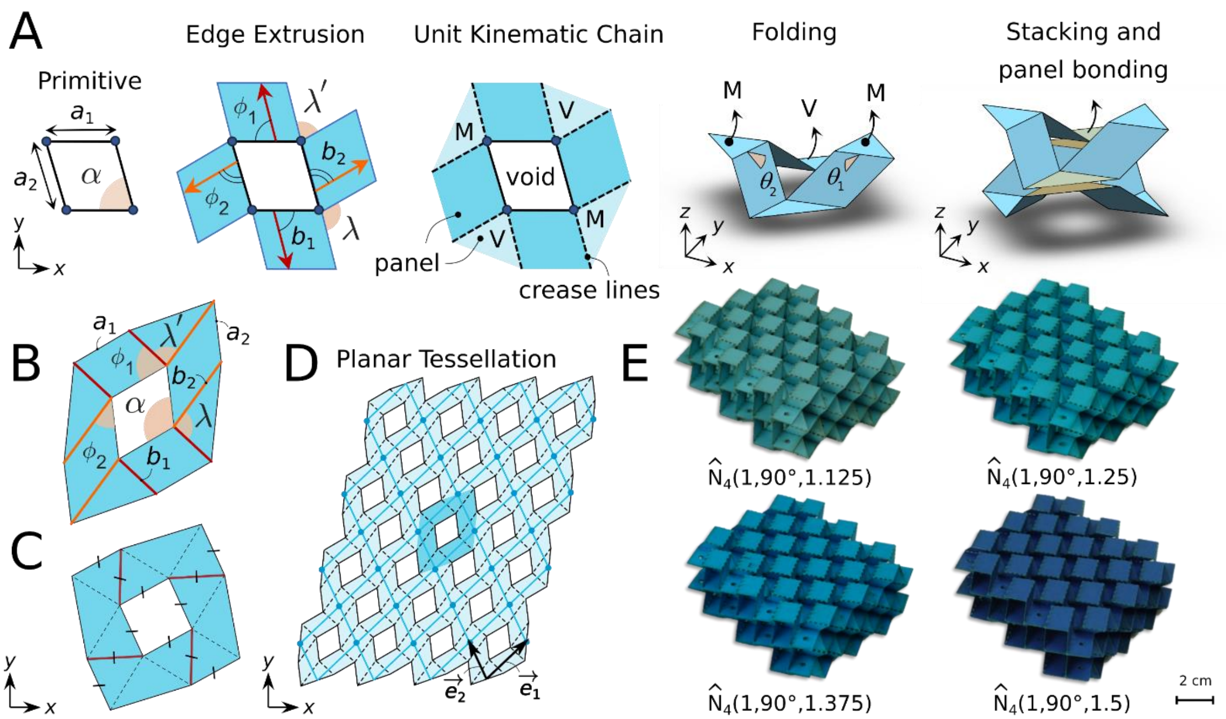

Figure 3-1 Quadrilateral based unit chain and origami-based metamaterial. **A** Conceptual process for generating a representative building block for a rigidly foldable metamaterial. Primitive regular polygon with non-orthogonal angles describing a four-bar linkage, followed by in-plane angled extrusion (red arrow of length b) of constitutive links; connection of extruded panels with triangular panels; addition of fold lines and assignment of a mountain (M) and valley (V). Unit chain reconfiguration upon folding and layer stacking of unit kinematic chain obtained by bonding valley triangular faces of the upper layer to the mountain triangular faces of the lower layer. **B** Visualization of $(\bar{a}, \alpha, \bar{b}_1, \bar{b}_2, \phi_1, \phi_2)$, the six independent geometric parameters defining the kinematic unit chain. **C** Unit kinematic chain with additional constraints: i) parallelograms assumed with shorter diagonal equal to their free edges; ii) free edges of extruded parallelograms around the central void assumed equal. **D** In-plane tessellation of N_4 kinematic unit chain with tessellation vectors, $\vec{e}_1$ and $\vec{e}_2$. **E** Paperboard proof-of-concept samples, each consisting of four layers bonded to the mountain face of an upper layer and connected to the valley face of a lower layer. Prototypes shown in their stable post-snapped configuration.

The generative process visualized in Figure 3-1A guarantees that the crease lines (orange and red lines in Figure 3-1B) are parallel, and the triangular faces (mountain and valley) remain planar during folding. As a result, multiple kinematic unit chains can be stacked along the *z* direction by bonding each mountain face of a bottom layer to its valley counterpart on the adjacent top layer.

While a single layer of a unit kinematic chain has multiple degrees of freedom, stacking multiple layers can reduce the degrees of freedom to one, hence generating a one DoF reconfigurable system [22].

Without losing generality and unless otherwise specified, we now assume the diagonal and the edges of the parallelograms around the central void are equal (Figure 3-1C), and reduce the number of independent geometric parameters to $\bar{a}$, α, and $\bar{b}$ $(= \bar{b}_1 = \bar{b}_2)$ hence simplifying our notation to $\widehat{\mathrm{N}}_n(\bar{a}, \alpha, \bar{b})$. Tessellating our unit in plane with respect to the periodic vector, $\vec{\mathrm{e}}_1$ and $\vec{\mathrm{e}}_2$ yields a periodic system, e.g., in Figure 3-1D, able to fold with its voids and panels through their rotation along its creases. Figure 3-1E depicts a demonstrative set of proof-of-concept specimens made of paperboard for four $\widehat{\mathrm{N}}_4$ patterns of given geometric parameters as indicated at the top of each of them. Each specimen consists of four layers, each bonded to the upper and the lower layer through their mountain and valley faces. While in this study we focus on patterns with translationally symmetric kinematic unit chain, other patterns beyond N_4 exist as explained in Section 3.9.1. In addition, the primitive parallelogon is not bound to be quadrilateral, as explained in Sections 3.9.2 and 3.9.3, for the cases with $N > 4$.

3.3 Rigid reconfigurability

The reconfiguration process of our origami systems involves both rigid and non-rigid folding, intrinsic characteristics defining their reconfiguration and studied now in-depth. The former is examined in this section and the latter in section 3. In our origami system, rigid reconfiguration denotes a process that folds our system through the crease lines only until a state where panels are in contact. In the following, we first explain the kinematics of folding with a snapshot at a given transition state, and then we focus on the final state, which in our system corresponds to the attainment of locking through panel contact.

3.3.1 Kinematics

To examine rigid foldability, we assume panels as infinitely rigid and fold lines as rotational hinges. Given the periodicity, we examine a representative unit cell N_4 (Figure 3-2A) where ① and ② refer to the directions of folding although the analysis reported here can be readily generalized to other patterns.

During reconfiguration from an initial fully developed configuration (Figure 3-2A), our unit folds into a transition state (Figure 3-2B), where the angle θ_1 and θ_2 assume a positive value. For N_4, two layers suffice to endow the system with one DoF [22] regardless of the values chosen for h_1 and h_2. Since layer stacking enables valley (or mountain) faces to remain in their initially flat plane, we can study rigid reconfigurability by analyzing the co-planar faces of adjacent layers. The distance between parallel faces, Δz, is governed by the dihedral angles, i.e., θ_i, and is given by

$$\Delta z = h_1 \sin\theta_1 = h_2 \sin\theta_2 = \cdots = h_i \sin\theta_{N/2} \quad (3\text{-}1)$$

For N_4, only θ_1 and θ_2 are necessary to describe the kinematics (Figure 3-2C and Figure 3-2D) as their values govern one kinematic path, among others, the unit cell follows during folding. Each path is described by a given relation between dihedral angles; for simplicity here, we simply characterize the paths through the relative values of h_1 and h_2. Generalizing the kinematic analysis above to patterns with $N > 4$ is straightforward and requires the inclusion of $N/2$ terms in Eq. (3-1). In the case of N_N, the reconfiguration landscape consists of $N-2$ kinematic paths in an $N/2$ dimensional space (see Section 3.9.2 for the case of N_6).

Case *I*: $\boldsymbol{h_1 = h_2}$

Figure 3-2C shows the possible paths that emerge by ensuring height equality, $h_1 = h_2$. From a flat configuration, i.e., point a ($\theta_1 = \theta_2 = 0$), our kinematic chain can fold along the branch I

($\theta_1 = \theta_2$) until $\theta_1 = \theta_2 = \pi/2$, point *c*. Here, it undergoes a kinematic bifurcation, where the number of degrees of freedom instantaneously increases from one to two [22]. Any of the branches *II*, *III*, and *IV* may represent the post-kinematic bifurcation path as determined by the relative magnitude of the applied forces [22].

Post bifurcation, the mechanism reverts to a single degree of freedom system [22] and follows either the kinematic path 1, $\theta_2 = \theta_1$, or the kinematic path 2, $\theta_2 = \pi - \theta_1$ (Figure 3-2C). Each of them has two branches, and switching between them is always possible through their intersection point, the bifurcation pass, hence ensuring continuity in the kinematic path.

Case *II*: $\boldsymbol{h_1 \neq h_2}$

Without losing the generality, we examine the case $h_1 < h_2$. In contrast to the previous case, here the kinematic landscape consists of two non-intersecting kinematic paths showing mutual discontinuity (Figure 3-2D). From an initially flat state, point *a*, the unit cell reconfigures along the kinematic path 1 for increasing folding angle θ_1. Point *g* is a representative transition state in the reconfiguration process which continues until point *h*, where the panels, P_1 and P_3 (Figure 3-2B), become perpendicular to the central parallelogram, C. Point *h* (Figure 3-2D) is a limiting configuration that connects branch 1 and branch 2 of the kinematic path 1. Folding along branch 2 requires a decrease in θ_2 for an increasing θ_1.

Besides the kinematic path 1, Eq. (3-1) admits another solution. If ($\theta_1^* < 90°$, θ_2^*) are a pair of solution, (θ_1^*, $\pi - \theta_2^*$) also satisfies Eq. (3-1). This explains the existence of a second kinematic path, which also encompasses two branches sharing the critical point *k*, Figure 3-2D. In this case, a switch between kinematic paths through the trajectory *h-k* is no longer possible under the rigid foldability assumption. The jump *h-k* becomes admissible only if the panels are admitted deforming, as explained in Section 3.4.

While the kinematic paths in Figure 3-2C and Figure 3-2D visualize the relation of the dihedral angles, θ_i, at a transition state during reconfiguration, the final state of our unit cell is not captured in those maps. The final configuration the unit cell reaches at the end of the folding process, can be either locked or flat-foldable. The former is determined by contact between faces in an intermediate point along the kinematic path. The latter appears if at least one θ_i is π (see Section 3.9.4).

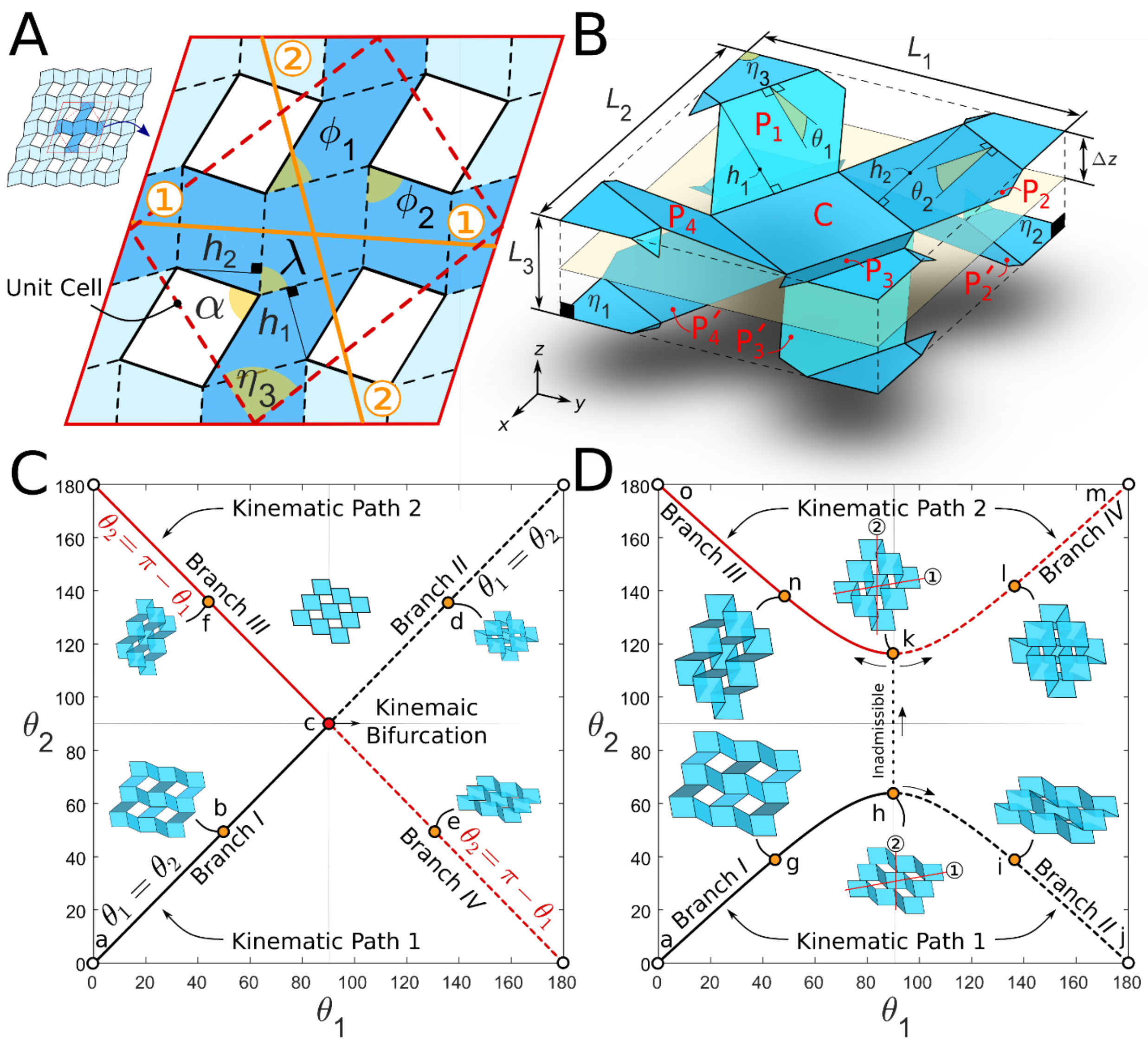

Figure 3-2 **A** Top view of an $N_4(0.8, 103^\circ, 1, 0.95, 45^\circ, 75^\circ)$ pattern with its governing geometric parameters; red dash line denotes unit cell boundary, orange lines describe folding directions. **B** Three-

dimensional unit cell in a representative transition state with its main reconfiguration parameters, red letters denote panels above and below (with superscript) the yellow horizontal plane. **C** Kinematic path landscape for $h_1 = h_2$. Dash lines emphasize the existence of two branches on each kinematic path. Intermediate points, b, d, e, f, in orange describe representative transition states. Terminal points in white correspond to flat-foldable configurations, and kinematic bifurcation point in red enable continuous switch between paths. **D** Kinematic path landscape for $h_1 \neq h_2$ and plotted for demonstrative value $h_1/h_2 = 0.9$. Representative paths are non-intersecting. Other values of h_1/h_2 generates similar kinematic landscape consisting of two branches transitioning at configuration points h and k.

The rigid reconfiguration of N_4 can be described as a mapping from the initial unit cell shown in Figure 3-2B to the final configuration. The energy stored in the hinges can be interpreted as the internal energy resisting further deformation enabling pattern reconfiguration. As a result, an energy function can be used to correlate the deformation and the external forces acting on the boundaries of the unit cell (see Section 3.9.5 for the formulation of the smooth rigid reconfiguration of the N_4 pattern)

3.4 Non-rigid reconfigurability in single snapping unit

A rigid foldable origami unit with $h_1 \neq h_2$ is intrinsically unable to switch its kinematic path due to the non-intersecting nature of its paths, 1 and 2. One way to make the path switch admissible is to relax the assumption of panel rigidity and consider deformable panels. Here we study the deformation of a reconfigurable unit and examine its most representative and smallest portion (Figure 3-3A). This consists of two layers where P_i refers to the panels of the top layer, and P_i' (with the prime sign) denotes those on the bottom layer. Since the panels are compliant, the unit cell panels can deform and snap following a distinct mechanism as described below.

The behavior of our compliant reconfigurable unit is investigated through a large set of simulations (see Sections 3.9.6 and 3.9.7) and experiments (Section 3.9.11). Key conditions we enforce on both the model and physical prototypes we built are on the degrees of freedom of each panel. In our computational model, the faces P_2 and P_2' can move in a direction perpendicular to their face, i.e., z direction, and all their rotational DoFs are fixed. Face P_1 can move in the y direction, while the rotational DoFs are constrained. Face P_3 is free to move. Similarly, in our experiment (Figure 3-3B) we replicate the boundary conditions of our model. To do so, the faces P_4 and P'_4 are screwed to very stiff panels made of acrylic plate and mounted on a slider that can move only in the $\pm z$ direction. The face P_5 is screwed between two stiff acrylic panels. The upper platen is attached to the upper grip of our tensile tester (Instron 6800 series) while the lower plate is fixed to the lower grip (see Section 3.9.14 for additional information.)

Figure 3-3C compares the experiment and finite element results of the force-displacement behavior of a single snap unit, and Figure 3-3D shows the corresponding snapshots. In Figure 3-3C, the force, F, normalized by F_{cr}, is the critical buckling force of a square panel hinged along two opposite edges and free along the other two; Δy is the displacement of the upper platen, normalized by the length of the hinge b_1. F_{cr}, is given by

$$F_{cr} = \frac{\pi^2 E t^3}{12(1-\nu^2)b_1} \tag{3-2}$$

where E and ν are the Young's modulus and Poisson's ratio of the material. B and t, respectively, represent the side and the thickness of the panel.

Starting from the initial configuration, point a (Figure 3-3C and Figure 3-3D), the unit undergoes rigid folding up to point b. At this stage, due to the difference between h_1 and h_2, rigid folding is no longer possible, and what we observe is a hardening of the response from point b to point c. While P_5 and P'_5 are in compression, P_4 and P_4' undergo tensile forces. At point c, the structure withstands the maximum load, beyond which P_2 and P'_2 undergo a mechanical instability leading to the snap-through of the whole origami specimen. This is visualized in Figure 3-3C by the negative value of the incremental stiffness from c to e. During instability, the tensile forces in P_4

and P'_4 and the compressive forces in P_5 and P'_5 are released, and the reconfigurable unit reverts to a rigid folding mode from point e to point f. At point f, P_2 and P'_2 come into contact with P_3 and P'_3 leading to a sharp rise in the force-displacement curve. After contact, the reaction force continues to increase. When the loading cycle is completed through the unloading process, we observe the loading and unloading curves do not coincide resulting in a net dissipation of energy mainly due to the viscoelastic behavior of the hinges and the friction generated by the sliders and the rail.

Figure 3-3E provides a qualitative representation of the loading curve of our origami unit with the main descriptors of the snap-through therein specified: the maximum and minimum force (red points) as well as the energy contributions (shaded domains). $F_{\max}$ is the peak force required to generate instability in the forward direction, and $F_{\min}$ can be interpreted as the peak force required to generate instability in the reverse direction (backward instability) in an ideal dissipative-free scenario. E_{snap} is the energy required to initiate elastic instability in the panels, while E_{in} is the work exerted by the external force to shift the structure to its second stable State. E_{out} is the energy released during the snap-through instability; it can also be interpreted as the energy barrier in the reverse direction. In an ideal scenario of snap-through instability, $E_{in} = E_{out}$, an equality indicating that the energy barrier in the forward and backward instability (Figure 3-3D) does not change.

The metrics in Figure 3-3E become now handy to define regimes of post-snap contact deformation, each describing a modality of panel contact. The emergence of a given regime is governed by the values assumed by the main governing parameters, $\bar{a}$, i.e. the normalized primitive void size, and, $\bar{b}$, the normalized extrusion length of the origami unit (Figure 3-1A). We can identify four post-snap contact regimes of deformation, each visualized in Figure 3-3F-I for a representative unit cell of prescribed $\bar{a}$ and $\bar{b}$. For comparative purposes, we also plot the response of a hypothetical contact-free model (dash lines), here used as baseline.

- Figure 3-3F depicts the first scenario where contact is established prior to instability. The subset of Figure 3-3F shows that the panel P_2 and P_2' deform significantly and come into contact before their instability takes place. Compared to the contact free model (dash line in Figure 3-3F), here we observe that contact influences the magnitude of the maximum load, $F_{\max}$, that the unit can attain (red point). This is due to contact between P_2 and P_2', a phenomenon that restricts their flexural deformation and hence stiffens the structural response of the unit; as a result, a larger peak force is required to trigger elastic instability. As our unit undergoes snap-through, the contact area between P_2 and P_2' reduces until a new point of contact is formed between another pair of panels, i.e., P_2 with P_3, and P_2' with P_3' (Figure 3-3A)), denoted with the white point on the downward portion of the curve between the red circles. Again, this contact - newly formed during instability - limits the release of flexural deformation from P_2 and P_2'. As a result, the absolute value of the minimum force, $F_{\min}$, for instability (red point with negative force value) is larger than the contact free model. As per the energy contributions, we also observe that the contact between faces poses a higher energy demand to trigger instability in both (forward and backward) directions (Figure 3-3D).
- Figure 3-3G describes the second case where contact is formed during snap-through instability. Here, the flexural deformation of P_2 and P_2' during instability is sufficiently large to allow contact between P_2 (and P_2') and P_3 (and P_3'). Similar to the deformation mechanism shown in Figure 3-3F, also here a higher magnitude of the minimum force of instability, $F_{\min}$, is required than the contact free model. As a result, in the backward

loading cycle, the peak load, $F_{\min}$, and the energy required for backward instability, E_{out}, are higher. In this case, however, the load required for the forward instability, $F_{\max}$, and the input energy of instability, E_{in}, are identical to those of the contact free model.

- Figure 3-3H shows the third regime, characterized by a post-snap contact that occurs with an applied force at a negative value during the loading cycle. Contact here forms first between P_2 (and P_2') and P_3 (and P_3'), followed by contact between the edges of P_5 and P_7.(Figure 3-3A). Establishing contact in this regime reduces the energy released during the snap-through instability, E_{out}, compared to the ideal contact-free case. As a result, the backward snap-through instability requires lower energy than the contact free case.
- Figure 3-3I depicts the case where contact occurs in the post-snap response at a positive force value. Here, the sequence of contact is similar to the previous regime, first between panels P_2 (and P_2') (see the onset of contact in inset) and P_3 (and P_3') and then between the edges of P_5 and P_7 (Figure 3-3A). In this regime, the response diverges from that of the contact free model only in the post contact portion of the force displacement curve, yielding a sharp increase of stiffness. As a result, contact has no influence on the metrics defined in Figure 3-3D.

We now explore the role played by the characteristic parameters $\bar{a}$ and $\bar{b}$ in the four contact regimes each described by a characteristic force-displacement curve (Figure 3-3F-I). To do so, we sweep $\bar{a}$ and $\bar{b}$ in a selected portion of the design space ($0.7 < \bar{a} < 1.1$ and $1< \bar{b} <1.25$) for prescribed θ_2, and discuss the changes in the force and energy metrics, $F_{\max}$, $F_{\min}$, E_{in}, E_{out}, E_{snap}, defined in Figure 3-3E. Each map in Figure 3-3J-O shows the emergence of five regions enclosed by red boundaries, four corresponding to the contact regimes and the fifth indicating a geometrically unattainable region (grey) for the given value of θ_2 here assumed. A difference in shading of the full colors denotes whether contact takes place in a given zone, whereas the semitransparent shading indicates that a given contact regime cannot be attained for the corresponding range of parameters, $\bar{a}$ and $\bar{b}$, yet the metrics are plotted to provide the comparison baseline of the contact-free case.

The map in Figure 3-3J plots the intensity of F_{max} over F_{cr}, a metric that denotes the highest force our unit can withstand prior to snap-through instability. This is the contact regime 1 shown in Figure 3-3F for a representative unit of given $\bar{a}$ and $\bar{b}$. This regime describes contact preceding instability; it can be accessed by a range of values $\bar{a}$ and $\bar{b}$, which delineate the corresponding region 1 in Figure 3-3J. Within this region, F_{max} is inversely proportional to $\bar{a}$. The lower $\bar{a}$, the higher the maximum load of instability, a behaviour governed by the effective buckling length of P_2 or P_2', i.e., the smaller panel dimension, undergoing buckling. On the other hand, F_{max} is in direct correlation with $\bar{b}$. For given $\bar{a}$, the higher $\bar{b}$, the larger the maximum force required for snap-through due to the increasing difference between h_1 and h_2.

Similarly to Figure 3-3J, in the parameter space $\bar{a}$ versus $\bar{b}$, Figure 3-3K maps the absolute value of the minimum force of instability $|F_{min}|$ over F_{cr}. Since Figs 3F and 3G show that contact can take place either prior (regime 1) or post (regime 2) snap-through instability for given values $\bar{a}$ and $\bar{b}$, Figure 3-3K shows that a range of $\bar{a}$ and $\bar{b}$ can also attain those regimes as visualized by their corresponding regions 1 and 2. Compared to the free- contact model, the higher value of $|F_{min}|$ indicates that in a reverse loading cycle the peak load for the onset of instability is higher. This is not only valid in ideal conditions where there is no energy dissipation, e.g., the viscoelasticity of the hinge material and/or friction between rails and sliders are not considered, but it also provides a reasonable estimate of a real sample response where viscous and/or frictional effects are present. As with F_{max}, F_{min} shows a similar dependence on $\bar{a}$ and $\bar{b}$. A decrease of $\bar{a}$ results in a larger force required to initiate instability in the reverse loading cycle due to the length reduction of panel

P_2 or P_2' undergoing buckling. Similarly, for increasing $\bar{b}$, the difference of panel heights, h_1 and h_2, raises and hence culminates in an increase of $|F_{\min}|$.

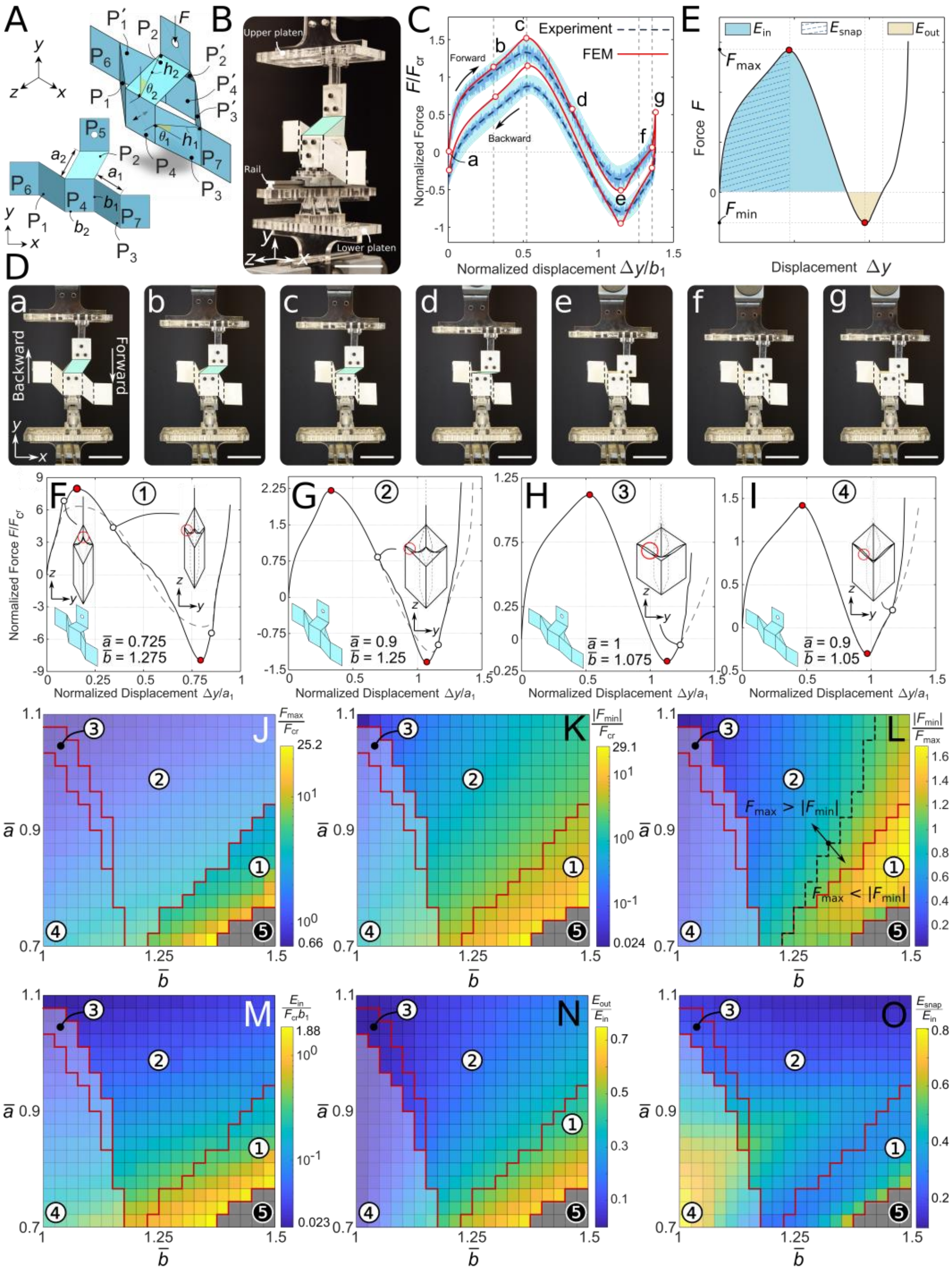

Figure 3-3 Deformation based reconfigurations of single snap units. **A** Geometry of a single snap unit. **B** Experimental setup consisting of upper and lower platens, respectively fastened to upper and lower grippers of tensile tester. A pair of stiff plates connect face P_5 to upper platen. P_4 and P_4' are screwed to sliders that allow translation motion on a rail mounted on the lower platen. **C** Experimental (dash line) and finite

element analysis (red solid line) of a single snap unit with representative values $\bar{a} = 1$ and $\bar{b} = 1.125$. Shaded area visualizes the envelope of the dispersion curve. Representative points a to g along loading cycle correspond to reconfiguration snapshots in **Fig 3D**. **D** Front view configurations of single snap unit during loading corresponding to points in the loading curve in **Fig 3C**. Dash lines specify creases, i.e. rotational hinges. Shaded blue panel represents P_2 face. Scale bar: 40 mm. **E** Definition of characteristic metrics, i.e., energies and forces during loading, used to specify the four contact regimes. **F-I** Four representative load displacement curves (continuous line) obtained for given values of $\bar{a}$ and $\bar{b}$, each corresponding to a contact regime of deformation. Contact-free response (dash line) shown for baseline comparison. Red dots correspond to absolute load peak values. Onset of contact visualized as white circles, each referring to an *x-z* view (inset) of the contact event of specific panels. **J-O** Design maps exploring the role of geometric parameters $\bar{a}$ and $\bar{b}$ ($\bar{a}$ from 0.7 to 1.1 and $\bar{b}$ from 1 to 1.5.). Light shading designates regions where contact does not play a role. Dash black line in **J-L** corresponds to boundary of regions between $F_{max}>|F_{min}|$ and $F_{max}<|F_{min}|$. Characteristic forces in **J-K** are normalized with respect to the critical buckling load of a square panel hinged along two edges and free along the other two, i.e., $F_{cr} = \pi^2 E t^3/12(1-\nu^2) b_1$ where b_1 is the side of the panel. Each number is representative of a region presented in maps **J-O**. **M-O** Characteristic energies on the loading curve. Dash black line in **N** indicates $E_{in}=E_{max}$, separating regions with $E_{in}> E_{out}$ and $E_{in}< E_{out}$.

Given contact plays a role in both F_{max} and F_{min} as shown in Figure 3-3J and Figure 3-3K, we can compare the peak load of instability in the forward and backward loading cycles. This is achieved by plotting the ratio $|F_{min}|/F_{max}$ as shown in Figure 3-3L. The results in this map are valuable for differentiating and tailoring the peak force for the forward and backward bistability in the reconfigurable unit. $|F_{min}|/F_{max}=1$ is the boundary threshold (black dash line) that splits domain 2 into two regions, where the peak force ratio is either above or below 1. The emergence of the boundary in domain 2 attests that contact between P_2 and P_3, as well P_2' and P_3', plays a major role in controlling $|F_{min}|/F_{max}$. For lower values of $\bar{b}$, contact between P_2 and P_3 (also P_2' and P_3') occurs close to the end of the instability process, downward portion of the load history. As a result, its contribution to $|F_{min}|$ is low. On the other hand, for larger $\bar{b}$, contact takes place at the early stage of instability. As shown in the right-hand side inset of Figure 3-3F, P_2 and also P_2' undergo a large flexural deflection along a span smaller than their height, h_2, hence leading to an increase in $|F_{min}|$.

Similar to the force-metrics maps (Figure 3-3J to Figure 3-3L), we can explore the role of $\bar{a}$ and $\bar{b}$ on the energetic fronts. Figure 3-3M shows an example, where the energy released during snap-through instability, E_{in}, normalized by $F_{cr}b_1$ is mapped for varying $\bar{a}$ and $\bar{b}$. E_{in} can capture not only the influence of F_{max} but also that of the displacement required to switch the unit from one stable configuration to the other. Since contact can occur prior and during snap-through instability, as depicted by regime 1 and 2 in Figure 3-3F and Figure 3-3G, there exists a range of parameters for $\bar{a}$ and $\bar{b}$ that can give rise to those regimes. These are respectively visualized by the regions 1 and 2 in Figure 3-3M. We can draw similar insights to those gained in the discussion of the force-metrics map, where here there is an inverse relation between E_{in} and $\bar{a}$, as opposed to between E_{in} and $\bar{b}$.

Figure 3-3N maps the ratio E_{out}/E_{in} in the parameter space $\bar{a}$ versus $\bar{b}$. We recall that E_{out} (Figure 3-3E) is the energy required to trigger instability in the reverse loading cycle in the absence of energy dissipation. In this ideal case, there is no change in the energy barrier, i.e. $E_{out}/E_{in}=1$, between the forward and backward loading cycle. In practice, however, there are mainly three factors contributing to the deviation from the ideal case. First, during the forward loading cycle, the creases due to their rotational stiffness of the hinges store a moment that resists the rotation of the faces about their common hinge. This moment is released in the backward cycle, making E_{out} significantly lower than E_{in}. Another factor is the contact between faces during snap-through instability. As shown in the load-displacement curves of Figure 3-3F and Figure 3-3G, contact limits the span of P_2 and P_2' that undergo buckling. This process increases the minimum force of instability and the displacement of snap-through instability leading to an increase in E_{out}. The three regimes in Figure 3-3F, G and H obtained for given values of a and b can be attained by a range of a and b parameters which define their corresponding regions 1, 2, and 3 in Figure 3-3N. E_{out} increases inversely with $\bar{a}$ and directly with $\bar{b}$. The third factor that contributes to the deviation of response from the ideal case is the existence of dissipative elements, such as viscous damping in the hinges and frictional damping in the sliders.

Finally, Figure 3-3O maps the ratio E_{snap}/E_{out} where E_{snap} is the energy required to generate buckling in the forward loading cycle. This metric is important because by comparing Figure 3-3N and Figure 3-3O, we observe that the maximum value of E_{out}/E_{in} does not coincide with the maximum of E_{snap}/E_{out}. Reconfigurable units with large $\bar{a}$ and $\bar{b}$ therefore require, on one hand, a small amount of energy to undergo buckling, E_{snap}, in P_2 and P_2' (top right corner of Figure 3-3N), and, on the other hand, a large displacement to undergo snap-through instability.

3.5 Interacting snapping units

The snapping behavior of a single unit can differ from the response explained in the previous section if the panels of more units start to interact during reconfiguration. This section studies the role of two representative units whose snapping interaction brings multiple points of their panels into contact. Here our analysis combining experiments and numerical simulations focuses on the unit geometric parameters governing the snapping interaction.

Figure 3-4A shows a representative specimen consisting of two snapping units that interact during reconfiguration. Similar to the single snapping unit, the specimen comprises two layers bonded in series at selected horizontal faces, i.e., P_5 to P_7 and P_9. Circular holes are embedded in faces P_5 and P_9 to mount and brace the specimen on the testing apparatus shown in Figure 3-4B. This experimental setup consists of an upper and a lower platen fastened, respectively, to the upper and lower grippers of the tensile tester (see Section 3.9.14). The force-displacement curve during a forward/reverse cycle is illustrated in Figure 3-4C from results obtained via experiments (dash line) and finite element analysis (solid line). The former parallels the latter with a reasonable level of accuracy. Deviations exist and can be attributed to multiple factors including sample imperfections, mounting-specimen misalignment, friction in the bearings, and assumptions behind the simplified model of the hinges (see Sections 3.9.6 and 3.9.10). The stable configurations during the forward (global compression) and reverse (global tension) loading cycles are identified with green and yellow dots at the intersections of the load-displacement curve with the horizonal axis. Between stable configurations, the specimen undergoes a sequence of deformations, which we track in Figure 3-4D and plot as sample snapshots, *a* to *i*, corresponding to their respective points in Figure 3-4C. These snapshots help gaining insights into the evolution of the snapping events between interacting panels as described below.

From the initial configuration (Figure 3-4D(a)), the forward loading cycle moves the upper platen of the testing setup downward and induces the rotation of the faces P_2 and P_2' as well as P_8 and P_8' about their shared hinges with P_4 and P_4' (Figure 3-4D(b). The governing mechanism in this intermediate configuration is mainly controlled by panel rotation. Upon further compression (point c), the panels not only rotate but also start to deform, hence generating a pseudo-hardening response with an increase in the slope of the loading curve (Figure 3-4C). At this stage, the pairs of panels P_2 and P_2', and P_8 and P_8', undergo compression, whereas the other two pairs, P_1 and P_1', and P_3 and P_3', are under tension, a phenomenon caused by the difference in height of the parallelogram faces surrounding the central panels P_4 and P_4'. The slope in the stiffening region from point c to point d reaches a maximum that corresponds to the apparent stiffness of the first snap-through instability, k_1 shown in Figure 3-2E.

At point d (Figure 3-4C and Figure 3-4D(d)), the elastic panels P_8 and P_8' buckle, and a snap-through instability from point d to point f follows, with point e (also shown in Figure 3-4D(e)) denoting a representative configuration of the snap-through. Upon advancing the forward loading cycle, the load-displacement curve from point f onwards exhibits a steep increase, which is caused by a load reversal in panels P_8 and P_8', i.e., the forces in the faces P_8 and P_8' switch from compression to tension. An additional loading compresses the faces P_2 and P_2' further, as opposed to P_1 (also P_1') and P_3 (also P_3') which are in tension. The compression increase culminates at point g with the elastic buckling of P_2 and P_2' (also shown in Figure 3-4D(g)), followed in turn by a second snap-through instability, this time undergone by the pair of panels P_2 and P_2'. The specimen reaches the minimum load of the second instability in the forward loading cycle at point h, after which any further loading results mainly in panel rotation of P_2 (and P_2') and P_8 (and P_8') about their common hinges with P_4 and P_4'. This reconfiguration continues until the pairs of faces P_2-P_2', P_3-P_3', P_1-P_1', and P_8-P_8' come into contact leading to a sharp increase in the load-displacement curve (point i shown in Figure 3-4 D(i)).

Upon a reversal of the loading cycle, the specimen response travels along a similar path (Figure 3-4E), which is down-shifted from the forward counterpart due to energy dissipation, and it is also characterized by two snap-through events. In our case, the temporal order of snap-through instability is retained between the forward and backward loading cycle, i.e., the pair of facesP_8 and $P_{8'}$, undergoing first snap-through instability in the forward loading cycle, is also the first in the reverse loading cycle followed by the other pair, faces P_2 and P_2'. Figure 3-4E is a qualitative representation of the loading/unloading curve of a pair of interacting units with the main descriptors of the snap-through interaction therein specified, i.e., the maximum forces in the forward and backward loading cycles (F_i and $\bar{F_i}$), the minimum forces of instability (f_i and $\bar{f_i}$), the apparent stiffness of snap-through instabilities (k_1 and k_2) as well as the dissipated energy (cyan) in the loading cycle (E_{diss}) due to the viscous damping of the hinges.

One interesting observation we can draw from the loading cycle in Figure 3-4C is that the stiffness and the maximum force corresponding to the second instability are noticeably larger than their counterparts corresponding to the first instability. This phenomenon appears regardless of the loading type, either tensile or compressive. To explain the root cause of this response, we to track the evolution of the reconfiguration process from the side view, i.e., *y-z* plane, as shown in Figure 3-4F, which enables to monitor the specimen folding from the initial state (Figure 3-4F(a)) onwards. As the upper platen is moved downward (Figure 3-4F(b)), P_2 and P_2' as well as P_8 and P_8' rotate about their common hinges with P_4. As the forward loading cycle proceeds, prior to the first instability we can measure the angle between faces P_2 and P_2' (as well as P_8 and P_8') (Figure 3-4F(c)), which is 144˚ as opposed to 114˚ (Figure 3-4F(d)), the angle preceding the second instability. The underlying physics for the angle change can be understood by inspecting the reconfiguration sequence in Figure 3-4D. The first snap-through instability causes a drop in the reaction force, which in turn releases the moment stored in the common hinges of P_1 (P_1'), P_2 (P_2') and P_3 (P_3') with P_4 (P_4'). As shown in Figure 3-4D(f) the decrease in the reaction force culminates in the displacement of P_6 and P_7 in the -*x* and +*x* directions respectively.

As the upper platen continues to move downward, the reaction force increases as shown in Figure 3-4C. As a result, faces P_1 (also P_1') and P_3 (also P_3') further rotate around the hinges they share with P_4 and P_4'. During this reconfiguration, faces P_8 and P_8' come into contact with faces P_1 and P_1' (Figure 3-4D(e)), and the contact between these pairs restricts further the rotation of P_1 and P_1', hence limiting the rigid body reconfiguration. This panel interaction leads P_2 (and P_2') to buckle (Figure 3-4D(f)). The panels buckled in a way that is not unique and lead to distinct configurations. To compare the difference in panel configuration between the two buckling events, we can monitor the angle formed between P_2 (also P_2') and P_8 (also P_8') prior to the onset of the first (144˚ in Figure 3-4F(c), and the second buckling, (114˚ in Figure 3-4F(d) In the former case, P_2 and P_2'

undergo instability as in a von Mises truss at a more acute angle than in the second case, hence explaining the larger force required for the second instability.

To better understand the role of snapping interaction in a single snap-through unit (Figure 3-3A) and in two interacting snap-through units (Figure 3-4A), we now compare the energy barriers required to trigger their snap-through instability. Before analyzing both the forward and reverse loading cycles, we first define the characteristic energies in Figure 3-4G, a qualitative plot of the loading/unloading curve for a pair of interacting units in the forward cycle (blue) and backward cycle (yellow). E_{in}^{i} is the energy required to cause snap-through instability where the superscript denotes the order of instabilities, where *i*=1 is for a single snap-through unit and *i*=2 for two interacting snap-through units. E_{out}^{i} is the energy released in each event of instability. An overbar denotes the corresponding characteristic energies in the reverse loading, highlighting the dominant role of displacement and the reduced energy requirement for the second snapping in the two snapping units.

As per the reverse loading cycle (yellow in Figure 3-4G), the energy contributions resemble those of the forward cycle (blue), but in a reversed order and with a downward shift due to the dissipated energy. Here $\bar{E}_{in}$ and $\bar{E}_{out}$ account for the stored moment in the elastic hinges which are now released during the snap-through instability in the reverse loading cycle. For this reason, Figure 3-4H shows a lower energy requirement to trigger instability in the reverse cycle $\bar{E}_{in}^{i}$, than in the forward loading cycle. Moreover, the energy required to cause snap-through instability in the reverse cycle is smaller in the specimen comprising two interacting units compared to its counterpart in a single snap unit; this is because two interacting units have stored larger moments in their hinges prior to undergo bistable snapping in the reverse cycle. As a result, two snapping units release more energy than one single snapping unit during the reverse cycle, i.e., $\bar{E}_{out}^{i} > E_{out}^{i}$.

Furthermore, Figure 3-4H shows that a pair of two interacting units can dissipate five times the energy of a single snapping unit. This phenomenon can be mainly attributed to the difference between E_{in}^{i} and $\bar{E}_{out}^{i}$,and can be leveraged to generate a reconfigurable metamaterial with remarkable dissipative response. This is demonstrated in the next section where a tessellated assembly (in series) of interacting snapping units, i.e., a foldable origami-inspired dissipator, can boost energy dissipation through a cyclic sequence of snapping events occurring in the forward and backward loading paths.

3.6 From unit cell to periodic metamaterial system

With the insights gained above, we now examine the role of panel interaction in a periodic metamaterial consisting of multiple units. For demonstration purposes, we consider a 5×5 units system with two stacked layers and dimensions $\bar{a} = 1.125$ and $\bar{b} = 1$; we experimentally and computationally investigate the response of a set of proof-of-concept prototypes under compression and tension. As shown in Figure 3-5A, the faces of the interface of the two layers on the plane of the material symmetry are attached to sliders that can freely move along the *x* axis. The rail is attached to a platen fastened to the gripper of our tensile tester, and the middle slider at the bottom is fixed to prevent the rigid body movement of the specimen. We also examine to role of the clamp inclination onto the specimen response by comparing a sample mounted at a given angle (Figure 3-5B) with one mounted parallel (Figure 3-5C) to the sliders.

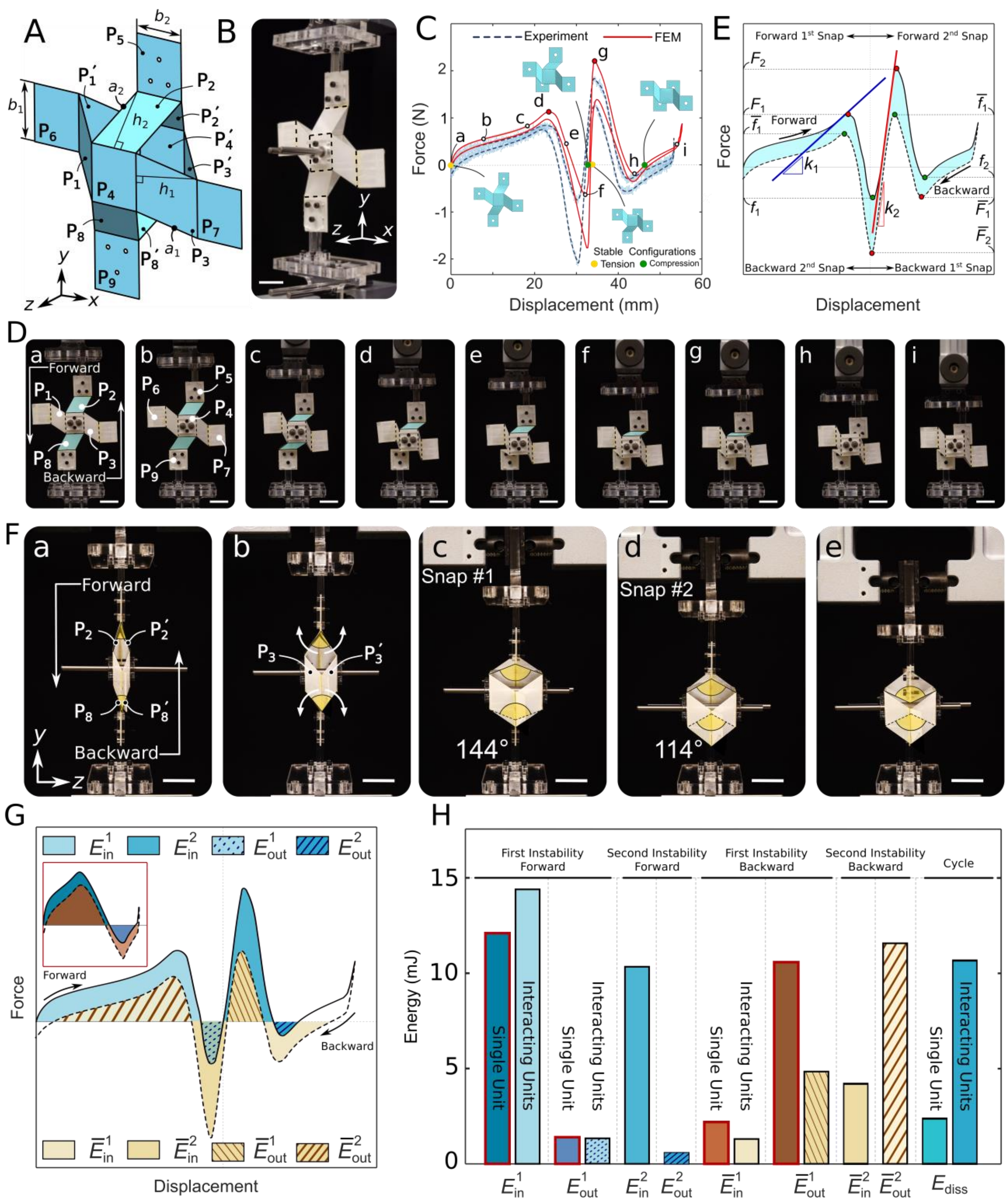

Figure 3-4 Interaction of two snapping units. **A** Geometry of a specimen with two interacting units undergoing bistable snap-through instability. **B** Experimental setup consisting of upper and lower platens, respectively fastened to upper and lower grippers of tensile tester. A pair of stiff plates connect face P_5 and P_9 respectively to upper and lower platens. A pair of stiff faces are screwed to faces P_4 and P_4', which carry two bearings (See Section 3.9.12). A pair of bars run through the bearings on P_4 and P_4', which prevent the rotation of face P_4 and P_4' about the *x* axis. **C** Experimental (dash line) and finite element analysis (red solid

line) of a single snap unit with prescribed values $\bar{a} = 1$ and $\bar{b} = 1.125$. Representative points (a) to (i) along the loading cycle correspond to reconfiguration snapshots in **Fig 4D**. Green/Yellow dots indicate stable configurations in forward/reverse loading directions, respectively. **D** Front view configurations of the single snap unit during loading correspond to the points in the loading curve in **Fig 4C**. Dash lines specify the creases, i.e., rotational hinges. Shaded blue panel represents P_2 and P_8 faces. Scale bar: 20 mm. **E** Definition of characteristic metrics, i.e., forces and stiffnesses during loading cycle. Shaded blue region represents dissipated energy during loading cycle. **F** Side view of reconfiguration process of two snapping units during loading corresponding to points on the loading curve of **C**. Scale bar: 20 mm. **G** Definition of characteristic metrics, i.e., energies during forward and reverse loading directions for single snap unit (inset) and interacting units. **H** Comparison of characteristic energies between a single snap unit and two interacting units in a loading cycle obtained from finite element analysis. Red border denotes the corresponding metrics for the single snap unit. (See Section 3.9.8 for comparison of experimental results and finite element simulations).

Figure 3-5B shows the load-displacement curve with the corresponding snapshots in Figure 3-5A of a sample mounted at a given angle with the sliders. From the response, we observe four events of snap-through instability, a number that equals the number of rows containing voids in the initial origami system, where a 5×5 in plane tessellation contains 4×4 voids. Given here panel interaction takes place among multiple units, the periodic metamaterial response resembles the mechanism observed in two interacting units (previous section), but the cumulative effect is here even more pronounced. The tangential stiffness increases with the specimen displacement and the peak force corresponding to snap-through amplifies at the snapping of each row of voids. As explained in the previous section, one reason for the peak force magnification can be attributed to the interaction and sequence of snapping events, each occurring at an increasingly acute angle between the inclined faces of a pair of snapping units. Another reason is the panel entanglement observed under tension during the unit cell reconfiguration, a phenomenon that reduces the acute angle between the inclined faces in the last snapping row of the specimen.

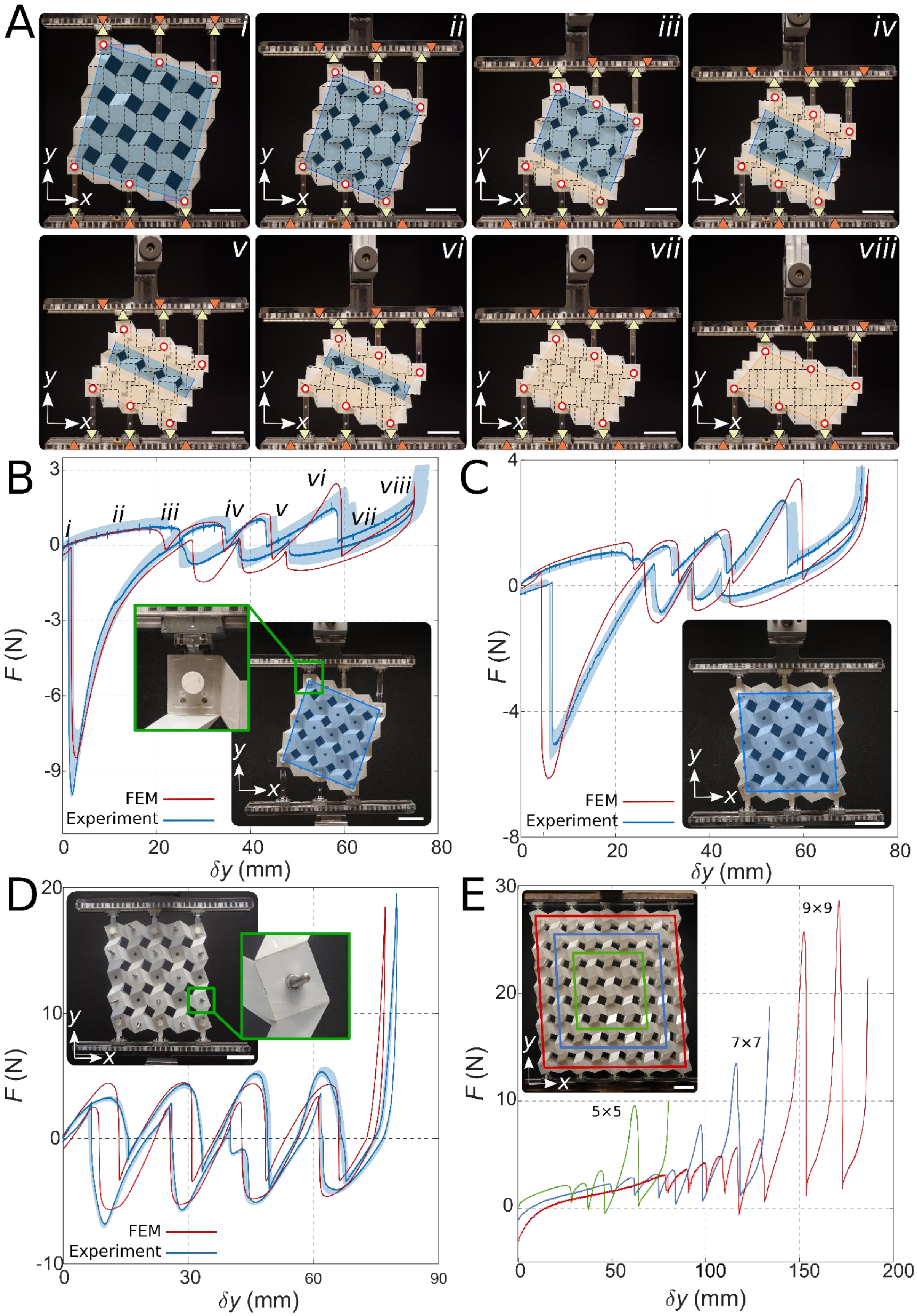

A
i
ii
iii
iv
v
vi
vii
viii
B
C
D
E
FEM
Experiment
F (N)
δy (mm)
5×5
7×7
9×9

Figure 3-5 Reconfiguration process of a bilayer 5×5 multi-cell metamaterial **A** $\widehat{N}_4(1{,}90^{\circ}, 1.125)$ with aligned mounting. Orange and yellow triangles denote respectively initial and instant locations of the sliders from (*i*) to (*vii*). Pre- and post-snap units highlighted respectively in blue and pale brown. Red circles indicate the pinned position of the panel-connectors. Scale bars = 40 mm. **B** Comparison between experimental and finite element analysis results for a 5×5 $\widehat{N}_4(1{,}90^{\circ}, 1.125)$ specimen with inclined mounting under cyclic load. **C** Result comparison between the experiment and finite element analysis of a 5×5 $\widehat{N}_4(1{,}90^{\circ}, 1.125)$ connected with parallel mounting and subject to a compression and tension cycle. **D** Result comparison between experiments and finite element analysis for a confined bilayer 5×5 $\widehat{N}_4(1{,}90^{\circ}, 1.125)$ with parallel mounting under cyclic compression-tension. **E** Role of in-plane unit cell periodicity (5×5, 7×7, 9×9) on experimental force-displacement response during compression. Each specimen is made of four layers

Figure 3-5C shows the response of a specimen with the bottom side, in particular the hinges connected to the snapping faces, parallel to the sliders. With this mounting method, the pair of P_4 - P_4' faces here experience a mixture of bending and axial deformation, as opposed to the pure axial deformation undergone by the panels in Figure 3-5B. While the peak force amplification is larger with the mounting in Figure 3-5C for large ratios of $\overline{\boldsymbol{a}}$, the panel can collapse laterally (along the smooth reconfiguration direction) and does not undergo snapping instability. In contrast, the mounting in Figure 3-5B can ensure the pertinent panels always undergo snapping.

One characteristic of the responses observed in Figure 3-4B and Figure 3-4C is the peak force amplification, which can be considered to have a positive as well as negative outcome. On one hand, one way to remove this phenomenon is through confinement. Figure 3-5D shows the application of this strategy to tuned to specimen response. The parallel faces are constrained via screws running through their central holes to preserve their mutual distance during reconfiguration with the result of cancelling out the maximum force amplification and the specimen stiffness increase before the limit point. Confinement is thus an effective strategy to tune the load-displacement response. On the other hand, the magnification of the peak force can be leveraged by increasing the periodicity of the in-plane tessellation. Figure 3-5E shows an example where we compare the compressive response of four-layer specimen with 5×5, 7×7, and 9×9 in-plane unit cells. As can be observed, the maximum force and stiffness associated with each instability cumulate and bring about a gradual increase in their value during the compression process, a characteristic that can be used for dissipative purposes as shown in the next section.

3.7 Leveraging multistability in origami-inspired metamaterials

Multistability and snap-through have been used in mechanical metamaterials with lattice and other non-origami architectures to program a range of mechanical properties including energy absorption [17, 18, 49], energy dissipation [50, 51] and programmable stiffness [50]. Here we focus on an origami-inspired architecture and showcase the promise of leveraging multistability for *in-situ* reprogrammability of i) elastic stiffness and ii) energy dissipation.

In the first application, our goal is to tap into the multiple foldable paths our origami-inspired system can access via multistable snapping. Our target function here is to attain a reversible post-fabrication switch of configurations between states with tailored high elastic stiffness under out-of-plane loading. Figure 3-6A (top view) shows a 5×5 $\widehat{\mathrm{N}}_4(1, 94.23^{\circ}, 1, 1.125, 90^{\circ})$ representative specimen with four stacked layers designed with two types of reconfigurable directions, one enabling smooth folding, and the other multistable folding. If the system is compressed in direction ①, the smoothly reconfigurable direction, we observe rigid body reconfiguration described by the kinematic path 1 in Figure 3-2D. In contrast, in the multistable direction, we observe a non-smooth reconfiguration due to the incompatibility between the heights of the parallelograms, a phenomenon that induces snap-through instability in the panels and enables to bridge the gap between the kinematic paths shown in Figure 3-2D.

As discussed in section 5, snap-through instability occurs sequentially row by row. Given the specimen in Figure 3-6A has four rows of panels (light blue shading), four events of snap-through can be expected in the multistable direction. Since each snap-through in our 4-rows periodic system corresponds to a switch between two stable configurations, there exist 2^4 stable configurations in the multistable direction. The top of Figure 3-6B shows a pre-snap through configuration, and the bottom the counterpart configuration where all rows underwent snap-through. As expected, compression along the multistable direction causes the system to snap and then spontaneously maintain its post-snap-through configuration, as opposed to along the smoothly reconfigurable direction, where the system responds to load removal by returning to its initial state To maintain the configuration in the smoothly reconfigurable direction, we can either maintain the compressive forces or apply an out-of-plane confinement [22].

Figure 3-6C shows 9 possible configurations (top view - along the *z* axis of the coordinate system in Figure 3-6B) among others defining the whole configuration space of a 5×5 structure. In the first five configurations, the specimen is compressed in direction ①. In Figure 3-6C, from left to right the number of rows that are set to lie in the post snap-through state increases, with configurations 5 and 9 being fully compressed in the multistable direction. The highlighted blue region in Figure 3-6C emphasizes the compression in the multistable direction. To ensure the specimen maintains its configuration in direction ①, an elastic band is introduced to confine the outer boundary of the specimen in the first five configurations. For the last four configurations, the elastic band is removed, and as the panels in direction ① unfold, the specimen regains the configuration with the least energy. Figure 3-6C shows only representative states among the admissible ones. For example, the second configuration in Figure 3-6C shows a case where only one row is in the pre-snap configuration; this state is one among all the other four possible configurations (not visualized here), as denoted by the number in the yellow circle, which specifies the number of all admissible configurations. In general, the total number of possible configurations in the multistable direction is $\binom{n-1}{r}$ where *n* is the size of the pattern in the multistable direction and *r* denotes the number of rows in their post-snap configuration. It can be shown that the sum of possible configurations in the yellow circles is 2^4, and that this number holds regardless of the direction of compression, either ① or ②. The last configuration shown in Figure 3-6A depicts the specimen not compressed in direction ①.

The configurations shown in Figure 3-6C are load-bearable if loaded along the *z* axis in Figure 3-6B. Their load-bearing capacity stems from the contact between the parallelogram faces [22], which can generate a distinct value of the out-of-plane stiffness in each locked configuration. Figure 3-6D compares the stiffness of a 5×5 $\widehat{\mathrm{N}}_4(1, 94.23°, 1, 1.125, 90°)$ pattern in the configurations shown in Figure 3-6C. As more rows switch to their post snap-through configuration, the stiffness of the specimen raises as the number of load-bearing faces coming into contact increases upon the application of the external load. In addition, by compressing the specimen along direction ②, a larger number of configurations become available for stiffness tuning.

Exploiting multistability enables to obtain multiple responses, hence demonstrating that multistability can be considered as a pathway to program *in-situ* the mechanical properties. We observe that for a prescribed number of rows set in their post-snap-through configurations, if the system is compressed along direction ②, a larger stiffness can be obtained compared to the case where the system is not compressed along direction ②. The resulting increase in stiffness can be attributed to the larger number of faces establishing contact. For a general pattern, beyond the N_4 pattern examined in this section, and multistable in one direction only, an N_n pattern can exhibit multistability in $\frac{n}{2} - 1$ in-plane directions (see Section 3.9.3), hence endowing multistable snapping with multidirectionality.

The second application taps into the potential for energy dissipation and instability-induced damping of our origami-inspired metamaterial. Here the target function of our system is to deliver mechanical damping under cyclic vibrations. Figure 3-6D and Figure 3-6E show the experimental setup we designed for the purpose (details in Section 3.9.16). It is a mass-spring apparatus that consists of a frame, a sliding stage and a rotary exciter which carries an unbalanced rotating mass driven by a 24-volt DC gearmotor and controlled by a DC generator, which is used to regulate the input voltage and the rotational speed of the motor. During the experiment, we gradually increase the input voltage of the DC gearmotor, which in turn changes the rotational speed of the motor and hence the unbalanced mass. As a result, the rotation of the unbalanced mass causes the sliding stage to oscillate about the initial position. The oscillations of the sliding stage are recorded through a high-speed camera, whose data are stored and post-processed to obtain the amplitude versus rotational speed curve of the motor.

Figure 3-6G shows the amplitude versus frequency of excitation for the cases of undamped and damped oscillation. The samples are tested by sweeping the 24-voltage range of the input with 0.5 volt intervals. The inset of Figure 3-6G compares the response of undamped and damped ($\bar{a} = 1.5$ and $\bar{b} = 1.125$) oscillations. The undamped oscillations (red curve in the inset) generate a nonlinear response featuring a jump with two limit points (green), in the speed up and slow down sweep of the excitation frequency range. The damper can reduce the peak magnitude of the oscillations by 43% as well as the nonlinearity of the vibrations by supplying damping to the oscillatory system. To better understand the role of the geometric parameters on the damping capacity of our metamaterial, four groups of specimens with prescribed $\bar{b} = 1.125$ and dissimilar

$\bar{a}$ are tested, three specimens for each group (Figure 3-6G). The peak value of the oscillations decreases for lower values of $\bar{a}$, a result that parallels those in sections 3 and 4, where a decrease in $\bar{a}$ raises the amount of energy dissipated in a loading/unloading cycle for a prescribed value of $\bar{b}$. Compared to the undamped vibrations, the specimens with $\bar{a}$ =1.375, 1.25, and 1.125 can reduce the amplitude of the oscillations 48%, 51%, and 56% respectively. Furthermore, the frequency associated with the peak value in Figure 3-6G shifts to the right with an increase in $\bar{\boldsymbol{a}}$, a phenomenon attributed to the higher stiffness and more pronounced damping provided by specimen with lower values of $\bar{a}$.

In the oscillatory system shown in Figure 3-6E, the damping mechanisms arise mainly from the existence of drag forces, frictional interactions between slider/rail pairs, the damping induced by multistable metamaterials and the viscoelasticity of the hinge material. The extent, to which each factor governing damping contribute, is influenced by the amplitude of oscillation. At small amplitudes of oscillation, the primary damping contribution arises from the frictional forces between the sliders and the guides along with the viscoelastic dissipation of the hinge material. In contrast, at larger amplitudes, the dominant governing factors comprise the instability-induced damping of the specimen and the drag forces exerted on the sliding stage. By comparing the amplitude of oscillation with and without the specimen mounted on the frame, we can ascertain the role of instability-induced damping in significantly reducing the vibration amplitudes of the system, hence demonstrating how to leverage instability for vibration mitigation in origami-inspired metamaterials.

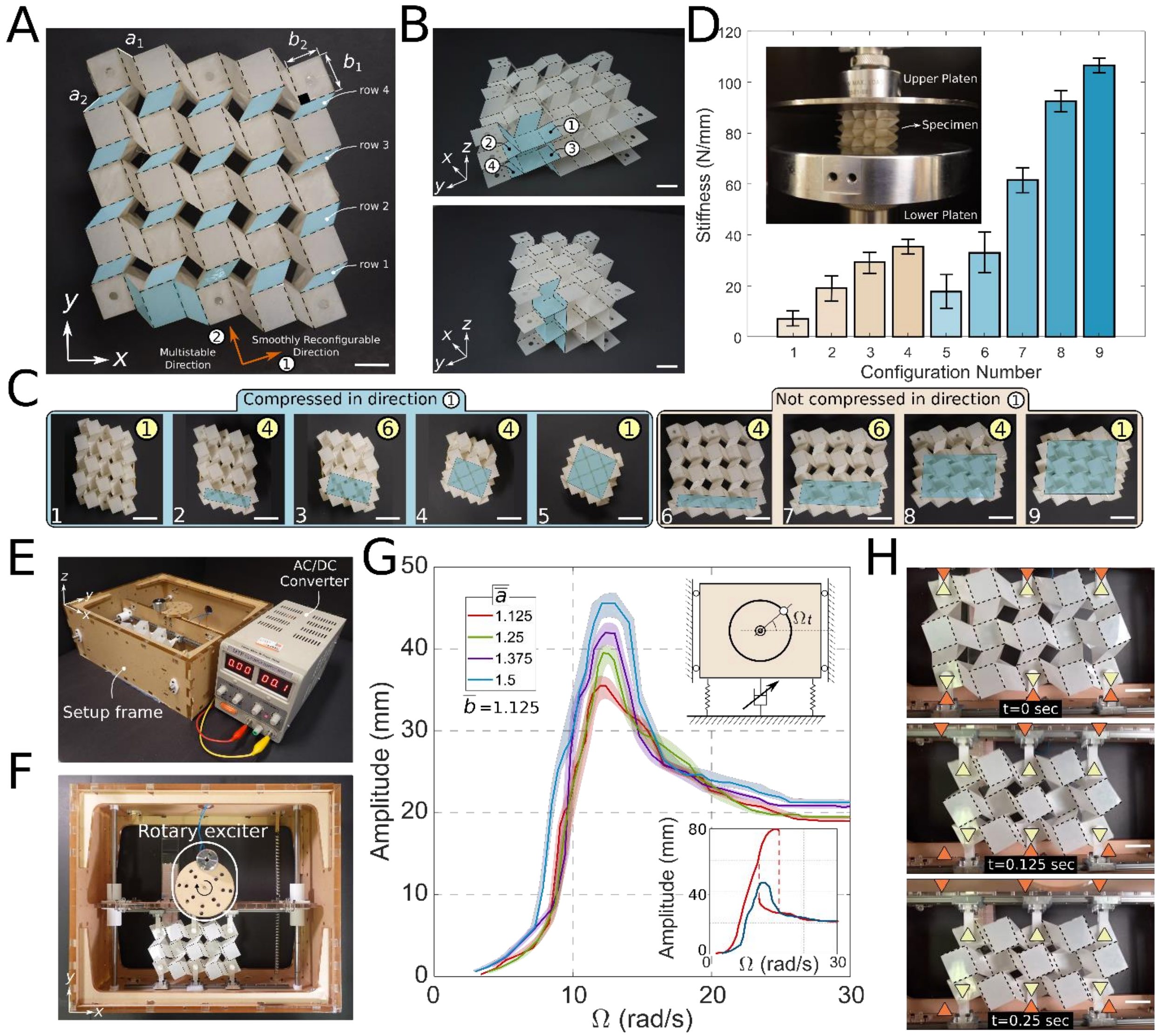

Figure 3-6 Applications of multistable origami inspired metamaterial **A** Multilayered origami-inspired mechanical metamaterial using the $\boldsymbol{N_4}$ pattern with creases shown in dash lines. Two principal directions, i.e., ①: smoothly reconfigurable direction, and ②: multistable direction) of N_4 pattern shown perpendicular to the hinges of the central rectangle. **B** Two representative configurations of the material, pre-snap-through (top) and fully compressed in the multistable direction (bottom). Light blue shade added to discriminate between pre- and post-snap states. Panel numbers (1 to 4) denote the layer the panels belong to. Scale bar: 10mm. **C** Nine representative configurations of 5×5 N_4 pattern. In configurations 1 to 5 the specimen is compressed along the monostable direction, whereas in configurations 6 to 9 the specimen is not compressed in the smoothly reconfigurable direction. From left to right the number of rows set to the post-snap state increases. Pale blue shading indicates the location of rows in their post-snap state. Yellow circles enclose the total number of admissible configurations obtained by setting a given number of rows in the post-snap state; each configuration differs only from location of the row in the post-snap state. **D** Out of plane stiffness (along *z* axis in **B**) of the specimen in the multiple configurations shown in **C**. **E** Vibration testing setup consisting of a frame featuring a slider and a rotary exciter and an AC/DC converter. **F** Front view of the vibration testing setup consisting of rotary mass exciter, springs, sliders, and the origami-

inspired damper. **G** Amplitude versus exciter rotational speed for a set of 5×3 N_4 patterns with dissimilar values of $\bar{\boldsymbol{a}}$; inset at the top right corner schematically indicates the configuration of the vibration testing setup; inset at the bottom right corner compares the amplitude versus rotational speed of the undamped case (no specimen is mounted) with the case of $\bar{a} = 1.5$ and $\bar{b} = 1.125$. H Snapshots of the configurations of a multistable specimen acting as a damper at distinct time values. Orange triangles indicate the initial location of the sliders and yellow triangles denote their current location.

3.8 Concluding remarks

This work has introduced a class of reprogrammable multistable metamaterials that merges origami-folding and kirigami-cuts to generate snapping foldable patterns with periodically arranged excisions enabling the formation of multiple degrees of freedom which can be reduced to one upon layer stacking. The study of the unit cell kinematics has revealed that the heights of the slanted faces play a pivotal role in governing the attainable space of rigid folding. For a rigid-foldable system, a difference in height between the parallelogram faces forbids the smooth transition between kinematic paths, which on the other hand can be promoted by lifting the panel rigidity assumption. Panel compliance allows the emergence of snap-through instability which in turn permits to travel from one kinematic path to another, hence enlarging the admissible design space of non-rigid folding.

The study of the geometric parameters governing the snap-through response of a single snap has revealed the existence of four deformation regimes, each characterized by a specific type of panel contact. Validated through experiments, design maps have been presented to tailor the multistable response of a single primitive as well as the interaction of snapping events occurring in a unit made of two primitives arranged in series. The results have shown that the peak load and the tangential stiffness accrued at the second instant of instability are significantly larger than the values registered in the first instant. Snap-trough instability has also been leveraged to program *in-situ* the out of plane response of our origami-inspired system.

Furthermore, we have demonstrated the benefit of the cumulative effect of multistable snapping from interacting units under cyclic loading, which holds promise for energy dissipation and mechanical damping. We have shown that multi-cell patterns tested in a setup that eliminates lateral constraints can undergo consecutive instabilities exhibiting strong interactions that synergically work to augment energy dissipation. Multistable snapping in interacting panels has been demonstrated as a pathway to generate mechanical damping with reduced oscillation amplitude in a system under unbalanced rotary excitation.

3.9 Appendix

3.9.1 Generalization of crease patterns

The main text examines a demonstrative crease pattern (N_4) encompassing a periodic tessellation of the kinematic unit chain shown in Figure 3-1. Here we explain the generative process to obtain its geometric variations and extend them to other polygonal crease patterns, such as N_6.

As discussed in the main text, the N_4 pattern has two periodic directions perpendicular to the hinges of the mountain or valley faces (Figure 3-7A). The parallelogram faces in these two directions are shown with red and green edges. The parallelograms in each row or column can be reshaped without affecting the rest of the pattern. Figure 3-7B and Figure 3-7C show the process applied to the first and the second directions, respectively. To maintain periodicity, we alternate two parallelograms in each direction. However, there is no restriction on the parallelograms in each direction as they can be modified independently in each row or column. Figure 3-7D depicts a case where the parallelograms are reshaped in both directions.

While the main text examines the case of patterns made of similar parallelograms in each direction, the process described here enables to enrich the design space for generating other in-plane behaviors.

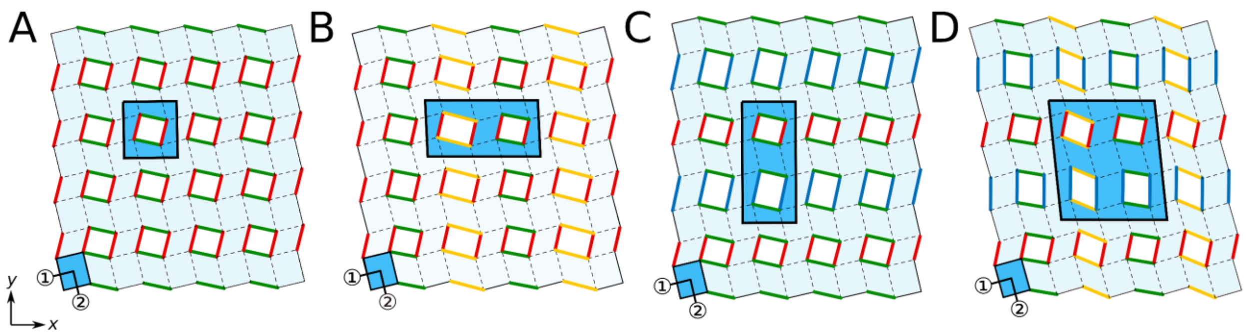

Figure 3-7 In-plane variations of N_4 pattern; **A** N_4 pattern with extruded parallelogram faces with green and red edges and two in-plane programming directions (1) and (2); **B** Alternating two sets of parallelograms, green and yellow, in direction (1), enables to program the crease pattern in direction (1) only; **C** Alternating two sets of parallelograms, red and blue, in direction (2) allows to programming the response along this direction; **D** Combining **B** and **C** enables bi-directional in-plane programming of N_4 pattern.

3.9.2 Other periodic patterns – N_6 pattern

Any even-sided parallelogon with equal parallel sides can be considered as the primitive of our kinematic unit chain. In the main text we focus on N_4, and here we discuss its extension to other parallelogons.

3.9.2.1 Geometric parameters of N_6 pattern

To generate a hexagonal-based pattern (N_6), we start with a core hexagon with parallel opposite edges (Figure 3-8A) and defined by the lengths of its sides a_1 to a_3 and the internal angles $\alpha_1$and α_2.

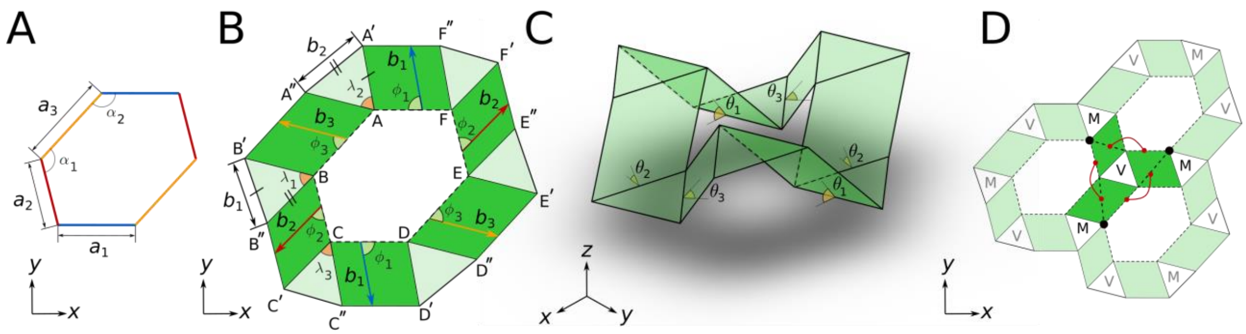

Figure 3-8 Process of generating N_6 kinematic unit chain **A** Hexagonal parallelogon as the primitive of $\boldsymbol{N_6}$ pattern; five independent geometric parameters are required to fully define a hexagonal parallelogon $(a_1, a_2\ a_3, \alpha_1, \alpha_2)$; **B** Kinematic unit chain along with the constraints required for tessellating the kinematic unit chain; in general |AA′|=|B′B″| and |A′A″|=|BB″| are required to ensure the tessellation of the kinematic unit chain; **C** Three dimensional configuration of an N_6 kinematic unit chain with pairs of angles required to describe its configuration; **D** A tessellation of three kinematic unit chain where mountain and valley faces are shown.

Extruding the edges of the core polygon enables the formation of a series of parallelograms connected at their corners. We fill the gaps between the parallelograms with triangles, as shown in Figure 3-8B. A three-dimensional configuration of the kinematic unit chain is shown in Figure 3-8B, where three pairs of angles, θ_1, θ_2, and θ_3 , are required to describe its spatial form.

Imposing the rigidity of the panels and considering the shared edges of the panels as rotational hinges allows to obtain a kinematic unit chain with multiple degrees of freedom. For N_6, we need two additional constraints to ensure the kinematic unit chain can be tessellated in the plane, i.e.,

$$|\mathrm{AA}'| = |\mathrm{B}'\mathrm{B}''| = b_1 \tag{3-3}$$

And

$$|\mathrm{A}'\mathrm{A}''| = |\mathrm{BB}''| = b_2 \tag{3-4}$$

Where | | in (S1) and (S2) denotes the length of the line segment. Satisfying (S1) and (S2) enables the tessellation of the kinematic unit chain shown in Figure 3-8D. The foregoing discussion leads to the most general N_6 tessellation, which has eleven parameters, including the sides of the initial hexagon, $(a_1, a_2,$ and $a_3)$, two internal angles, (α_1 and α_2), the lengths of three extrusion vectors,

(b_1, b_2, and b_3), and three directions of the extrusion angles, (ϕ_1, ϕ_2, and ϕ_3). Given two constraints are required for tessellation, the number of independent geometric parameters reduces to nine.

3.9.2.2 Kinematic analysis of N_6 pattern

The kinematics of N_6 pattern can be explained by studying a core triangle along with its hinged parallelograms (Figure 3-8D). For demonstrative purpose, here we study a subclass of N_6 where the diagonal of each parallelogram is equal to the free edge of a neighbor parallelogram that converges to the same vertex on the central triangle. These pairs are shown as red lines in Figure 3-8D. This constraint makes the three vertices indicated with black circles meet upon folding at a single point following the mountain/valley assignment therein indicated.

To understand the diversity of the N_6 response from that of its N_4 counterpart, we investigate the role of the governing geometric parameters. Figure 3-9 shows the central triangle with three hinged parallelograms for three cases. Figure 3-9A depicts the case where the central triangle is arbitrary. In the initially flat configuration, the extensions of the heights of the parallelograms intersect at the center of the incircle of the central triangle. The two-dimensional pattern is also shown in Figure 3-9B. In this case, $h_1 = h_2 = h_3$, and hence, we expect a continuous kinematic path upon folding.

As discussed in the main text, the rigid folding of N_6 is possible if

$$h_1 \sin\theta_1 = h_2 \sin\theta_2 = h_3 \sin\theta_3 \tag{3-5}$$

Figure 3-9B shows the kinematic landscape for $h_1 = h_2 = h_3$. It consists of four kinematic paths intersecting at a kinematic bifurcation point, i.e., point e, where $\theta_1 = \theta_2 = \theta_3 = \frac{\pi}{2}$. As explained in the main text for N_4, the transition from one kinematic path to the other requires the structure to undergo kinematic bifurcation. We assume the initial configuration is fully flat with $\theta_1 = \theta_2 = \theta_3 = 0$ at point a; upon folding, the structure reconfigures to point e, where the number of degrees of freedom increases from 1 to 4, and new paths become available as visualized in Figure 3-9B. Passed this point, the degree of freedoms reverts to one.

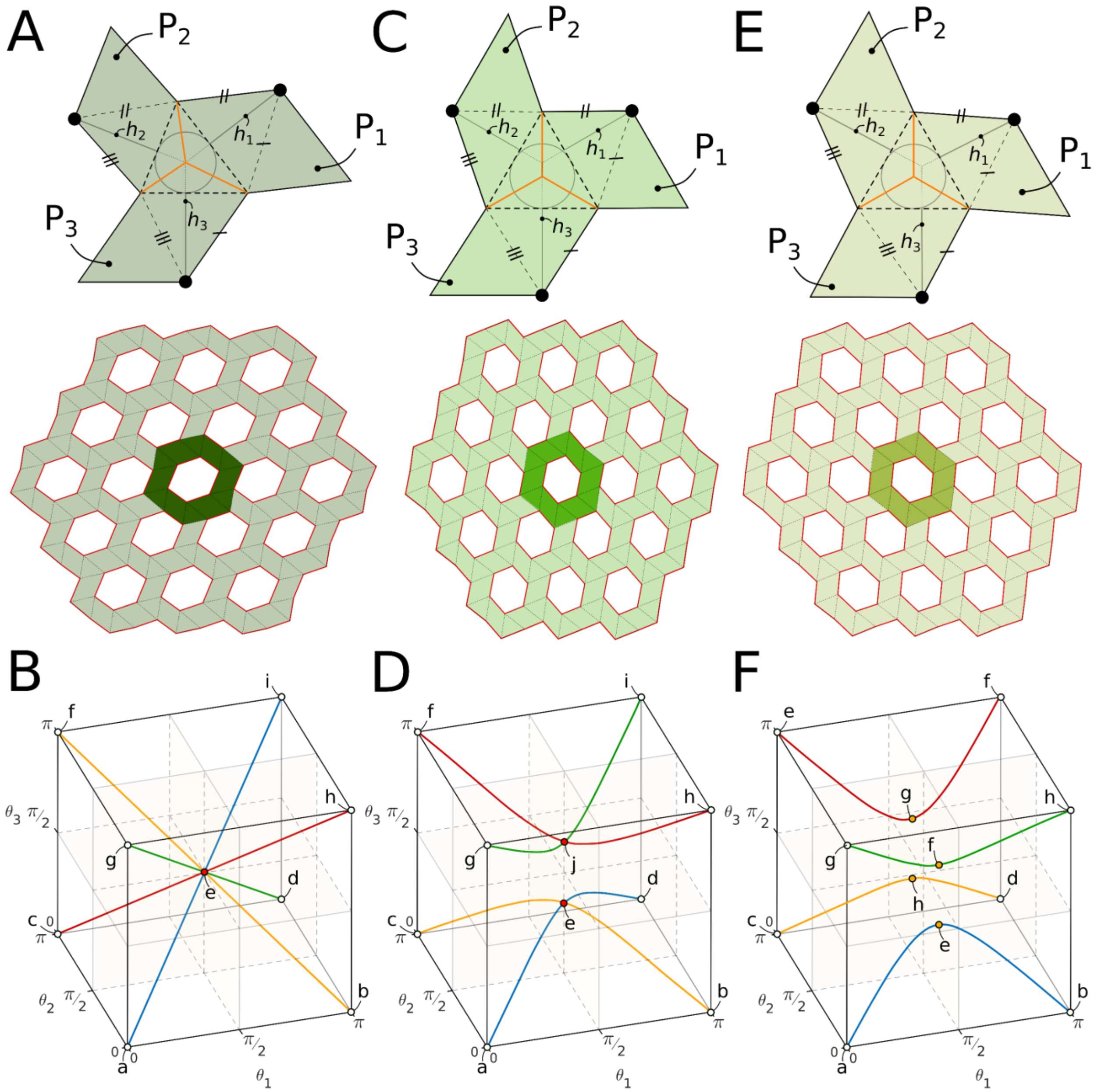

Figure 3-9 Reconfiguration space of generalized N_6 patterns. **A** $\boldsymbol{N_6}$ pattern with extensions of the parallelogram heights, here $h_1 = h_2 = h_3$, meeting at the center of the incircle of the central triangle. In this case. **B** Kinematic landscape for the case shown in **A** consisting s of four kinematic paths intersecting

at the point of kinematic bifurcation;, the continuity of the kinematic paths ensures rigid reconfiguration between paths is possible; **C** N_6 pattern when with extensions of two parallelogram heights, $h_1 = h_2 \neq h_3$where $h_1/h_3 = h_2/h_3 = 0.9$, of parallelograms meet at on the bisector of their common angle. In this case, $h_1 = h_2 \neq h_3$where $h_1/h_3 = h_2/h_3 = 0.9$. **D** Kinematic landscape for the case shown in case **C** consisting of four kinematic paths in two groups of intersecting paths; The reconfiguration between the intersecting paths involves a kinematic bifurcation. However, rigid body reconfiguration between non-intersecting paths is not admissible between non-intersecting paths. **E** N_6 pattern where the extensions of the parallelogram heights do not meet at any point of the bisectors of the central triangle. In this case, $h_1 \neq h_2 \neq h_3$where $h_1/h_3 = 0.97$ and $h_2/h_3 = 1.04$, selected as representative values. **F** Kinematic landscape for the case shown in **E** consisting of four non-intersecting kinematic paths. All rigid reconfigurations are bound to a single kinematic path while no rigid-body reconfiguration is admissible between the kinematic paths.

Figure 3-9C shows a case where the extensions of the heights of P_1 and P_2 ($h_1 = h_2 < h_3$) intersect at a point along the bisector of the angle formed by two edges to which P_1 and P_2 are hinged.

The third case, where $h_1 = h_2 > h_3$, is shown in Figure 3-9D, where the difference in the parallelogram heights leads to two pairs of intersecting kinematic paths. However, unlike the case in Figure 3-9D, the reconfiguration between the intersecting kinematic paths is not smooth since the range of rigid reconfigurations is governed by the smallest height of the parallelograms i.e., h_3. This means the kinematic bifurcation point is not an admissible configuration if the panels are assumed as rigid.

In Figure 3-9E, the extensions of the parallelogram heights intersect at a point that does not lie on any of the bisectors of the central triangle. In this case, $h_1 \neq h_2 \neq h_3$ and the kinematic landscape in Figure 3-9F consists of 4 non-intersecting kinematic paths. Reconfiguration along each kinematic path only allows one of the angles θ_1, θ_2 and θ_3 to switch from a value below $\frac{\pi}{2}$ to values above $\frac{\pi}{2}$, while the other two angles remain on the same interval with respect to $\frac{\pi}{2}$. Switching from one path to another is possible only if the faces are assumed deformable.

3.9.2.3 Multistability of N_6 pattern

The foregoing discussion suggests that once the rigidity constraint is lifted, we can expect multistability in any N_6 pattern featuring parallelograms of unequal heights. As a result, the patterns shown in Figure 3-9C and Figure 3-9E undergo unidirectional and bidirectional multistability during reconfiguration, as shown in Figure 3-10.

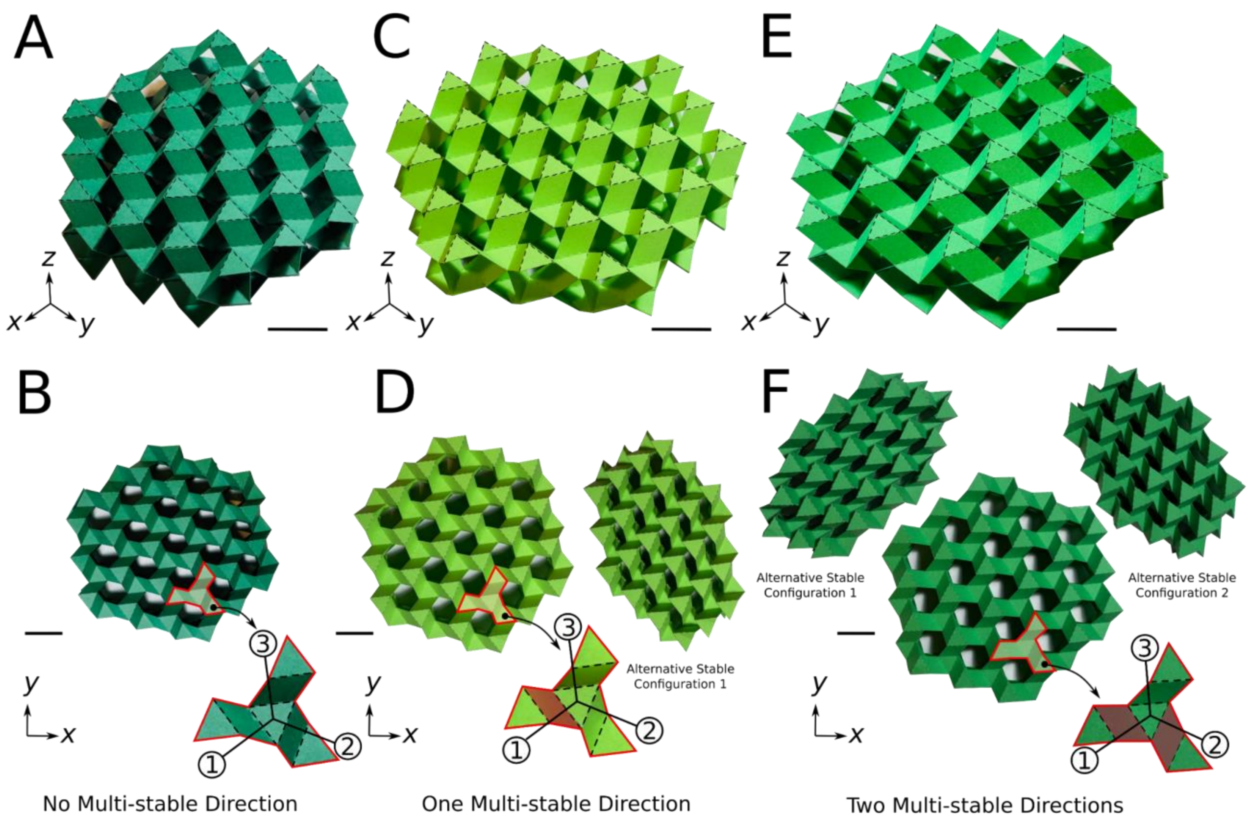

Figure 3-10 Cardboard prototypes corresponding to the cases shown in **Figure 3-9**. Each prototype consists of three layers and is shown in a transition state, where $0 < \theta_1, \theta_2$ and $\theta_3 < \pi/2$. Scale bar =30mm. **A** Three-layer prototype with $h_1 = h_2 = h_3$. **B** Top view of the transition case shown in A. This combination of geometric parameters does not yield a multistable material. **C** Three-layer prototype with $h_1 = h_2 \neq h_3$ where $h_1/h_3 = h_2/h_3 = 0.9$. D Top view of the transition case shown in C. Specimen multistable only along direction ①. **E** Three-layer prototype of the third case where $h_1 \neq h_2 \neq h_3$ with $h_1/h_3 = 0.97$ and $h_2/h_3 = 1.04$. **F** Top view of the transition case shown in **E**. Specimen multistable along both directions ① and ②.

As shown in Figure 3-10, the second and the third case undergo unidirectional and bidirectional multistability due to the height mismatch of the parallelograms surrounding the central triangle. The second pattern is multistable along direction ①, while the third pattern exhibits multisability in both directions ① and ②.

3.9.3 Other Patterns – *N* > 6

The previous section has discussed N_6 in more detail as more constraints than with N_4 should be applied to make its kinematic unit chain tessellable in both planar dimensions. Our strategy, however, is not restricted to N_4 and N_6, as any even sided parallelogram can serve as the primitive polygon to generate the corresponding unit chain.

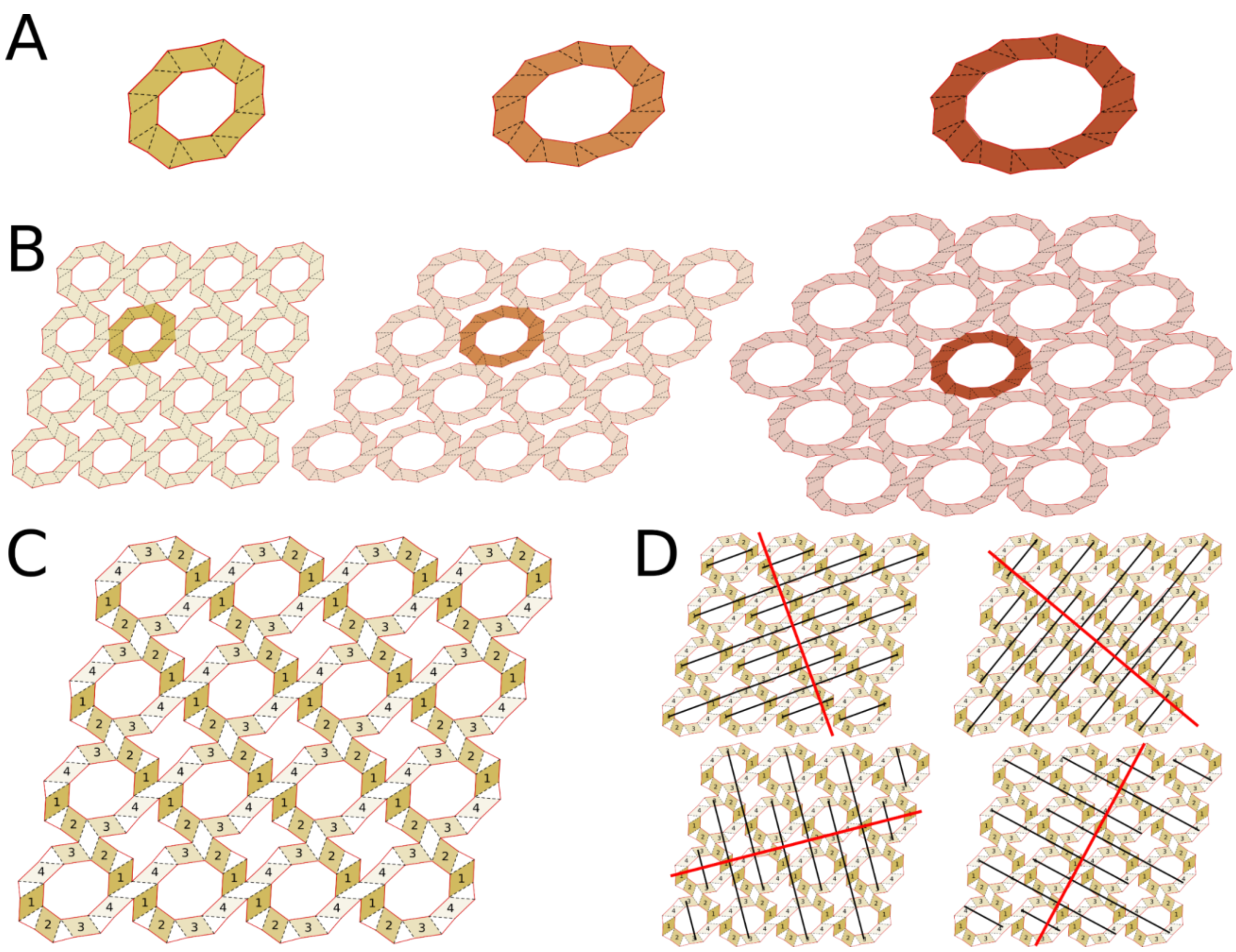

Figure 3-11 Other patterns with $N > 6$. **A** Kinematic unit chains of representative patterns: N_8, $N_{10,}$ and N_{12}; **B** Patterns generated from unit chain tessellation ; **C** Four groups of similar faces in N_8 are indicated with numbers and distinct color shades; **D** Upon reconfiguration, similar faces perpendicular to the loading direction undergo snap-through simultaneously. Black lines emphasize corresponding faces that

sequentially undergo snap-through provided the loading direction is along the red lines. All faces connected by black lines experience snap-through instability simultaneously.

Figure 3-11A shows the kinematic unit chains of eight, ten, and twelve-sided initial polygon. Figure 3-11B also shows the tessellation of each kinematic unit chain shown in Figure 3-11C. Contrary to N_6 pattern, no additional requirement is required to ensure the kinematic unit chains can tessellate the plane.

To demonstrate the level of attainable programmability, we examine the N_8 pattern in Figure 3-10C, where the faces with parallel hinges are numbered. As expected, N_8 consists of four sets of panels with parallel hinges. Provided the faces are assumed to be deformable and each set of parallelograms has a unique height, we observe one direction with smooth reconfiguration corresponding to the smallest height among the four sets of parallelograms. As a result, along the other three directions the pattern is multistable, as shown in Figure 3-11D, where the black lines denote faces that undergo instability simultaneously if the specimen is compressed along the red lines.

3.9.4 Final configuration of N_4 pattern

While the kinematic paths in Figure 3-8C and Figure 3-8D describe the pattern reconfiguration, they do not provide any information on the final state a given pattern can reach. The final configuration can be locked or flat-foldable in one or both directions. Locking occurs if the faces come into contact along the kinematic path at any point other than the terminal points of the branches. On the other hand, a flat-foldable configuration is characterized by the condition of either θ_1 or θ_2 attaining π, i.e., points j, m, and o in Figure 3-8D.

To study the final configuration of the pattern we investigate a central parallelogram with its attached panels (Figure 3-12). Our investigation shows that in addition to the geometric parameters, the extrusion direction of the sides of the initial polygon also plays a role in determining the final configuration of the pattern. Figure 3-12 shows two-unit cells and their corresponding patterns with identical central and extruded parallelograms. The extrusion angle in Figure 3-12B ($\phi_i{}'$) is complementary to the extrusion angle of Figure 3-12A. Figure 3-12C and Figure 3-12D depict the patterns generated from the units in Figure 3-12A and Figure 3-12B respectively.

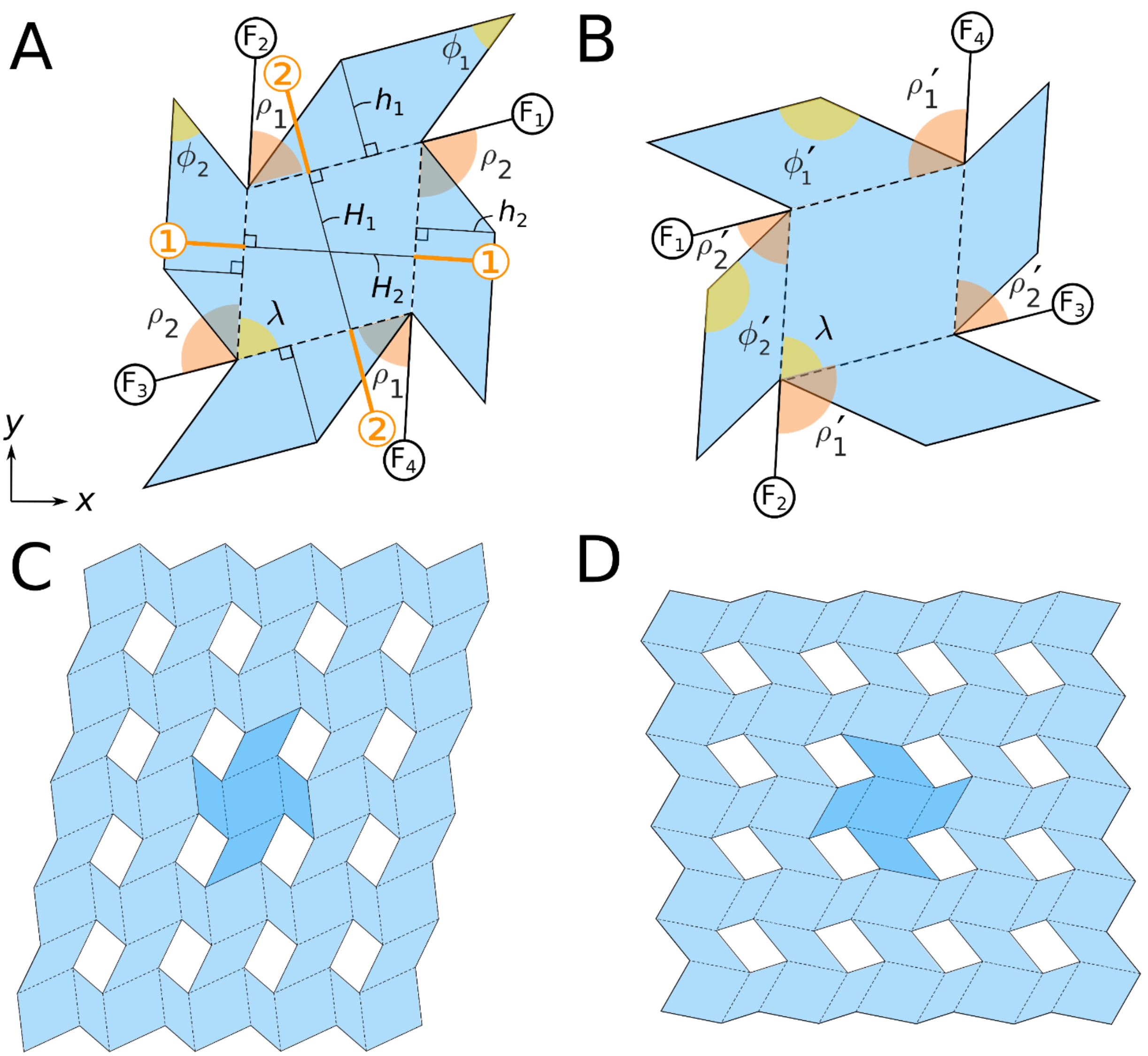

Figure 3-12 N_4 pattern with parallelogram mountain/valley faces; **A** Clock-wise extrusion of the parallelogram faces **B** Counter clock-wise extrusion of the parallelogram faces; some geometric parameters

are dependent on the direction of the extrusion. In the main manuscript, we adopt the extrusion shown in **A**; all the derivations are valid for case **B** as well, provided the convention complies with this figure. **C** and **D** The patterns derived from the primitives of **A** and **B** are distinct. While the kinematic landscapes of these patterns are similar, their final configurations are different.

Figure 3-12 shows how the governing geometric parameters are affected by the direction of extrusion. Any mathematical derivation for each pattern is also valid for the other, provided the notation in Figure 3-12 applies. Without losing the generality of our discussion, we adopt the extrusion angle shown in Figure 3-12A, i.e. ϕ_1 and $\phi_2 < 90^{\circ}$. To derive the required conditions for flat-foldability in each direction, we show the assumed flat-folded configurations from the top view in Figure 3-13B to Figure 3-13F regardless of the prospect of reaching a given configuration.

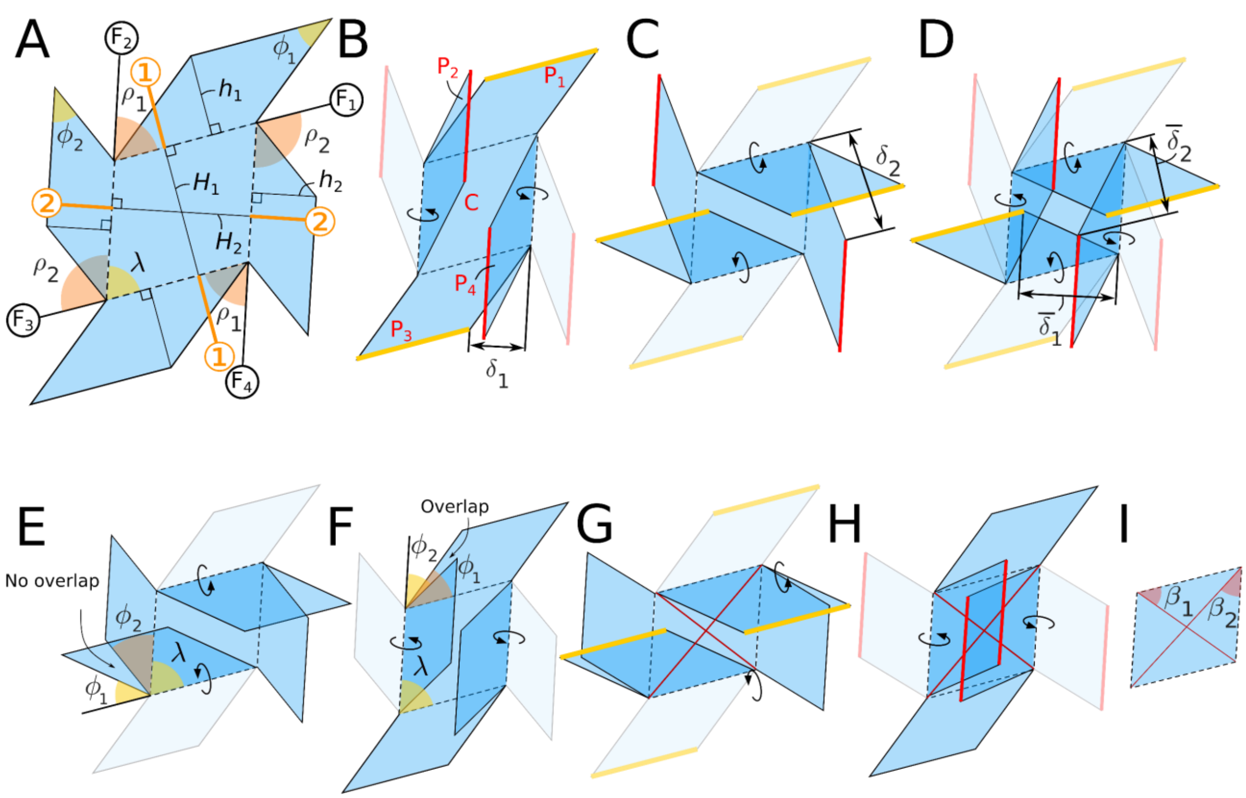

Figure 3-13 Illustration of the flat-foldability conditions for N_4 pattern. **A** Geometric parameters governing the final configuration **B-H** Different scenarios are possible for the final state; **B-D** Satisfying the first condition of flat-foldability; i.e. the existence of contact between the yellow and red edges; **B** and **C** Flat-foldability in the directions shown in **A**; **D** Bi-directional flat-foldability; **E** and **F** Satisfying the second condition of flat-foldability; i.e. existence of overlap of parallelograms with corner angles ϕ_1 and ϕ_2; **E** There is no overlap of parallelograms with corner angles ϕ_1 and ϕ_2 in the folded configuration in the first

direction; hence, this configuration is flat-foldable; **F** Overlap of ϕ_1 and ϕ_2 in the folded configuration in the second direction; as a result the structure is non-flat-foldable in the second direction. **G** and **H** Satisfying the third condition of flat-foldability, i.e., existence of contact between the edges (red and yellow) of faces on opposite edges in the central parallelogram. **G** Flat-foldable pattern in the first direction ensured by $\phi_1 < \beta_1$. H Non-flat-foldable pattern in the second direction due to $\phi_2 > \beta_2$.

The first condition can be obtained from Figure 3-13B and Figure 3-13C. C is the central parallelogram. P_1 (or P_3) and P_2 (or P_4) are the faces of two converging fold lines F_1 (or F_3) and F_2 (or F_4) (Figure 3-13A to Figure 3-13C). Upon folding P_2 (or P_4), the edge of P_2 (or P_4) parallel to F_2 (or F_4) may not penetrate the edge of P_1 (or P_3) parallel to the fold lines F_1 (or F_3). Graphically the first condition of flat-foldability prevents the red and yellow edges in Figure 3-13B to Figure 3-13D from getting into contact. This condition states the following

$$\text{If } h_i < a_j \sin(\rho_i - \phi_j)\text{, then } h_j < \min\{\delta_i, \bar{\delta_i}\} \text{ for } i,j = 1,2 \tag{3-6}$$

Where ρ_i is the complementary external angle of the central parallelogram constructed by the extension of the fold lines shown in Figure 3-13A. δ_j and $\bar{\delta_j}$ are the distances between the vertex of each parallelogram and its adjacent fold line in the developed and folded configurations. They are given by

$$\delta_i = a_i \sin(\rho_i - \phi_i) \text{ and } \bar{\delta_i} = a_i \sin(\rho_i + \phi_i) \tag{2-7}$$

which can be rewritten in terms of the parallelogram heights as

$$\delta_i = h_i \frac{\sin(\rho_i - \phi_i)}{\sin \phi_i} \text{ and } \bar{\delta_i} = h_i \frac{\sin(\rho_i + \phi_i)}{\sin \phi_i} \tag{3-8}$$

After rearrangement, Eq. (3-6) can be written as

$$\text{If } h_i < a_j \sin(\rho_i - \phi_j) \text{ then } \tan \phi_j < \min\left(\frac{\sin \rho_i}{\frac{h_i}{h_j} + \cos \rho_i}, \frac{\sin \rho_i}{\frac{h_i}{h_j} - \cos \rho_i}\right) \tag{3-9}$$

Figure 3-13C and Figure 3-13D show unidirectional folding in the second direction and bidirectional folding, respectively. The second condition of flat-foldability pertains to the condition where $h_i > a_j \sin(\rho_i - \phi_j)$ and it states

If $h_i > a_j \sin(\rho_i - \phi_j)$ then $\phi_i + \phi_j < \rho_i$ (3-10)

Figure 3-13E and Figure 3-13F shows the graphical interpretation of the second condition. In Figure 3-13E, the second condition of flat-foldability is satisfied in the first direction, where in the folded configuration there is no overlap between the angles ϕ_1 and ϕ_2. In Figure 3-13E, on the other hand, there is an overlap between ϕ_1 and ϕ_2, hence , the unit is non-flat-foldable in the second direction.

The first and the second conditions must be both satisfied to ensure flat-foldability for any choice of the governing parameters. However, if $h_i > \frac{H_i}{2}$, the panels on the opposite edges of the core parallelogram C may come into contact. Figure 3-13G depicts a case when this condition is satisfied in the first direction. While in Figure 3-13H, the third condition of flat-foldability is not satisfied in the second direction. As a result, the third condition can be mathematically expressed as

If $h_i > \frac{H_i}{2}$ then $\phi_i < \beta_i$ (3-11)

where β_i is the angle of the diagonal of the central parallelogram and its edge as shown in Figure 3-13I. This condition can be written as

If $h_i > \frac{H_i}{2}$ then $\phi_i < \sin^{-1} \frac{b_j \sin \rho_j}{\sqrt{b_i^2 + b_j^2 + 2 b_i b_j \cos \rho_i}}$ (3-12)

As described by the conditions 1 (S7), 2 (S8), and 3 (S10), an N_4 pattern can be flat-foldable respectively in one, both or neither of its folding directions. These conditions can be compiled graphically in a map, namely the *kinematic phase diagram* (Figure 3-148), which defines the final configuration of the structure as function of its geometric parameters.

Figure 3-14A shows the kinematic phase diagram for $\mathrm{N}_4(a_1 = \frac{h_1}{\sin\phi_1}, a_2 = \frac{h_2}{\sin\phi_2}, \alpha = \frac{\pi}{2} + \phi_1 - \phi_2, b_1 = b_2 = \bar{b}, \phi_1, \phi_2)$. Here we assume the height of the parallelograms are equal, $h_1 = h_2 = \bar{h}$. Moreover, the sides of the mountain and valley faces are also assumed to be equal, $b_1 = b_2 = \bar{b}$. Lines 1 to 3 in Figure 3-14 correspond to the boundaries defined by conditions 1 to 3 respectively. In region *i* all three conditions are satisfied, and therefore we expect flat foldability in both directions. As a result, three flat-foldable configurations are feasible. In regions *ii* and *iii*, the second condition of flat-foldability is not satisfied; accordingly, only one flat-foldable configuration exists in these two regions. Finally in region *iv* none of the flat-foldability conditions is satisfied, and no flat-foldable configuration exists in this region.

In Figure 3-14C, the role of b_1 and b_2 are investigated for $\mathrm{N}_4(a_1 = \frac{\bar{h}}{\sin\phi_1}, a_2 = \frac{\bar{h}}{\sin\phi_2}, \alpha = \frac{\pi}{2} + \phi_1 - \phi_2, b_1 = \bar{b}_1, b_2 = \bar{b}_2, \phi_1, \phi_2)$. Here we assume the following representative values: $\bar{h}$ = 9 mm, $\bar{b}_1$ = 25 mm and $\bar{b}_2$ = 20 mm. In this case, the third condition of flat-foldability is affected. In other words, only if $\bar{h} > \frac{H_1}{2}$ or $\bar{h} > \frac{H_2}{2}$ the boundaries of lines 3 determine the flat-foldability condition. In this case, we observe an unsymmetric boundary for lines 3 as the angle between the diagonal and the fold lines (Figure 3-13) are not identical for directions 1 and 2.

Finally, Figure 3-14D shows the kinematic phase diagram for $\mathrm{N}_4(a_1 = \frac{\bar{h}}{\sin\phi_1}, a_2 = \frac{\bar{h}}{\sin\phi_2}, \alpha = \bar{\lambda} + \phi_1 - \phi_2, b_1 = b_2 = \bar{b}, \phi_1, \phi_2)$. Here we prescribe $\bar{h}$ = 9 mm, $\bar{h}$ = 20 mm and $\bar{\lambda}$ = 75°. In this case, all three flat-foldability conditions vary compared to the case of Figure 3-14A. First, the boundaries defined by lines 1 shrink compared to Figure 3-14A. Second, the skewness of the central polygon shifts the boundary of the second condition, shown by line 2. Finally similar to the case of Figure 3-14C, we observe unsymmetric boundary for the third condition of flat-foldability, due to the difference of β_1 and β_2.

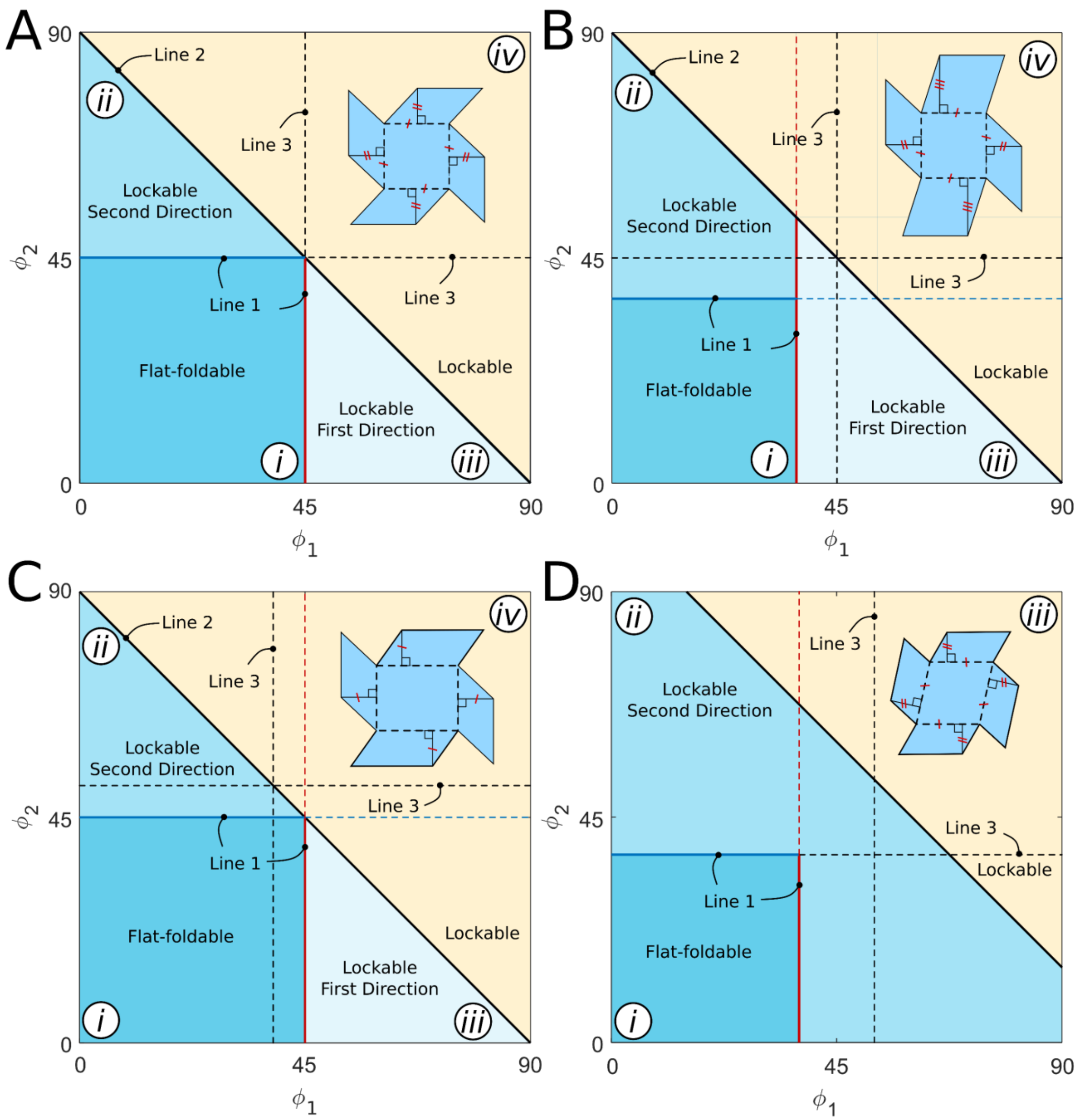

Figure 3-14 Kinematic phase diagrams defining the final configuration of N4 as a function of different combination of geometric parameters **A** Kinematic phase diagram of $N_4(a_1 = \frac{\bar{h}}{sin\,\phi_1}, a_2 = \frac{\bar{h}}{sin\,\phi_2}, \alpha = \frac{\pi}{2} +$

$\phi_1 - \phi_2, b_1 = b_2 = \bar{b}, \phi_1, \phi_2)$; **B** Kinematic phase diagram of $N_4(a_1 = \frac{\bar{h}_1}{sin\,\phi_1}, a_2 = \frac{\bar{h}_2}{sin\,\phi_2}, \alpha = \frac{\pi}{2} + \phi_1 - \phi_2, b_1 = b_2 = \bar{b}, \phi_1, \phi_2)$, in this case $\bar{h}_1 \neq \bar{h}_2$. **C** Kinematic phase diagram of $N_4(a_1 = \frac{\bar{h}}{sin\,\phi_1}, a_2 = \frac{\bar{h}}{sin\,\phi_2}, \alpha = \frac{\pi}{2} + \phi_1 - \phi_2, b_1 = \bar{b}_1, b_2 = \bar{b}_2, \phi_1, \phi_2)$, in this case $\bar{b}_1 \neq \bar{b}_2$. **D** Kinematic phase diagram of $N_4(a_1 = \frac{\bar{h}}{sin\,\phi_1}, a_2 = \frac{\bar{h}}{sin\,\phi_2}, \alpha = \bar{\lambda} + \phi_1 - \phi_2, b_1 = b_2 = \bar{b}, \phi_1, \phi_2)$.

To investigate the role of each geometric parameter, we have studied three additional cases. Figure 3-14B shows the kinematic phase diagram of $N_4(a_1 = \frac{\bar{h}_1}{\sin\phi_1}, a_2 = \frac{\bar{h}_2}{\sin\phi_2}, \alpha = \frac{\pi}{2} + \phi_1 - \phi_2, b_1 = b_2 = \bar{b}, \phi_1, \phi_2)$. Here we assume the demonstrative values: $\bar{h}_1$ = 12 mm, $\bar{h}_1$ = 9 mm and $\bar{b}$ = 20 mm. In this case we observe that only the boundaries of the first constraint, Lines 1, change compared to the first case.

3.9.5 General formulation of rigid body reconfiguration in N_4 pattern

In this section, we present a general framework for rigid body reconfiguration of N_4 pattern. We start our investigation from the governing geometric parameter followed by the formulation of the deformation metrics.

3.9.5.1 N_4 pattern unit cell

As described in the main text, the reconfiguration of N_4 involves both rigid and nonrigid reconfiguration. This section provide the geometric relations that describe its rigid reconfiguration.

Figure 3-15 depicts the geometric parameters defining a generalized N_4 pattern, where the sides of the unit cell L_1, L_2 and the angle between the diagonals ω are given by

$$
\begin{aligned}
L_1 &= \sqrt{l_1^2 + l_2^2 - 2 l_1 l_2 \cos\omega} \\
L_2 &= \sqrt{l_1^2 + l_2^2 + 2 l_1 l_2 \cos\omega} \\
\omega &= \lambda + \psi_1 + \psi_2
\end{aligned}
\tag{3-13}
$$

with ψ_1 and ψ_2 as

$$\psi_i = \tan^{-1}\frac{e_i}{H_j + h_i\cos\theta_i} = \tan^{-1}\frac{e_i}{a_j\sin\lambda + h_i\cos\theta_i} \qquad \text{for } i,j = 1 \text{ and } 2 \qquad (3\text{-}14)$$

where e_1 and e_2 can be calculated as

$$e_i = a_i - p_i \qquad \text{for } i = 1 \text{ and } 2 \qquad (3\text{-}15)$$

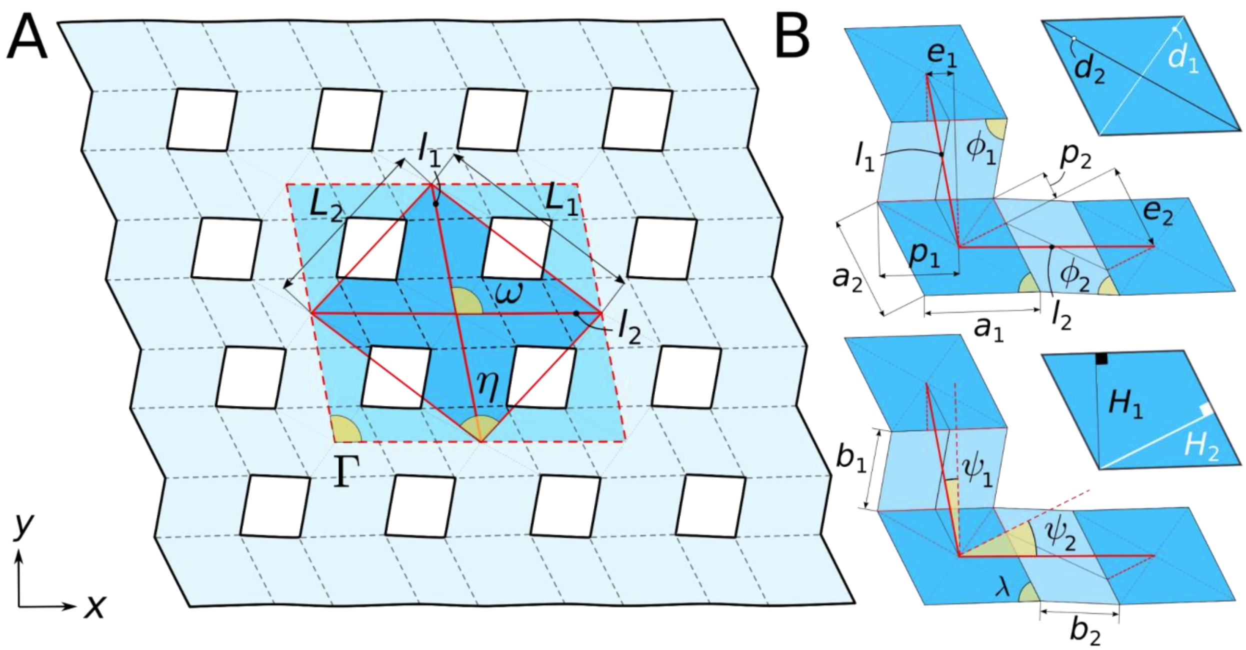

Figure 3-15 Geometric parameters of N_4 pattern. **A** General $5\times5N_4$ pattern in its planar configuration. Unit cell shown at the center with parametric dimensions. **B** Geometric parameters defining the unit cell and its kinematics.

and p_i can be obtained from

$$p_i = \frac{\sqrt{d_i^2 - H_i^2}}{2} \qquad \text{for } i = 1 \text{ and } 2 \qquad (3\text{-}16)$$

The parameter definitions above are now used to define the deformation metrics of the unit cell in N_4 as reported in the next section.

3.9.5.2 Kinematics

To understand the effect of reconfiguration on the rigid deformation of our material system, we study the finite strain tensor E. We consider the representative unit cell of the N_4 pattern. At each configuration, we can map the initial representative unit cell to the current one with a linear transformation as

$$x_1 = C_1 X_1 + C_2 X_2$$

$$x_2 = C_3 X_2 \tag{3-17}$$

$$x_3 = C_4 X_3$$

Where (x_1, x_2, x_3) are the current coordinates of a specific point in the representative unit cell, while its initial coordinates are (X_1, X_2, X_3). C_1 to C_4 are the constants of the linear transformation, which can be related to the lattice parameters as

$$C_1 = \frac{L_1}{L_{1_0}}$$

$$C_2 = \cot\eta - \cot\eta_0$$

$$C_3 = \frac{L_2 \sin\eta}{L_{2_0} \sin\eta_0} \tag{3-18}$$

$$C_4 = \frac{L_3}{L_{3_0}}$$

The partial derivative of the deformed coordinates with respect to the initial coordinates defines the deformation gradient as

$$dx_i = \frac{\partial x_i}{\partial X_J} dX_J, F_{iJ} = \frac{\partial x_i}{\partial X_J} \tag{3-19}$$

Therefore, the deformation gradient can be written as

$$\overleftrightarrow{\mathrm{F}} = F_{iJ}\overrightarrow{\mathrm{e}_i} \otimes \overrightarrow{\mathrm{e}_J} = \begin{bmatrix} C_1 & C_2 & 0 \\ 0 & C_3 & 0 \\ 0 & 0 & C_4 \end{bmatrix} \tag{3-20}$$

The local changes in distances can be obtained from the Cauchy-Green tensor as

$$d\mathrm{x}^2 = d\mathrm{X}\,.\,\mathrm{C}\,.\,d\mathrm{X} \tag{3-21}$$

Where the Cauchy-Green deformation tensor is defined as

$$\mathrm{C} = \mathrm{F}^T\mathrm{F} \tag{3-22}$$

3.9.5.3 Constitutive equations of rigid body reconfiguration

Neglecting the viscous damping effect of hinges and assuming an isothermal process of deformation, we can assign a Helmholtz free energy to the material, $\Psi(\mathrm{F})$. We can obtain the first Piola-Kirchhoff stress tensor, P, from

$$\mathrm{P} = \frac{\partial \Psi(\mathrm{F})}{\partial \mathrm{F}} \qquad \text{or} \qquad \mathrm{P}_{aA} = \frac{\partial \Psi}{\partial F_{aA}} \qquad \text{for } A, a = 1,2,3 \tag{3-23}$$

Which can be converted to the Cauchy stress tensor through

$$\sigma = J^{-1}\mathrm{F}\mathrm{P}^{\mathrm{T}} \tag{3-24}$$

Where J is the Jacobian of the deformation or the determinant of F. Moreover T denotes the transpose operation. We confine our analysis to the rigid rotation of the faces around their connecting hinges. In this case, the deformation takes place solely in the hinges. Hence, a change in energy can be attributed to a change of the dihedral angles, and the Helmholtz free energy can be written as

$$\Psi = \frac{1}{V}\sum_{i=1}^{n} \Delta E_i \tag{3-25}$$

Where V denotes the volume of the unit cell, n is the number of equal-length hinges and E is the energy of the hinge. The volume of the unit cell can be written as

$$V = L_1 L_2 L_3 \sin\eta \tag{3-26}$$

If the hinges are considered linear, the energy expression for the hinges can be simplified as

$$\Delta E_i = \frac{1}{2} k_i (\theta_i^2 - {\theta_i}_0^2) \tag{2-27}$$

From relations S21 to S25, we can obtain the constitutive relations of the rigid body deformation.

3.9.6 Finite element model

To better capture the deformation mechanism of our reconfigurable patterns, a finite element model is developed in ABAQUS (Dassault Systemes). Conventional bar and hinge formulations developed for origami-based structures fail short in assessing the response of our systems because the so-called bar and hinge models assume the edges do not undergo any flexural deformation. However, in our patterns bending occurs along the free edges of the panels. In addition, the study of contact in simplified origami formulations is challenging, motivating our choice to resort to a fully detailed finite element analysis.

3.9.6.1 Details of Finite Element Modelling

We model each panel as a shell with thickness much smaller than the in-plane geometric dimensions of the panel. We have used S4R shell elements to mesh the panels (Figure 3-16A) after ensuring mesh size convergence, and the coincidence of nodes on the two edges of the hinge (detailed view in Figure 3-16B), enabling the connection of corresponding nodes through connectors.

In Figure 3-16B, two coincident edges are shown with an enlarged distance for visualization purpose. The red ovals emphasize the coincidence of nodes. Figure 3-16C shows a pair connection with nodes in their local coordinate system. Perfect connection is enforced to all nodes ensuring equal translational degrees of freedom. Unconstrained here is only the relative rotation, θ_i, between corresponding nodes the unit vector $\hat{\mathrm{e}}_{\mathrm{t}}$. Here θ_i^n refers to the hinge rotation of the n^{th} node on the i^{th} edge.

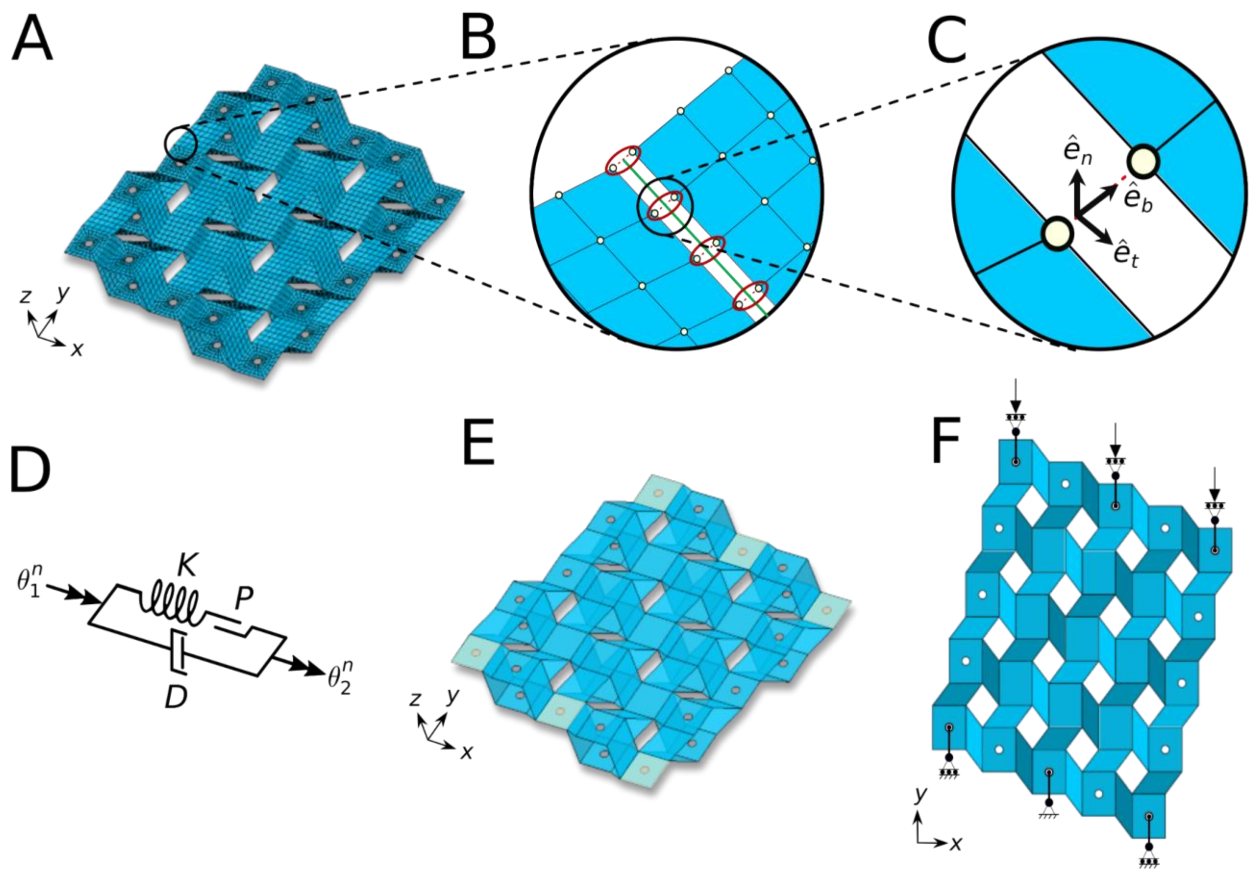

Figure 3-16 Details of finite element analysis. **A** Finite element model of a double layer 5×5 N_4 pattern. **B** Hinge magnified to better visualize the connection details. Coincident points of adjacent portions connect via corresponding constraints. Red ellipses emphasize the application of coincident points, and green line shows the rotational axis direction of the hinge. **C** Details of a connection showing unit vector directions of a connection. All displacement DoFs of the two coinciding points are constrained except the rotation about $\hat{e}_t$, which is allowed. **D** Reduced order model of a joint including elastic, viscous, and plastic components. Reduced order model applied between rotational DoFs about $\hat{e}_t$ of coincident points in **C**. **E** Double layer 5×5 N_4 pattern. Highlighted faces correspond to the locations where boundary conditions are applied. **F** Double layer 5×5 N_4 pattern with visualization of applied boundary conditions.

We adopt a simplified model Figure 3-16D to describe the behavior of the rotational connector between coincident nodes of panels with overlapping edges. It consists of an elastic element acting connected in series with a plastic element, and a dashpot acting in parallel so as to capture the viscoelastic behavior of the hinge. The choices of these model elements stem from observations of the experimental response of a hinge made of paper and composite samples (see Section 3.9.10). For small rotations, the hinge elastically returns to its original configuration upon load removal. As we increase the initial rotation, the hinge shows a permanent fold indicating a permanent set indicating the occurrence of plasticity. In response to a complete fold, the hinge exhibits a lag reminiscent of a viscous effect. For these reasons, we have adopted a model to incorporate elastic, plastic and viscous effects.

For the simulation of the multi cell material of Figure 3-16E, we apply the boundary conditions on the faces on the middle plane of the specimen. The DoFs of the nodes on the circumference of the hole are kinematically constrained to the center point. The boundary conditions are applied on the center nodes of the holes (Figure 3-16F). The displacement is constrained along the y and z axes of the coordinate system. In addition, we fix the middle node on the bottom row along x axis to prevent the specimen from rigidly sliding along this direction.

To model the friction caused by the sliders and the rails, we define a translational connector between the center nodes of the holes and a fixed reference point on the x axis (Figure 3-17A and Figure 3-17B). To associate the displacement of the center of a hole to the points laying on its circumference, we use a constraint (LINK in ABAQUS) that allows rotation and prevents the node from radially translating with respect to the center (Figure 3-17C). The role of this constraint replicates to action exercised by our experimental frame that attaches the sliders to the panels through pins (See Sections 3.6 and 3.9.14). The coefficient of friction is 0.05, similar to the coefficient of friction between zinc alloy and Teflon, the materials used in the corresponding elements of the experimental apparatus. The friction between the rail and the sliders is modeled as a separate linear constraint between the center point of a hole and an arbitrary fixed point (Figure 3-17D).

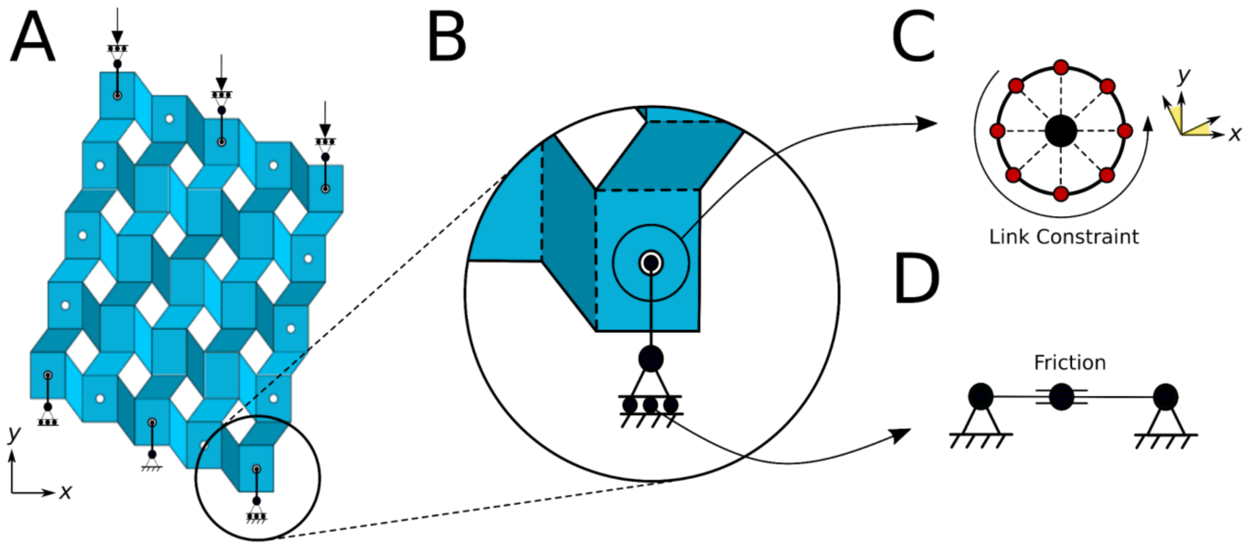

Figure 3-17 Details of connections. **A** A 5×5 N_4 pattern with mounting points. **B** Details of sliders and frame. **C** Connection detail of slider and mounting panel, where a link constraint connect the panel to the pin. A link constraint maintains the distance between the circular hole and the center point. Friction is here neglected as an undersized pin is used in the experimental set up to connect the panel to the sliders. **D** In the finite element model, the sliders are modelled as linear constraints as in the experiments they have a low coefficient of friction; a coulomb friction model is used for the linear slider.

We have developed an in-house python code that generates the model in ABAQUS. The code receives the geometric parameters and the initial configuration as input. In addition, the material properties including Young's modulus and hinge properties are also another set of input for the code. The code generates and allocate the panels in the pattern, besides defining the hinges between the connection nodes.

3.9.6.2 Imperfections

The specimen reconfiguration involves both rigid-folding as well as deformation of its constituent elements. The former pertains to the rotation of the faces P_1, P_2, and P_3 about their joint hinges with P_4 (Figure 3-18A) the rotation continues until P_1 (and P_1') and P_3 (and P_3') prevent from further rigid folding due to the smaller h_1 than h_2, the height of P_2 (and P_2'). The latter, on the other hand, mainly stems from the displacement caused by the snap-through instability of P_2 (and P_2') panels.

To capture the post-instability response of the specimen, we impose an initial imperfection to P_2 (and P_2') to guide the search of the solution (Figure 3-18B). As customary done, for the initial imperfection we adopt a fraction of the spatial displacement obtained from the analysis of the buckling modes of a parallelogram with hinged edges. As shown in Figure 3-18C, we assume the top and bottom edges are hinged and their displacement is prevented along the *x* axis, whereas the rotation about that axis is allowed. The other two edges are assumed free (Figure 3-18C). Figure 3-18D depicts the first four mode shapes under compression along the *y* axis. Each color illustrates a value of the out-of-plane deformation of the panel. The red line in modes 2 to 4 denotes the line of zero displacement.

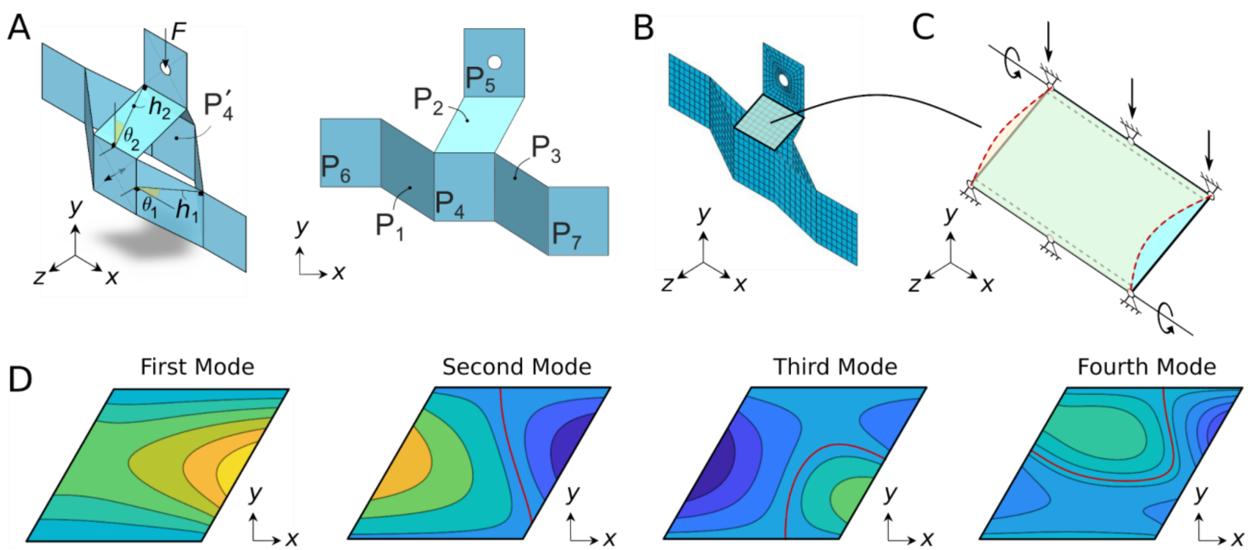

Figure 3-18 Implementing inperfections. **A** Single snap unit with panels and heights of the parallelogram faces. Snap-through instability is caused by the difference between h_1 and h_2. **B** Finite element model of single snap unit, where faces are modeled as shells and meshed with S4R elements. **C** A small imperfection is assumed in our models to capture the post-snap-through behavior of the unit and represents the first mode of buckling of a parallelogram face with opposite edges hinged and undergoing uniform force on its planar edge. **D** Mode shapes of parallelogram face, where the contours visualize the out-of-plane displacement. In red is the curve with zero-displacement.

For our analysis we assume the imperfection is a multiple of the first mode with the largest amplitude equal to 5% of the thickness of the panel. The deformation type of the panel is shown in Figure 3-18C. Once obtained from the buckling mode analysis, the imperfection is directly inserted in the ideal model of the panel.

3.9.7 Deformation regimes

This section provides additional details on the finite element analysis of the single snap unit. The study here focuses on the cases where $\lambda = 90^{\circ}$. As discussed in Section 3.4, the contact between the faces plays a key role in the mechanical response of the single snap unit. Figure 3-3 reports the results of our parametric study on models with prescribed values of $\bar{a}$ and $\bar{b}$. The energy metric maps identify four regions, each corresponding to the occurrence of either contact and/or snap-through instability. In this section, we provide additional snapshots of the deformation history of the cases studied in the main text.

Figure 3-19 presents the representative cases along with their load-displacement behavior. snapshots corresponding to points along the force-displacement curve are included. Figure 3-19A shows three dimensional snapshots of the deformation history for the case with $\bar{a}$ = 1 and $\bar{b}$ = 1.25, where we can clearly observe the snap-through instability of the inclined panels. Four cases have been identified in the text with respect to the nature of contact between panels in a single snap unit.

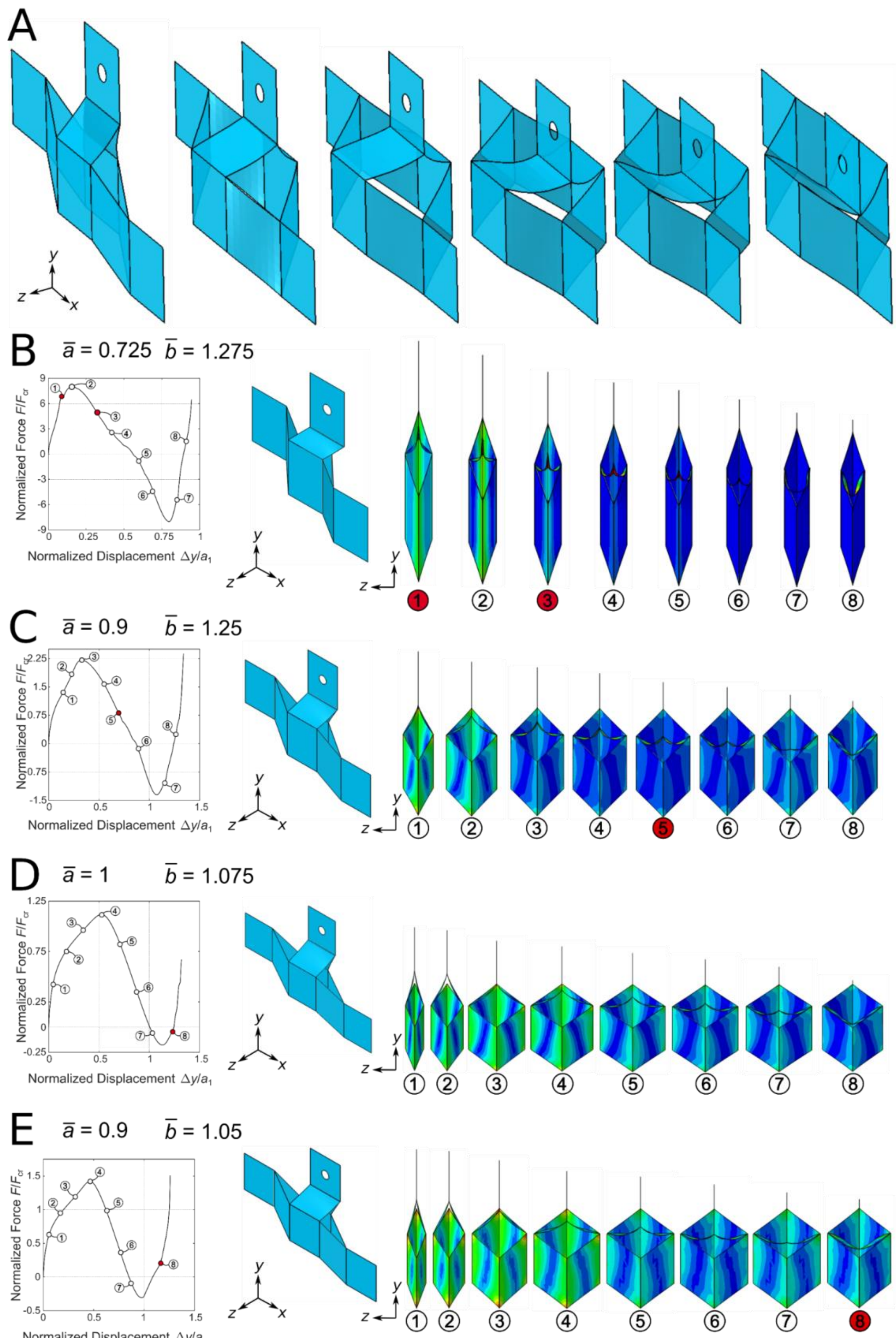

Figure 3-19 Snapshots of a single snap unit undergoing snap-through instability **A** with $\bar{a}$ = 1 and $\bar{b}$ = 1.25 undergoing snap-through instability. **B-E** Deformation cases and load-displacement curves shown on the

left-hand side, three-dimensional view of the single snap unit is shown in the middle, and snapshots of 8 time history points along the force-displacement curves on the right-hand side Red dots on the curves represent the points where contact is established between faces.

- Case 1: Contact here is established prior to instability (Figure 3-19B). Panel P_2 and P_2' deform significantly and come into contact before their instability takes place. As our unit undergoes snap-through, the contact area between P_2 and P_2' reduces until a new point of contact is formed between another pair of panels, i.e., P_2 with P_3, and P_2' with P_3'.
- Case 2: Figure 3-19C describes the second case where contact is formed during snap-through instability. Here, the flexural deformation of P_2 and P_2' during instability is sufficiently large to allow contact between P_2 (and P_2') and P_3 (and P_3').
- Case 3: Figure 3-19D shows the case where a post-snap contact occurs at a negative value of the applied force during the loading cycle. Contact here forms first between P_2 (and P_2') and P_3 (and P_3'), followed by contact between the edges of P_5 and P_7.
- Case 4: Figure 3-19E depicts the case where contact occurs in the post-snap response at a positive force value. Here, the sequence of contact is similar to that of the previous regime, first between panels P_2 (and P_2') (see the onset of contact in inset) and P_3 (and P_3') and then between the edges of P_5 and P_7.

3.9.8 Force and Energy metrics of interacting units

Section 3.5 in the main text discusses the interaction of two snapping units from results obtained from FEA. In this section, we compare the results from experiments and computations for a representative specimen with $\bar{a}$ = 1 and $\bar{b}$ = 1. Figure 3-20A shows the characteristic stiffnesses, forces, energies of the snap-through instabilities in qualitative plot of the loading/unloading curve for a pair of interacting units in the forward and backward cycle. The definition and physical significance of these metrics have been presented in the main text.

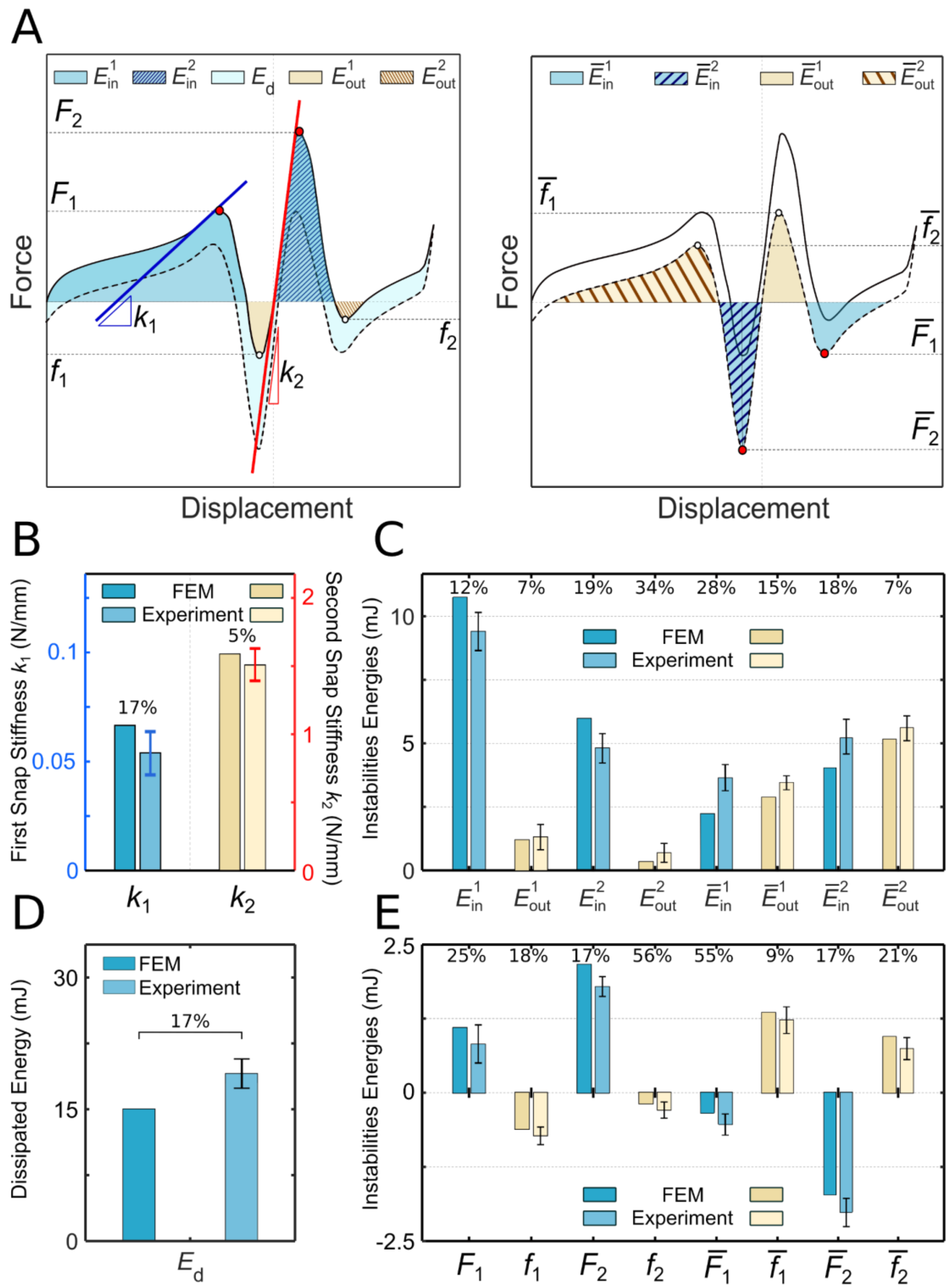

Figure 3-20 Comparison of experimental and computational results for interacting snap-through instabilities **A** Definition of characteristic metrics, i.e., stiffnesses, forces, and energies during forward and reverse loading directions for interacting units. **B-D** Comparison of finite element analysis and experiment for (**B**) Stiffness, (**C**) Characteristic energies, (**D**) Dissipated energy, and (**E**) Characteristic forces. Percentage of deviation between finite element analysis and experiment are shown for each characteristic metric.

In our experiments we tested five samples, whose results are compared with the simulation results for each performance metric Figure 3-20B shows the stiffness of the structure prior to each instability. As discussed in the main text, due to the interaction of two snapping units we observe that the stiffness of the second instability is significantly larger than the first regardless of the loading cycle. The difference between the experiment and simulations can be attributed to manufacturing imperfections. The characteristic energies of the instabilities for two interacting units are presented in Figure 3-20C, where we observe the good alignment of our experimental data to the FEA results.

The difference between the two can be attributed to several factors. First, manufacturing imperfections causing deviations from the ideal (as-designed) behavior. Given we have minimized the effect of this imperfection by ensuring the removal of air bubbles between the cover tape and the core during the manufacturing, we attribute the cause of the deviation to the delamination between the cover tape and the mylar core. The second reason is the friction between the slide bearings and the guide pins, which we intentionally attenuated by introducing lubricant between the brass sliders and the guide pins prior to the testing.

The dissipated energy in a loading cycle is the area enclosed by the forward/backward loading paths in Figure 3-20A. Figure 3-20D presents the comparison between the dissipated energy in a loading cycle from both simulations and experiments. Although the experimental data parallels those from simulations, a deviation exists and can largely be attributed to the friction of the sliders and the guiding pin in the experimental setup. Finally, Figure 3-20E compares the forces of instability recorded from the experiments and the simulations, the former in acceptable agreement with the latter.

3.9.9 Experiments

3.9.9.1 Base material considerations

Paper, characterized by its affordability and extensive variety of styles and qualities as well as its capacity to readily create pliant creases, is an optimal choice for the creation of origami specimens. Nonetheless, due to its composition consisting of a fairly oriented arrangement of natural fibers, a piece of paper conceals intricate attributes. Furthermore, the stiffness properties associated with folding are contingent upon the type of paper material, as well as the nature of the crease method implemented, such as perforation, hemming, or scoring. Many challenges of characterizing paper as the base material for origami has been discussed [52]. In particular, the rest angles of the hinges depend largely on the history of the deformation.

In addition to the challenges documented in the existing literature [52], our preliminary experiments involving multistable paper-based origami patterns have uncovered a multitude of additional challenges. As detailed in the main text, one of these challenges relates to the occurrence of a snapping instability, which involves the bending of the origami panels. Paper-based specimens exhibit a limited elastic range and undergo permanent flexural deformations during snapping instability. This permanent deformation introduces a novel dimension of complexity in the emergent behavior of the entire specimen.

Furthermore, the deformation of the panels is notably contingent upon the sequence of snapping instabilities. In each cycle, the panels within a structure exhibit varying flexural characteristics as they experience dissimilar deformation from the preceding cycle. Panels undergoing the initial instability experience the least inelastic deformation, while those subject to the final instability event encounter substantial deformation from the previous cycles.

The progressive plastic damage of these panels poses an additional challenge. In each loading cycle, the panels and perforated hinges gradually experience irreversible damage, which subsequently impacts their mechanical response in the subsequent loading cycles. Panels subject to the highest flexural deformations in a particular cycle exhibit the greatest initial imperfections in subsequent cycle due to the irreversible inelastic deformation accumulated in the previous cycle. Consequently, the maximum load required to induce instability in imperfected panels is significantly reduced compared to panels in other rows. The order of instabilities is also influenced by the history of instabilities in the previous cycles.

Finally, during the reverse loading cycles, the panels become entangled, leading to an increase in the force necessary to induce instability. Our experimental investigation of paper samples reveals that the hinges lack the necessary strength and tend to tear under load during the very first loading cycle.

3.9.9.2 Base Material Characterization

We tested five samples of the base material under tension. A Instron tensile tester (5965 series) equipped with a 2kN load cell is used to obtain the Young's modulus. The specimens follow the standards ASTM D882-10, i.e. tensile properties of thin plastic sheets. Figure 3-21A shows the tensile sample, made of thin Mylar core of 0.127 mm covered on both sides with 0.045 mm thick tapes. The rectangular sample is made by laser cutting the three-layered stack. Tensile testing is conducted at the grip separation rate of 25 mm/min. The tensile response of a representative sample is shown in Figure 3-21B suggesting a linear elastic response within the tested range of strain. Table 3-1 summarizes the results obtained from the tensile specimens, showing excellent repeatability.

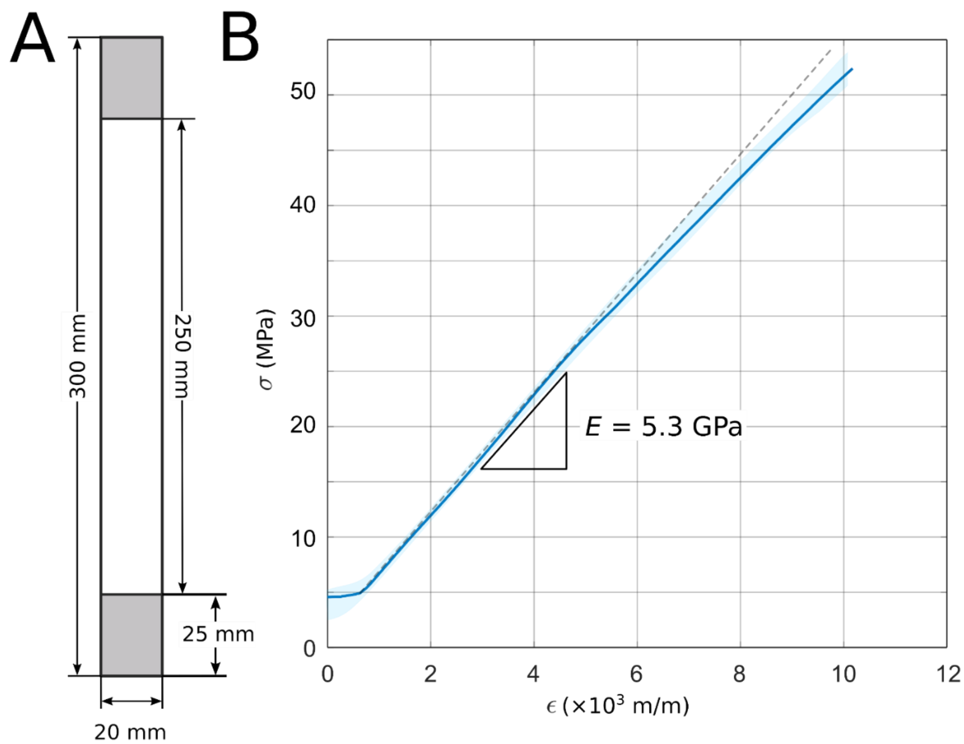

Figure 3-21 Tensile testing specimen and its response. **A** Tensile test specimen as per ASTM D882-10, **B** Tensile behavior of the sample

Table 3-1 Test results for five samples

Specimen number	1	2	3	4	5	Average	Standard Deviation
Young's Modulus	5.3	5.25	5.21	4.96	5.36	5.21	0.15

3.9.10 Hinge characterization

Hinges play a major role in governing the behavior of our foldable specimens. To simulate the reconfiguration process and calibrate the parameters of the reduced model in Figure 3-22D, we characterize the stiffness and viscous behavior of the hinges. We assume that each fold line is made of a series of rotational hinges, and assume the behavior of each hinge can be captured by a reduced order model made of an elastic element acting in series to a plastic element along with a viscous damper (Figure 3-22D).

Two types of materials and fabrication methods are studied in this work. The first is paper, and the corresponding specimen are fabricated by perforating the paper sheets through a laser cutter (Figure 3-22A). The second is a composite material with a Mylar core sandwiched between two tapes (3M 336 polyester tape) (Figure 3-22B); the corresponding fabrication process involves first the laser cut of slits in the Mylar core, and then the coating of both sides with tape. As a result, the two layers of tape only make up the hinge. Our choice to examine this composite specimen is that previous studies have shown the fairly complex behavior of paper, which has an orientation dependent elasto-visco-plastic behavior with an anisotropic damage that cumulates during repeated folding/unfolding cycles.

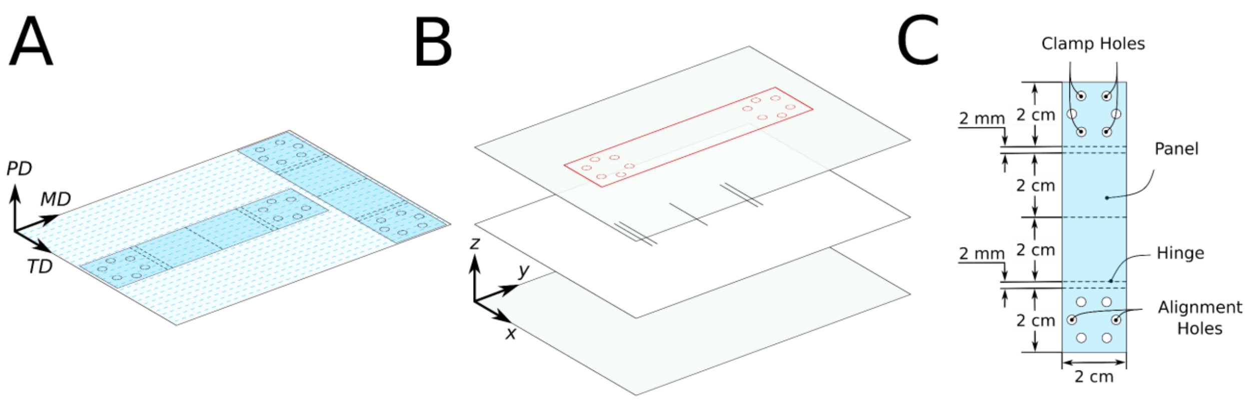

Figure 3-22 Specimen fabrication methods, **A** Paper sample with indication of machine direction (MD), transversal direction (TD) and perpendicular direction (PD). Paper is an orthotropic material much stiffer (higher Young's modulus) and stronger (higher yield strength) in MD than in TD. **B** Composite sample made in a multi-step fabrication method; first the slits are laser cut on the mylar core, then two cover layers made of tapes are applied to two sides of the mylar core; finally, the contour of the sample and the holes for fixing and aligning the sample in the experimental test setup are laser cut. The final contour and the holes are shown in red. **C** Specimen dimensions with two sets of holes. The first is used for aligning the specimen with the test setup; pins with a tight tolerance run through the alignment holes to ensure the correct alignment of the sample. The second is used to clamp two of the faces between panels that fix the sample in the experimental setup.

The specimen is initially flat with rectangular snape and dimensions a 20 mm ×84 mm (Figure 3-22C). The specimen consists of four 20 mm ×20 mm panels with six holes designed to clamp two panels of the specimen. Two holes serve as alignment holes. A pin runs through each of these holes to ensure perfect alignment of the specimen and the fold line with respect to the testing setup. The other four holes on the clamp panel are intended for four screws that clamp a stiff acrylic panel on the specimen.

Figure 3-23 shows the setup for testing the bending behavior of the hinge. The setup consists of two assemblies designed to be fastened in the grippers of a tensile testing machine (Figure 3-24). In this study we have used an Instron model 5965 equipped with a 10 N load cell to perform tests on five samples. Figure 3-23B depicts the front view of the setup with the specimen. Two sets of panels are used to mount the specimen on the testing setup. The clamp panels hold the clamp faces of the specimen. The support panels ensure the hinges are aligned along the z axis of the coordinate system as shown in Figure 3-23A and Figure 3-23B. To ensure the proper mounting of the panels we introduce several holes. By aligning the holes, we ensure the proper alignment of platens, panels and specimen. The first set of alignment holes (Figure 3-23B) are used to ensure the platens are properly mounted on the gripper. The second set aligns the two platens while the third set ensures the specimen, the support plate and the clamp plate are positioned appropriately.

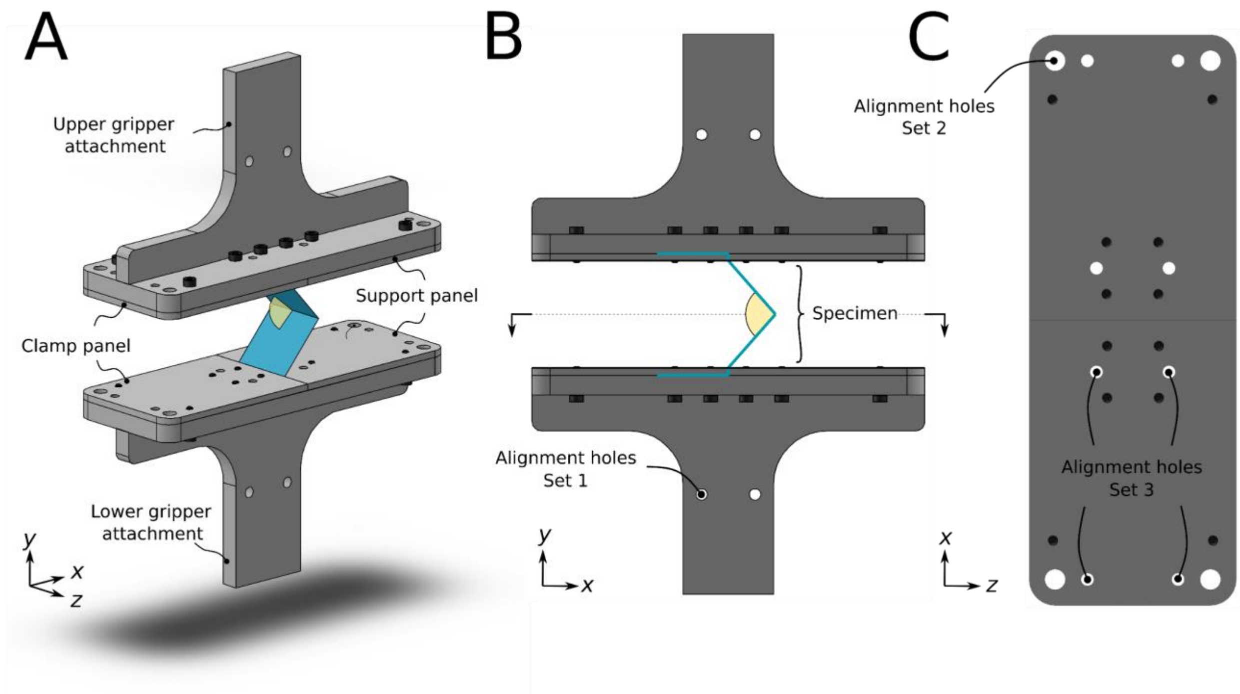

Figure 3-23 Bending test setup. **A** Bending test setup visualizing also the specimen clamped between the clamp panels and the platens. The setup features two support panels which ensure the alignment of the sample B Front view of the bending test setup designed to be clamped in the grips of a tensile tester. Two alignment holes accommodate aligning pins which ensure the *y* axis in **B** is aligned with the axis of the tensile tester. **C** Top view of the platens of the bending test setup. Two alignment hole sets are shown. The alignment holes set 2 are intended to ensure the two platens are parallel. Prior to testing four alignment pins run through these holes from the upper platen to the lower one. However, after the grips are fastened the pins are removed. The alignment holes of set 3 are used to ensure the specimen is mounted correctly on the testing setup.

Once the setup is mounted on the tensile testing, the movement of the crosshead of the tester cause the folding and unfolding the specimen, as shown in Figure 3-24. The process starts from a state where the load cell reads a zero-force value and continues with the crosshead moving downward to induce the hinge folding.

To calibrate the parameters of the reduced model in Figure 3-16D, we cyclically load the specimen, where the crosshead moves first downward and then upward (reverse direction). This pattern is repeated until the specimen response stabilized. Figure 3-16D shows the stable response only, neglecting those of the intermediate cycles. The difference between the initial, the intermediate and the stabilized folding cycles is negligible for the composite sample.

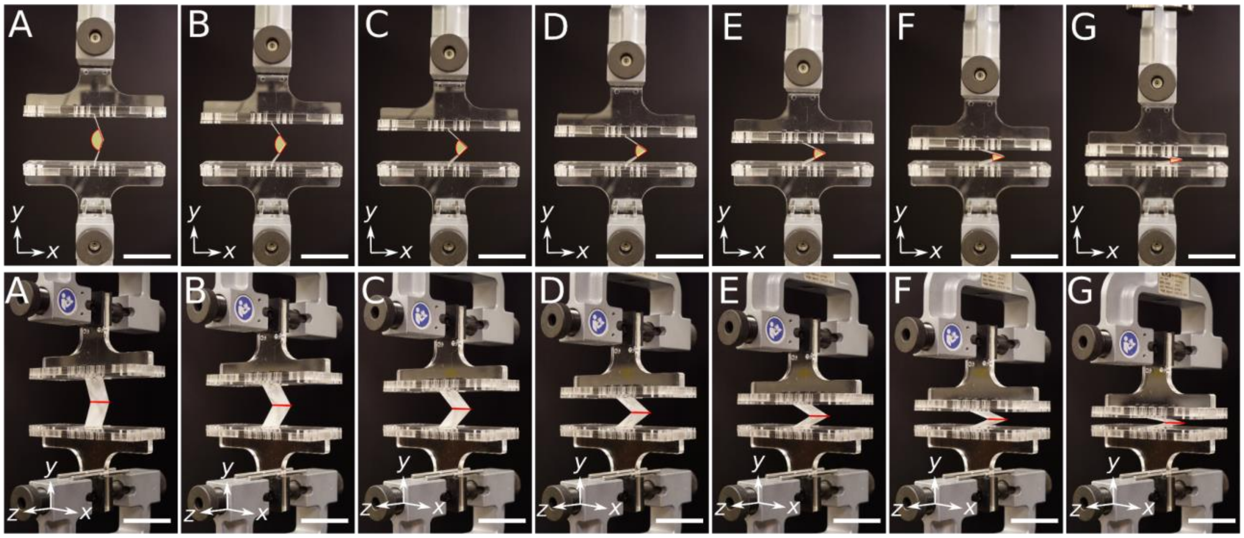

Figure 3-24 Bending test. **A-G** Bending testing of the specimen at sequential stages of compression. The setup is mounted on a tensile tester with upper and lower platens fastened in the upper and lower grips of the tester. The top row shows the front view snapshots while the bottom row presents the three-dimensional view of the setup and the specimen. The red line in the figures of the bottom row emphasizes the location of the hinge during folding.

Figure 3-25A shows the counterpart finite element simulation of the experiment shown in Figure 3-24. The coincident nodes of the adjacent panels in the model are connected with the reduced order model of the hinge shown in Figure 3-16D. Figure 3-25B shows the stabilized cyclic folding/unfolding behavior of a composite specimen after 3 cycles. The experimental results are visualized with a light blue shading and the dashed line represents the mean response. The black curve describes the calibrated response of the finite element simulation, where the viscoelastic behavior is evident and the plastic response almost negligible. On the other hand, for the paper sample, the comparison of the experimental results and the finite element response shown in Figure 3-25C and Figure 3-25D for two direction shows the sizeable role of plasticity in the response of the paper specimen.

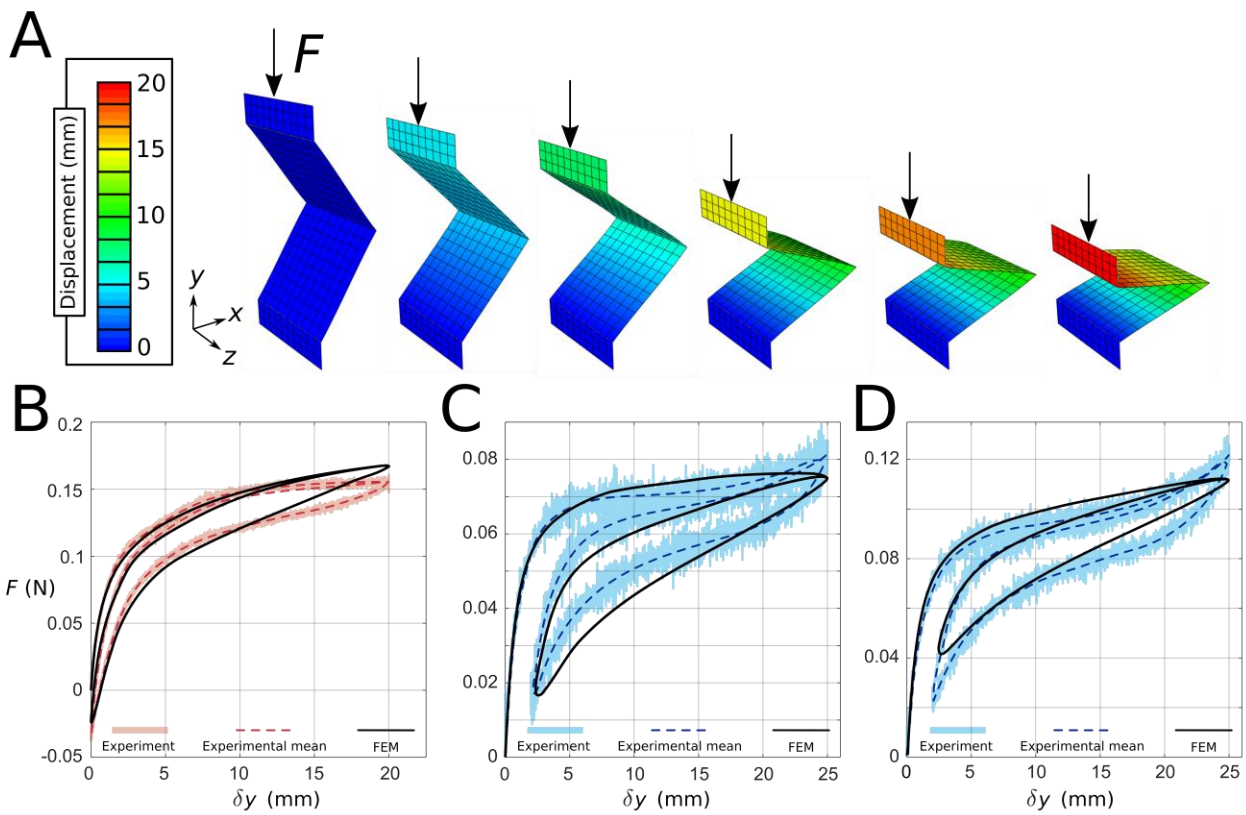

Figure 3-25 Comparison of FEM and experiment results of the bending test. **A** Finite element model of bending specimen, where a connector similar to that shown in **Figure 3-16** is applied to coincident nodes of adjacent panels. **B** Load-displacement curve of composite specimen with negligible plastic behavior. **C** Load-displacement curve of paper specimen cut aligned with the transverse direction (TD) in **Figure 3-22A**. **D** Load-displacement curve of the paper specimen cut aligned with machine direction (MD) in **Figure 3-22A**.

Figure 3-26 shows the details of the experimental set up we developed to test the snap-through instability of our single unit. The calibrated coefficients are summarized in Table 3-2 for the composite and paper specimens.

Table 3-2 Coefficients of calibration for the finite element model

Sample	Rotational Stiffness (Nmm/mm)	Viscous Component (Ns/rad)	Plastic Component (Nmm/mm, η)
Composite	0.0459	0.0275	-
Paper (MD)	0.0312	0.459	0.0293, 0
Paper (TD)	0.0254	0.368	0.0221, 0.02

3.9.11 Single snap test setup

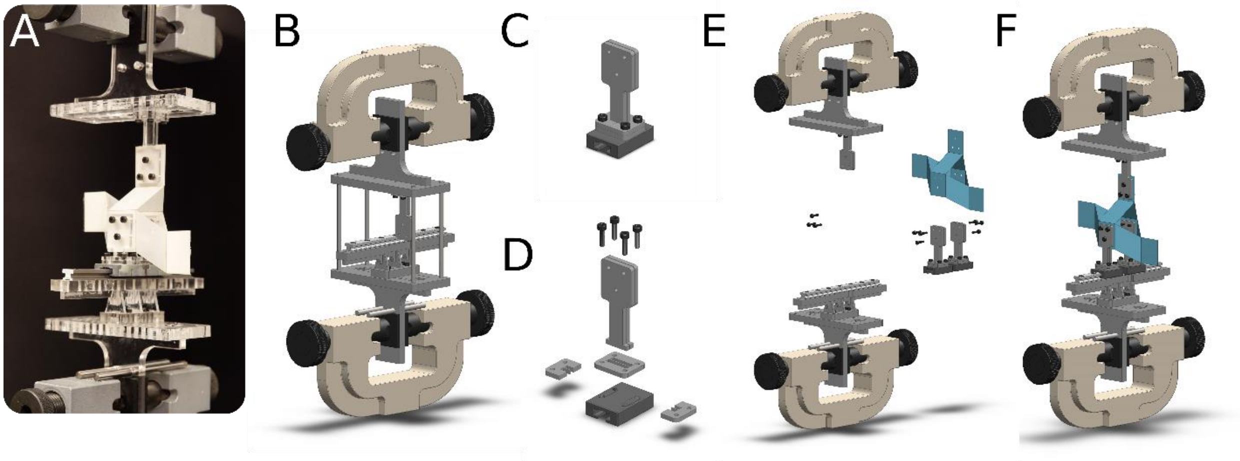

Figure 3-26 Single snap unit test setup. **A** Single snap testing setup with upper and lower platens fastened to the grips of a tensile tester. **B** Alignment of upper and lower platens. **C** Slider assembly consisting of a linear slider made of Teflon, a pair of acrylic panels, attachment panels and screws **D.** Exploded view of slider assembly. **E** Specimen mounting process. First the sliders are screwed to the opposite faces of the specimen; next, the specimen is placed on the linear guide; then the upper grip is lowered to place the remaining face of the specimen between the mounting panels on the upper platen. Finally, the upper mount faces are screwed to the sample. **F** Single snap testing setup with inserted specimen.

Figure 3-26A shows the assembly of the testing setup on our tensile tester. The first set of aligning pins are used to ensure that the two platens are parallel and their normal is coaxial with the axis of the tensile tester (Figure 3-26B). With the lower platen as the reference, we use the second set of aligning pins to ensure the two platens are parallel. Once the grippers are fastened, we remove the second set of the aligning pins. To mount a sample on a slider, we screw a pair of stiff acrylic panels to each slider (Figure 3-26C and Figure 3-26D). The acrylic panels guarantee that the displacement takes place only along the sliding direction. Figure 3-26E shows the mounting process. First, we screw the central faces of the sample to the acrylic panels of each slider. Next, we slide the sliders along the guide rail to the point where P_5 face aligns with the acrylic faces on the top platen. Then we lower the top platen and finally P_5 is screwed to the acrylic faces of the top platen. Figure 3-26F shows the final assembly of the sample on the test platform.

3.9.12 Testing setup of double snapping unit

To investigate the interaction of two snap-through instabilities, we study the compression/tension behavior of two single snap units acting in series. Figure 3-27 shows the test set up designed for the purpose.

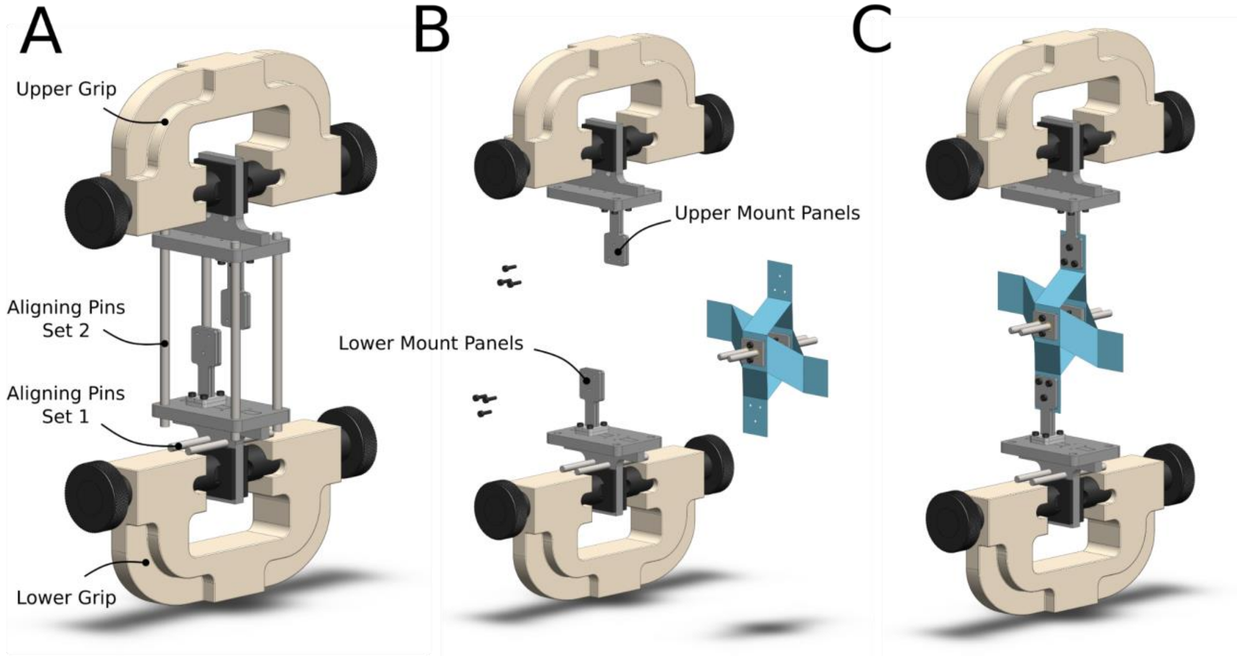

Figure 3-27 Interacting units test setup. **A** Framework mounted on the tensile tester. The first set of aligning pins are used to ensure the axis of the tester and the face of the platen are perpendicular. The second set of aligning pins ensure the face of the platens are parallel and they share a common axis. After alignment, the grips are fastened, and the second set of the aligning pins are removed. **B** Specimen insertion on the tester. The holed faces of the specimen are screwed to the mounting panels of the platens. **C** The specimen consists of two interacting snap-through instabilities mounted on the tester.

Figure 3-27A shows the process of mounting the setup on a tensile testing machine. As with the setup of the single snap unit, also here we use two sets of aligning pins. The first ensures that the faces of the platens are perpendicular to the axis of the tensile tester. The second guarantee the mount panels are at their correct location. The second set of the aligning pins are removed after the grips are fastened (Figure 3-27B and Figure 3-27C). We use two sets of acrylic panels (mount panels) to screw the faces of the sample to the platens of the testing setup, Figure 3-27B and Figure 3-27C. The assembly with the sample mounted on the testing setup is shown in Figure 3-27C.

Figure 3-28 depicts a specimen made of two interacting units. In our experimental setup, we need to ensure the panels P_4 and P'_4, shown in Figure 3-28A, move parallel to their normal direction to obtain the interactions of two snap-through instabilities accurately. To this end, each panel, P_4 and P'_4, is screwed between two acrylic panels (Figure 3-28B). We insert two brass bearings on each set of acrylic panels. Two guiding pins perpendicular to the P_4 run through the brass bearings. Therefore, the panels P_4 and P'_4 can slide along the guiding pins. We screw P_5 and P_9 to stiff acrylic panels that are attached to the upper and lower platens respectively.

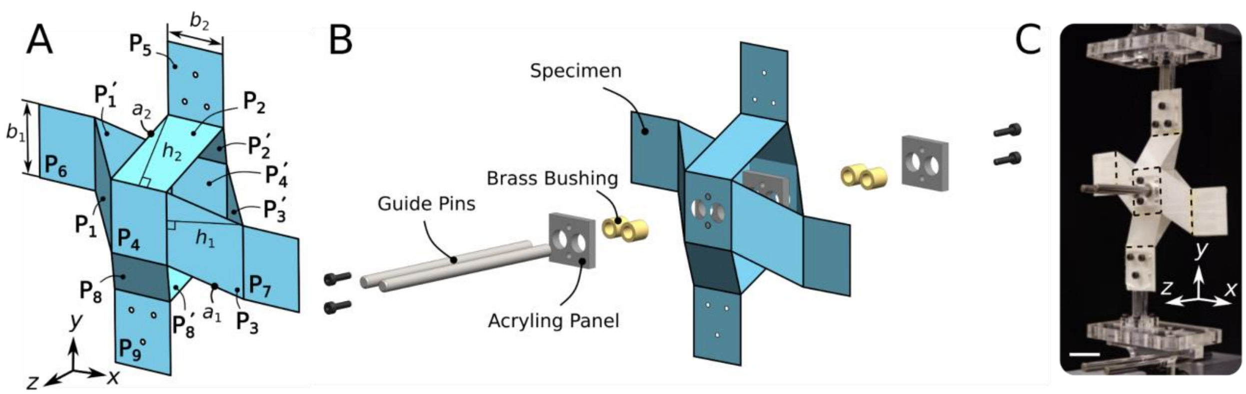

Figure 3-28 Specimen consisting of two interacting snapping units. **A** Specimen made of two interacting units with its geometric parameters. **B** Exploded view of the linear slider assembly. Two sets of brass bushings are mounted on the faces P_4 and P'_4 of **A**. Two acrylic panels are used to mount the brass bushings on the faces P_4 and P'_4. As the faces P_5 and P_9 are compressed in the y direction, the faces P_4 and P'_4 slide along the guide pins. **C** Assembly of specimen and testing apparatus.

The key features of our experimental setup are the linear sliders. Figure 3-29 shows results from our computational and experimental results demonstrating that the removal of the guiding pins make the faces P_4 and P'_4 rotate about x axis (Figure 3-27A) and move out of their initial plane. As a result, the experimental values of stiffness and force corresponding to instability underestimate their computational counterpart representing for a periodic domain.

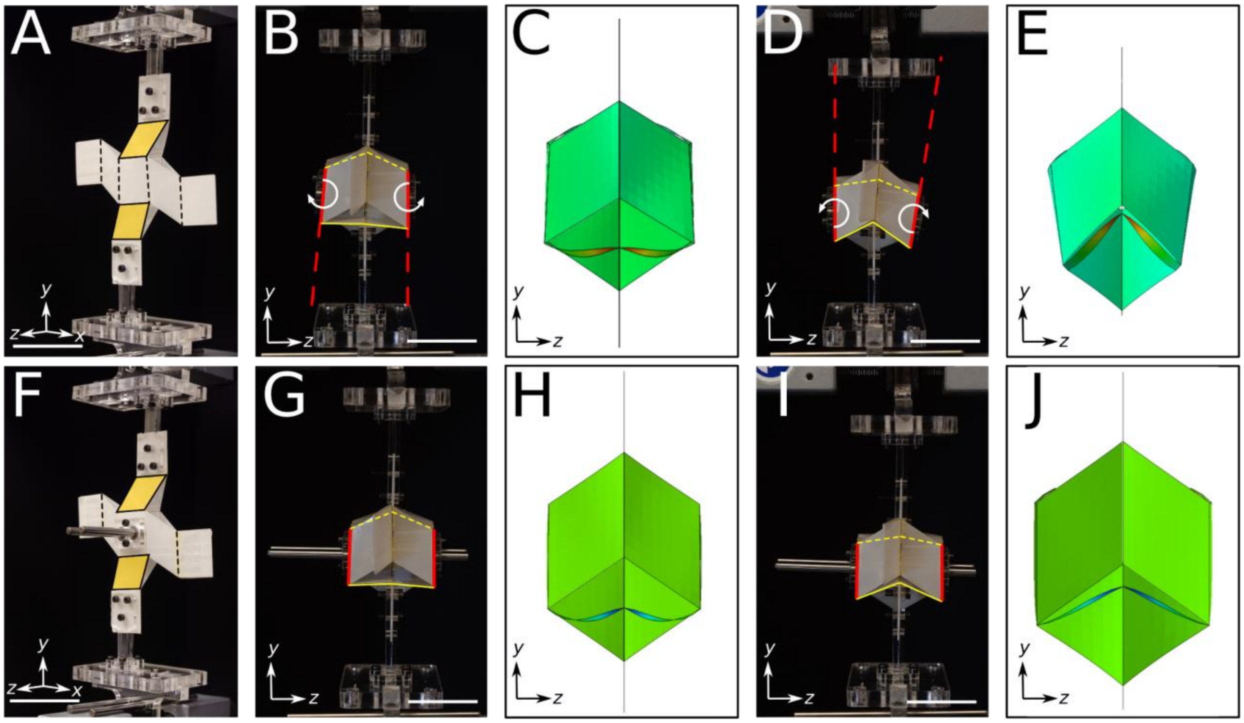

Figure 3-29 Comparison between the behavior of the interacting unit specimen without **(A-C)** and with **(D-F)** guiding pins. **A** Specimen without guiding pin on testing setup. **B** Side view of specimen without guiding pin at the onset of the first snap-through instability. Curved arrows show rotation direction of faces P_4 and P'_4. **C** Side view of specimen shown in **A** at the onset of the second instability. A direction reversal of rotation occurs for faces P_4 and P'_4 from **B**. **D** Specimen with guiding pin on testing setup. **E** Side view of specimen with guiding pin at the onset of the first snap-through instability. As opposed to the previous case, faces P_4 and P'_4 do not rotate about the *z* axis out of their initial plane. **F** Side view of specimen shown in **D** at the onset of the second instability.

Figure 3-29 shows the effect of the guiding pins. Figure 3-29A to Figure 3-29C show the case when linear guides are not used to constrain the rotation of the panels P_4 and P'_4 about *x* axis. As a result, during the first snap-through instability, the panels P_4 and P'_4 rotate to accommodate the distance required for the panels P_8 and P'_8 (Figure 3-29B). During the second snap-through instability, the direction of rotation is reversed as the panels P_2 and P'_2 undergo instability. The rotation of the panels P_4 and P'_4 leads to an underestimation of the force required for snap-through instability. To overcome this problem, the setup of Figure 3-28 is used. When the guide pins constrain the rotation of the panels P_4 and P'_4, as shown in Figure 3-29F to Figure 3-29J, we observe the movement of the panels P_4 and P'_4 away from the plane of symmetry, *x-y* plane, without rotation about the *x* axis.

3.9.13 Specimen fabrication

Our foldable specimens are made by stacking layers of pre-folded materials (either paper or composite). The fabrication process for both materials requires a sequence of steps to enable folding. Paper samples are first laser cut from cardboard paper, and then manually folded along the crease pattern before bonding the mountain faces of a bottom layer to the valley counterpart of the adjacent top layer. This sequence of steps is repeated for each layer, as required.

Since paper samples have a complex anisotropic behavior, we resort to another base material, a polymer sheet that can undergo large deformation and resist breakage upon entanglement. The major drawback of a polymer sheet is the relative high elastic range which makes folding a challenging task, yet we use a method that provide high resilience and prevents the over-stiffening of the hinges.

To fabricate a composite specimen, the process starts with laser cutting guiding holes on the polymeric sheet (Figure 3-30A). These guiding holes serve as a reference to ensure that in the subsequent step the polymeric sheet is placed at the identical position in the laser cutter. The references are of utmost importance to ensure the alignment of the sheets with respect to the laser cutter. Next, guiding pins with tight tolerance are inserted inside the guiding holes and run through the holes of the plates fixed to the laser cutter bed.

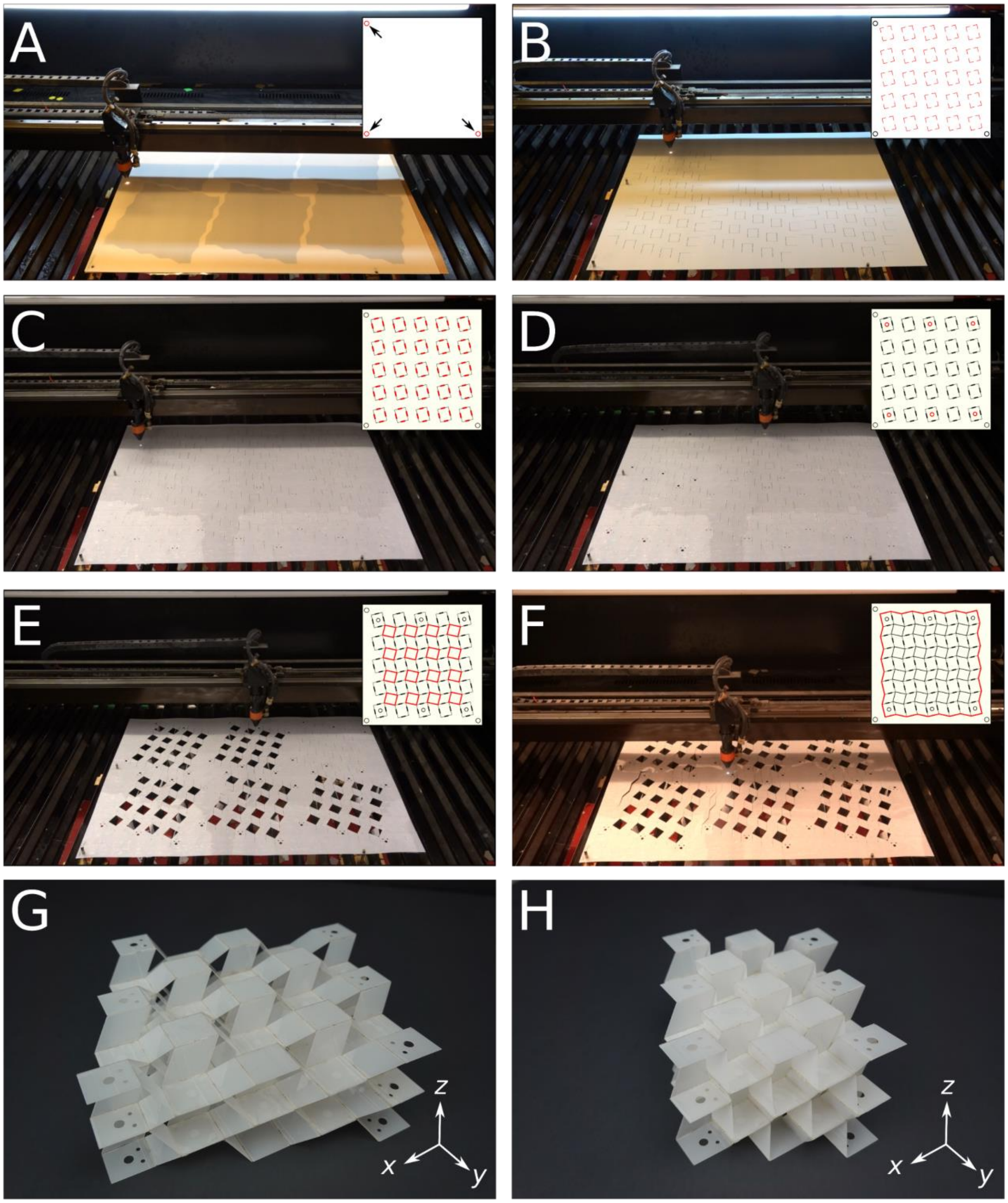

Figure 3-30 Manufacturing process of N_4 pattern with composite sheets. **A** Laser cutting of guiding holes, **B** Cutting of hinges on the Mylar sheet core. A small ligament is left uncut to keep the central polygon in place. After this step, the Mylar sheet is fully covered on both sided with tape, which covers the previously cut hinge pattern and serve as the hinge. **C** The composite sheet made of the Mylar sheet core and the tapes are placed in the laser cutter. The guiding pins fixed to the laser cutter run through the guiding holes of the composite sheet and ensure the appropriate position of the sheet. The remaining ligament of the Mylar core

from the step shown in **B** is cut. **D** Cutting of mounting holes. These holes are intended to mount the sample on the test setup. **E** Cutting the holes in the pattern **F** Cutting the outer contour of the pattern. After this step the patterns are collected from the laser cutter and are manually folded to assign mountain and valley folds; then a double-sided tape is used to bond the adjacent layers. This process can be repeated as required to stack as many layers as needed. **G** A stack of three layers in pre-snap-through configuration **H** The same stack once all the units are set in their stable post-snap-through configuration.

In the second step, we laser cut the hinges. We leave a small ligament uncut to avoid detachment of the faces surrounded by the cut pattern of the hinges, Figure 3-30B.

Mylar is a hard-to-bond polymer and it may pose challenges as the powder residual released by laser cutting cannot be easily removed. To ascertain an acceptable bonding between layers, after the first step of laser cutting we have cleaned both faces of the Mylar sheet with 75% ethanol in an effort to remove as much debris as possible.

Next, we remove the Mylar sheet and cover both sides with a 0.04 mm thick acrylic tape. The tape covers both the cuts and the faces and serves as hinge in the previously cut regions. The tape shows excellent bonding to the Mylar sheet. We place the covered sheet on the laser cutter bed using the guiding pins as reference. The remaining ligaments are cut in this step, Figure 3-30C. Next, we laser cut the mounting holes, Figure 3-30D. These holes are used to mount the attachment of the sliders. Then the polygonal holes are cut, Figure 3-30E. Finally, the outer contour is cut, Figure 3-30F.

Each layer is manually folded to impart the characteristic mountain-valley fold pattern. Then we use double-sided acrylic based adhesive transfer tape (3M 468MP) to bond the mountain faces from a bottom layer to the valley face of the top layer. We repeat the process to stack as many layers as required.

The translucent nature of the Mylar sheet helps detecting air gaps emerging after layer stacking. These air gaps can be easily removed. In addition, we observe that even with several months of shelf storage, the inter-layer bonding with double side adhesive is sufficiently strong and durable, hence allowing for the repetition of experiments at later stages without compromising the quality of the results.

3.9.14 Testing of tessellated specimens

The properties of a tessellated specimen are tested in compression and tension through a custom-made fixture mounted on our mechanical tester (Figure 3-31). The fixture consists of two platens that carry two guiding rails, that prevent the specimen from lateral displacement. To avoid lateral constraints, we have used a series of sliders that are attached to the faces in the middle plane of the specimen. To ensure the alignment of the platens we utilize two sets of aligning pins (Figure 3-31A).

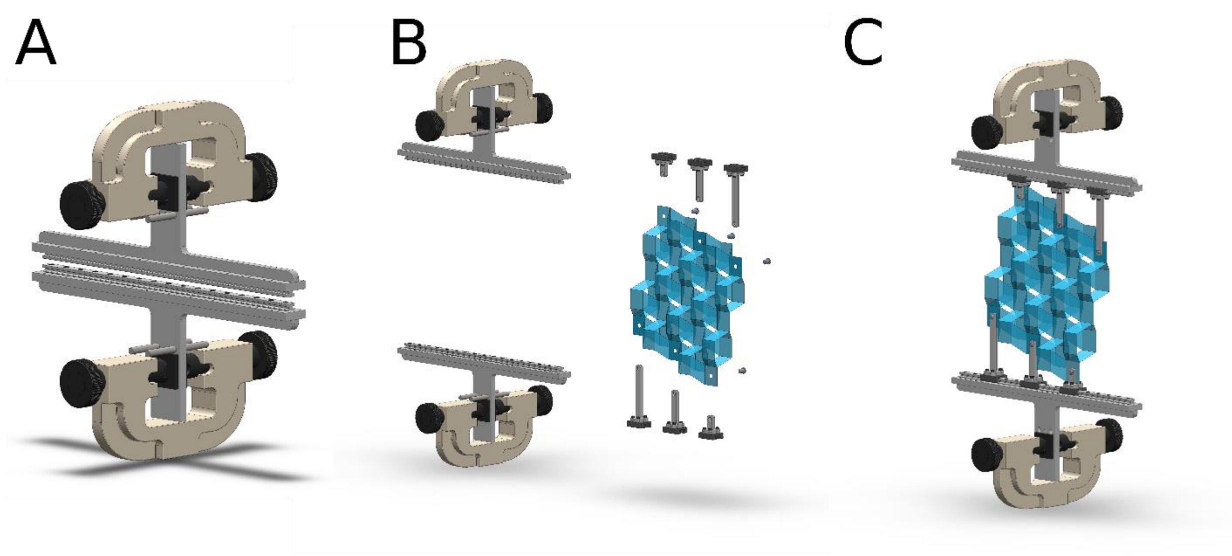

Figure 3-31 Multi-cell specimen test setup. **A** Mounting and alignment of the multi cell testing setup on the grips of a tensile tester. A set of aligning pins on each rail carrier ensures the rail is perpendicular to the axis of the tensile tester. To check the parallelism of the rails, the grips are lowered prior to mounting the specimen. Once the rails are in contact, their parallelism can be verified by inspecting the gaps and the displacement of one end of the pairs with respect to the other. **B** Mounting of the specimen on the testing setup. Three slider assemblies similar to that shown in Figure 3-26C are used on each rail to mount the specimen on the rails. Instead of screws in Figure 3-26, a set of pins are used to connect the panel to the slider assemblies. **C** A double layer 5×5 specimen mounted on the testing setup.

Figure 3-31B shows the mounting of a sample on the tester. We screw links made of stiff acrylic sheets to each slider. To attach acrylic panels to a face on the material, a clevis pin is used, (Figure 3-31B). The sliders guarantee the lateral displacement can be achieved with minimum resistance. The assembly of the specimen on the testing fixture is shown in Figure 3-31C.

3.9.15 Methods for mounting frame

As described in the main manuscript, each sample can be mounted on the fixture at given angles. In this work, we examine two mounting methods as explained in this section.

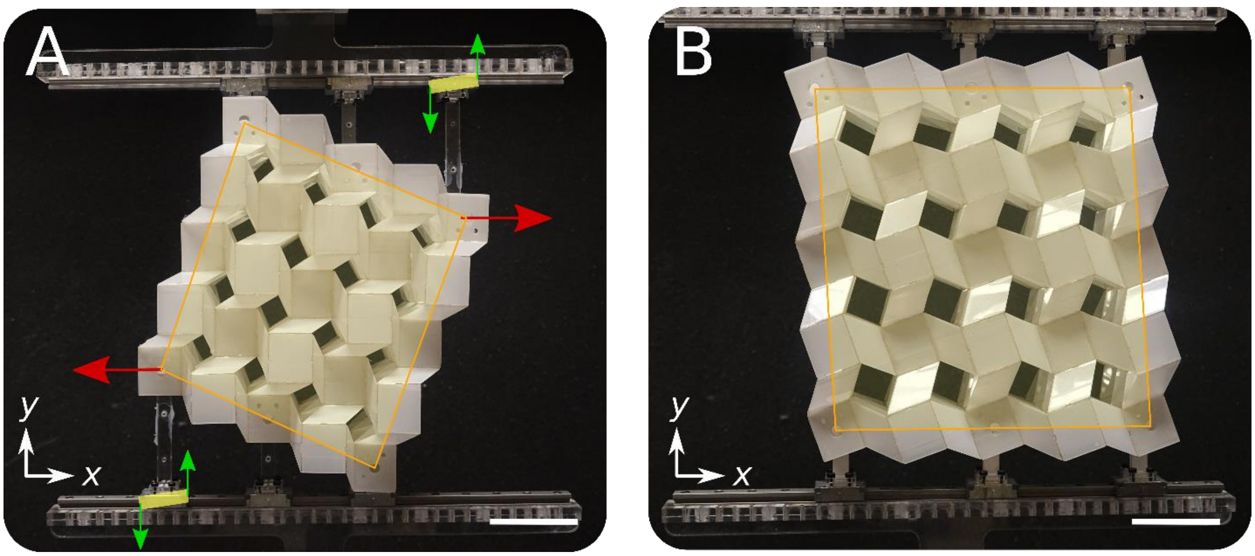

Figure 3-32 Two mounting methods hosting the N_4 pattern. **A** Aligned mounting method where the hinges are parallel to the rails of the testing setup. Here, the slider assemblies consist of distinct heights ensuring the mounting faces remain at a fixed distance from the rails. For lager patterns, the lateral (*x* direction) force exerted by the specimen leads to large forces on the slider due to the clearance of the sliders and the rail. The large normal force at the location of the contact between the slider and the rails lead to large frictions. For this reason, this mounting method is mainly useful for small size specimens or when the sliders does not allow a tilt. **B** Parallel mounting method where the slider assemblies with equal heights are used to mount the specimen on the testing setup. In this method the mounting point are along a hypothetical line which is parallel to the rail. For samples with large value of $\bar{\boldsymbol{a}}$, this method the specimen collapses laterally and does not undergo instability.

Method 1

In the first case, the hinges of the snapping faces (P_4) are parallel to the guide rails (Figure 3-32A). Here, only P_4 faces undergo flexural deformation. During compression, the specimen always undergoes snap through instability. However, as the periodicity of the finite tessellation increases, the uniform distribution of the displacement is challenging to enforce as the lateral load on the clevis pins on longer links exerts larger moments about the z axis. Larger moment causes further friction in the sliders, and hence larger deviation from the expected behavior (Figure 3-32A). This problem can be solved by using longer sliders, however longer sliders may contact during the reconfiguration, and hence adversely affect the specimen performance.

Method 2

The problem encountered with the first mounting method has leads us to develop another mounting method. Instead of links of different heights, here we use equal length links to attach the faces to each slider (Figure 3-32B). The line passing through the points of the attachment remains parallel to the guiding rails during the reconfiguration. Our study shows that during the snap through instability, P_5 faces undergo bending, while P_4 experiences a combination of axial and flexural deformation. Our experimental investigation shows this method allows the accommodation of specimen with a very large number of unit cells. However, for large values of $\boldsymbol{a_2/a_1}$, the specimen no longer undergoes snap-through instability due to skewness of the specimen with respect to the loading direction; rather it collapses transversely.

3.9.16 Vibration tester

One application demonstrates the use of our metamaterial as mechanical damper. To this end we have developed a testing platform (Figure 3-33). Figure 3-33A shows the front view of the testing setup with the specimen mounted on the setup. Figure 3-33B presents the process of mounting the structure on the testing setup. The process is similar to mounting a sample on the compression/tension testing setup in Figure 3-31B.

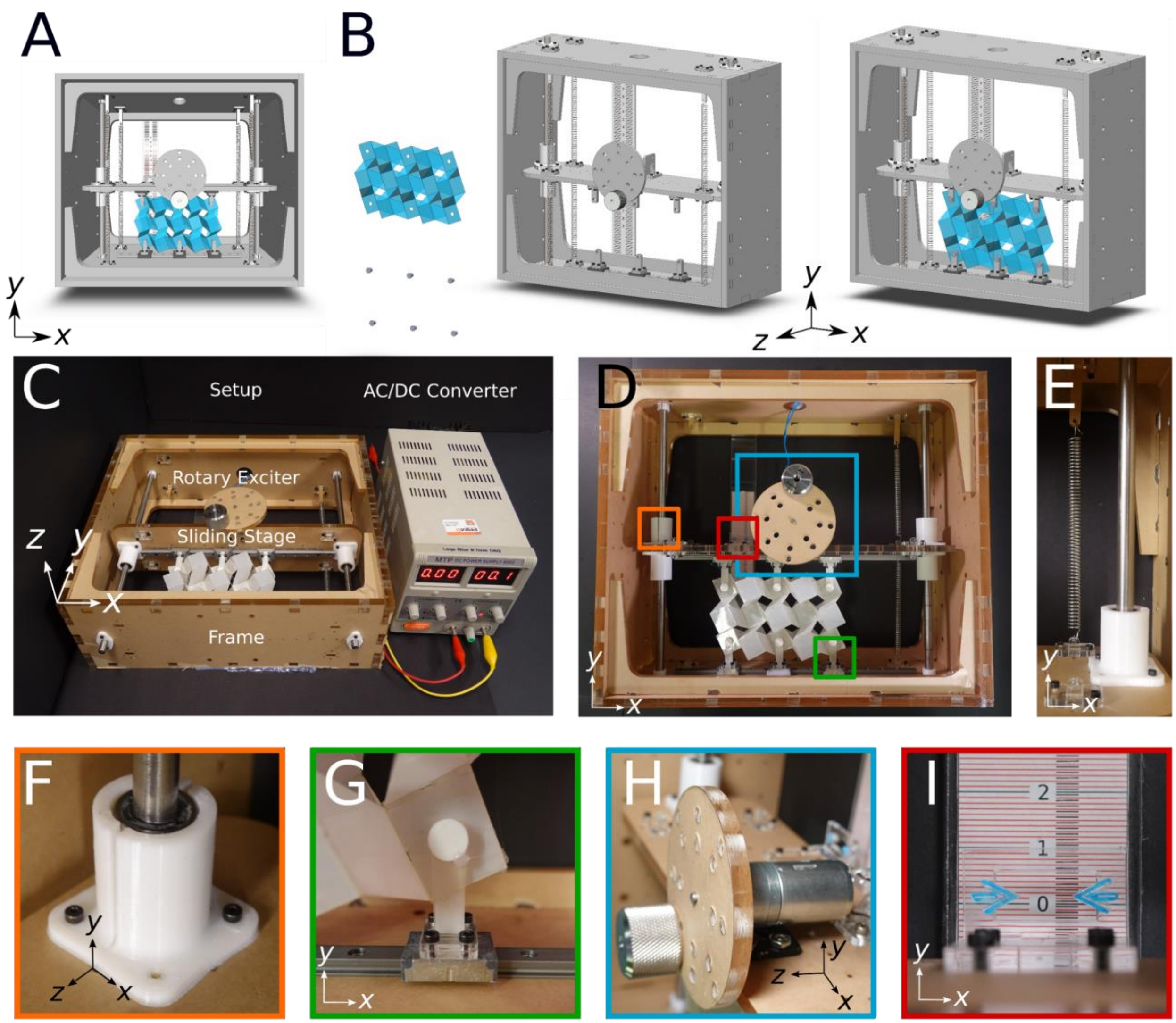

Figure 3-33 Vibration test setup. **A** Setup consisting of a frame and an AC/DC converter, **B** Front view of the oscillatory testing assembly **C-D** Components of the oscillatory testing assembly **C** Spring **D** Linear ball bearing and housing mounted on a round slide. Each side of the sliding stage is carried on two linear ball bearings. **E** Slider assembly. The sliders are free to move along rails mounted on the frame and the sliding stage, except for the middle bottom slider which is fixed to prevent from any rigid body movement of the multi-stable test specimen along the rails (*x* axis). The assembly is similar to that shown in Figure 3-26C and Figure 3-26D except for the mounting method. In this setup, pins are used to mount the setup on the testing setup. **F** Rotary exciter consisting of a gearmotor, a round disk featuring eccentric holes and a mass screwed to one of the eccentric holes on the disk. **G** Ruler and indicator, a ruler is mounted on the frame of the setup. An indicator is attached to the sliding stage. As the sliding stage oscillates the indicator

slides on top of the ruler. Using a high-speed camera, the slow motion of the displacement of the indicator on top of the ruler is recorded and later analyzed to obtain the amplitude of the vibrations.

Figure 3-33C shows the experimental setup comprising a frame, a sliding stage and a rotating unbalanced exciter. The sliding stage can slide along two guiding shafts (Figure 3-33D and Figure 3-33E). The sliding panel is attached to the frame using extension springs (Figure 3-33E). Four linear ball bearings are used to facilitate the movement of the sliding panel with respect to the guiding shafts (Figure 3-33E and Figure 3-33F). The ball bearing housings are 3d-printed and screwed to the sliding stage (Figure 3-33F). Similar to the tensile/compression testing setup, we use sliders to mount the sample on the experimental setup, Figure 3-33D and Figure 3-33G. The assembly can be considered as a mass-spring-damper system that can vibrate upon excitation or non-zero initial conditions.

The excitation is provided through a rotating unbalanced mass (Figure 3-33D and Figure 3-33H). In our setup we include a 24-volt DC gearmotor with the maximum speed of 620 rpm, Figure 3-33H. We use a 24 volts AC/DC converter to supply power to the motor (Figure 3-33C). By controlling the input voltage, we can control the speed of the motor and hence the frequency of the excitation. To obtain the amplitude of oscillation, we use a high-speed camera to record the displacement of an indicator panel with respect to a ruler, Figure 3-33I. The results are analyzed to obtain the amplitude of the vibrations at each excitation frequency.

3.10 References

1. Melancon, D., et al., *Multistable inflatable origami structures at the metre scale.* Nature, 2021. 592(7855): p. 545-550.
2. Liu, Z., et al., *Nano-kirigami with giant optical chirality.* Science Advances, 2018. 4(7): p. 1-9.
3. Overvelde, J.T.B., et al., *Rational design of reconfigurable prismatic architected materials.* Nature, 2017. 541(7637): p. 347-352.
4. Lin, Z., et al., *Folding at the Microscale: Enabling Multifunctional 3D Origami-Architected Metamaterials.* Small, 2020. 16(35): p. 1-9.
5. Kim, S.-J., et al., *An origami-inspired, self-locking robotic arm that can be folded flat.* Science Robotics, 2018. 3(16): p. eaar2915-eaar2915.

6. Rafsanjani, A., et al., *Kirigami skins make a simple soft actuator crawl.* Science Robotics, 2018. 3(15): p. eaar7555-eaar7555.
7. Teoh, Z.E., et al., *Rotary-actuated folding polyhedrons for midwater investigation of delicate marine organisms.* Science Robotics, 2018. 3(20): p. 1-9.
8. Ze, Q., et al., *Soft robotic origami crawler.* Science Advances, 2022. 8(13): p. 1-10.
9. Novelino, L.S., et al., *Untethered control of functional origami microrobots with distributed actuation.* Proceedings of the National Academy of Sciences of the United States of America, 2020. 117(39): p. 24096-24101.
10. Wu, S., et al., *Stretchable origami robotic arm with omnidirectional bending and twisting.* Proceedings of the National Academy of Sciences of the United States of America, 2021. 118(36): p. 1-9.
11. Melancon, D., et al., *Inflatable Origami: Multimodal Deformation via Multistability.* Advanced Functional Materials, 2022. 32(35).
12. Ze, Q., et al., *Spinning-enabled wireless amphibious origami millirobot.* Nature communications, 2022. 13(1): p. 3118.
13. Nauroze, S.A., et al., *Continuous-range tunable multilayer frequency-selective surfaces using origami and inkjet printing.* Proceedings of the National Academy of Sciences of the United States of America, 2018: p. 201812486-201812486.
14. Tao, K., et al., *Origami-inspired electret-based triboelectric generator for biomechanical and ocean wave energy harvesting.* Nano Energy, 2020. 67: p. 104197.
15. Lamoureux, A., et al., *Dynamic kirigami structures for integrated solar tracking.* Nature Communications, 2015. 6: p. 8092-8092.
16. Boatti, E., N. Vasios, and K. Bertoldi, *Origami metamaterials for tunable thermal expansion.* Advanced Materials, 2017. 29(26): p. 1700360-1700360.
17. Sareh, P., et al., *Rotorigami: A rotary origami protective system for robotic rotorcraft.* Science Robotics, 2018. 3(22): p. eaah5228.
18. Yasuda, H., et al., *Origami-based impact mitigation via rarefaction solitary wave creation.* Science Advances, 2019. 5(5): p. 1-9.
19. Choi, G.P.T., L.H. Dudte, and L. Mahadevan, *Programming shape using kirigami tessellations.* 2018(December).
20. Dudte, L.H., et al., *Programming curvature using origami tessellations.* Nature Materials, 2016. 15(5): p. 583-583.
21. Zhang, Q., et al., *Origami and kirigami inspired self-folding for programming three-dimensional shape shifting of polymer sheets with light.* Extreme Mechanics Letters, 2017. 11: p. 111-120.
22. Jamalimehr, A., et al., *Rigidly flat-foldable class of lockable origami-inspired metamaterials with topological stiff states.* Nature Communications, 2022. 13(1): p. 1816-1816.
23. Overvelde, J.T.B., et al., *A three-dimensional actuated origami-inspired transformable metamaterial with multiple degrees of freedom.* Nature Communications, 2016. 7: p. 1-8.
24. McClintock, H.D., et al., *A fabrication strategy for reconfigurable millimeter-scale metamaterials.* Advanced Functional Materials, 2021. 31(46): p. 2103428.
25. Iniguez-Rabago, A., Y. Li, and J.T.B. Overvelde, *Exploring multistability in prismatic metamaterials through local actuation.* Nature Communications, 2019. 10(1): p. 1-10.
26. Nayakanti, N., S.H. Tawfick, and A.J. Hart, *Twist-coupled Kirigami cells and mechanisms.* Extreme Mechanics Letters, 2018. 21: p. 17-17.
27. Rafsanjani, A. and D. Pasini, *Bistable auxetic mechanical metamaterials inspired by ancient geometric motifs.* Extreme Mechanics Letters, 2016. 9: p. 291-291.
28. Kamrava, S., *Origami-based structures with programmable properties.* 2017(August).
29. Kamrava, S., et al., *Programmable Origami Strings.* Advanced Materials Technologies, 2018. 3(3): p. 1-8.
30. Liu, K., et al., *Triclinic Metamaterials by Tristable Origami with Reprogrammable Frustration.* Advanced Materials, 2022. 2107998: p. 1-11.

31. Tang, Y., et al., *Programmable Kiri-Kirigami Metamaterials.* Advanced Materials, 2017. 29(10): p. 1604262-1604262.
32. Zhang, X., et al., *Kirigami-based metastructures with programmable multistability.* Proceedings of the National Academy of Sciences, 2022. 119(11): p. e2117649119.
33. Pratapa, P.P., K. Liu, and G.H. Paulino, *Geometric Mechanics of Origami Patterns Exhibiting Poisson's Ratio Switch by Breaking Mountain and Valley Assignment.* Physical Review Letters, 2019. 122(15).
34. Zhai, Z., Y. Wang, and H. Jiang, *Origami-inspired, on-demand deployable and collapsible mechanical metamaterials with tunable stiffness.* Proceedings of the National Academy of Sciences, 2018. 0: p. 201720171-201720171.
35. Lv, C., et al., *Origami based mechanical metamaterials.* Scientific Reports, 2014. 4.
36. Cheung, K.C., et al., *Origami interleaved tube cellular materials.* Smart Materials and Structures, 2014. 23(9).
37. Yasuda, H., et al., *Origami-Based Cellular Structures with In Situ Transition between Collapsible and Load-Bearing Configurations.* Advanced Engineering Materials, 2019. 21(12): p. 1-8.
38. Filipov, E.T., G.H. Paulino, and T. Tachi, *Origami tubes with reconfigurable polygonal cross-sections.* Proceedings of the Royal Society A: Mathematical, Physical and Engineering Sciences, 2016. 472(2185).
39. Filipov, E.T., T. Tachi, and G.H. Paulino, *Origami tubes assembled into stiff, yet reconfigurable structures and metamaterials.* Proceedings of the National Academy of Sciences, 2015. 112(40): p. 12321-12326.
40. Silverberg, J.L., et al., *Using origami design principles to fold reprogrammable mechanical metamaterials.* Science, 2014. 345(6197): p. 647-650.
41. Silverberg, J.L., et al., *Origami structures with a critical transition to bistability arising from hidden degrees of freedom.* Nature Materials, 2015. 14(4): p. 389-393.
42. Liu, K., T. Tachi, and G.H. Paulino, *Invariant and smooth limit of discrete geometry folded from bistable origami leading to multistable metasurfaces.* Nature Communications, 2019. 10(1).
43. Li, S., et al., *Fluid-driven origami-inspired artificial muscles.* Proceedings of the National academy of Sciences, 2017. 114(50): p. 13132-13137.
44. Cui, J., F.R. Poblete, and Y. Zhu, *Origami/Kirigami-Guided Morphing of Composite Sheets.* Advanced Functional Materials, 2018. 28(44): p. 1-7.
45. Zang, X., et al., *Laser-Induced Molybdenum Carbide–Graphene Composites for 3D Foldable Paper Electronics.* Advanced Materials, 2018. 30(26): p. 1800062-1800062.
46. Faber, J.A., A.F. Arrieta, and A.R. Studart, *Bioinspired spring origami.* Science, 2018. 359(6382): p. 1386-1391.
47. Wang, L.C., et al., *Active reconfigurable tristable square-twist origami.* Advanced Functional Materials, 2020. 30(13): p. 1909087.
48. Dalaq, A.S., S. Khazaaleh, and M.F. Daqaq, *An origami-inspired design of highly efficient cellular cushion materials.* Applied Materials Today, 2023. 32: p. 101835.
49. Shi, J., et al., *Programmable Multistable Perforated Shellular.* Advanced Materials, 2021. 33(42).
50. Wu, L. and D. Pasini, *In-situ Activation of Snap-through Instability in Multi-response Metamaterials through Multistable Topological Transformation.* Advanced Materials, 2023: p. 2301109.
51. Seyedkanani, A. and A. Akbarzadeh, *Magnetically Assisted Rotationally Multistable Metamaterials for Tunable Energy Trapping–Dissipation.* Advanced Functional Materials, 2022: p. 2207581.
52. Grey, S.W., F. Scarpa, and M. Schenk, *Mechanics of paper-folded origami: A cautionary tale.* Mechanics Research Communications, 2020. 107: p. 103540.

Chapter 4

Discussion, conclusion, and future work

Chapter 4: Discussion, conclusion, and future work

This thesis has proposed a class of origami-inspired mechanical metamaterials focusing on two intertwined aspects: (1) the design of its rigidly foldable architecture enabling multiple locked and flat-folded configurations and (2) the study of its compliant architecture capable of undergoing multistable states.

4.1 Summary of the main results

Chapter 2 has examined a strategy to impart multi-directional load-bearing capacity to a stacked structure of cellulose-based papers. Existing origami-inspired metamaterials offer a certain level of programmability, yet they fall short in attaining concurrently load-bearing capacity and rigid foldability along the deployment direction. The reason can be attributed to the kinematics of deployment and the mechanism of load-bearing they use in their crease patterns. In general, the direction of their load-bearing capacity is distinct from the direction of their deployment. This characteristic limits their application. In particular, any perturbation of the loading direction can deviate the material from its folding path and ultimately changes its response from rigid to floppy.

In response to these shortcomings, chapter 2 has introduced a rigidly foldable class of cellular metamaterials, whose folding is mainly governed by their *kinematics* rather than their *structural instability*. This class of origami materials can flat-fold and lock into several stiff states across multiple directions, including the deployment direction. Notions of origami folding with kirigami cuts have been combined to generate reconfigurable patterns made of chains shaped with N even-sided regular polygonal primitives that define the inner void. Cellular cuts relax the deformation constraints imposed by the connectivity of the parent origami. These metamaterials rigidly fold with one degree of freedom due to the constraints imposed by their adjacent layers. At the onset of bifurcation, however, the degrees of freedom increase, leading to multiple reconfiguration paths. Each path leads to post-bifurcation modes, which can be either flat-foldable or lockable states.

Locking under compression yields topology and symmetry changes that impart multi-directional stiffness. Additionally, folding paths and mixed-mode configurations can be activated *in-situ* to modulate their properties. Their load-bearing capacity, flat foldability, and programmability of shape can be harnessed for deployable structures, reconfigurable robots, and low-volume packaging. The main findings in chapter 2 are summarized as follows:

- Starting from any even-sided uniform polygon, we have shown that the proposed strategy can achieve a class of reconfigurable materials.
- Layer stacking is proposed to reduce the mobility of kinematic unit chains. A matrix-based kinematic analysis with pertinent planarity constraints has identified the minimum number of stacked layers to reduce the degrees of freedom to one. A predictor-corrector algorithm has been employed to obtain the post-kinematic bifurcation behavior. Post-bifurcation, the patterns can follow multiple kinematic paths.
- Using an enumeration theorem, we have classified the post-bifurcation modes into locked and flat-folded configurations. The multi-modal response has been interpreted as a pathway for reprogramming their folding and mechanical response *in-situ*. In particular, it has been shown that post kinematic bifurcation a change in the kinematic path can be harnessed to modulate their compressive stiffness and elastic limit.
- It has been shown that the load-bearing capacity stems from the contact between the surfaces and the edges of interlocking panels. Although this method has already been explored in the literature, previous studies have not investigated how to achieve multi-directional load-bearing capacity. Moreover, the load-bearing performance of these

structures was yet to be experimentally evaluated. The major limitation of existing load-bearable structures originates from the excessive forces exerted on the hinges upon the application of an external load. In contrast, this thesis has shown that once the structure is set in one of their locked configurations, it can withstand an external load applied along multiple directions.

- A simple manufacturing method has been proposed involving a combination of laser cutting excision, crease pattern folding, and layer stacking. It has been shown that the layers can be stacked by bonding the mountain faces of the lower layer to the valley faces of the upper layer. Although in our prototypes the layers have been assembled manually, this layer-wise process can be easily automated.

Chapter 3 has built upon the insights gained from chapter 2. Although the structures introduced in chapter 2 lock under an external load, upon unloading, they tend to revert to their initial configuration. This behavior might limit their performance under cyclic loading since upon the removal of the external load the proposed structures tend to unfold. Multistability can serve as a potential solution to enable the structure to maintain its programmed configuration even after unloading.

Multistability has gained attention in developing programmable mechanical metamaterials in the past decade. Most ideas on multistable materials rely on unit cells made of inclined beams and shallow doubly-curved shells supported by bulky frames. The bulky frames limit the reconfiguration range of existing multistable materials. In response to this inefficient use of material, chapter 3 has presented a methodology to impart multistability in the class of origami materials introduced in chapter 2. The structures can benefit from the reliable deployment of multistability while proffering minimum packaging volume due to their large reconfiguration space and flat-foldability.

To this end, chapter 3 has examined the main governing geometric parameters and identified the parallelogon as the most general primitive polygon for a quadrilateral-based pattern. The parallel edges play a pivotal role in ensuring that the subsequent mechanism is reconfigurable between two parallel planes, known as mountain and valley planes. A single-layer structure has multiple degrees of freedom. The stacking strategy used in chapter 2 has been also employed here to reduce the degrees of freedom to one. By manipulating the geometric parameters, the final configuration can be changed from locked to flat foldable. Hence, this study has enlarged the design space explored in the first paper.

Furthermore, the kinematic analysis has shown that the extent of rigid-body reconfiguration is controlled by the height of the inclined faces that connect the layers of origami system. Relaxing the rigidity constraint of the panels has enabled the emergence of multistability. The rigid-body motion and the mechanical instabilities synergically enlarge the reconfiguration space. In addition, the load bearing capacity has been achieved in a direction perpendicular to the loading direction. Mechanical instabilities can thus be regarded as an enabler for modulating elastic stiffness. The multistability behavior stems from the flexural and axial stiffness of the origami faces. As a result, the need for stiff frames is obviated since the axial stiffness is several orders larger than the flexural stiffness. The main findings of chapter 3 are:

- Definition of the conditions required to achieve flat-foldability in multiple folding directions. The results of our analysis have been summarized in a map, namely the kinematic phase diagram, which shows the boundary for flat-foldable and lockable regions.

- Explanation of the role played by the hinges in the overall multistable behavior of the origami structure. The folding/unfolding behavior of the hinges can be captured by a reduced-order model consisting of elastic, plastic, and viscous elements. The hinge parameters can be tuned from data obtained from experiments.

- Identification of four deformation regimes governing the response of a single snapping unit. Each regime is governed by a set of geometric parameters. We have shown that contact between the panels can dramatically change the behavior of the snap-through instability, and we have verified our simulation results against experimental data.

- Understanding the interaction between two snapping units arranged in series, and the transition from snap-through to snap-back instability. It has been observed that the combination of rigid folding and snap-through instability increases the force of the secondary instability and plays a key role in the occurrence of snap-back instability. In addition, it has been shown that the interaction of two snap-through instabilities can increase the energy dissipation capacity of the system.

- Construction and testing of multicell patterns demonstrating the advantages of the interaction mechanism between instabilities. The results of two experiments have been used to explain the role of interactions. In the first experiment, the faces of a two-layer structure were constrained in the out-of-plane direction using screws that keep the faces at a predefined distance. In the second experiment, the parallel faces were free to move in the out-of-plane direction. The results have shown the important role of panel interactions in the snapping behavior of the overall system.

- Demonstration of the use of multistability in origami specimens delivering mechanical damping for vibration attenuation. The experimental results have indicated that in each loading/unloading cycle, energy is dissipated due to the snapping behavior of the structure and other factors, hence suggesting their use to damp the oscillation caused by a rotary unbalanced mass. As a result, the proposed structures can reliably decrease the resonant amplitude of vibrations.

4.2 Future work

The following is proposed as continuation for future work:

- The foam-like architecture of the origami-inspired materials described in this thesis makes them a possible candidate for packaging. The structures studied in this work feature tubular forms that can lock cylindrical objects upon folding. Our preliminary observation can be further investigated to evaluate their potential for package protection. Paper-based materials can thus potentially be used for environmentally friendly packaging.

- One of the emerging applications of origami-inspired structures is wearable and flexible electronics. For example, in one application, the parallel faces of our structures can serve as the panels of a variable capacitor. The change in the distance can serve as feedback for sensing. In another example, the parallel faces can be coated with small antennas. Upon reconfiguration, the area covered by the antenna can changed, hence offering opportunity to control the frequency.

- Our class of foldable materials possesses high stiffness-to-weight ratio. In their closed cell configuration, they can offer increased resistance against penetration. A potential application is thus for the core of rigid sandwich panels that can be multi-directionally load-bearing. Our preliminary investigation corroborates this assumption; further study is required to assess their performance compared to that of existing sandwich panel cores.

- The damping capacity has been demonstrated with an oscillatory system for two interacting instabilities. Future work can investigate the snapping interaction of multiple unit cells. Since the force required to generate instability can largely vary between subsequent instabilities, our metamaterials can serve as vibration insulators offering sizeable band gaps.

4.3 Publications

4.3.1 Refereed journals

- **A. Jamalimehr**, A. Akbarzadeh, and D. Pasini, A multistable class of origami-inspired metamaterials for mechanical damping and vibration mitigation under oscillatory motion. *To be submitted*, 2023
- **A. Jamalimehr**, M. Mirzajanzadeh, A. Akbarzadeh, and D. Pasini, Rigidly flat-foldable class of lockable origami-inspired metamaterials with topological stiff states. Nat Commun 13, 1816 (2022). https://doi.org/10.1038/s41467-022-29484-1

4.3.2 Conference abstracts

- **A. Jamalimehr**, A. Akbarzadeh, and D. Pasini, A class of origami-inspired multistable mechanical metamaterials, in SES 2021, Online.
- D. Pasini, **A. Jamalimehr**, and M. Mirzajanzadeh, Topological, reconfigurable load-bearing cellular origami, in APS March Meeting 2021, 2021.
- **A. Jamalimehr**, M. Mirzajanzadeh, A. Akbarzadeh, and D. Pasini, Topological, reconfigurable load-bearing cellular origami, in IDTEC-CIE 2021, Online.
- **A. Jamalimehr**, M. Mirzajanzadeh, A. Akbarzadeh, and D. Pasini, A class of origami-inspired mechanical metamaterials with multiple flat-foldable and load-bearing states, in SES 2020, Online.

4.3.3 Patent

- **A. Jamalimehr**, M. Mirzajanzadeh, A. Akbarzadeh, and D. Pasini, A load-bearing multi-state material, Filed for US Patent